

TOPOLOGICAL EXCITATIONS IN AN ATOMIC
BOSE GAS &
SEXUAL HARASSMENT REPORTED BY
UNDERGRADUATE PHYSICISTS

A Dissertation

Presented to the Faculty of the Graduate School
of Cornell University

in Partial Fulfillment of the Requirements for the Degree of
Doctor of Philosophy

by

Lauren Moïse Aycok

August 2016

© 2016 Lauren Moise Aycock

ALL RIGHTS RESERVED

TOPOLOGICAL EXCITATIONS IN AN ATOMIC BOSE GAS &
SEXUAL HARASSMENT REPORTED BY UNDERGRADUATE PHYSICISTS

Lauren Moïse Aycock, Ph.D.

Cornell University 2016

Cold atoms are highly tunable and controllable systems that can explore the impact of quantum statistics on many-body physics and realize topological states.

This thesis presents three experiments toward these goals:

1. We implemented a measurement technique to optimize imaging of s -wave scattering halos in degenerate Fermi gases (DFGs) and took preliminary steps toward realizing effective p -wave interactions.
2. We launched solitons in elongated Bose-Einstein condensates (BECs) and observed a soliton's Brownian motion. We also showed that a dilute background of impurities dramatically effects the soliton. The added impurities scatter off the much larger soliton, contributing to its Brownian motion and decreasing its lifetime.
3. We created a hybrid two-dimensional (2-D) lattice with synthetic flux. This hybrid 2-D lattice was only three sites wide in one dimension, ideal for studying edge states. We directly imaged the localized edge and bulk eigenstates of BECs in this quantum Hall ribbon. Further, we observed both the skipping orbits of atoms traveling down our system's edges and a universal dynamical Hall conductivity.

For future studies, loading a soliton into a Bose quantum Hall ribbon would add the complexity of interactions.

In the remainder of this thesis, I turned my attention to the study of the community of physics, focusing on a measurement of sexual harassment experienced and observed by undergraduate women while studying physics. We conducted an internet-based survey (n = 522) of attendees of the American Physical Society's (APS) Conferences for Undergraduate Women in Physics (CUWiP) to measure the extent to which attendees personally experienced or observed sexual harassment in a context associated with physics. Forty-nine percent of the respondents reported having experienced sexual harassment in physics and forty-eight percent of respondents reported 'sometimes' or 'often' observed harassment in physics. Sexual harassment contributes to a chilly or unwelcome climate for both harassment targets and observers. It is unknown how prevalent sexual harassment is in the field of physics and whether or not it is a contributing factor to the field's inability to recruit and retain female students.

BIOGRAPHICAL SKETCH

Lauren Moïse Aycock attended the University of Illinois at Urbana-Champaign (UIUC) from 2004 to 2008, when graduated with a Bachelor of Science in Physics. As an undergraduate, she was introduced to research with ultracold atoms by her academic advisor, Professor Brian DeMarco. In addition to her academic work and research in physics, she co-founded and was president of the Society for Women in Physics at UIUC, an organization that is still going strong today.

In August 2008, she began her doctoral studies at Cornell University in the field of physics and she became a National Science Foundation's Graduate Research Fellow in 2010. From January 2009 to October 2012, she pursued her research in the lab of Mukund Vengalattore, where she took the lead role in the construction of a Bose-Einstein condensate apparatus.

In January 2013, Lauren joined the Laser Cooling and Trapping Group at the National Institutes of Standards and Technology (NIST) in Gaithersburg, Maryland to complete her graduate studies as an in-absentia Cornell student working at the Joint Quantum Institute (JQI). More specifically, she joined the Rubidium-Potassium (Rb-K, formerly known as RbII) team and her thesis research was supervised by Dr. Ian Spielman, a NIST and JQI Fellow.

For survivors,
I am sorry this happened to you.
It's not your fault. I believe you.
You are not alone.

ACKNOWLEDGEMENTS

First, I would like to thank the National Science Foundation's (NSF) Graduate Research Fellowship program for their support. The research in this thesis was partially supported by the Army Research Office's (ARO) Atomtronics Multidisciplinary University Research Initiative (MURI) program, by the Air Force Office Scientific Research's (AFOSR) Quantum Matter MURI, National Institute of Standards and Technology (NIST), and the NSF through the Physics Frontier Center at the Joint Quantum Institute (JQI). In addition, the research presented in Chapter 8 was supported in part by the National Science Foundation (NSF) (PHY-1346627) and by the Department of Energy (DOE) (DE-SC0011076). Opinions, findings, or conclusions expressed in this thesis are my own and do not necessarily reflect the views of the NSF, DOE, APS, ARO, AFOSR, JQI, NIST or Cornell University.

I am delighted to thank my thesis advisor, Ian Spielman for the opportunity to join his lab, his guidance and boundless enthusiasm on research from the mundane to the profound, and his fabrication of motivational posters. The Laser Cooling Group at NIST and the JQI has been a fantastic community to work in. Thanks to Bill Phillips, Paul Lett, Steve Rolston, Trey Porto, Gretchen Campbell, and Emily Edwards for their useful discussions about science and the doing of science. My time at NIST has been fantastic thanks to all of the wonderful people I had the benefit of hobnobbing with: Jeremy Clark, Roger Brown, Avinash Kumar, Steve Eckel, Chris Billington, Paco Salces-Carbona, Seiji Sugawa, Andika Putra, Elizabeth Goldschmidt, Nichole Nadermann, and Katie Schwarz. I would like to thank Victor Galitski for his fascination with having a classical object in a BEC which inspired our results in Chapter 6. Hilary Hurst has been an invaluable collaborator and I enjoyed our time working on soli-

tons together as an experimentalist/theorist team. My sincere thanks to Ross Williams, Matt Beeler, and Lindsay LeBlanc for setting a high bar and their adept handing off of the Rb-K apparatus. Heartfelt thanks go to Abigail Perry, who pushed me and gave me a scientific and professional attitude to aspire to. My sincere thanks to Ben Stuhl for always knowing the precisely correct wording with which to express an idea, to Hsin-I Lu for her relentless determination and sense of humor when brilliantly tackling a puzzle, and to Dina Genkina for her insightful questions and ideas which always kept me on my toes. I am grateful to our German interns Marcell Gall, Max Schemmer, and Martin Link for their fresh jolt of enthusiasm and excitement in lab.

I would like to thank my first year cohort at Cornell University, in particular Kasturi Saha, Zach Lamberty, Dusty Madison, Julia Mundy, Gala Nicolas-Kaufman, and Kendra Letchworth-Weaver (honorary 2008 cohort member), for their support, community, and shared struggles. My sincere thanks to my special committee, Erich Mueller, Dan Ralph, and Carl Frank, for enabling me to complete my thesis research in my chosen field, for reading this thesis, and providing helpful comments and suggestions. Heartfelt thanks to Nate Ellis for teaching me to machine, and to Collin Reynolds, Kristina Colladay, and Srivatsan Chakram for being excellent lab mates to learn from and with. I grateful to the several amazing undergraduates I had the pleasure of working with: Shannon Harvey, Scott Flanz, Sam Roland, Eli Fox, Chandler Kemp, John Lombard, Benjamin Nosarzewski, and Airlia Shaffer.

I am profoundly grateful to Ritchie Patterson and Julia Thom-Levy for their leadership making the physics department a more inclusive community. Thanks to Beth Livingston, the unofficial member of my special committee, whose insights were invaluable. I am grateful to my collaborators: Kate Clancy,

Eric Brewe, Zahra Hazari, Renee Michelle Goertzen and Ted Hodapp, for assisting me with my aspirations to include a social science result in my physics thesis.

Lastly, the completion of this thesis would have been impossible without the love and support of William McGehee, my sisters Amanda and Lizzy, and my parents Claudia and Rickey. Thank you.

TABLE OF CONTENTS

Biographical Sketch	iii
Dedication	iv
Acknowledgements	v
Table of Contents	viii
List of Tables	xi
List of Figures	xii
1 Introduction	1
2 Manipulating particles with external fields	5
2.1 Atomic structure and interaction with external magnetic fields . .	5
2.1.1 Atomic structure at zero magnetic field	5
2.1.2 Interacting with external magnetic fields	6
2.2 Optical dipole potentials	9
2.2.1 Optical Lattices	11
2.3 Charged particle interacting with magnetic fields	12
2.3.1 Aharonov-Bohm effect	14
2.3.2 Quantum Hall Effect	16
2.4 Fooling neutral atoms to act like charged particles in magnetic fields	17
2.4.1 Artificial gauge fields	18
3 Degenerate quantum gases	21
3.1 Brief review of quantum statistics	21
3.1.1 Identical particles	21
3.1.2 Bose-Einstein Condensates	24
3.1.3 Degenerate Fermi Gases	26
3.2 Scattering in ultracold atomic gases	29
3.2.1 <i>s</i> -wave scattering length	29
3.2.2 Scattering between different internal states	31
3.2.3 Feshbach resonances	32
3.3 Brief Intro/Overview of the Gross-Pitaevskii Equation	33
4 Rubidium-Potassium Apparatus	37
4.1 Experimental sequence for creation of a BEC	37
4.2 Experimental sequence for creation of a DFG	41
4.3 Lasers!	43
4.3.1 Potassium cooling lasers	43
4.3.2 Optical dipole trap	49
4.3.3 Optical lattices and Raman lasers	50
4.3.4 Green plug beam	52
4.3.5 Imaging systems	54

4.4	Magnetic fields	55
4.4.1	Magnetic field stabilization with microwave servo	57
5	s-Wave Scattering of Fermions	61
5.1	Introduction	61
5.2	<i>s</i> -wave scattering experiment	62
5.2.1	Preparation of 50/50 spin mixtures in DFGs	63
5.2.2	Mapping out the Feshbach Resonance	63
5.2.3	Magnetic field calibration	65
5.2.4	Optical lattice for ^{40}K	67
5.3	<i>s</i> -wave scattering results	70
5.3.1	Image processing	70
5.3.2	<i>s</i> -wave scattering halos	71
5.3.3	Determination of Feshbach resonance magnetic field position	75
5.3.4	Conclusion	76
5.4	Outlook: synthetic partial waves with ^{40}K	77
5.4.1	Technique: Optical dressing then lattice pulsing	77
5.4.2	Technique: Pulse Raman, pulse lattice, optically dress	81
6	Solitons in the presence of Impurities	84
6.1	Introduction	84
6.2	Solitons in elongated condensates	85
6.2.1	Soliton creation and optimization.	86
6.2.2	Soliton oscillations	87
6.2.3	Microwave tomography	89
6.3	Injecting impurity atoms	93
6.3.1	Injection and number calibration	93
6.3.2	Temperature measurements with impurities	96
6.4	Solitons in the presence of impurities	97
6.4.1	Impact on oscillations	97
6.4.2	Impact on lifetime	98
6.4.3	Enhanced diffusion	102
6.5	Conclusions and outlook	105
7	Bose-Einstein Condensates in the quantum Hall regime	107
7.1	Introduction	107
7.2	Synthetic Dimensions: Particle in a Box	108
7.3	Synthetic Flux: Quantum Hall Ribbon	114
7.3.1	The Harper-Hofstadter Hamiltonian	115
7.3.2	Eigenstates of the Harper-Hofstadter Hamiltonian	116
7.4	Dynamic Hall effect	119
7.5	Edge magnetoplasmons: skipping orbits	122
7.6	Conclusions and Outlook	125

8	Physics, we have a problem: sexual harassment	126
8.1	Introduction	126
8.2	Methods	128
8.2.1	Ethics Statement	128
8.2.2	Participant Recruitment	129
8.2.3	Participant Demographics	130
8.2.4	Survey Design	133
8.2.5	Enumeration and Analysis	135
8.3	Results and Discussion	136
8.3.1	Female undergraduate physics majors experience and observe sexual harassment	136
8.3.2	Correlations with belief in serious gender issues in physics and physics GPA	139
8.3.3	Study Limitations	143
8.4	Outlook and Moving Forward	144
A	Nondestructive imaging of an ultracold lattice gas	146
B	Visualizing edge states with an atomic Bose gas in the quantum Hall regime	151
C	Feshbach enhanced s-wave scattering of fermions: direct observation with optimized absorption imaging	157
D	Geometrical pumping with a Bose-Einstein condensate	172
	Bibliography	178

LIST OF TABLES

4.1	Bias fields during experiment sequence	42
4.2	Potassium repumping beams.	46
4.3	Potassium cooling beams	47
4.4	Optical dipole trap beam waists	49
8.1	Sample demographics	132
8.2	Pre-survey Questions	134
8.3	Post-survey Questions	135

LIST OF FIGURES

2.1	Atomic Structure for ^{87}Rb (^{40}K)	6
2.2	Hyperfine structure of ^{87}Rb and ^{40}K	8
2.3	Band structure for 1-D optical lattice	13
2.4	Particle with charge q confined to a 2D plane with perpendicular magnetic field \mathbf{B}	13
2.5	The Aharonov-Bohm effect	15
2.6	Conducting edge states	17
2.7	Synthetic magnetic field with artificial gauge fields.	19
3.1	Identical particle under exchange	22
3.2	The chemical potential μ versus temperature T for constant density n	23
3.3	The condensate fraction versus temperature	26
3.4	Fermi distribution of occupation number versus energy	27
3.5	Results from a 1-D GPE solver	35
4.1	Schematic of Rb-K BEC/DFG machine	38
4.2	Schematic of custom Evanescent Optics Inc. fiber splitter.	39
4.3	Potassium Error Signal	44
4.4	Potassium repumper laser system	45
4.5	Potassium cooling laser	48
4.6	Schematic of our 1-D optical lattices and Raman lasers	51
4.7	Beam shaping our green plug beam	53
4.8	xy imaging system	54
4.9	Large coils: H-bridge and current feedback	56
4.10	Microwave source schematic	58
4.11	Magnetic field stabilization	60
5.1	Atom loss near Feshbach resonance.	65
5.2	Feshbach molecule creation and dissociation.	66
5.3	DFG after a $\pi/2$ Raman pulse at $\delta = 4E_R$	68
5.4	Our experimental setup.	70
5.5	Examples of our corrected and uncorrected absorption images.	72
5.6	Corrected images of s -wave scattering halos	73
5.7	Inverse Abel transform of corrected image.	74
5.8	Normalized scattered population plotted versus bias field B	76
5.9	π -pulse with low Raman coupling	79
5.10	Motion of optically dressed ^{40}K atoms	80
5.11	Pulse Raman, then pulse lattice	82
6.1	Elongated BEC setup	86
6.2	Soliton tracking	88
6.3	Soliton oscillations	90

6.4	Microwave tomography of in-situ width	91
6.5	Effect of gravitational sag	92
6.6	rf-Tomography of solitons	94
6.7	Impurity Characterization	96
6.8	Impact of impurities	99
6.9	Measured survival probability.	100
6.10	Soliton lifetime in the presence of impurities.	101
6.11	Brownian diffusion for different impurity fractions.	103
6.12	Brownian diffusion constant versus impurity fraction.	104
7.1	Particle in a Box with Synthetic Dimensions	109
7.2	Bloch bands for hybrid 2-D lattice	111
7.3	Particle in a box in e_s data	113
7.4	Experimental schematic for hybrid 2-D lattice with flux	115
7.5	Bloch bands for hybrid 2-D lattice with magnetic flux	117
7.6	Eigenstates for positive and negative flux	119
7.7	Chiral Current in Quantum Hall Strip	120
7.8	Dynamic Hall effect	122
7.9	Schematic of Skipping Orbits	123
7.10	Skipping orbits	124
8.1	Observed and experienced sexual harassment in physics	137
8.2	Sexual harassment in physics reported by female undergraduate physics majors by their race and ethnicity.	138
8.3	Experienced versus frequency of observed sexual harassment.	140
8.4	Correlation between belief in unresolved gender issues in physics and either frequency of observation or personally experienced sexual harassment in physics.	142
8.5	Correlation between physics GPA and either frequency of observation or personally experienced sexual harassment in physics.	143

CHAPTER 1

INTRODUCTION

We are interested in studying new topological phases of matter, where non-local topological properties emerge from local degrees of freedom. Cold atom systems offer a good venue to create and study topological matter because they are tunable and easy to probe quantum systems. Twenty years ago, laser cooling and trapping of bosonic atoms led to the observation of a new state of matter, Bose-Einstein condensates (BEC) [7]. Shortly after, the onset of Fermi degeneracy in a cold gas of fermions was observed as well [46]. A degenerate Fermi gas (DFG) was not a new state of matter, for example, the electrons in a room temperature metal (e.g. a penny). In contrast to their solid state counterparts, many features of quantum gases can be straightforwardly calculated and give insight to many-body physics of fermions. These atomic gas samples are created in vacuum and trapped by magnetic fields and laser light, which can be configured to any arbitrary potential and even be a knob for tuning the inter-particle interactions. Experimental dynamics occur on millisecond timescales and single-atom resolution is now possible with quantum gas microscopes [13, 119]. For these reasons, we believe cold atom systems are ideal systems to realize topologically interesting states of matter and study many-body quantum physics. This thesis details three experiments toward that goal.

The quintessential topological effect is the quantized conductance in 2D electron gases called the Quantum Hall Effect [65]. This effect was originally observed at the large magnetic field of $\sim 15\text{T}$. We experimentally realized a large artificial magnetic field for a ^{87}Rb BEC in a 2-D hybrid lattice [35]. This lattice we created existed in both spin and position space. Introducing complex tunneling

allowed us to create a synthetic magnetic field equivalent to $\sim 20,000$ T in a condensed matter system¹. Our spin dimension only had 3 sites, which naturally created a hard walled potential ideal for studying edge states. We observed localized chiral currents and cyclotron orbits[124, 93].

After measuring these single-particle effects in the quantum Hall regime, we wanted to build on our understanding by adding a new level of complexity: interactions. Typical measurements of the effects of interactions in a BEC are performed through observing collective modes or solitons. Once we made long lived solitons, we began to explore measurement options. Our theorist collaborator, Victor Galitski, suggested having a small fraction of atoms in a different internal state interacting with a soliton would be interesting. A soliton in a BEC is similar to a classical object in a quantum gas. We observed that these impurity atoms dramatically decreased the soliton lifetime and enhanced its Brownian diffusion.

An another example of a topological state is a Majorana fermion. In solid state superconductors or in DFGs, these Majorana fermions are exotic quasiparticle excitations, which are their own anti particle and exhibit non-abelian braiding statistics [131]. Interactions characterized by p -wave and other higher odd partial waves in a spin polarized Fermi gas are critical for engineering DFGs to support Majorana fermions [138]. The first measurement presented in this thesis explored an s -wave Feshbach resonance by directly imaging elastic scattering of two DFGs with opposite momenta [54]. We then report on preliminary attempts to modify the fermionic interaction by laser dressing, an extension of a technique already demonstrated to introduce d - and g -wave contributions to scattering in BECs [134]. Using this technique to create p -wave interactions would

¹This is calculated for a material with a 5 \AA lattice spacing.

be a step towards observing Majorana fermions in a DFG.

In parallel with these traditional physics experiments, I turned my attention to studying the physics professional environment, focusing on the issue of sexual harassment. At the American Physical Society's (APS) March Meeting 2015 during the panel discussion at the end of Session F33: Supporting the Recruitment and Retention of Women in Physics, I brought up sexual harassment and assault in professional contexts and asked how it impacted women at other universities. After my question, a member of the lesbian, gay, bisexual, and transgender (LGBT) community also shared her concerns. She credited my speaking up with her ability to speak up as well. After the session, many women approached me and shared their stories. A majority of the stories were of assault and rape perpetrated by other physicists. Other conference attendees continued to seek me out and share their stories for the duration of the conference.

Recently, a survey academic field experiences (SAFE) in anthropology reported 64% of respondents experienced sexual harassment and 22% experienced sexual assault [40]. I wanted to perform a similar survey in physics. In May 2015, I contacted the lead author on the SAFE study, Professor Kathryn Clancy. In June 2015, I met with Theodore Hodapp, Director of Education at APS, to advocate for such a survey. Together in collaboration with Eric Brewé, Renee Michelle Goertzen, and Zahra Hazari, we added a few questions on sexual harassment to their annual evaluation survey for the APS Conference for Undergraduate Women in Physics (CUWiP). I hope our results from this study assist in persuading others a broader survey of physics professional environments would be a useful endeavor. I believe this result is the beginning of quantitatively studying how prevalent sexual harassment is in the field of physics

and whether it's a contributing factor to the field's inability to recruit and retain female students.

Lastly, appendices A-D are peer-reviewed, published articles to which I contributed to during the course of my PhD.

CHAPTER 2

MANIPULATING PARTICLES WITH EXTERNAL FIELDS

Ultracold atoms are easily manipulated with magnetic fields, laser light and radio-frequency (rf) magnetic fields. This chapter reviews some basic atomic structure and interactions between electromagnetic fields and atoms. Additionally, we discuss an interaction of a charged particle with a magnetic field and how charge neutral atoms behave in an analogous fashion when manipulated by external fields.

2.1 Atomic structure and interaction with external magnetic fields

All results in this thesis were with alkali atoms, which have one valence shell electron and in their ground state the total angular momentum $\mathbf{L} = 0$. This places them in the first column of the periodic table and they are often referred to as hydrogen-like. For our experiments with Bose-Einstein condensates, we used ^{87}Rb atoms. For our experiments with degenerate Fermi gases, we used ^{40}K . For more details on laser cooling and trapping and physical and optical properties of ^{87}Rb and ^{40}K , I recommend Refs. [95], [121], and [127].

2.1.1 Atomic structure at zero magnetic field

Spin-orbit coupling of the spin $\mathbf{S} = 1/2$ of the one valence electron and the spin \mathbf{L} associated with its angular momentum gives rise to fine structure of an alkali

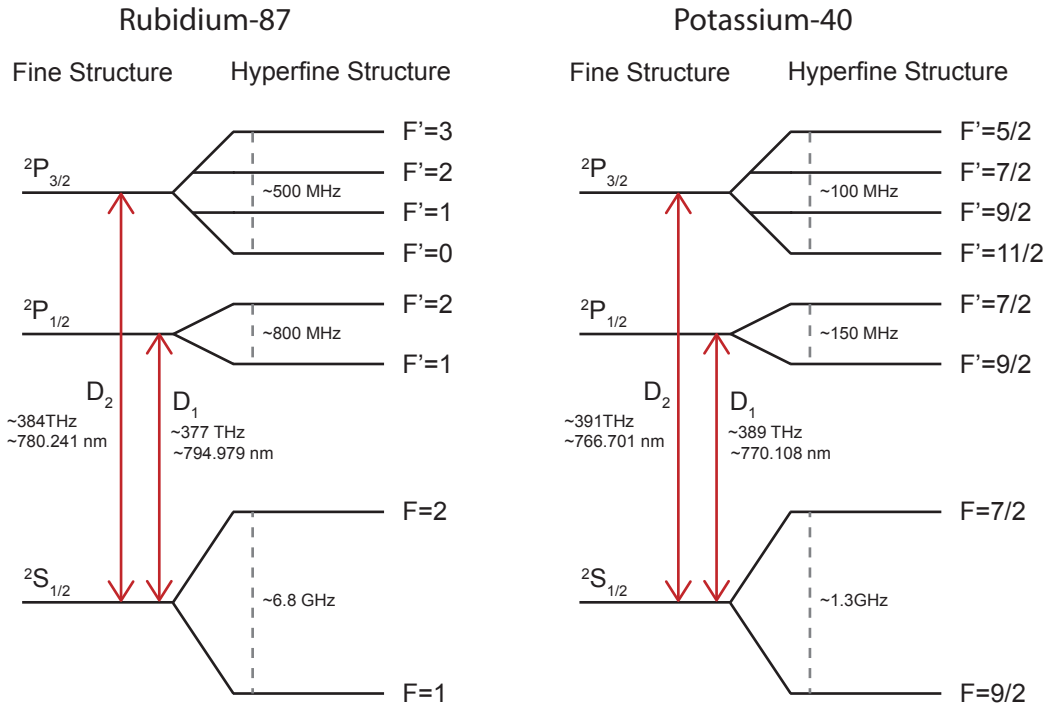


Figure 2.1: Level diagram of the fine and hyperfine structure of ^{87}Rb (^{40}K). Energy levels are not to scale. Energy splitting [121, 127] is provided to show orders of magnitude.

atoms. For the first excited state $L = 1$, thus the total angular momentum \mathbf{J} can be either $1/2$ or $3/2$ for the Fraunhofer D1 and D2 lines, respectively. Fine structure states are further divided into hyperfine states. The total angular momentum of the electron \mathbf{J} couples to the nuclear spin \mathbf{I} giving the total angular momentum of the atom $\mathbf{F} = \mathbf{I} + \mathbf{J}$. Figure 2.1 displays the fine and hyperfine structure for ^{87}Rb (^{40}K).

2.1.2 Interacting with external magnetic fields

An alkali atom's hyperfine manifold consists of $(2\mathbf{I} + 1) \times (2\mathbf{J} + 1)$ Zeeman sublevels. An applied static magnetic field can shift the energy of these sublevels

because magnetic moments due to spin and orbital angular momentum interact with such fields similar to how a loop of current would¹. In terms of the atom's total magnetic dipole $\boldsymbol{\mu}_A$ and external magnetic field \mathbf{B} , the shift in energy for a Zeeman sublevel is

$$H_B = -\boldsymbol{\mu}_A \cdot \mathbf{B} = \frac{\mu_B}{\hbar}(g_S \mathbf{S} + g_L \mathbf{L} + g_I \mathbf{I}) \cdot \mathbf{B} \quad (2.1)$$

where g_S, g_L , and g_I are the electron spin, the electron orbital and the nuclear g-factors that correspond to the different magnetic dipole moments arising from specified angular momenta. For small bias magnetic fields where the electronic spin has not become uncoupled from the nuclear spin and \mathbf{F} is a good quantum number, the energy shift can be approximated by $\Delta E_{|F m_F\rangle} = \mu_B g_F m_F B$, where g_F is the Landé g-factor of the atomic state. This regime is dubbed the linear Zeeman regime because the energy shifts linearly depend on the magnetic field.

For the ground state of alkali atoms, H_B can be exactly solved. This solution is the Breit-Rabi formula, which describes energy shifts due to an external magnetic field from small (linear Zeeman) to intermediate to larger (hyperfine Paschen-Back regime) as compared to the hyperfine energy splitting. The energy shifts of ⁸⁷Rb and ⁴⁰K ground states, given by

$$E_{|J=1/2 m_J I m_I\rangle} = -\frac{\Delta E_{hfs}}{2(2I+1)} + g_I \mu_B m B \pm \frac{\Delta E_{hfs}}{2} \left(1 + \frac{4mx}{2I+1} + x^2\right)^{1/2}, \quad (2.2)$$

are plotted in Fig. 2.2. ΔE_{hfs} is the hyperfine splitting, $m = m_I + m_J = m_I \pm 1/2$ assigns the sign in Eqn. 2.2, and we define

$$x = \frac{(g_J - g_I)\mu_B B}{\Delta E_{hfs}}. \quad (2.3)$$

Equation 2.2 is not correct for the “stretched” $m = \pm(I + 1/2)$ states due to a sign

¹We focus on the regime where energy shifts caused by the applied magnetic field compared to fine structure energy splitting, thus \mathbf{J} remains a good quantum number

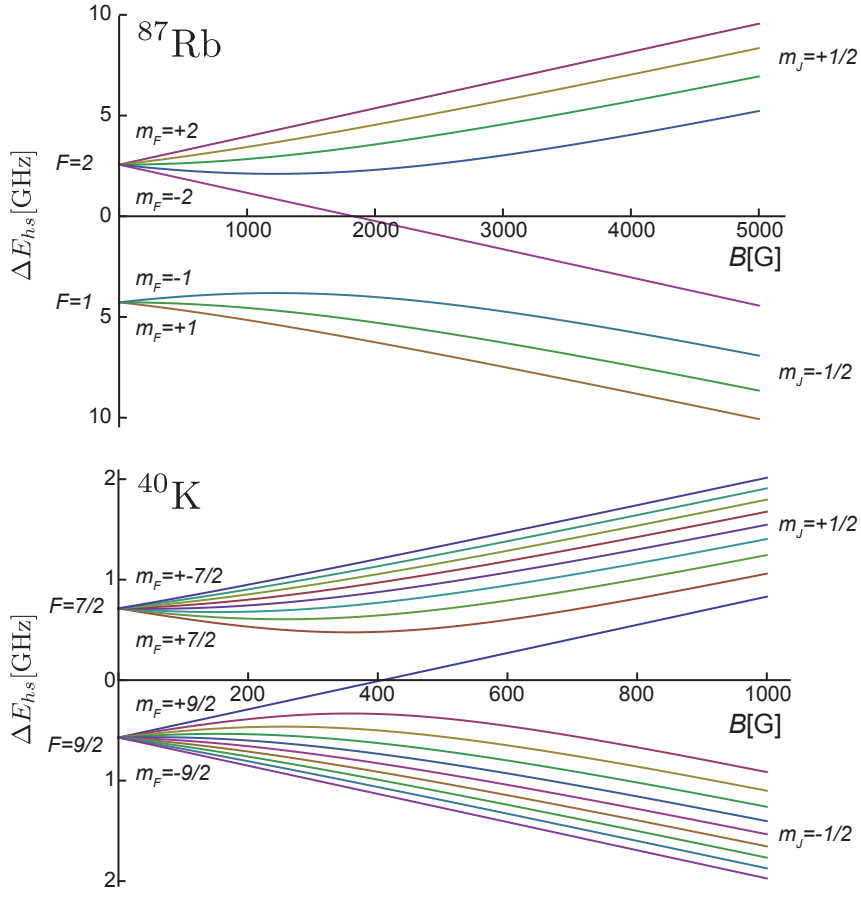


Figure 2.2: Hyperfine energy shifts of the ground states of ^{87}Rb and ^{40}K versus external magnetic field.

ambiguity. The energy shifts of the stretched states are

$$E_{|J=1/2, m_J, I, m_I\rangle} = -\frac{\Delta E_{hfs}}{2(2I+1)} + g_I \mu_B m B + \frac{\Delta E_{hfs}}{2} (1 \pm x), \quad (2.4)$$

where the \pm is selected to be the sign of m .

Shifting topics from native internal coupling in the atoms giving rise to its structure, we can change the internal state of the atom by applying external fields. We can couple different Zeeman sublevels of our atoms by illuminating them an oscillating magnetic field with frequency ω_{rf} . For ^{87}Rb , we worked with condensates in the $F = 1$ hyperfine manifold and operated at bias magnetic field

where both the $|F = 1, m_F = +1\rangle \rightarrow |F = 1, m_F = 0\rangle$ and the $|F = 1, m_F = 0\rangle \rightarrow |F = 1, m_F = -1\rangle$ transitions were close in frequency. Our energies E_{+1} , E_0 , and E_{-1} are the solutions of Eqn. 2.2 for the $|J = 1/2, m_J = -1/2, I = 3/2, m_I = +3/2, 1/2, -1/2\rangle$ or $|F = 1, m_F = +1, 0, -1\rangle$ states. We can define resonance as $\omega_{rf} = \omega_z$, where

$$\hbar\omega_z = \frac{E_{-1} - E_{+1}}{2}. \quad (2.5)$$

In the rotating frame, this defines a detuning $\delta = \omega_{rf} - \omega_z$ and a quadratic Zeeman shift² $\hbar\epsilon = |E_0 - (E_{+1} + E_{-1})/2|$. For ⁴⁰K, we work at fields where the $|F = 9/2, m_F = -9/2\rangle \rightarrow |F = 9/2, m_F = -7/2\rangle$ were not close in frequency to another transition.

2.2 Optical dipole potentials

All of our experiments were performed in optical dipole traps (ODTs) [60]. Using the semi-classical approach to an atom in a light field, the electronic states of the atom are quantized and the light is an oscillating electric field $\mathcal{E}(\mathbf{r}, t) = \mathbf{e}_z \mathcal{E}(\mathbf{r}) \exp(-i\omega t) + c.c..$ Let's consider that our atom has a ground state $|g\rangle$ and an excited state $|e\rangle$ with an optical transition frequency ω_0 defined by the energy difference between $|g\rangle$ and $|e\rangle$. Coupling to the continuum of empty modes of the electric field gives the excited state a spontaneous decay rate

$$\Gamma_0 = \frac{\omega_0^3}{3\pi\epsilon_0\hbar c^3} |\langle e | \mu_{eg} | g \rangle|^2 \quad (2.6)$$

with the dielectric constant ϵ_0 , speed of light c and the dipole matrix element μ_{eg} between the ground and excited states. For our multilevel atoms, there is

²The quadratic Zeeman shift is usually expressed as an approximation that varies quadratically with field, hence the name. Additionally, the quadratic Zeeman shift is negative, but to keep in line with our convention where we express the quadratic Zeeman shift as explicitly negative, I define $\hbar\epsilon$ as an absolute value.

more than one ground and one excited state. We can write down our transition matrix element more generally for states $|i\rangle$ and $|j\rangle$ as $\mu_{ij} = c_{ij}\|\mu\|$, where c_{ij} is a real transition coefficient and $\|\mu\|$ is a reduced matrix element.

For our Hamiltonian, which describes an atom in an electric field, the temporal variation of \mathcal{E} is important, but the spatial variation is not. The atomic charge distribution is much smaller than the wavelength of light. In this dipole approximation, our Hamiltonian is $H_{\mathcal{E}} = -\boldsymbol{\mu}_{\mathcal{E}} \cdot \boldsymbol{\mathcal{E}}$ with electric dipole operator $\boldsymbol{\mu}_{\mathcal{E}} = -e\mathbf{r}$. We use second-order time-independent perturbation theory to write down the AC stark shift

$$\Delta E_i = \sum_{j \neq i} \frac{|\langle j|H|i\rangle|^2}{\mathcal{E}_i - \mathcal{E}_j} = \frac{3\pi c^2 \Gamma_0}{2\omega_0} I \times \sum_j \frac{c_{ij}^2}{\Delta_{ij}}, \quad (2.7)$$

with dressed state energies \mathcal{E}_i and \mathcal{E}_j such that our detuning $\Delta_{ij} = (\mathcal{E}_i - \mathcal{E}_j)/2 = \omega - \omega_0$. This shift is linearly proportional to laser intensity $I = 2\epsilon_0 c^2 |\mathcal{E}|^2$.

Our conservative optical potentials in this thesis are all made with linearly polarized, $\lambda = 1064$ nm light from IPG fiber amplifiers. We show the different ground and excited states of ^{87}Rb in Fig. 2.1. Our 1064 nm laser light resolves the fine structure, but not the hyperfine structure. The expressions for the dipole potential and the scattering rate simplify to

$$U_{dip}(\mathbf{r}) = \frac{\pi c^2 \Gamma_0}{2\omega_0^3} \left(\frac{2}{\Delta_2} + \frac{1}{\Delta_1} \right) I(\mathbf{r}) \text{ and} \quad (2.8)$$

$$\Gamma_{sc}(\mathbf{r}) = \frac{\pi c^2 \Gamma_0^2}{2\omega_0^3} \left(\frac{2}{\Delta_2^2} + \frac{1}{\Delta_1^2} \right) I(\mathbf{r}), \quad (2.9)$$

where the optical transition frequency $\omega_0 = (\omega_1 + \omega_2)/2$ is an average of the transitions frequencies ω_1, ω_2 for the D_1 and D_2 lines, respectively. Additionally, we have defined an average spontaneous decay rate $\Gamma_0 = 3\Gamma_1\Gamma_2/(2\Gamma_1 + \Gamma_2)$ and associated detunings $\Delta_2 = \omega - \omega_2$ and $\Delta_1 = \omega - \omega_1$.

For our experiments, we used a crossed-beam ODT, with one beam frequency shifted from the other. Both of these beams were focused at the atoms. The intensity of a focused Gaussian beam is

$$I_{GB}(r, z) = \frac{2P}{\pi\sigma^2(z)} \exp\left(-2\frac{r^2}{\sigma^2(z)}\right), \quad (2.10)$$

where P is the power, σ is the $1/e^2$ radius, and z is the direction of propagation. The radius $\sigma(z) = \sigma_0 \sqrt{1 + (z/z_R)^2}$ depends on both the beam waist or minimum radius ω_0 and Rayleigh length $z_R = \pi\sigma_0/\lambda$. Because our laser wavelength $\lambda = 1064$ nm corresponds to a frequency that is smaller than the optical transition frequencies, our trap is red-detuned and atoms are attracted to the intensity maxima.

2.2.1 Optical Lattices

Two counter-propagating laser beams along \mathbf{e}_x with the same laser frequency ω and wavevector $k = 2\pi/\lambda$ will create an interference pattern. With V_0 representing the potential at the intensity maxima, an atom will see a periodic potential $V_{lat}(x) = -V_0 \cos^2(kx)$ and its wavefunction have the same periodicity. Borrowing from solid state physics, we can write the atom's wave function $\phi_{k_x}^{(n)}(x) = e^{ikx} \cdot u_{k_x}^{(n)}(x)$ as a product of a plane wave e^{ikx} and a function $u_{k_x}^{(n)}(x)$ with the same periodicity of the lattice [8]. In atomic physics, we call the crystal momentum k_x , the quasimomentum³. An atom in a periodic potential obeys the Schrödinger equation, so we insert ϕ_{k_x} into the Schrödinger equation

$$\left[\frac{1}{2m}(\hat{p} + k_x)^2 + V_{lat}(x) \right] u_{k_x}^{(n)}(x) = E_n(x) u_{k_x}^{(n)}(x) \quad (2.11)$$

³Rumored to be due to some one's faulty memory of the name in Ashcroft and Mermin [8]

to find a new equation for $u_{k_x}^{(n)}(x)$. We can express $u_{k_x}^{(n)}(x)$ as a Fourier series $\sum_{\ell} c_{\ell} e^{2ik_{\ell}x}$ with $-\infty < \ell < \infty$. Our potential $V_{lat}(x)$ can also be written as a Fourier series $V_{lat}(x) = -V_0(e^{ikx} + e^{-ikx} + 2)/4$, we will drop the constant term because it solely shifts the overall energy. Equation 2.11 becomes

$$\sum_{\ell} \frac{(2\hbar k_{\ell} + k_x)^2}{2m} c_{\ell} e^{2ik_{\ell}x} + \frac{V_0}{4} \sum_{\ell} c_{\ell} (e^{2ik(\ell+1)x} + e^{2ik(\ell-1)x}) = E_n \sum_{\ell} c_{\ell} e^{2ik_{\ell}x}. \quad (2.12)$$

Notice that the lattice couples together the ℓ component to the $\ell \pm 1$ components. We can now write our Schrödinger equation in matrix form

$$\sum_{ell} H_{lat} \cdot c_{\ell} = E_n \sum_{ell} c_{\ell} \quad \text{with} \quad H_{lat} = E_R \begin{cases} (k_x + 2l)^2 & l = l' \\ V/4 & |l - l'| = 1 \\ 0 & \text{otherwise,} \end{cases} \quad (2.13)$$

where we express energy in units of recoil energy $E_R = \hbar^2 k_R^2 / 2m_{\text{Rb}}$ with atomic mass m_{Rb} [57]. Additionally, the quasimomentum k_x is in units of the recoil momentum $\hbar k_R = 2\pi\hbar/\lambda_L$. Figure 2.3 displays band structure for varying lattice depths from diagonalizing this Hamiltonian. We plot the lowest three bands for a numerically evaluated spectrum with $-5 < \ell < 5$.

2.3 Charged particle interacting with magnetic fields

In quantum mechanics, the Hamiltonian of a charged particle q with momentum \mathbf{p} and mass m in a magnetic field \mathbf{B}

$$H = \frac{1}{2m} (\mathbf{p} - q\mathbf{A})^2, \quad (2.14)$$

where \mathbf{A} is the vector potential defining by $\mathbf{B} = \nabla \times \mathbf{A}$ and \mathbf{p} is momentum operator. A charged particle confined in 2-D subject to a perpendicular magnetic

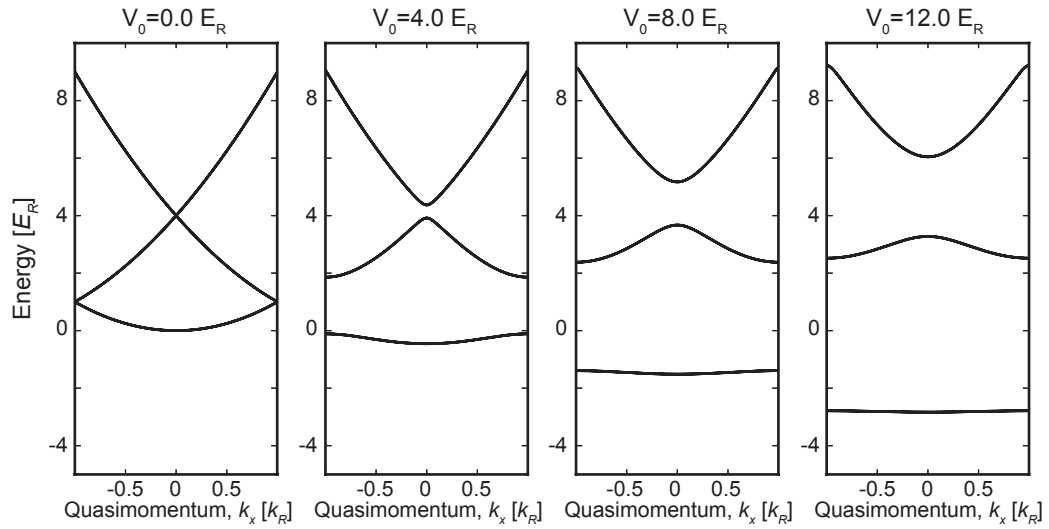


Figure 2.3: Band structure for 1-D optical lattice for varying lattice depths V_0 in the first Brillouin zone. For $V_0 = 0$, the band structure is merely the free particle dispersion folded back on itself.

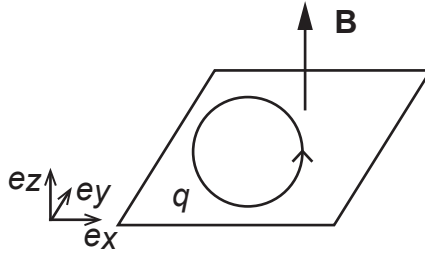


Figure 2.4: Particle with charge q confined to a 2D plane with perpendicular magnetic field \mathbf{B}

field \mathbf{B} will undergo cyclotron orbits at a constant angular frequency $\omega_c = q|\mathbf{B}|/m$ as shown in Fig. 2.4. The radius $R_c = \mathbf{v}/\omega_c$ of the orbit depends on the charged particle's velocity $\mathbf{v} = (\mathbf{p} - q\mathbf{A})/m$. For the perpendicular field $\mathbf{B} = B\mathbf{e}_z$, where $B = |\mathbf{B}|$, we can make the Landau gauge choice and define $\mathbf{A} = xB\mathbf{e}_y$. This gauge choice is slightly inconvenient because it breaks the rotational symmetry of our problem, but it will make reducing our 2-D problem to being described by a 1-D harmonic oscillator easier. Note, \mathbf{e}_x is no longer translationally invariant.

Inserting our gauge choice into Eqn. 2.14, our Hamiltonian becomes

$$H = \frac{1}{2m}(p_x^2 + (p_y + qBx)^2). \quad (2.15)$$

The trial wavefunction $\psi_k(x, y) = \psi_k(y)\psi_k(x) = e^{iky}f_k(x)$ is separable in \mathbf{e}_x and \mathbf{e}_y and is an eigenstate of p_y . Combining $\psi_k(x, y)$ and Eqn. 2.15, our Hamiltonian reduces to

$$H\psi_k(x, y) = \frac{1}{2m}(p_x^2 + (p_y + qB)^2)e^{iky}f_k(x) = \frac{1}{2m}(p_x^2 + (\hbar k + qB)^2)f_k(x) = H_k\psi_k(x), \quad (2.16)$$

where

$$H_k = \frac{1}{2m}p_x^2 + \frac{1}{2}m\omega_B^2(x + k\ell_B^2)^2 \quad (2.17)$$

is a simple 1-D harmonic oscillator Hamiltonian. The physics of our 2-D electron was reduced to a 1-D harmonic oscillator problem with the center of mass motion shifted by $-k\ell_B^2$, where we have defined a magnetic length $\ell_B = \sqrt{\hbar/m\omega_c}$. The reduction from 2-D to 1-D implies that each of the harmonic oscillator energy levels of our system are degenerate.

2.3.1 Aharonov-Bohm effect

A charged particle can still be impacted by a magnetic field \mathbf{B} even where $\mathbf{B} = 0$. An extremely long solenoid with current I and cross sectional area \mathcal{A} will create a uniform \mathbf{B} inside and outside the field will be zero. If we restrict our charged particle to a plane perpendicular to the solenoid, we can define a curl free vector potential $\mathbf{A}(\mathbf{r}) = (\Phi/2\pi r)\hat{\phi}$, where $\Phi = \mathcal{A}B$ is the flux through the solenoid. As a charged particle travels down one of the two paths illustrated in Fig. 2.5, the effect of the vector potential becomes an overall phase factor $e^{i\phi_{AB}/2}$ on the wavefunction ψ of our charged particle. We can calculate the phase

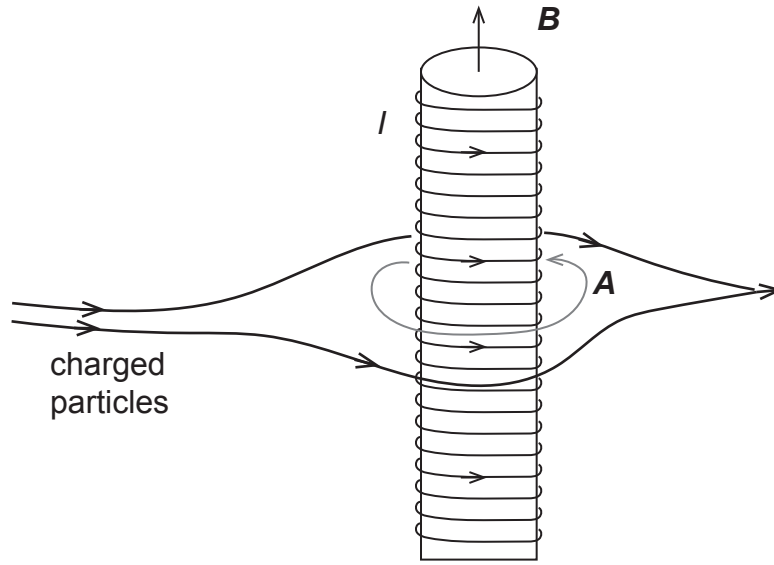


Figure 2.5: The Aharonov-Bohm effect: charged particles acquire a phase even when $\mathbf{B}=0$ as they travel on either side of a long solenoid because of a nonzero vector potential \mathbf{A} .

difference around these two paths

$$\frac{\phi_{AB}}{2} = \frac{q}{\hbar} \int \mathbf{A} \cdot d\mathbf{r} = \frac{q}{\hbar} \frac{\Phi}{2\pi} \int \left(\frac{1}{r} \hat{\phi} \right) \cdot (r \hat{\phi} d\phi) = \pm \frac{q\Phi}{2\hbar}. \quad (2.18)$$

The total phase difference between the paths is $\phi_{AB} = q\Phi/\hbar$ and depends on the magnetic field \mathbf{B} . The Aharonov-Bohm effect was first observed in shifting the interference fringes of an electron beam by adjusting the magnetic field through a solenoid [36]. In Ch. 7, we used an engineered Aharonov-Bohm phase ϕ_{AB} to define a synthetic magnetic field. This phase is order unity, which is only possible in engineered materials [53, 71], or in atomic [74, 3, 97, 79, 4, 93] and optical [62] settings.

2.3.2 Quantum Hall Effect

The signatures of the integer quantum Hall effect (IQHE) are quantized Hall conductance plateaus and their associated vanishing longitudinal resistivity [129]. Conceptually, the IQHE can be explained by the existence of protected edge states, often visualized as skipping orbits [31, 43, 65, 99]. Placing our charged 2-D particle in a strong perpendicular magnetic field \mathbf{B} closer to an infinitely hard edge than its magnetic length ℓ_B , the charged particle will reflect from the edge before completing its orbit and acquire a drift velocity along the edge. Examples of these trajectories are shown in Fig. 2.6A.

A quantum Hall bar (Fig. 2.6B) is a good conceptual tool. A voltage can be applied across contacts 1 and 4. Contacts 2, 3, 5, and 6 are voltage probes and do not supply or draw current. We will now consider our charged particle to be an electron $q = -e$. We have N available edge states. There are edge states on both edges, which are spatially separated and travel opposite directions. Applying a voltage V_1 at contact 1 injects an electron with energy $-eV_1$ into an available edge state. Because contacts 2 and 3 do not draw current, $V_1 = V_2 = V_3$. Similarly, all of the bottom contacts have the same voltage $V_4 = V_5 = V_6$. Using our total current is $I = -N(e^2/h)V_1$, we can calculate the longitudinal and Hall resistance. Our longitudinal resistance is $(V_3 - V_2)/I = 0$. The resistance across the Hall bar is the signature $(V_3 - V_5)/I = h/(Ne^2)$ quantized resistance. There are many limitations on this conceptual model, however, it provides the framework for the appearance of analogous localized edge states in Chapter 7.

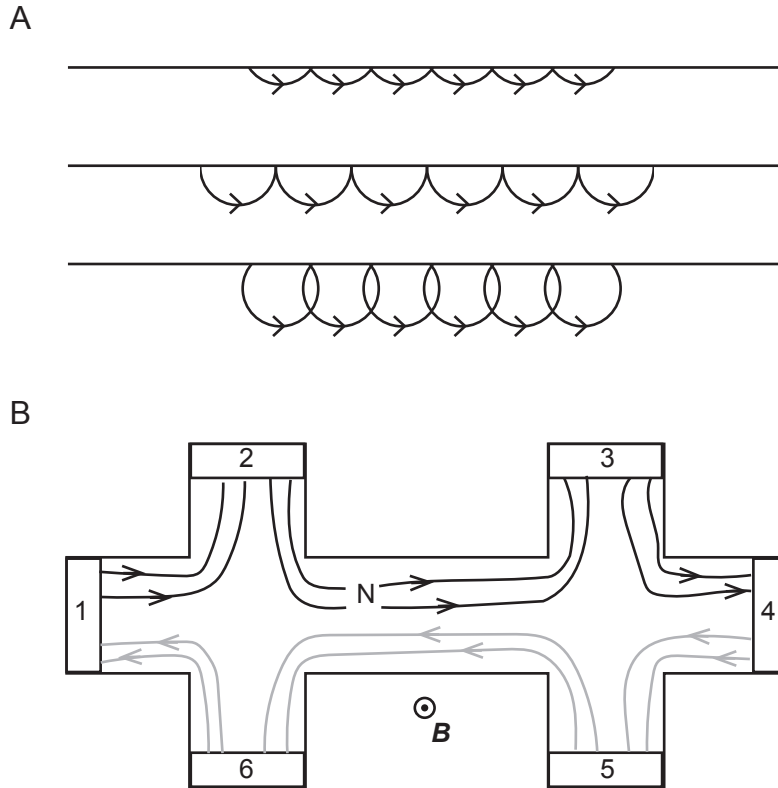


Figure 2.6: Conducting edge states. (A) Semi-classical skipping orbits offer a visualization of the conducting edge states. (B) A quantum Hall bar showing conducting edge states which can be visualized as the skipping orbits above.

2.4 Fooling neutral atoms to act like charged particles in magnetic fields

One of the first ways to make neutral atoms behave like charged particles in a magnetic field was to use the similarity between the Lorentz force $\mathbf{F}_L = q(\mathbf{v} \times \mathbf{B})$ and the Coriolis force $F_C = -2m(\boldsymbol{\Omega} \times \mathbf{v})$. This led to some awesome vortex lattices [2, 115]. However, because the magnetic field is directly proportional to the rotation rate, reaching the quantum Hall regime through rotation is diffi-

cult. The added energy heats the gas and reaching the quantum Hall regime requires the ratio of the number of vortices to the number of atoms to be of order unity. Another method is to create an artificial gauge field explained in the next section. There are many methods to accomplish this, such as shaking optical lattices to introduce a vector potential [123, 79] or laser-assisted tunneling in a tilted optical lattice [3, 97]. Here, I will describe how a two-photon Raman transition and a magnetic field gradient can create an effective magnetic field [88, 120]. For this section we will focus on ^{87}Rb .

2.4.1 Artificial gauge fields

We use a two-photon Raman transition to couple together different Zeeman sublevels in the $F = 1$ hyperfine manifold with different relative momentum $\pm 2k_R$, where k_R is the single-photon recoil momentum $\hbar k_R = 2\pi\hbar/\lambda$. This momentum defines our recoil energy $E_R = \hbar^2 k_R^2 / 2m_{\text{Rb}}$, where m_{Rb} is the atomic mass and $\lambda \approx 790$ nm is the wavelength of our Raman lasers. Populations in the different spin and momentum states will coherently oscillate with Rabi frequency Ω_R set by the laser intensity. Our counter-propagating Raman lasers have a frequency difference $\Delta\omega_R$ which is selected to be near resonance for ω_z (defined in Eqn. 2.5) at our bias field $\mathbf{B} = B_0\mathbf{e}_z$. This defines a detuning $\delta = \Omega_L - \omega_z$. Our Hamiltonian in the reference frame rotating at $\Delta\omega_L$ and in the basis $|+1, k_x + 2k_R\rangle, |0, k_x\rangle, |-1, -2k_R\rangle$ basis is

$$H = E_R \begin{pmatrix} (k_x + 2)^2 - \delta & \hbar\Omega_R/2 & 0 \\ \hbar\Omega_R/2 & k_x^2 - \epsilon & \hbar\Omega_R/2 \\ 0 & \hbar\Omega_R/2 & (k_x - 2)^2 + \delta \end{pmatrix} \quad (2.19)$$

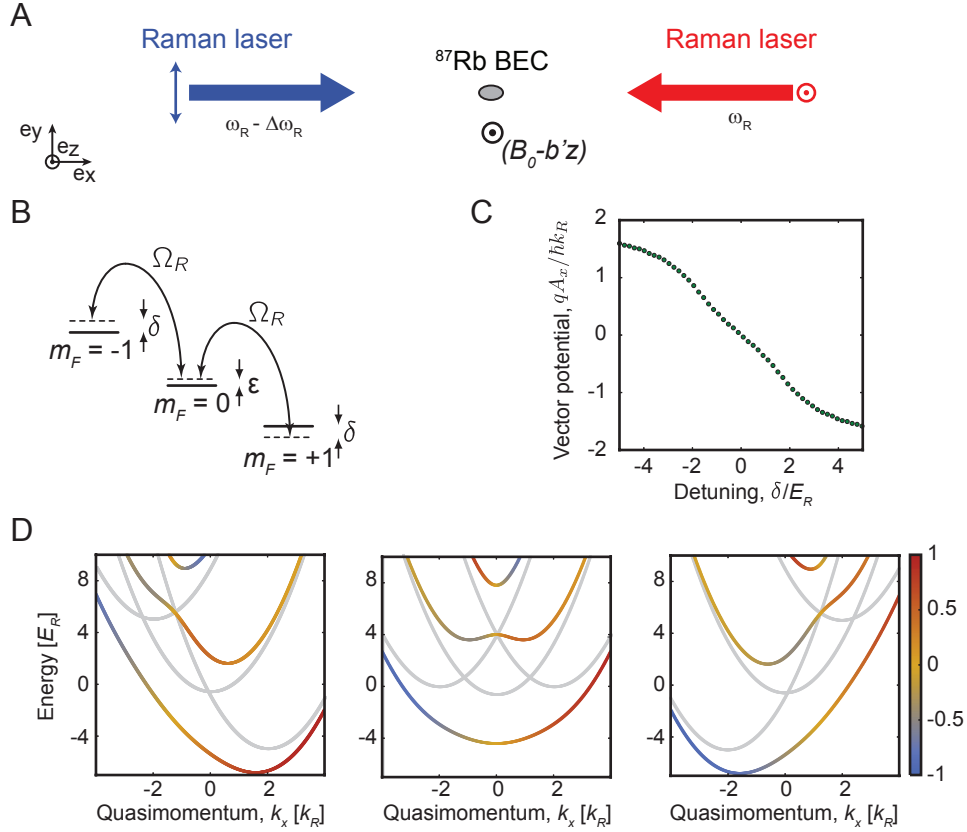


Figure 2.7: Synthetic magnetic field with artificial gauge fields. (A) Experimental setup: two counter-propagating laser beams with orthogonal linear polarization and frequency difference $\Delta\omega_R$. (B) Internal states of an $F = 1$ hyperfine manifold being addressed with a two-photon Raman transition. (C) Our simulation's vector potential $qA_x/\hbar k_r$ versus detuning δ . Due to the magnetic field gradient in \mathbf{e}_z , δ is a function of z . (D) Calculated energy bands (colorful curves) of our Raman coupling Hamiltonian for coupling strength $\hbar\Omega_R = 8.0E_R$, quadratic Zeeman shift $\hbar\epsilon = 0.6E_R$, and detunings $\hbar\delta = -5.0 E_R, 0, 5.0 E_R$ from left to right. The gray curves indicate the bare states and the colorbar indicates spin.

To engineer a spatially varying vector potential to generate a synthetic magnetic field, we create a spatially varying detuning δ .

Figure 2.7A shows a schematic of a laser geometry with an applied gradient $b'z \mathbf{e}_z$ to vary the detuning $\delta(z) \approx g_F\mu_B\Delta B(z)$ across a condensate. This change in δ shifts the minimum k_{min} of the dispersion. Our Hamiltonian for motion along

\mathbf{e}_x becomes

$$H_x^* \approx \frac{\hbar^2(k_x - k_{min})^2}{2m_{Rb}} = \frac{\hbar^2(k_x - qA_x^*/\hbar)^2}{2m_{Rb}}, \quad (2.20)$$

where we have defined an engineered vector potential qA_x^*/\hbar . Our vector potential $\mathbf{A}^* = A_x^*\mathbf{e}_x$ is a Landau gauge choice for synthetic magnetic field $\mathbf{B} = B^*\mathbf{e}_y$, where $B^* = \partial A_x^*/\partial z = (\partial A_x^*/\partial \delta)(\partial \delta/\partial z)$. For our simulated qA_x^*/\hbar in Fig. 2.7, we assumed a realistic laboratory gradient of 5.5 G/cm and a cloud extent $\sim 50 \mu\text{m}$ leading to a $10E_R$ span in detuning δ across the cloud. This method for creating synthetic magnetic fields is limited by the linear extent of the BEC because the synthetic field is proportional to the difference in detuning from one end of the cloud to the other. In Ch. 7, we extend on this method by using an optical lattice instead of a magnetic field gradient to create spatial differences in phase. There, the limit of accumulated phase difference is set by the ratio of the mismatched wavelengths between the Raman and optical lattice lasers as opposed to the linear extent of the cloud.

CHAPTER 3

DEGENERATE QUANTUM GASES

In this chapter, I will review some basic quantum statistics to define relevant energy scales for our experiments such as the chemical potential, the condensation temperature T_c for BEC, the Fermi energy ϵ_F and corresponding temperature T_F . Then we will discuss scattering in cold atoms, characterize atomic interactions with the s -wave scattering length and introduce magnetic Feshbach resonances. Finally, we will look at a derivation of the Gross-Pitaenskii equation (GPE) using an effective interaction potential characterized by s -wave scattering. For more details on Bose-Einstein condensates and degenerate Fermi gases, I recommend Refs. [107] and [44].

3.1 Brief review of quantum statistics

A feature of laser cooling and trapping atoms is that all atoms are the same. An ^{87}Rb atom in Ithaca, NY is identical to an ^{87}Rb in Gaithersburg, MD. The “quantum” in quantum degenerate gas is due to this indistinguishability. Degenerate implies the gas is in a regime where this indistinguishability is relevant. For this section, I found [80] and [69] to be useful for reviewing quantum statistics.

3.1.1 Identical particles

Imagine we have two identical particles as in Fig. 3.1. If we switch or exchange the two particles, any description we have written down of that two particle

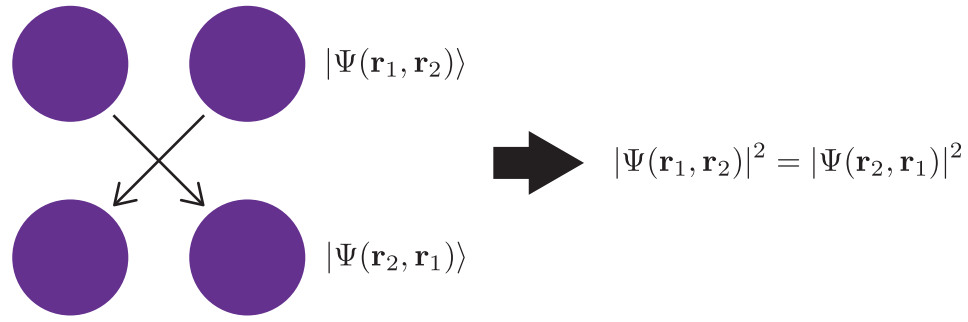


Figure 3.1: For indistinguishable particles the probability distribution has to be the same before and after exchange because they are identical.

state must be the same as before the exchange. $|\Psi(\mathbf{r}_1, \mathbf{r}_2)|^2$ is the probability of finding particle 1 at position \mathbf{r}_1 and finding particle 2 at position \mathbf{r}_2 . Similarly, if the particles in the opposite positions, the probability for that state is $|\Psi(\mathbf{r}_2, \mathbf{r}_1)|^2$. These probabilities must be equal. If we only consider single-valued solutions, there are two allowed wavefunctions:

$$|\Psi(\mathbf{r}_1, \mathbf{r}_2)\rangle = +|\Psi(\mathbf{r}_2, \mathbf{r}_1)\rangle \quad (3.1)$$

and $|\Psi(\mathbf{r}_1, \mathbf{r}_2)\rangle = -|\Psi(\mathbf{r}_2, \mathbf{r}_1)\rangle$.

Consequently, there are two types of indistinguishable particles: bosons and fermions. Bosons are symmetric(+) under exchange and fermions are antisymmetric(-) under exchange. A degenerate quantum gas is where the inter-particle spacing is approximately the size of the characteristic length of the quantum wavefunction that describes that particle. For our ultracold atomic ensembles with density $n = N/V$, we can describe the characteristic length of the wavefunction as the thermal de Broglie wavelength $\lambda_{dB} = \sqrt{2\pi\hbar^2/mk_B T}$. When $n\lambda_{dB}^3 \sim 1$, then quantum statistics becomes important and we must treat our atoms as bosons or fermions. The chemical potential μ can be described as the amount of energy required to add an additional particle and behaves differently at low temperatures depending on the type of particle in the ensemble. In

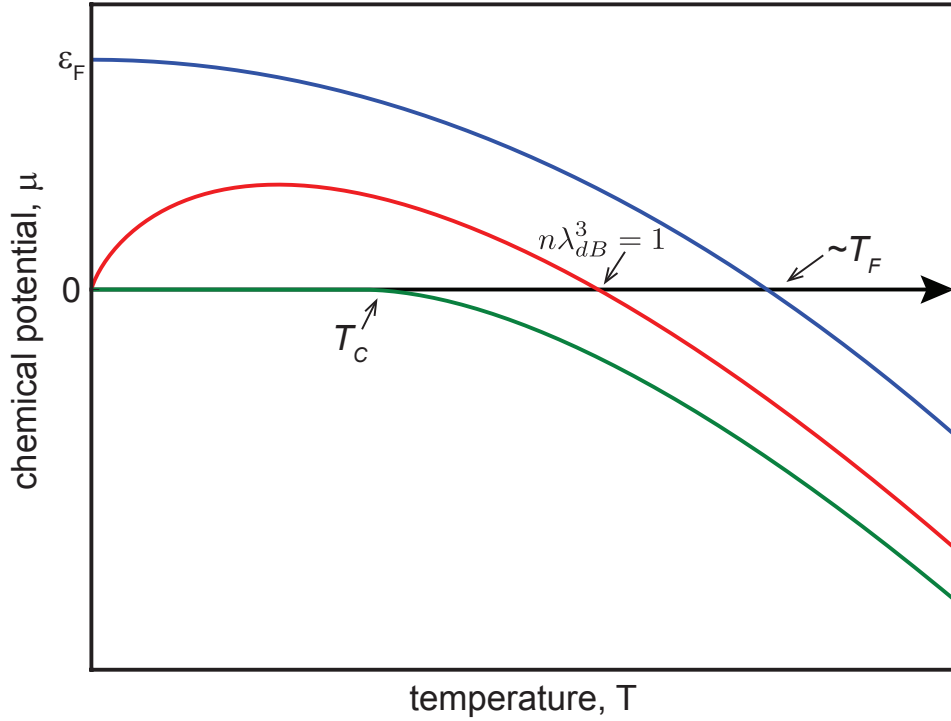


Figure 3.2: the chemical potential μ for fermions (blue), classical particles (red) and bosons (green) at constant density n versus temperature T .

Fig. 3.2, we plot the chemical potential μ for an ideal Fermi gas, an ideal classical gas, and an ideal Bose gas at constant density n . The chemical potential μ very clearly illustrates the impact of differences of quantum statistics in the degenerate regime.

There are more than bosons, fermions, and classical particles. Revisiting the wavefunction solutions for exchanging identical particles, we can write eqn. 3.1 in a more general fashion

$$|\Psi(\mathbf{r}_1, \mathbf{r}_2)\rangle = e^{i\theta}|\Psi(\mathbf{r}_2, \mathbf{r}_1)\rangle, \quad (3.2)$$

where $\theta = 0$ for bosons and $\theta = \pi$ for fermions. Anyons are particles for which θ is any other value besides 0 or π . Anyons with non-trivial phases can have inter-

esting properties when braided [102]. Majorana fermions are a specific type of fermion, which are their own anti-particle. In this thesis, I focus on fermions and bosons. However, the quest for Majorana modes in p -wave superconductors is the motivation for the proposed experiment in Chapter 5. Majorana modes are composite quasiparticles where the simple physical exchange operations we describe in this section alter the quantum wavefunctions in non-trivial ways [131].

3.1.2 Bose-Einstein Condensates

A Bose-Einstein condensate (BEC) is a macroscopic occupation of the ground state by a gas of bosons. This macroscopic occupation occurs when for a given volume V , there are no more higher momentum states available when we add the N th+1 boson. Derived from the Bose distribution,

$$n_{\vec{k}} = \frac{1}{z^{-1}e^{\beta\epsilon_k} - 1}, \quad (3.3)$$

describes the occupation in a momentum state \vec{k} at a temperature T with $\beta = 1/k_B T$, $\epsilon_k = \hbar^2 k^2 / 2m$, and $k = |\vec{k}|$. z is the fugacity, defining a chemical potential through $z = e^{\beta\mu}$. To calculate the available \vec{k} states for a uniform density $n = N/V$, we sum over k and then take the thermodynamic limit to arrive at the integral

$$n = \int \frac{d^3k}{(2\pi)^3} \frac{1}{z^{-1}e^{\beta\epsilon_k} - 1} = \frac{1}{2\pi^2} \int_0^\infty dk \frac{k^2}{z^{-1}e^{\beta\epsilon_k} - 1}. \quad (3.4)$$

We will define V to be a cube with sides of length λ_{dB} . We can simplify Eqn. 3.4 with a substitution $\beta\epsilon_k = x^2$ and $k = x\sqrt{2m/\beta\hbar^2}$. Combining our substitution and specified volume, we get

$$n\lambda_{dB}^3 = \frac{4}{\sqrt{\pi}} \int_0^\infty dx \frac{x^2}{z^{-1}e^{x^2} - 1} = \text{Li}_{3/2}(z), \quad (3.5)$$

where $\text{Li}_{3/2}(z)$ is a polylogarithm. Notably, the derivative of this polylogarithm is itself a polylogarithm

$$z \frac{d}{dz} \text{Li}_{3/2}(z) = \text{Li}_{1/2}(z) = \sum_{\ell=1}^{\infty} \frac{z^{\ell}}{\ell^{1/2}}. \quad (3.6)$$

At $z = 1$, this geometric series diverges. This is unphysical. Our integral is essentially counting N atoms in a box λ_{dB}^3 . The integrand can't diverge, so $z \leq 1$. However when we took the thermodynamic limit, we assigned no weight to the $k = 0$ atoms because $4\pi k^2 dk$ vanishes at $k = 0$. Once the density is high enough or the temperature is low enough, any additional atoms will occupy the ground $k = 0$ state no energy cost. For non-interacting bosons, we can fit an arbitrary number N_0 atoms in the ground state. Our total $N = N_0 + N_{ex}$ atoms is the sum of the number $N_{ex} = n\lambda^3$ atoms in states $k > 0$ and N_0 .

The distribution of atoms in the excited states defines the temperature T of a condensate. The critical temperature T_c of a condensate is when $n\lambda_{dB}^3 = \text{Li}_{3/2}(z = 1) = \zeta(3/2) \approx 2.612$ and no more atoms are allowed in the excited states. For a given, uniform density n , the critical temperature is

$$T_c = \frac{2\pi\hbar^2}{mk_B} \left(\frac{n}{\zeta(3/2)} \right)^{3/2}. \quad (3.7)$$

For a fixed density n , we plot the condensate fraction

$$\frac{N_0}{N} = 1 - \frac{N_{ex}}{N} = 1 - \frac{\zeta(3/2)}{n\lambda_{dB}^3} = 1 - \left(\frac{T}{T_c} \right)^{3/2} \quad (3.8)$$

as a function of temperature in units of T_c in Fig. 3.3. At $T = 0$, all of the atoms are in the condensate. As T increases, N_0/N decreases. However, below T_c , we see that a significant fraction of the atoms occupy the ground state. This state is a BEC.

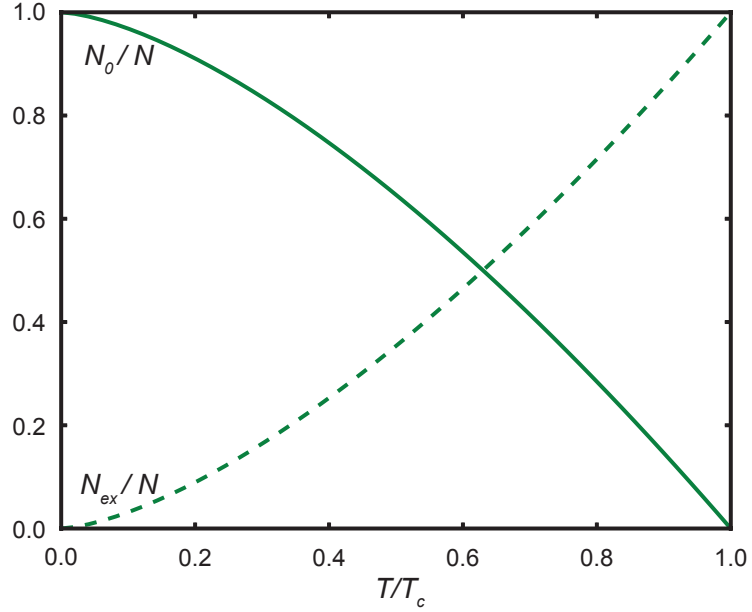


Figure 3.3: The condensate fraction N_0/N (solid) and fraction in the excited states N_{ex}/N (dashed) versus temperature T/T_c .

3.1.3 Degenerate Fermi Gases

A degenerate Fermi gas is a gas of N fermions below the Fermi temperature T_F derived from the energy of the N atoms at $T = 0$. The occupation of a fermion in a state \vec{k} is

$$n_{\vec{k}} = \frac{1}{z^{-1}e^{\beta\epsilon_k} + 1}, \quad (3.9)$$

valid for $T \neq 0$. At $T = 0$, $n_{\vec{k}}$ is one for $\epsilon_k < \epsilon_F$ and zero for $\epsilon_k > \epsilon_F$, where ϵ_F is the Fermi energy. Our Fermi momentum k_F is the momentum k corresponding to $\epsilon_k = \epsilon_F$. At $T = 0$,

$$N = \sum_{k < k_F} 1 = \frac{V}{(2\pi)^3} \frac{4\pi}{3} k_F^3 \quad (3.10)$$

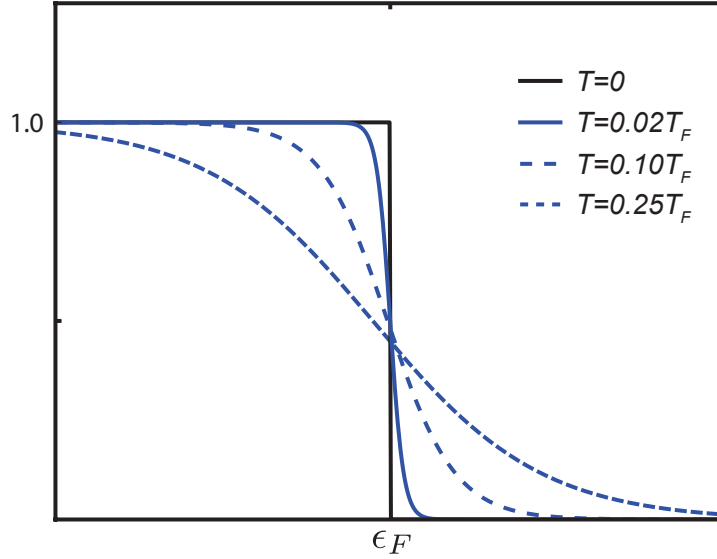


Figure 3.4: The Fermi distribution of occupation number $n(\epsilon)$ versus energy ϵ . The occupation at absolute zero is plotted for comparison.

atoms occupy all of the momentum states below k_F . Thus, for a given atomic density $n = N/V$, we can define a Fermi energy ϵ_F , a Fermi momentum k_F and a Fermi temperature T :

$$\begin{aligned}
 k_F &= (6\pi^2 n)^{1/3} \\
 \epsilon_F &= \frac{\hbar^2}{2m} (6\pi^2 n)^{2/3} \\
 T_F &= \frac{\epsilon_F}{k_B}.
 \end{aligned} \tag{3.11}$$

In Fig.3.4, the occupation $\langle n_\epsilon \rangle$ is plotted versus energy for different fractions of the Fermi temperature at a constant density n . As the temperature becomes larger, there is less occupation in the lower energy states and the distribution begins to resemble the distribution for classical atoms. For temperatures that are small fractions of the Fermi temperature T_F , the occupation deviates from

the zero temperature distribution around ϵ_F .

To approximate the chemical potential for constant density, we again consider a volume with sides the length of the λ_{dB} and make the same substitution:

$$n\lambda_{dB}^3 = \frac{4}{\sqrt{\pi}} \int_0^\infty dx \frac{x^2}{z^{-1}e^{x^2} + 1}. \quad (3.12)$$

Because z is small for fermions at a low temperature, we cannot do the series expansion like in the boson case. Instead, we will look at the $T \rightarrow 0$ limit and use that case to approximate the chemical potential at low temperatures around T_F . As $T \rightarrow 0$, the chemical potential $\mu \rightarrow \epsilon_F$. At $T = 0$, there is a sharp change in occupation number at ϵ_F . Our density as defined by the Fermi distribution at low temperatures is

$$n\lambda_{dB}^3 = \frac{4}{\sqrt{\pi}} \int_0^\infty dx \frac{x^2}{z^{-1}e^{x^2} + 1} \approx \frac{4}{3\sqrt{\pi}} \left[(\ln z)^{2/3} + \frac{\pi^2}{8} \frac{1}{\sqrt{\ln z}} + \dots \right] \quad (3.13)$$

If we only keep the first term and look at the zero temperature limit and defining n by the Fermi energy,

$$\ln z \approx \left(\frac{3\sqrt{\pi}}{4} n\lambda_{dB}^3 \right)^{2/3} = \frac{T_F}{T}, \quad (3.14)$$

we correctly find $\mu = k_B T \ln z = k_B T_F = \epsilon_F$. Including the next order, we solve for

$$\ln z = \left(\frac{3\sqrt{\pi}}{4} n\lambda_{dB}^3 - \frac{\pi^2}{8} \frac{1}{\sqrt{\ln z}} \right)^{2/3}. \quad (3.15)$$

Substituting in $\ln z = T_F/T$ on the right-side of the equation and using a series expansion at $T = 0$, we find the chemical potential

$$\mu \approx \epsilon_F \left[1 - \frac{\pi}{12} \left(\frac{T}{T_F} \right)^2 \right]. \quad (3.16)$$

This approximation is what is plotted in Fig. 3.2.

3.2 Scattering in ultracold atomic gases

In ultracold gases, most scattering events are s -wave and can be characterized with a single parameter, the s -wave scattering length. First, I will discuss calculating the s -wave scattering cross section for 2 distinguishable atoms, then for 2 identical atoms. Adding complexity, I will then discuss scattering between atoms with different internal states. Finally, I will introduce magnetically tunable Feshbach resonances, like the one studied in Ch. 5.

3.2.1 s -wave scattering length

For distinguishable atoms with mass m_1 and m_2 , the reduced mass is $M = m_1 m_2 / (m_1 + m_2)$. In the center-of-mass (COM) reference frame, we can write down their wavefunction at far distances as the sum of the incoming plane wave $e^{i\mathbf{k}\cdot\mathbf{r}}$ and the scattered wave

$$\sqrt{V}\psi = e^{i\mathbf{k}\cdot\mathbf{r}} + \psi_{sc}(\mathbf{r}) = e^{i\mathbf{k}\cdot\mathbf{r}} + f(k, k') \frac{e^{i\mathbf{k}'\cdot\mathbf{r}}}{r}, \quad (3.17)$$

where $|\mathbf{k}'| = |\mathbf{k}|$ is defined by the energy of the state $E = \hbar k^2 / 2M$, and $f(\mathbf{k}')$ is the scattering amplitude. Because we work with cold gases, we assume the atoms are in the ground state and, currently, do not take into consideration any internal degrees of freedom. Thus, the interaction is spherically symmetric and the scattering amplitude $f(\mathbf{k}') = f(\theta)$ is solely dependent on the scattering angle θ . Only considering s -wave scattering, $f(\theta) = a$ is fully characterized by the s -wave scattering length a .

To calculate if incoming particles will scatter, we define a differential cross section $d\sigma/d\Omega$ —the number of particles scattered into the solid angle $d\Omega$ per unit

time divided by the incident flux of particles in a unit of cross sectional area per unit time. To define a scattering cross section σ , we integrate $d\sigma/d\Omega$ over all solid angles

$$\sigma = \int \frac{d\sigma}{d\Omega} d\Omega = \int_{-1}^1 \cos\theta |f(\theta)|^2 = 4\pi a^2. \quad (3.18)$$

In polarized Fermi gases and BECs, the particles are not distinguishable. This has a direct effect on the scattering amplitude and σ . For indistinguishable particles, we need to symmetrize the wavefunction, which corresponds to changing the sign of the relative position vector from $\mathbf{r} \rightarrow -\mathbf{r}$ and $\theta \rightarrow \pi - \theta$. The wave function of the COM system is now

$$\sqrt{V}\psi = e^{i\mathbf{k}\cdot\mathbf{r}} \pm e^{i\mathbf{k}'\cdot\mathbf{r}} + [f(\theta) \pm f(\pi - \theta)] \frac{e^{i\mathbf{k}'\cdot\mathbf{r}}}{r}, \quad (3.19)$$

where the + is for bosons and the - is for fermions. The scattering amplitude vanishes for s -wave scattering of identical fermions and doubles for identical bosons leading. Therefore the scattering cross section

$$\sigma = \begin{cases} 8\pi a^2 & \text{bosons} \\ 0 & \text{fermions} \end{cases} \quad (3.20)$$

is different. For spin polarized fermions, this freezes out evaporative cooling. For bosons, this introduces a factor of two in approximating the interaction potential for a BEC in only one internal state.

We will use the Born approximation to the first order to define an effective interaction. A typical ^{87}Rb BEC with density $n \sim 10^{15} / \text{cm}^3$ has an inter-particle spacing of ~ 100 nm, which is much greater than the s -wave scattering length $a \sim 100a_0 \sim 5$ nm. So, it is valid to ignore the atomic potential at short length scales. Defining a spherically symmetric effective potential $U_{\text{eff}}(\mathbf{r})$, we calculate

an interaction potential

$$\int U_{\text{eff}}(\mathbf{r})d^3r \approx \frac{2\pi\hbar^2}{M}f^1(\theta) \approx \frac{4\pi\hbar^2a}{m_{\text{Rb}}} = U_0. \quad (3.21)$$

We will assume an effective contact interaction between atoms $U_{\text{eff}}(\mathbf{r}, \mathbf{r}') = U_0\delta(\mathbf{r}, \mathbf{r}')$ for identical bosons.

3.2.2 Scattering between different internal states

As discussed in Sec. 2.1, our alkali atoms have different internal states whose energy varies with an externally applied field. Considering them increases the complexity of our scattering problem because it introduces multiple exit channels which we have to sum over. Labeling the internal states $|\alpha\beta\rangle$ of our incoming atoms, our non-interacting Hamiltonian is

$$H_0 = \frac{\hat{p}^2}{2M} + H_B(\alpha) + H_B(\beta), \quad (3.22)$$

where $H_B|\alpha\rangle = \epsilon_\alpha|\alpha\rangle$. The total energy of our incoming atoms is

$$E_{\alpha\beta}(k_{\alpha\beta}) = \frac{\hbar^2k_{\alpha\beta}^2}{2M} + \epsilon_\alpha + \epsilon_\beta. \quad (3.23)$$

Labeling our exit channel states as the states as $|\alpha'\beta'\rangle$, we can generalize our single channel wave function in Eqn. 3.17 to include multiple exit channels:

$$\sqrt{V}\psi = e^{i\mathbf{k}_{\alpha\beta}\cdot\mathbf{r}}|\alpha\beta\rangle + \sum_{\alpha'\beta'} f(k_{\alpha\beta}, k'_{\alpha'\beta'}) \frac{e^{i\mathbf{k}'_{\alpha'\beta'}\cdot\mathbf{r}}}{r} |\alpha'\beta'\rangle. \quad (3.24)$$

When the exit channels are different than the entrance channels, the final relative momentum $k_{\alpha'\beta'}$ can be different than $k_{\alpha\beta}$ as long as the total energy E is conserved, $E = E_{\alpha\beta}(k_{\alpha\beta}) = E_{\alpha'\beta'}(k_{\alpha'\beta'})$. $k_{\alpha'\beta'}$ must satisfy

$$\frac{\hbar^2k_{\alpha'\beta'}^2}{2M} = \frac{\hbar^2k_{\alpha\beta}^2}{2M} + \epsilon_\alpha + \epsilon_\beta - \epsilon_{\alpha'} - \epsilon_{\beta'}. \quad (3.25)$$

When $k_{\alpha'\beta'}^2 \leq 0$, the channel is a closed.

3.2.3 Feshbach resonances

A Feshbach resonance occurs when a diatomic molecular state energetically approaches the two-atom continuum [39, 128]. Diatomic molecular bound states also have magnetic moments and the energy of those states can be tuned with a static magnetic field. Consequently, the Feshbach resonance can be accessed by changing the bias magnetic field. Tuning interactions in a DFG with a Feshbach resonance has led the creation of molecular Bose-Einstein Condensates (BECs) [58, 140, 78] as well as observation of the phase transition from the Bardeen-Cooper-Schrieffer (BCS) superconducting regime to the BEC regime at sufficiently low temperatures [18, 25, 139, 111].

When the energy $E_{\alpha\beta}$ of the open channel of two atoms approaches the energy of the molecule in the closed channel $E_{m'_{\text{cule}}}$, the coupling of those two states has a dramatic impact on the scattering length a of the two atoms. We can define the scattering length a as a function of magnetic field B and near a magnetic Feshbach resonance B_0 as

$$a = a_{bg} \left(1 - \frac{\Delta B}{B - B_0} \right) \quad (3.26)$$

where a_{bg} is the s -wave scattering length of the open channel states far from the resonance B_0 and ΔB is the width of the resonance related to the coupling between the closed and open channels and the wavefunction overlap of the bare atoms with the molecular states and their magnetic moments. Many experimental techniques have been used to characterize Feshbach resonances: atom loss due to three-body inelastic scattering, re-thermalization timescales from one axis to another, and anisotropic expansion of a cloud upon release from a confining potential [98, 73, 42, 104, 112]. In Ch. 5, we measured the location of the Feshbach resonance by imaging the elastic s -wave scattering halos.

3.3 Brief Intro/Overview of the Gross-Pitaevskii Equation

When fully condensed, all the bosons in a BEC will have the same single particle wavefunction. The Hartree approximation allows us write down the many-body wave function

$$\Psi(\mathbf{r}_1, \mathbf{r}_2, \dots, \mathbf{r}_N) = \prod_{i=1}^N \phi(\mathbf{r}_i) \quad (3.27)$$

for our N -particle system as a product of single particle wave functions $\phi(\mathbf{r})$. The single particle wave function is normalized such that $\int d\mathbf{r} |\phi(\mathbf{r})|^2 = 1$. Including the effective interaction potential from Sec. 3.2.1, the effective Hamiltonian for the N -particle system in a potential $V(\mathbf{r})$ is

$$H = \sum_{i=1}^N \left[\frac{\mathbf{p}_i^2}{2m} + V(\mathbf{r}_i) \right] + \frac{U_0}{2} \sum_{i=1}^N \sum_{j \neq i}^N \delta(\mathbf{r}_i - \mathbf{r}_j). \quad (3.28)$$

We find our energy functional by taking the expectation value of the Hamiltonian

$$\begin{aligned} E &= \langle \Psi^*(\mathbf{r}_1, \mathbf{r}_2, \dots, \mathbf{r}_N) | H | \Psi(\mathbf{r}_1, \mathbf{r}_2, \dots, \mathbf{r}_N) \rangle \\ &= \int d\mathbf{r} \left[\prod_{i=1}^N \phi^*(\mathbf{r}_i) \left(\sum_{i=1}^N \left[\frac{\mathbf{p}_i^2}{2m} + V(\mathbf{r}_i) \right] + \frac{U_0}{2} \sum_{i=1}^N \sum_{j \neq i}^N \delta(\mathbf{r}_i - \mathbf{r}_j) \right) \prod_{i=1}^N \phi(\mathbf{r}_i) \right] \\ &= N \int d\mathbf{r} \left[\frac{\hbar^2}{2m} |\nabla \phi(\mathbf{r})|^2 + V(\mathbf{r}) |\phi(\mathbf{r})|^2 + \frac{(N-1)}{2} U_0 |\phi(\mathbf{r})|^4 \right], \end{aligned} \quad (3.29)$$

and simplifying by evaluating the sums and products. Our typical ^{87}Rb BECs have $\sim 10^6$ atoms, thus $N \gg 1$ and $(N-1) \approx N$. We will assume a condensate wavefunction $\psi(\mathbf{r}) = \sqrt{N} \phi(\mathbf{r})$, where the density of the particles is $n(\mathbf{r}) = |\psi(\mathbf{r})|^2$. The energy for our system becomes

$$E = \int d\mathbf{r} \left[\frac{\hbar^2}{2m} |\nabla \psi(\mathbf{r})|^2 + V(\mathbf{r}) |\psi(\mathbf{r})|^2 + \frac{U_0}{2} |\psi(\mathbf{r})|^4 \right]. \quad (3.30)$$

We will now assume that our number N is constant and minimize $E - \mu N$ for fixed μ . Combining this with Eqn. 3.30, we get the time-independent Gross-

Pitaevskii equation (GPE)

$$-\frac{\hbar^2}{2m}\nabla^2\psi(\mathbf{r}) + V(\mathbf{r})\psi(\mathbf{r}) + U_0|\psi(\mathbf{r})|^2\psi(\mathbf{r}) = \mu\psi(\mathbf{r}). \quad (3.31)$$

From this equation, we can define a length scale over which the density of our condensate can change with minimal kinetic energy cost. The length scale is the healing length $\xi = \sqrt{\hbar^2/2mnU_0}$ of the condensate.

To study dynamics in a condensate, we adapted the time-independent GPE to be time-dependent. Propagating the GPE in time is difficult due to its non-linear term. Implementing a time-splitting spectral method (TSSP), we can study dynamics of our condensate [16]. I implemented a 1-D GPE solver for a harmonic trap $V(x) = m\omega_x^2x^2$ plotted in Fig. 3.5A. For simulations, we will make our Hamiltonian dimensionless. A natural length for a harmonic trap will be the harmonic oscillator length x_s and we'll scale the time by our oscillator frequency ω_x . Our dimensionless variables are

$$\tilde{t} = \omega_x t, \quad \tilde{x} = \frac{x}{x_s}, \quad \text{and} \quad \tilde{\psi}(\tilde{x}_s, \tilde{t}) = \sqrt{x_s}\psi(x, t). \quad (3.32)$$

The dimensionless Hamiltonian we numerically solve is

$$i\frac{d\psi}{dt} = -\frac{\beta}{2}\frac{d^2}{dx^2}\psi(x, t) + \alpha\frac{x^2}{2}\psi(x, t) + \gamma|\psi(x, t)|^2\psi(x, t), \quad (3.33)$$

where we have dropped the tildes. For the simulation, we set $\beta = \alpha = 1$. To determine a good value for γ , I used input parameters from our experiment. We wanted to simulate an elongated condensate in an approximately harmonic trap with trap frequency $\omega_x \approx 5.4$ Hz and Thomas-Fermi radius ≈ 100 μm . The trap frequencies in the other directions were $\sim 4 \times \omega_x$. Neither the dynamics in these dimensions nor the changing density profile in these directions along x are included in our modeling. I ran the simulation for different γ and selected $\gamma = 960$, where the simulated ground state's probability density matched

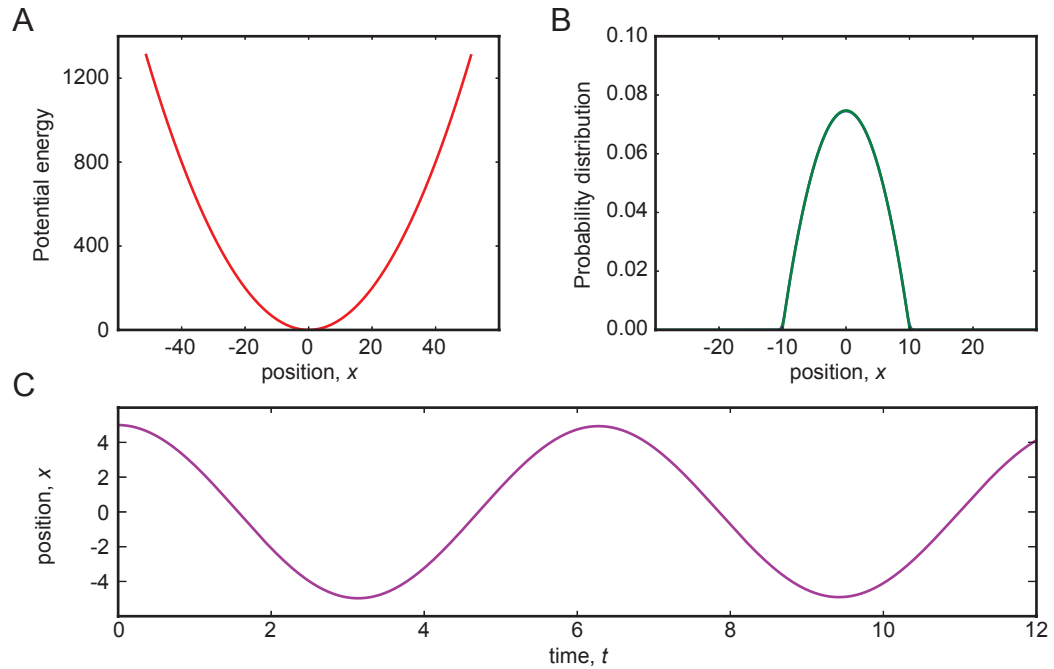


Figure 3.5: Results from a 1-D GPE solver using a time-splitting spectral method. All values are dimensionless, we dropped the tildes for simplicity. (A) The simulated 1-D harmonic potential versus position. (B) The ground state (green curve) found by seeding the solver with white noise and using imaginary time to add dissipation into the simulation. The Thomas-Fermi probability distribution (blue curve) is completely covered except at the edges. This deviation is not visible at this scale. (C) Oscillations in the harmonic trap after displacing the numerically found ground state to $x = 5$.

a Thomas Fermi probability distribution with radius $\approx 100 \mu\text{m}$ or 10.0833 in the dimensionless units.

To numerically find the ground state of the system, I set time to be complex. Including an imaginary term in the time introduced dissipation and increasing the proportion of imaginary time in a given time step would find the ground state more rapidly. When introducing imaginary time, the wavefunction was normalized after every time step. To determine if the state was the ground state, I calculated the overlap integral with the state from the previous time step. If the difference of this overlap integral and 1 was $< 1e - 9$, the

numerically found wavefunction was considered to be the ground state. Both of the Thomas-Fermi and the numerically simulated ground state probability distributions are plotted in Fig. 3.5B. The Thomas-Fermi distribution is almost completely covered by the probability distribution of the ground state. Because the Thomas-Fermi approximation sets the kinetic energy term to zero, there is no cost to rapidly changing the wavefunction, and the calculated probability density is an inverted parabola with sharp cusps where the probability density goes to zero. This is where the simulated probability deviates from the Thomas-Fermi approximation because the nonzero kinetic energy forces the probability density to change over the healing length ξ . If we displace the numerically found ground state from the center of the harmonic trap, the probability density will oscillate with periodicity $T = 2\pi/\omega_x$. The average position versus time is shown in Fig. 3.5C and we see the expected sinusoidal oscillations.

CHAPTER 4

RUBIDIUM-POTASIUM APPARATUS

Our experimental set-up at NIST in Gaithersburg, MD has been well documented initially in [87] and then with further detail [77]. My goal for this chapter is to document modifications and additions to the Rb-K (formerly known as RbII) apparatus that enabled the experiments discussed in this thesis. Figure 4.1 displays the basic geometry of our apparatus with important cooling and trapping laser beams for the creation of BECs and DFGs drawn.

4.1 Experimental sequence for creation of a BEC

We used a Zeeman slower to cool the ^{87}Rb atoms coming out of a combined Rb-K oven. The atoms are cooled on the $|F = 2, m_F = 2\rangle \rightarrow |F' = 3, m_F = 3\rangle$ transition with a laser beam propagating down the slower in the opposite direction of the collimated atomic beam. A $2 \rightarrow 2$ fiber splitter combined the slower light with \approx few mW of slower repumper light in resonance with the $|F = 1\rangle \rightarrow |F' = 2\rangle$ transition. The magnetic field provided by the Zeeman slower shifts the energy of the atoms, so they stay in resonance with the cooling and repumper lasers as their velocity changes. The atoms are then captured in a magneto-optical trap (MOT). We typically load the ^{87}Rb MOT for 2.5 s. For the MOT, we run a 25 A current through our large coils in anti-Helmholtz configuration providing $B'_z \approx 13$ G/cm. The light for our MOT is sent into a custom fiber splitter (Fig. 4.2) to create 3 sets of counter propagating beams with ~ 9 mW in each beam. The MOT cooling light was ≈ -20 MHz detuned from the $|F = 2\rangle \rightarrow |F' = 3\rangle$ transition. Our Rb MOT repump light was ≈ 1 MHz detuned

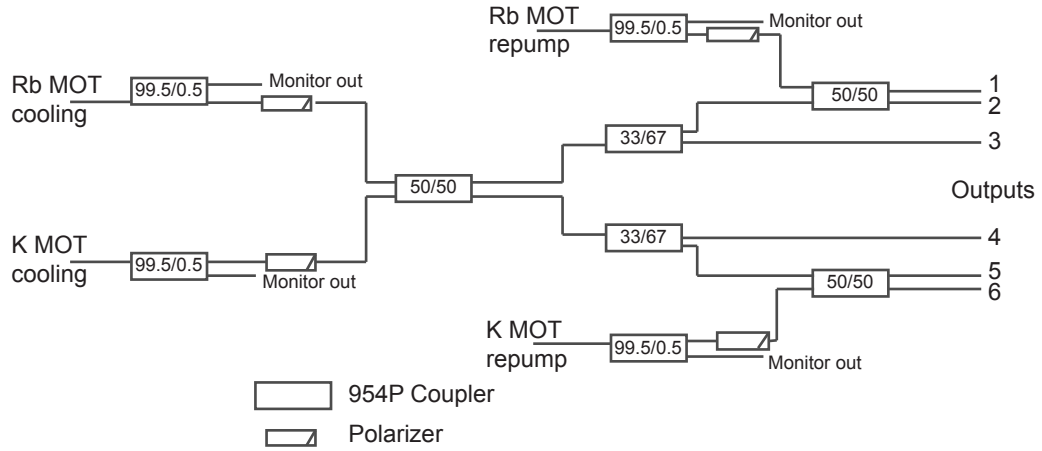


Figure 4.2: Schematic of custom Evanescent Optics Inc. fiber splitter. We used this device to combine the MOT cooling and repump light for our dual species apparatus.

atoms experienced the optical molasses created by the MOT cooling beams, we ramped the cooling light detuning 33 MHz to 104 MHz away from resonance to further cool the atoms. The lack of repump caused the atoms to be optically pumped into the $F = 1$ ground state. We optically pumped the atoms into the $|F = 1, m_F = -1\rangle$ for 1 ms state by illuminating them with the slower repumping light. We then turn on the xz imaging probe to blow away any remaining $F = 2$ atoms.

We then rapidly turned on a quadrupole magnetic trap with a current of 130 A in our large coils in an anti-Helmholtz configuration. After a 20 ms hold, we linearly ramped the current from 130 A to 250 A in 0.2 s to compress the atoms and increase their collision rate. After compression, we turn on our optical dipole trap. For all experiments in this thesis, the beam propagating along \mathbf{e}_x has the smallest beam waist (See Tab. 4.4 for specific beam waist information) in \mathbf{e}_z , the direction of gravity. We turned on the dipole trap with most of the power in this beam and at the highest power possible. We turned on our

rf magnetic field and linearly ramped the frequency from 22 MHz to 4 MHz in 4 s. This flipped the spin of the highest energy atoms and then allowed the remaining atoms to thermalize at a lower temperature. We decompressed the quadrupole trap by ramping the current in the coils from 250 A to 60 A in an exponential ramp with time constant $\tau = 1.5$ s over 3 s. While decompressing, we lowered the atoms into the dipole trap by ramping a smaller bias coil in Helmholtz configuration providing field in \mathbf{e}_z from 10 A to 8 A. This lowers the quadrupole zero toward the dipole trap.

We completed the evaporation to BEC in the optical dipole trap. The quadrupole is still on, just barely compensating for gravity. We evaporated in the optical dipole trap in either 3 s for typical BECs or 5 s for an elongated BEC. For the overall power in the dipole trap, we either used a linear ramp or sometimes we used an “O’Hara” ramp [103] to ramp from the initial power command to the final power command. The O’Hara ramp ramps the dipole potential more rapidly at first, then slows down. Also during this evaporation we linearly ramped the amplitude command to acousto-optic modulator (AOM) controlling the power balance in the two beams of our dipole trap. This further lowered the power in the beam along \mathbf{e}_x while increasing the power in the \mathbf{e}_y beam. After evaporation in the dipole trap, we ramped the quad current to 0 A with an exponential ramp with time constant $\tau = 0.8$ s over 5 s. Ramping off the quadrupole continued the evaporation by decreasing the optical trap depth due gravity. This sequence creates a $|F = 1, m_F = -1\rangle$ ^{87}Rb BEC in an optical dipole trap.

4.2 Experimental sequence for creation of a DFG

Our Zeeman slower slowed both ^{87}Rb and ^{40}K atomic beams. Because ^{40}K is lighter than ^{87}Rb , the atoms will “bloom” or acquire a transverse velocity at the output of the slower. To increase the number of ^{40}K atoms ultimately captured in the MOT, we cooled the atoms in an orthogonal direction to the slower immediately after the oven, but before the slower. We loaded the ^{40}K MOT first by turning on the slower cooling, slower repump, transverse cooling, MOT cooling, and MOT repump light for ^{40}K , but not ^{87}Rb . After 7 s of ^{40}K MOT loading, we also loaded ^{87}Rb for a 1.5 s of MOT loading. The current in the large, anti-Helmholtz was 25 A, similar to BEC creation.

We cooled both species in optical molasses for 2 ms. For ^{87}Rb , we did an abbreviated ramp of the MOT cooling light detuning from 33 MHz to 53 MHz away from resonance. For ^{40}K , we lowered the intensity of the MOT cooling light without modifying its detuning. We optically pumped both species into their maximally stretched magnetically trappable states, $|F = 9/2, m_F = 9/2\rangle$ for ^{40}K and $|F = 2, m_F = 2\rangle$ for ^{87}Rb . ^{40}K had a dedicated optical pumping beam. We used the slower repump and MOT repump light, as well. For ^{87}Rb , we pulsed on the slower light and both the slower and MOT repump light.

Both species were then loaded into a quadrupole magnetic trap with a current of 130 A in our large coils in anti-Helmholtz configuration. The currents in our 3 pairs of Helmholtz bias coils are listed in Tab. 4.2 for both the creation of a DFG and a BEC. Similar to the BEC sequence, we compressed the magnetic trap by linearly ramping the current in the large coils from 130 A to 160 A. After compression, we cooled our atoms evaporatively via forced rf evaporation,

Coils	Null	Rb mag cap	Rb opt pump	RbK mag cap	RbK opt pump
\mathbf{e}_x	-1.10	-6	-0.3	-15	1
\mathbf{e}_y	0.12	0	1	-4	2.35
\mathbf{e}_z	3.59	10	4.8	10	4

Table 4.1: Bias fields during the magnetic quadrupole trap capture (mag cap) and optical pumping (opt pump) experiment sequence. The coils are labeled by the direction they provide a bias field. All the currents are in amps. Rb(RbK) is labeling the bias fields used in the experiment sequence for creation of a BEC(DFG).

sweeping the rf frequency from 18 MHz to 2 MHz in 10 s. During evaporation, the magnetic trap was plugged by a $\lambda = 532$ nm beam, tightly focused to $\approx 30 \mu\text{m}$ and $\approx 5W$ in power, providing a repulsive potential around the quadrupole zero to prevent Majorana losses. Since the ^{40}K atoms were spin polarized and therefore only interacted by increasingly suppressed p -wave interactions, they re-thermalized largely due to sympathetic cooling with ^{87}Rb atoms.

After the 10 s evaporation in the plugged quadrupole trap, we turned on our crossed beam optical dipole trap at full power ($\sim 6W$) predominantly in the more tightly focused beam. Both the green plug beam and the optical dipole trap remain on as we decompressed the quadrupole trap by exponentially ramping the current from 160 A to 25.5 A with time constant $\tau = 1.5$ s over 3 s. Next, we evaporated in the optical dipole trap by ramping the relative power balance in the crossed beams to their final balance in 3 s. This reduced the overall dipole trap depth because more power was in a beam with a larger beam waist. We also ramped off the power in the green plug beam during this 3 s as well. We simultaneously evaporated from the dipole trap by lowering the overall optical power with an O'Hara ramp and using an exponential ramp to turn off the quadrupole field with time constant $\tau = 1.5$ s over 2 s. At this

juncture, we had $|F = 2, m_F = 2\rangle$ ^{87}Rb atoms and $|F = 9/2, m_F = 9/2\rangle$ ^{40}K atoms in our crossed beam optical dipole trap.

We then used adiabatic rapid passage (ARP) to transfer the ^{87}Rb atoms from the $|F = 2, m_F = 2\rangle$ state to the $|F = 1, m_F = +1\rangle$ ground state via 6.8556 GHz microwave coupling (20.02 MHz from the zero field resonance) followed by ramping the current in the bias \mathbf{e}_z coils 1 A in 50 ms. This state was chosen to minimize spin changing collisions with ^{40}K atoms during further evaporation [22]. After the ARP, we briefly applied an on-resonant probe laser, ejecting any remaining ^{87}Rb atoms in the $F = 2$ manifold from the trap. We evaporated further in the optical trap again using an O'Hara ramp for 1 s. The optical potential from the dipole trap no longer holds the ^{87}Rb against gravity. We used a second ARP to transfer the ^{40}K atoms into the $|F = 9/2, m_F = -9/2\rangle$ state by illuminating the atoms with a 3.3 MHz rf field and sweeping the current in the bias \mathbf{e}_z coils 5 A in 150 ms. At the end of this sequence, we had a DFG of about 75,000 ^{40}K atoms in the $|F = 9/2, m_F = -9/2\rangle$ state with temperature $\approx 0.4T_F$.

4.3 Lasers!

The real reason for this PhD: an excuse to play with lasers.

4.3.1 Potassium cooling lasers

Our potassium laser system at the writing of this thesis has been dismantled to be reconfigured to provide cooling light for a 2-D to 3-D MOT system. I will document the laser system as it was for our results discussed in Chapter 5. Our



Figure 4.3: A screen shot of our absorption (yellow) and error signal (pink) for locking the potassium laser with Digilock software connected to a Toptica Photonics Feedback Controlyzer connected to our repump laser system.

potassium laser cooling light was generated by two Toptica Photonics TA Pro systems. To stabilize our laser's frequency, we lock to a ^{39}K transition with a 93.26% natural abundance in contrast to the 0.0117% natural abundance of ^{40}K . The upper hyperfine structure of ^{39}K is unresolved, so saturation absorption spectroscopy of ^{39}K on the $D2$ -transition has 3 features: two absorption peaks of the two hyperfine ground states and an enhanced depletion at their crossover due to optical pumping effects. These 3 features are visible in Fig. 4.3, and we locked on the error signal derived from $F = 2 \rightarrow D2$ transition, the left most feature. To increase our absorption signal, we heat our potassium cell to 54°C controlled by a Thorlabs Temperature Controller TC200.

Figure 4.4 shows our repump laser system. To the left of the Toptica Photonics TA Pro is our Doppler-free saturated absorption spectroscopy.

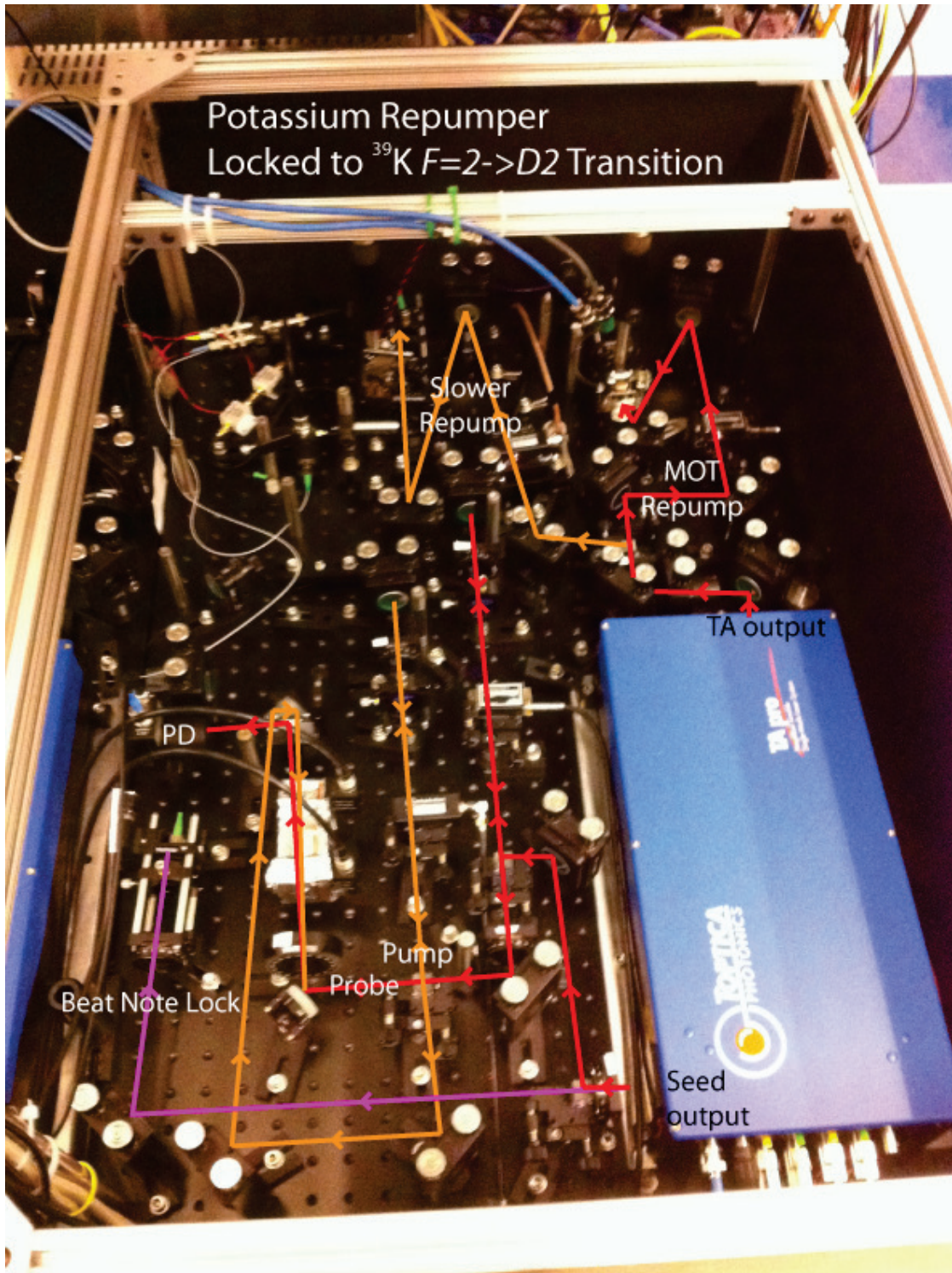


Figure 4.4: Potassium repumper laser system

Beam	Path color	AOM frequency [MHz]	Shift from res.[MHz]
MOT	Red	+80	0
Slower	Orange	-80	-160
Beat note	Pink	none	-80
Sat abs probe	Red	-80×2	-240
Sat abs pump	Orange	-350×2	-940

Table 4.2: Potassium repumping beams. Resonance (res.) is the $^{40}\text{K}|F = 7/2\rangle \rightarrow |F' = 9/2\rangle$ transition. We used an error signal generated from saturation absorption spectroscopy (sat abs) to stabilize the laser frequency.

We wanted the frequency of our repumper laser to be 80 MHz below the $^{40}\text{K}|F = 7/2\rangle \rightarrow |F' = 9/2\rangle$ transition. The ^{39}K transition we stabilized to is -511.9 MHz from our bare laser frequency set-point. We double passed our bare laser light through a 160 MHz AOM before sending the light to the spectroscopy set-up. We then shifted our pump laser frequency by 700 MHz (double pass a 350 MHz AOM) with respect to our probe. The shift from resonance atoms in the heat cell see is half of the frequency difference between the pump and probe beam, thus we have upshifted our bare laser light by $160 \text{ MHz} + 350 \text{ MHz} = 511 \text{ MHz}$. We send the bare seed output to the beat-note lock for our cooling laser. The TA output generated our repump light for our potassium MOT and Zeeman slower. Table 4.2 lists all the beams derived from both TA output and the seed output.

Our potassium cooling laser's frequency was stabilized by a beat-note lock to $\sim -100 \text{ MHz}$ from the $^{40}\text{K}|F = 9/2\rangle \rightarrow |F' = 11/2\rangle$ transition. The frequency of our laser could be adjusted during the sequence because we compared the beat-note to a signal from a Novatech 409A programmable frequency synthesizer multiplied by 16 by our electronics. During the MOT stage of our experimental sequence, we typically locked the cooling laser 1265 MHz away from the repumper laser. The cooling laser provided light for laser cooling, optical

Beam	Path color	AOM frequency [MHz]	Shift from res.[MHz]
MOT	Red	+80	-24
Slower	Orange	-80	-160
Opt. pump	Purple	$+80 \times 2$	+48.7
Beat note	Pink	none	-80
Transverse	Blue	+100	0
xz probe	Yellow	+100*	0
xy probe	Green	+100*	0

Table 4.3: Potassium cooling beams. Resonance (res.) is the $^{40}\text{K}|F = 9/2\rangle \rightarrow |F' = 11/2\rangle$ transition. Our optical pumping (opt. pump) used the same fiber launch and shutter as the Zeeman slower cooling beam. *These two are the same AOM

pumping, and absorption imaging. Figure 4.5 illustrates how we derive all the light we need from the TA output of our cooling laser system. Because so many beams are derived from the cooling laser, several of the 0th order beams from different AOMs are used. The unshifted 0th order light is the same color as the light heading into the AOM. The seed output was only used for diagnostics and the beat-note lock. We used two `New Focus Servo Controllers` to feedback on both the current and piezo of the seed laser our `TA Pro`. Table 4.3 lists the beams of our potassium cooling laser.

All of the laser light was piped from our laser systems table to our main apparatus illustrated in Fig. 4.1 with optical fibers, though how the rubidium and potassium cooling and imaging light was combined for our dual species apparatus varied. The MOT cooling and repump light for potassium were combined with the rubidium MOT light as shown in Fig. 4.2. The potassium slower and repump light were sent through a $2 \rightarrow 2$ fiber. The slower light was merged with the rubidium slower light on the apparatus table with a polarizing beam splitter and thus has the opposite helicity compared to the rubidium light. The transverse cooling was piped over on a optical fiber. There was no rubidium transverse cooling. Both the xy and xz imaging probes had there own $2 \rightarrow 2$

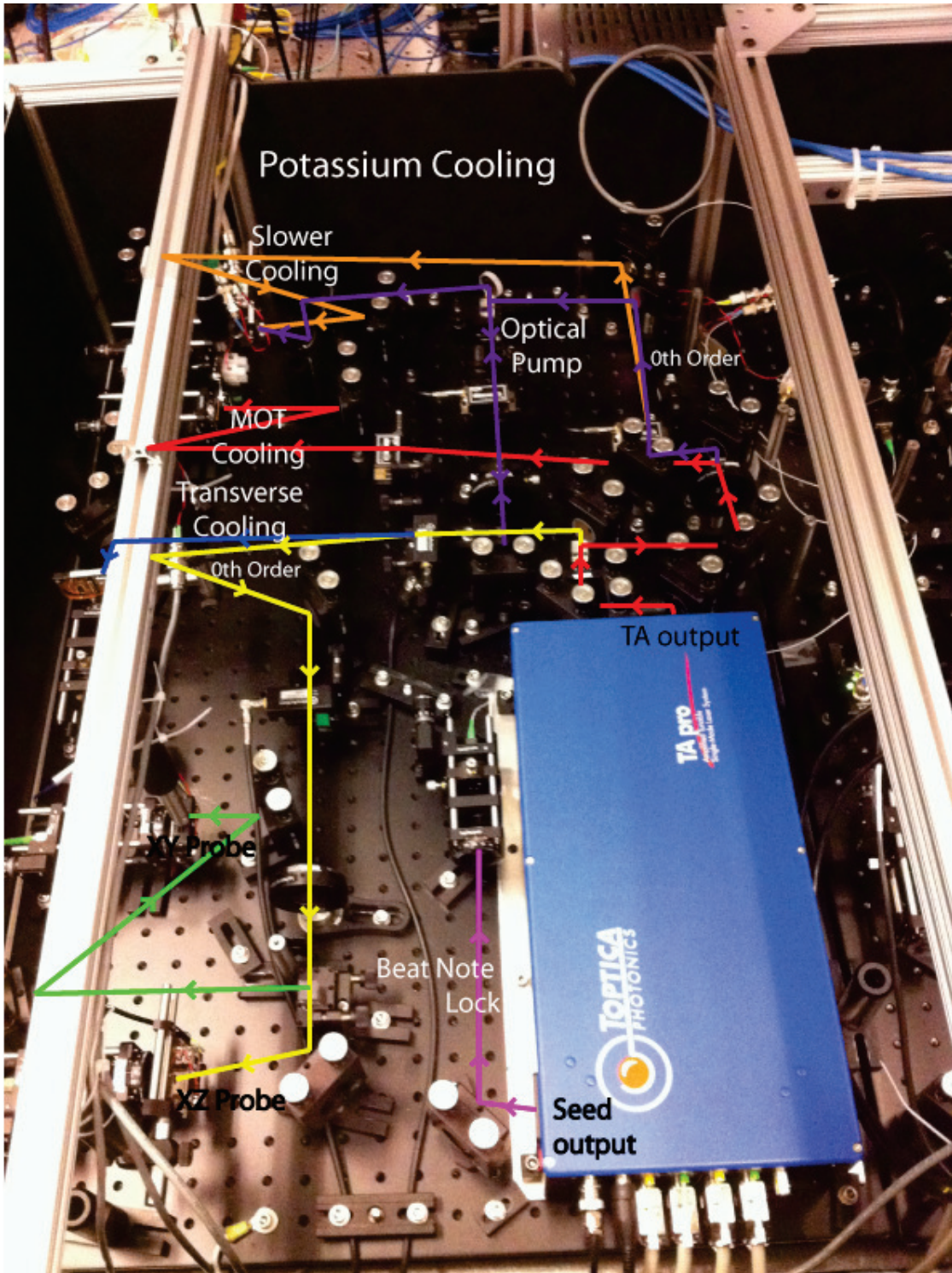


Figure 4.5: Potassium cooling laser

Experiment	Propagation direction	Order	Horizontal[μm]	Vertical[μm]
Chapter 5	\mathbf{e}_y	0th	150	98
	\mathbf{e}_x	+1st	118	34
Chapter 7	\mathbf{e}_y	-1st	96	104
	\mathbf{e}_x	0th	98	38
Chapter 6	\mathbf{e}_y	-1st	83	66
	\mathbf{e}_x	0th	46	38

Table 4.4: Optical dipole trap beam waists for the different experiments presented in this thesis. The orders are of the “Split” AOM. For work with solitons, we switched out cylindrical optics in the 0th order’s path for spherically symmetric ones.

fiber splitter to combine the rubidium and potassium probe light. The second output port was useful for alignment and power monitoring.

4.3.2 Optical dipole trap

A IPG YDL-10-LP 10W fiber laser provided 1064 nm light for both beams of our crossed optical dipole trap during our experiments presented in Ch. 5 and our preliminary work for Ch. 7. After our 10W fiber laser died in October 2014, we installed a IPG YDL-30-LP 30W replacement laser. This catastrophe proved useful because we modified our alignment to enable deflection of the beam propagating along \mathbf{e}_y . The output of either laser was sent through two AOMs: the “Power” AOM and the “Split” AOM. These AOMs were driven by 80 MHz IntraAction deflector drivers with both an amplitude and a frequency modulation input. The Power AOM was used to stabilize the intensity of our optical dipole trap. A beam sampler picked off light from the Power AOM’s 1st order and directed this light to a photodetector connected to our intensity stabilization feedback loop. The voltage to the amplitude input for the Power AOM was adjusted to maintain an intensity, linear with computer com-

mand, at a set-point. The Split AOM controlled the relative power in the 0th and ± 1 st order. During the replacement process, we switched from using the 0th order and the +1st order to using the -1 st order and the 0th order. With the 0th order providing most of the confinement against gravity, we created time-averaged-potentials with a few hundred kilohertz sawtooth from a function generator. Additionally, deflection of our -1 st order beam provides a momentum kick for our currently being implemented experiment of Bloch oscillations for optical lattices along \mathbf{e}_x .

Dipole trap alignment was slightly different depending on whether we wanted to make a DFG or a BEC. For BECs, we aligned our dipole trap beams to the quadrupole field zero with the nulling fields listed in Tab. 4.2. Then, we applied a bias field in the \mathbf{e}_z direction during rf evaporation in the quadrupole trap to have the field zero above the dipole trap. This configuration led to very efficient loading from our magnetic trap to our optical dipole trap. For DFGs, our green plug beam created a repulsive potential at the quadrupole field zero to prevent Majorana losses. We aligned our dipole trap about $50 \mu\text{m}$ below our quadrupole trap zero so the repulsive potential due to the green beam was not fighting the attractive potential of our dipole trap.

4.3.3 Optical lattices and Raman lasers

We have installed two co-propagating 1-D optical lattices. Our 766.704 nm potassium lattice light was from the monitor output for the MOT repump light of our custom fiber splitter (Fig. 4.2). This lattice was not intensity stabilized. We used it for rapid pulses in our scattering experiments. Our other 1-D optical

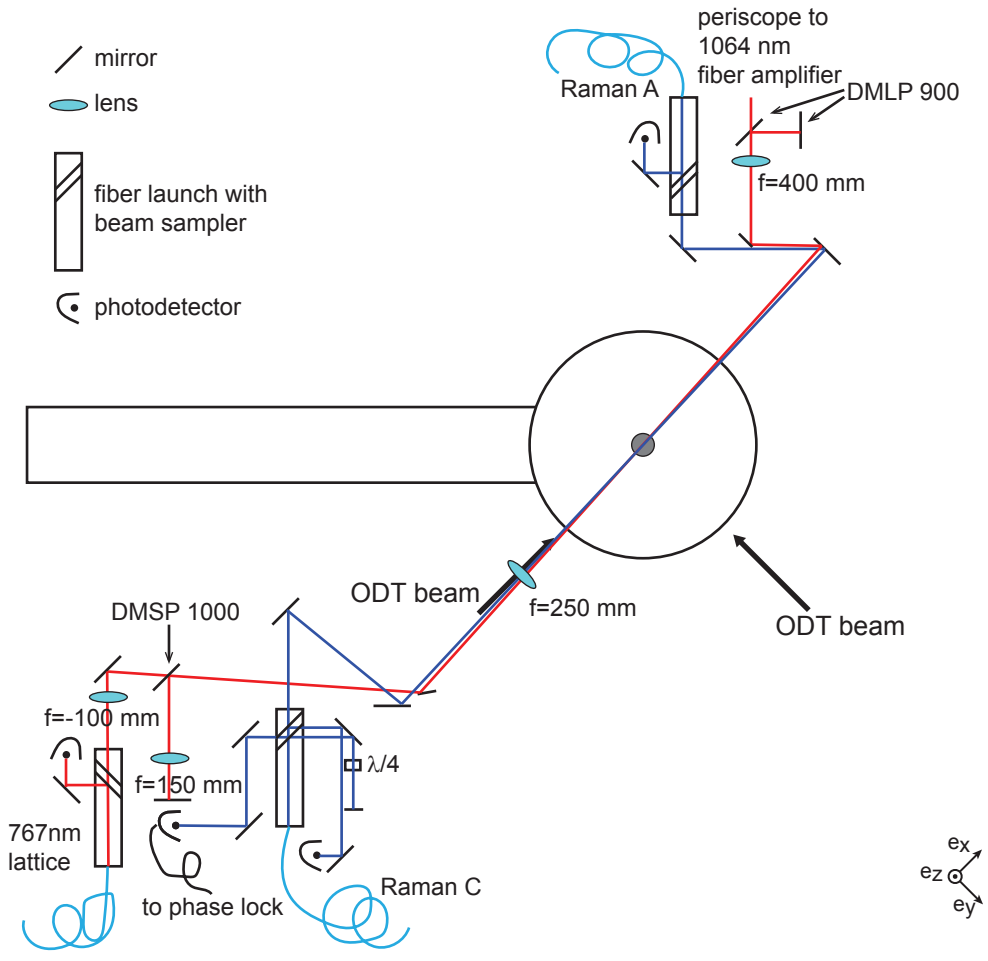


Figure 4.6: Schematic of our dual species apparatus highlighting 1-D optical lattices and Raman lasers. This figure is not to scale.

lattice was generated by a IPG YAR-10K-1064-LP-SF fiber amplifier seeded by 5 mW picked off from a shared NP Photonics fiber laser source. Figure 4.6 is a schematic of our optics alignment for merging these two beams.

This schematic also shows the configuration of our Raman lasers beams. The source for these beams was a Coherent MBR-110 Ti:Sapphire (Ti:Sapph) tunable laser pumped by a Coherent Verdi V-10 at 10 W on a separate optical table from our experiment. On our Ti:Sapph laser table was where we controlled the relative frequency of our Raman lasers by shifting their bare laser frequency

with an AOM. By controlling the amplitude of the rf tone on the AOMs, we could also control the intensity of our Raman beams. Even with the rf tone coming from the same source, phase noise was added to our Raman beams by traveling through the optical fibers. This additional phase noise was particularly apparent for experiments sensitive to optical phase, like our experiments presented in Chapter 7. So using a beam sampler on the Raman C fiber launch, we combined a small amount of light picked off from both Raman A and C and actively stabilized the phase. This stabilized the Raman frequency and optical phase at the atoms against the phase noise added by the optical fibers that conveyed the light from the laser table to the experiment. Additionally, the deliberate choice to install the phase stabilization adjacent to the 1064 nm optical lattice retro reflection mirror passively stabilized the phase of the Raman light to the 1-D optical lattice. Without the phase lock, we observed rapid dephasing and heating of a BEC loaded into our 2-D hybrid lattice with synthetic flux.

4.3.4 Green plug beam

The original plan for our green plug beam to plug our quad zero with 532 nm light generated by a Coherent Verdi V-5 operating at 5 W. This light was to be controlled with an AOM and coupled to a NKT Photonics LMA-PM-10 high-power polarization-maintaining fiber to improve pointing stability. We estimated we have ~ 3 W at the atoms. For a potential barrier of 1 mK for our ^{40}K atoms, we wanted a beam waist of about $10\ \mu\text{m}$. We never could get more than 2 W out of the fiber, even though we did not implement this with a 5 W Verdi but with a 18 W Verdi operating at 12.5 W. Increasing the operating power of our Verdi did not increase the power out of the fiber. Additionally, our green

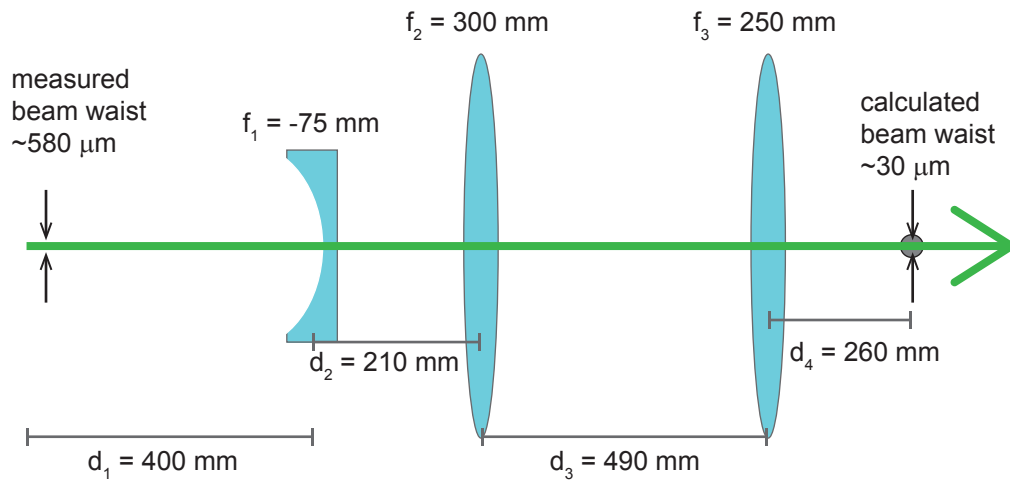


Figure 4.7: Beam shaping our green plug beam. The measured beam waist was after our green plug beam’s control AOM. Pictured is the telescope we used to expand the beam before focusing it onto the quadrupole zero at the atoms. This figure is not to scale.

beam’s position needed to be adjusted throughout the day. We monitored its position by in-situ imaging ^{87}Rb atoms in the quadrupole trap with the green plug on and adjusted its location with a mirror driven by a picomotor in the green beam’s path.

Often times a drop in ^{40}K atom number corresponded to the green beam moving. We decided to free space couple the green plug to achieve more power at the atoms and have a larger beam waist. We removed the fiber and profiled the beam directly after the AOM. We designed a telescope, illustrated in Fig. 4.7 to expand the beam before the $f_3 = 250$ mm lens focused it down to ~ 30 μm at the atoms. Our green plug beam was combined with our xz imaging probe beam using a DMLP567L dichroic mirror. We used another DMLP567L dichroic mirror to deflect the green beam after the experiment chamber. We protected our xz imaging camera with a filter. We minimized the green plug’s beam waist at the atoms by imaging the leakage light with amplitude to the AOM commanded

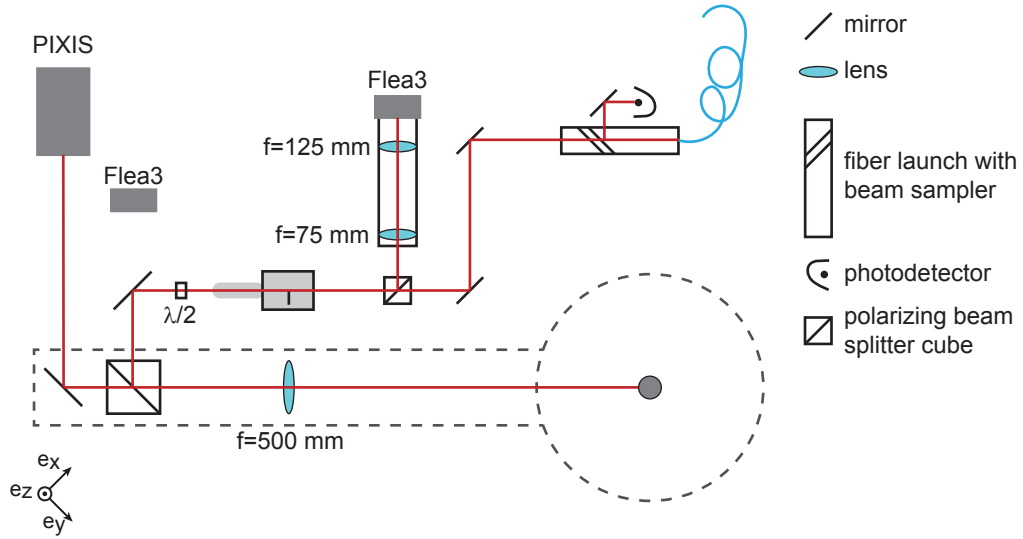


Figure 4.8: xy imaging system configured for phase imprinting. Our phase imprinting beam is sent backwards through our imaging system after backlighting a razor edge mounted to a translation stage. We roughly focused the edge onto the atoms with our relay imaging system. This figure is not to scale.

zero. Even with chromatic aberrations, this method was effective. Running the Verdi at 12.5 W, we had $\sim 5\text{ W}$ at the atoms. This did reduce our potential barrier, but the larger beam's position did not have to constantly be adjusted.

4.3.5 Imaging systems

We had two imaging planes in our experiment. Our xz imaging plane was defined by gravity in one direction and long axis of our apparatus in the other. Historically, our slower defined the e_x direction, hence the xz imaging axis name. Our xz imaging system has a magnification of 2. Our xy imaging plane is defined by our crossed dipole trap. The xy imaging system consisted of a compound lens with an effective focal length of 83 mm recessed in our chamber's bucket window and a 500 mm lense shown in Fig. 4.8. These lenses gave a magnification

of 6 and a resolution of about $2 \mu\text{m}$. Due to its superior resolution, we used this imaging axis to image an edge onto our condensate and launch solitons. Figure 4.8 shows our imaging system in its configuration for our experiments presented in Ch. 6. We used a polarizing beam splitter (PBS) to merge our soliton beam into our imaging optics. A kinematic base with a gold mirror directed our phase beam into the imaging system. When this base was removed, our Flea3 camera was focused in-situ for the microwave magnetic field lock used in Ch. 7. We installed a relay imaging system to roughly focus our edge at the location of the atoms. First, we focused the atoms onto our relay imaging camera. Then, we placed our razor edge in the focal plane of our relay imaging. The position of the razor edge for phase imprinting needed to be positioned within $\approx 5 \mu\text{m}$. Our relay imaging system did not have that resolution. The final focusing of our edge was completed by looking for the existence of long lived solitons as a function of position on the translation stage where the edge was mounted.

4.4 Magnetic fields

We have 3 pairs of bias coils in Helmholtz configuration for bias fields in the \mathbf{e}_x , \mathbf{e}_y , and \mathbf{e}_z directions, as shown in orange in Fig. 4.1. These bias coils were used to null fields or set bias magnetic fields < 10 G. Their currents were stabilized by proportional-integral control circuits and could be ramped or changed during the experimental sequence. An additional set of 4 coils were used to cancel out gradients in B_z along \mathbf{e}_x . Two coils are pictured in Fig. 4.1 and the other two are directly beneath them. Canceling out the gradient in \mathbf{e}_x was important for our studies with evenly distributed spin impurities in Ch. 6. We canceled the gradient by making 50/50 mixtures of elongated ^{87}Rb in $|F = 1, m_F = -1\rangle$

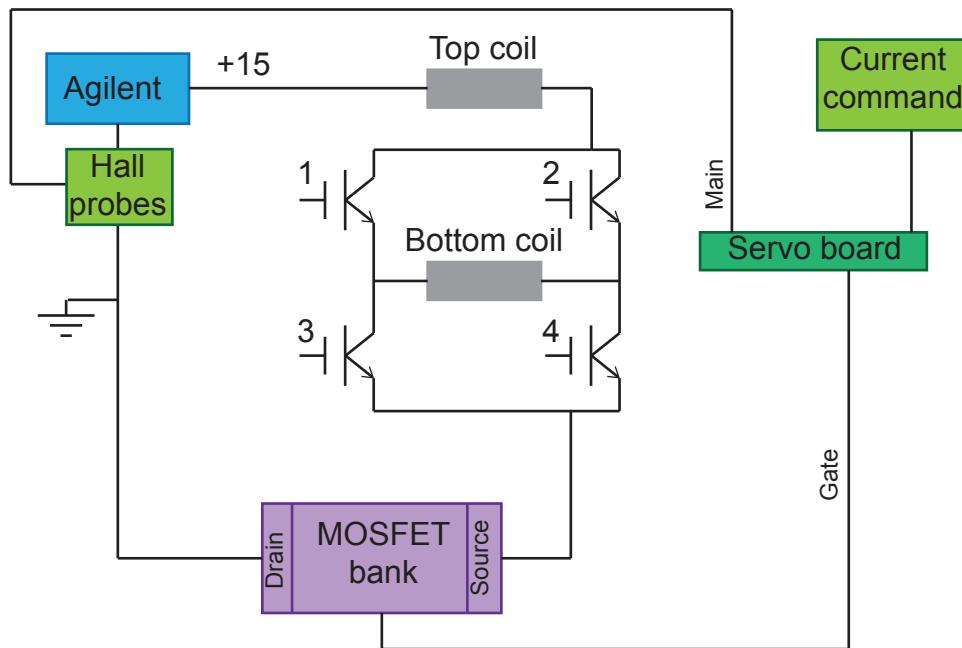


Figure 4.9: This schematic displays our H-bridge and current feedback for our large coils. When IGBT's 2 and 3 are gated on, our coils are in anti-Helmholtz configuration. When IGBT's 1 and 4 are gated on, our coils are in Helmholtz configuration.

and $|F = 1, m_F = 0\rangle$ states because these states are miscible at our experiment's operating fields. During time-of-flight (TOF), we applied a Stern-Gerlach pulse to separated the spin states. As we changed the current in the coils, the spin states went from being on either half of the condensate, to spatially overlapped, to the opposite location. We set the current to the middle of the range where the spin states were mixed.

An H-bridge changed our large coils from anti-Helmholtz configuration for

our MOT and quadrupole magnetic trap to Helmholtz to achieve ≈ 200 G fields for our studies of the ^{40}K $|F = 9/2, m_F = -7/2\rangle$ and $|F = 9/2, m_F = -9/2\rangle$ Feshbach resonance in the same sequence. Figure 4.9 shows our H-bridge with 4 insulated-gate bipolar transistors (IGBTs) controlled by 2 TTL signals from our control computer to switch configurations. In either configuration, our coils' current was supplied by an Agilent 6690A. We stabilized our current by comparing a voltage from a Hall probe to our computer command. Our servo board sent a voltage to the gate of our MOSFET bank—an array of 19 MOSFETs in parallel—to feedback on the current.

4.4.1 Magnetic field stabilization with microwave servo

We used microwaves to address transitions between the two ground hyperfine states of ^{87}Rb . As shown in Fig. 2.1, these states are ~ 6.8 GHz apart. Our microwave source was a Stanford Research Systems SG384. We duplicated the design of our colleagues at NIST in Trey Porto's rubidium lab (Fig. 4.10). We manually set the output of the source to be 100 MHz away from the zero field splitting. A mixer combined our microwave source with an ≈ 100 MHz frequency generated by our Novatech 409A to generate a frequency which addressed allowed transitions at a given bias magnetic field B .

We usually performed experiments with ^{87}Rb BECs in the $F = 1$ hyperfine manifold. By pulsing on-resonant microwaves and taking an absorption image without repump light addressing the $|F = 1\rangle \rightarrow |F' = 2\rangle$ transition, we could take images of our BEC in-situ and continue an experimental sequence

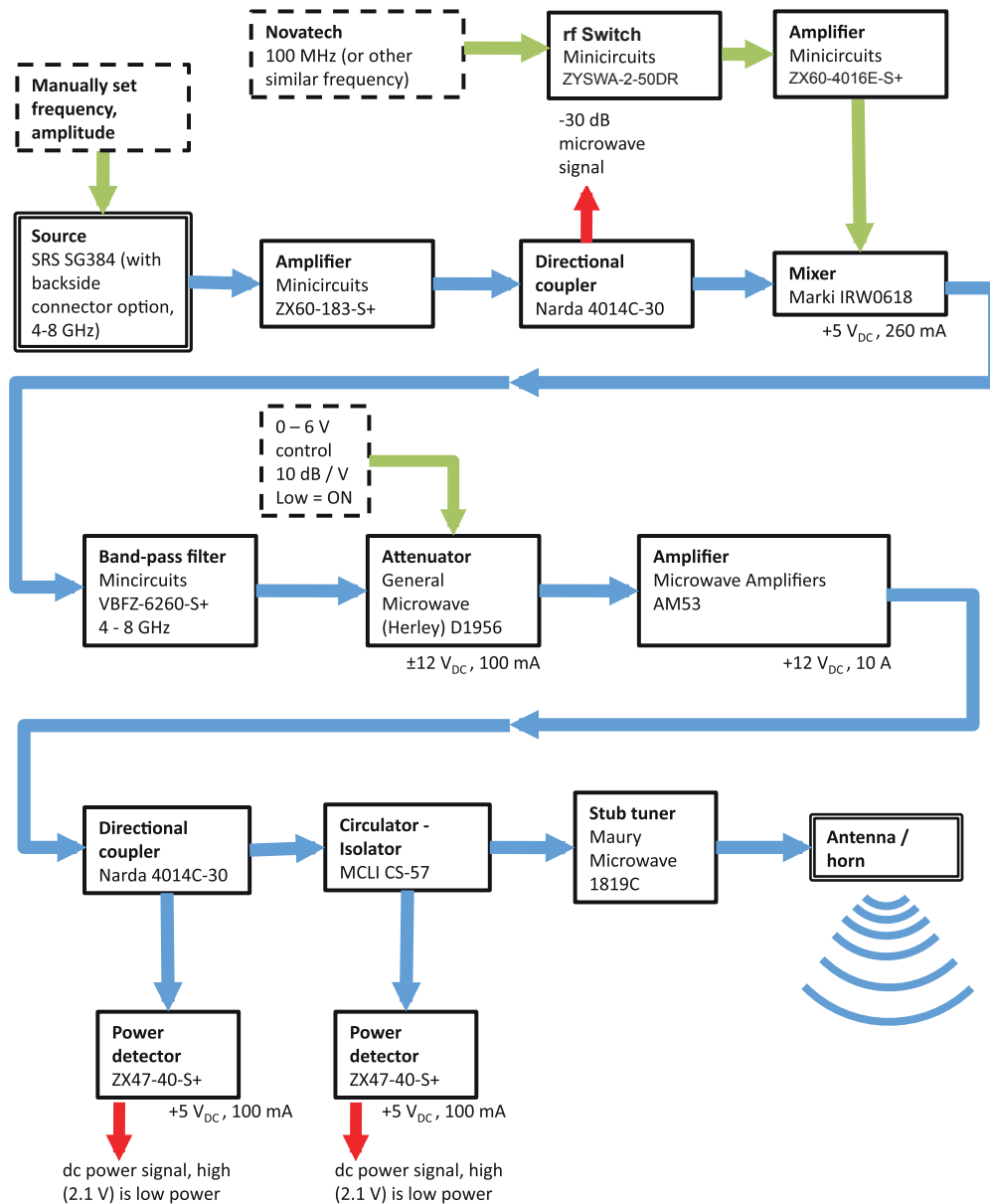


Figure 4.10: Microwave source schematic for all the components from source to antenna. Blue arrows denote the microwave frequency path, green arrows are inputs, and red arrow indicate outputs for monitoring, debugging or tuning. Components requiring power are marked. The high power microwave amplifier is water cooled. Modified image originally created by Lindsay LeBlanc for the laboratory's manual.

with a slightly depleted BEC. We used this technique to set up a microwave field lock that fed back on our bias coils in the \mathbf{e}_z direction. This stabilized our bias magnetic field against long-term drifts. During our sequence we applied a 1 ms pulse of our microwaves detuned by 500 Hz from our resonance with our bias field set point. Resonance was determined by which transition we were addressing. After each pulse, we absorption imaged the transferred atoms with a probe on resonance with the $|F = 2\rangle \rightarrow |F' = 3\rangle$ transition. Figure 4.11A shows an example of our counting the number (n_1, n_2) of transferred atoms after each pulse versus scanning the bias field. To calibrate the sensitivity of our microwave field lock we repeated this scan several times over a narrower field range. The normalized asymmetry $(n_1 - n_2)/(n_1 + n_2)$ produced a signal approximately linear in a ~ 0.5 mG range. The different markers in Fig. 4.11B represent different scans. The long term drift of our bias field is apparent. Converting from current to magnetic field, we found a slope of 0.35 ± 0.01 mG. Our field sensitivity was the root mean square of our residuals or 0.0027 mG. After every sequence, we sent a voltage to our bias coil command proportional to the normalized asymmetry. Our integrator constant for our bias field lock was ≈ 60 s, because that was the length of our sequence. We designed the rest of our sequence in phase with 60 Hz.

For our results sensitive to detuning, like the ones presented in Ch. 7, we also used these images to provide an unbiased veto against shots with substantial field errors [85]. For our results in Ch. 6, this gave us a very reliable state preparation which was sensitive to magnetic field. We have implemented the microwave field lock with both xy and xz imaging¹.

¹These are historical names. In the coordinate system I defined for the experiment they are the $\mathbf{e}_x\mathbf{e}_y$ and the $(\mathbf{e}_x + \mathbf{e}_y)\mathbf{e}_z$ imaging systems

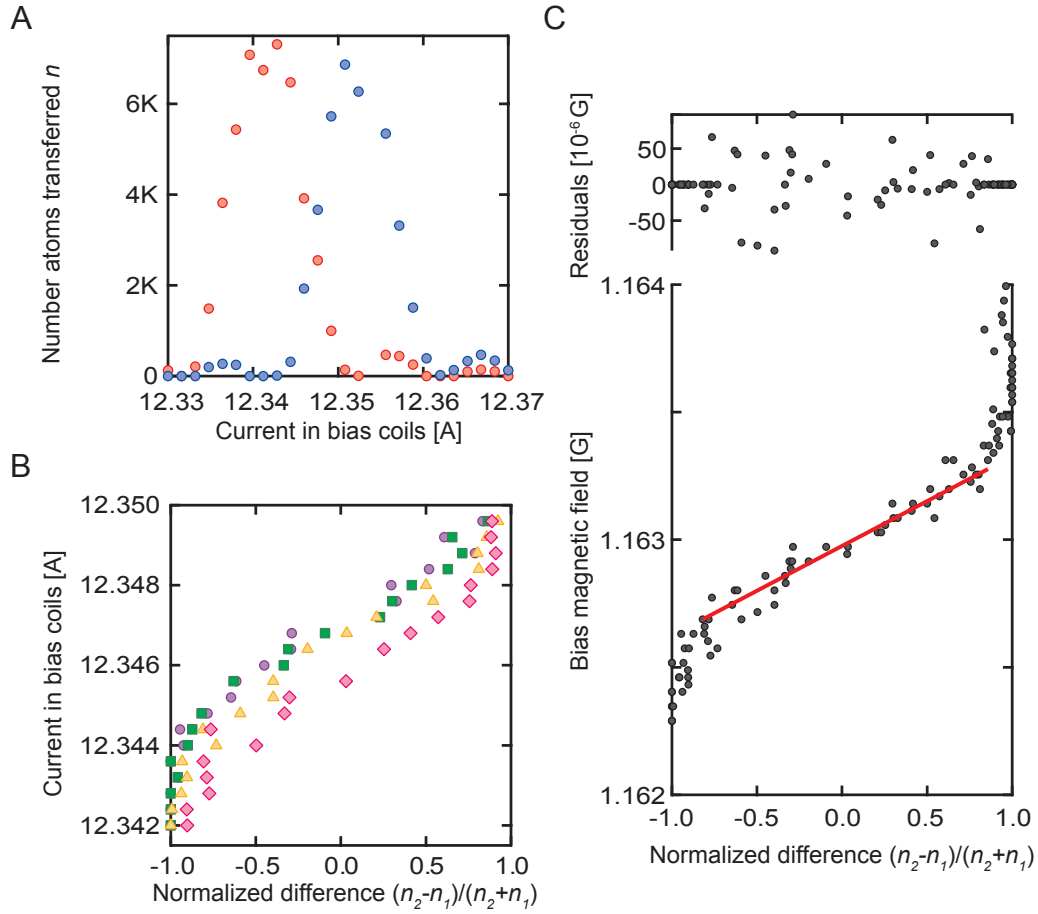


Figure 4.11: Magnetic field stabilization. (A) The red(blue) markers represent the number n_1 (n_2) of transferred atoms after the first(second) pulse versus current in bias coils. (B) Current in bias coils versus the normalized difference in transferred atoms between the two microwave pulses. Colors are for different data runs. Purple was taken first, pink last. This shows drift in a short time (~ 30 minutes). (C) Calibration for field sensitivity was calculated by finding the RMS average of the residuals from a linear fit of the field to the normalized difference of transferred atoms.

S-WAVE SCATTERING OF FERMIONS

5.1 Introduction

We are interested in engineering topologically interesting systems that can support Majorana modes, which have non-abelian statistics[131]. One system that can support these modes are $p_x + ip_y$ -wave superconductors that have Cooper pairs with orbital angular momentum $\ell = 1$ [131]. Section 3.2.1 discussed how we can use one parameter, the s -wave scattering length, to characterize interaction in our cold atom samples. However, to support Majorana modes in cold atom systems, interactions in the p -wave channel are required [138, 75]. For BECs, optically dressing the atoms with two-photon Raman transitions has been shown to introduce d -wave and g -wave contributions into typical s -wave scattering events [134]. This technique should be extend-able to fermions for simulating odd higher-order partial waves.

Our first step in this experiment was to characterize s -wave scattering halos for binary spin mixtures in a degenerate Fermi gases. Scattering halos appear as circles in 2-D images of the density distribution of 3-D atoms after colliding atomic clouds with different momenta. In BECs scattering halos are readily imaged with typical imaging techniques [55, 38, 125, 28], we found that the lower density of our DFGs compared to typical BEC densities to be a barrier to fully characterizing these low energy s -wave collisions. To enhance the number of collisions and increase our signal, we performed the measurement in the vicinity of a magnetically tunable s -wave Feshbach resonance (see Sec. 3.2.3). Even with this enhancement, absorption imaging still had detection uncertainty that

impacted the regions of low atomic density the most. We then used high intensity imaging to reduce our signal-to-noise. As the atoms absorb light from the probe beam, each scattered photon imparts momentum to the atoms. As the atoms accelerate due to the radiation pressure of the probe beam, the atoms are Doppler shifted out of resonance. This leads to under counting during the imaging process [82] and so we developed an image processing technique that accounted for this [54]. We were able to characterize a s -wave Feshbach resonance in ^{40}K directly through measuring the fraction of atoms scattered during the collision at different bias magnetic fields and deduced the location and width of the resonance without relying on proxy effects. This work is published in *New Journal of Physics* **18** (2016) 013001.

We never completed the experiment to induce higher order partial waves in ^{40}K . In the last section of this chapter, I report on a few different techniques we explored before deciding to postpone this experiment with ^{40}K due to the daily struggle with maintaining a constant, acceptably large atom number.

5.2 s -wave scattering experiment

In this section, I will discuss the procedures and ingredients for our s -wave scattering experiment that occur after creating a spin polarized $|F = 9/2, m_F = -9/2\rangle$ DFG of $\approx 4 \times 10^5$ atoms of ^{40}K at a temperature $T \approx 0.4 T_F$ in a crossed optical dipole trap with frequencies $(\omega_x, \omega_y, \omega_z)/2\pi = (39, 42, 124)$ Hz as described in Chapter 4.

5.2.1 Preparation of 50/50 spin mixtures in DFGs

To map out the wide s -wave Feshbach resonance at 202.1 G for $|F = 9/2, m_F = -9/2\rangle$ and $|F = 9/2, m_F = -7/2\rangle$ ^{40}K atoms, we devised a standard procedure for creating a spin mixtures above and below the resonance. We ramped the bias magnetic field to 190.5 G (217.1 G) and turned on a 42.42 MHz (47.11 MHz) rf field resonant with the Zeeman splitting between the two states when preparing the mixture below (above) the Feshbach resonance. We then sinusoidally modulated the bias field at 125 Hz for 0.5 s, with a 0.14 G amplitude, producing an equal mixture of the two hyperfine states. Because the rf circuit was optimized for frequencies of a few MHz, the rf intensity at ~ 40 MHz was too low for us to calibrate the coupling strength. Depolarizing a DFG decreased the T_F because the number of available states increased by a factor of two, decreasing the Fermi momentum k_F . Thus the temperature was larger in units of T_F . This depolarization allowed the fermions to re-thermalize [45]. We evaporated to a lower optical potential, decreased their temperature, and narrowed our atoms' momentum distribution.

5.2.2 Mapping out the Feshbach Resonance

After creating depolarized gases at fields $\approx \pm 15$ G away from the 202.1 G Feshbach resonance, we used traditional methods to map out the resonance [109]. First, we measure inelastic collision losses in atom number versus bias magnetic field. To approach the set-point quickly and avoid unintended, additional losses, we designed a two-step procedure using a pair of large coils and a concentric pair of small coils. Our large coils had a larger inductive time scale than

our small coils. We implemented an H-bridge to change the configuration of our large coils from anti-Helmholtz for the MOT and magnetic trapping staged of our experiment to Helmholtz to reach magnetic fields of hundreds of Gauss (See Sec. 4.4). We approached resonance from both above and below the Feshbach resonance to map out the loss. Figure 5.1 displays both sets of data. After creating a spin mixture at the desired field above (below) the resonance and evaporating further, we used the large coils to set the bias magnetic field B to a set-point 5.1 G above(below) the intended bias field. We held the atoms at this field for 100 ms to allow the eddy currents induced by the large coils to settle, and then used the smaller coils to quickly change the bias field the remaining 5.1 G. We held the bias field at its set-point for 200 ms. Our loss feature was shifted to the lower field, repulsive scattering length side of the resonance where a weakly-bound molecular state exists. This is consistent with previous measurements [110].

Next, we explored Feshbach molecule creation and dissociation [111]. When we ramped through the Feshbach resonance coming from the attractive, high-field side, Feshbach molecules were created. For accurate atom counting, we dissociated the molecules before taking an absorption image. The on-resonant probe beam for the bare atom states was not on resonance for the Feshbach molecule. In Fig. 5.2 we show our molecule creation and dissociation process. During time of flight (TOF), we held at the set-point for the bias field for 1 ms. After the 1 ms, we either continue to hold at the set-point to image or ramp away from the resonance to dissociate the Feshbach molecules. To create Feshbach molecules, we had to evaporate to a slightly lower temperature, we reduced our dipole trap depth by 10% compared to the depth used in our loss experiments. Dissociation during TOF recovers most of the atoms above the Feshbach

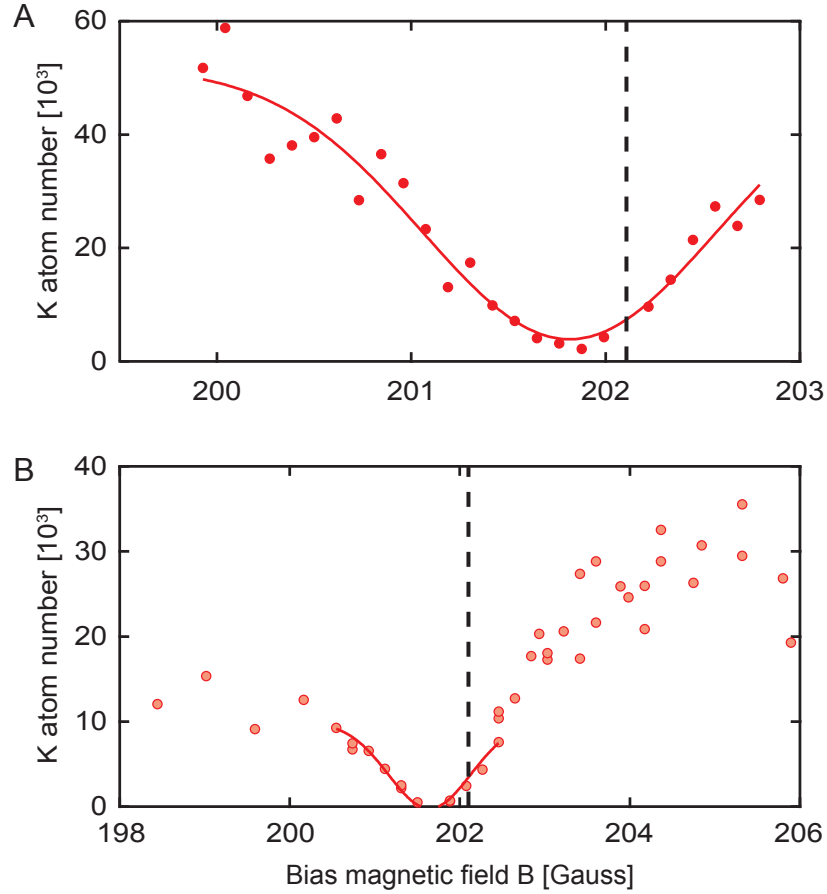


Figure 5.1: Atom loss near Feshbach resonance. (A) Approaching the Feshbach resonance with a spin mixture from lower field. The atom number was measured after a 200 ms hold time at the bias field. (B) Approaching the Feshbach resonance with a spin mixture made above the resonance. The dashed line is the location of the resonance B_0 .

resonance.

5.2.3 Magnetic field calibration

The magnetic fields produced by our large bias coils around 200 G were independently calibrated by rf-spectroscopy on the $|F = 9/2, m_F = -9/2\rangle$ to $|F = 9/2, m_F = -7/2\rangle$ transition of ^{40}K . We prepared a spin polarized DFG as

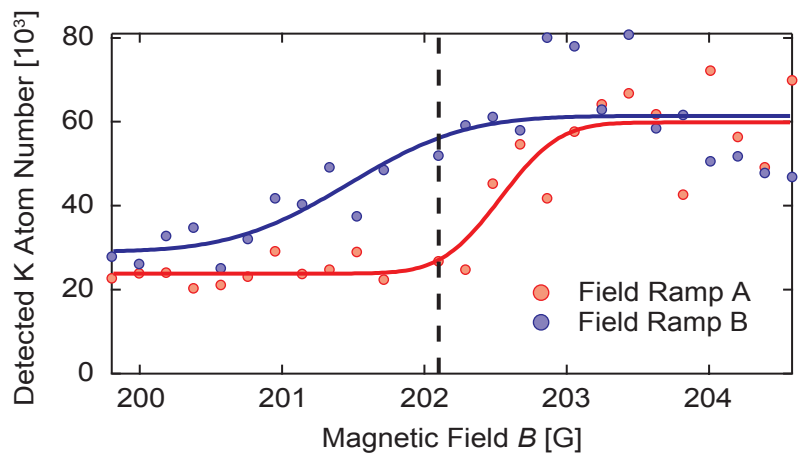
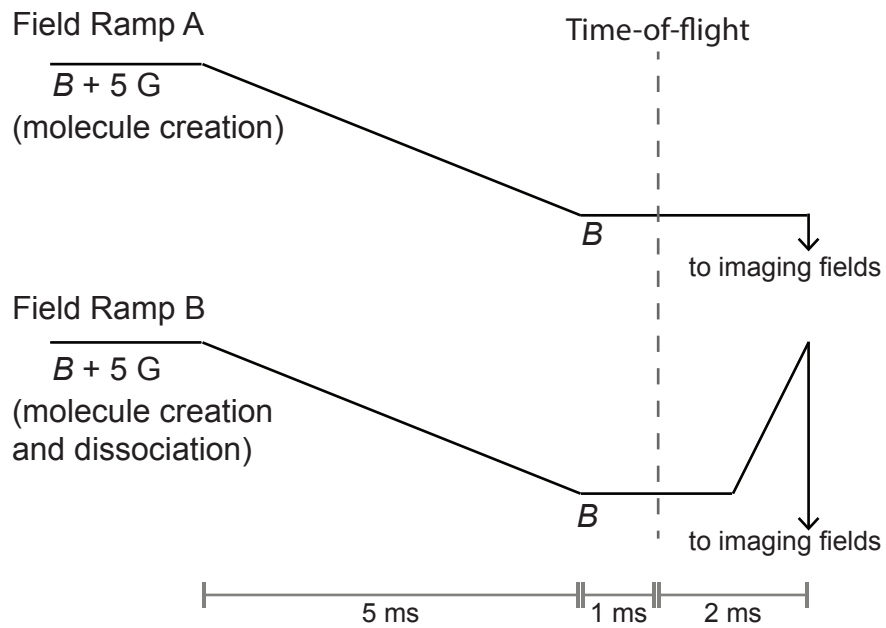


Figure 5.2: Feshbach molecule creation and dissociation. Schematics for the field ramps for approaching the Feshbach resonance from above. Field Ramp A does not dissociate molecules, field ramp B does. The detected atom number versus magnetic field is plotted for each ramp.

described in Ch. 4 and ramped the bias coils to variable set-points while keeping the smaller coils at their zero field setting. We illuminated the atoms with a rf field of frequency ν_{rf} and performed adiabatic rapid passage (ARP) by ramping the small bias coils 0.284 G or 2 A in 250 ms. We applied a Stern-Gerlach pulse by switching our large coils back to anti-Helmholtz configuration and imaged the atoms to measure the fractional population in the $|F = 9/2, m_F = -9/2\rangle$ and $|F = 9/2, m_F = -7/2\rangle$ states. We then fit the fractional population in the $|F = 9/2, m_F = -7/2\rangle$ state as a function of current to a Gaussian function. Due to our low rf coupling, we did not fit to the traditional Lorentzian model. Additionally, we often did not achieve complete transfer into the $|F = 9/2, m_F = -7/2\rangle$ state. The center of the Gaussian corresponded to the resonant magnetic field and the standard deviation of the fit parameters was our uncertainty. We used the Breit-Rabi formula to determine the resonant field value at ν_{rf} . We did this for 5 different ν_{rf} , and the magnetic field produced by our MOT coils varied linearly with their commanded current. Our fit included the uncertainties in the center position of the Gaussian and the uncertainty of the slope gave our field uncertainty. Our large bias coils produce 1.91 G/A with an uncertainty of 0.04 G.

5.2.4 Optical lattice for ^{40}K

For engineering higher order partial waves with ^{40}K as opposed to ^{87}Rb , modifications to the technique were necessary. ^{87}Rb is a BEC, therefore most of the atoms occupy only on momentum state. Because the spread in momentum was smaller for ^{87}Rb , the scattering halos were more readily imaged due to their higher densities as compared to DFG of ^{40}K . Loading a dressed state with atoms in a equal superposition in the $|F = 1, m_F = \pm 1\rangle$ internal states of

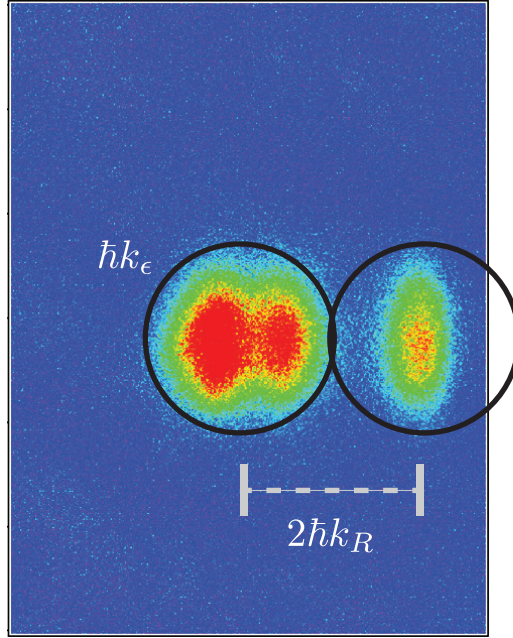


Figure 5.3: Absorption image of a DFG after a $\pi/2$ Raman pulse at $\delta = 4E_R$. The atoms close to 0 momentum are coupled to the other spin state.

^{87}Rb created two clouds with $\pm 2k_R$, where $\hbar k_R = 2\pi\hbar/\lambda_R$ is the recoil momentum associated with the two-photon Raman transition. The momentum spread of the BEC was negligible compares to k_R . In contrast, for our DFG of ^{40}K , k_R was comparable to the Fermi momentum k_F as pictured in Fig. 5.3. This image was taken with a weak Raman π -pulse with a detuning $\delta = 4E_R$ (see Sec. 5.4.1). Additionally, we opted to perform the experiment with the $|F = 9/2, m_F = -9/2\rangle$ and $|F = 9/2, m_F = -7/2\rangle$ internal states of ^{40}K to enhance their interactions with a Feshbach resonance. With only optical dressing, our fermions in the different spin states would move away from each other with only $2\hbar k_R$. We needed to have a modified procedure to engineer collisions with optically dressed ^{40}K .

I installed a 1-D optical lattice co-propagating with our Raman A/C beams (see Sec. 4.3.3). Kapitza-Dirac pulses—the scattering of matter from pulses of a standing wave light pulse—of this lattice created two spatially overlapping

clouds with opposite momenta $4\hbar k_L$, where $\hbar k_L = 2\pi\hbar/\lambda_L$ is the lattice recoil momentum. The optical lattice had a beam waist of $160\ \mu\text{m}$. We used near-resonant $\lambda_L = 766.704\ \text{nm}$ light by diverting a small amount of the ^{40}K repumping light used during laser cooling. We only needed $0.06\ \text{mW}$ for a lattice depth $\approx 8E_L$, where $E_L = \hbar^2 k_L^2 / 2m_K$ is the lattice recoil energy. We rapidly pulsed this lattice on and off with a double-pulse protocol [136]. The pulse sequence was optimized to transfer most of the atoms into the $\pm 2\hbar k_L$ momentum states, shown in Fig. 5.4B. The optimized pulse times were $\tau_1 = 23\ \mu\text{s}$ for the first pulse, $\tau_2 = 13\ \mu\text{s}$ off interval, and $\tau_3 = 12\ \mu\text{s}$ for the second pulse. Since the initial Fermi gas had a wide momentum spread and the lattice pulsing is a momentum dependent process [48], not all the atoms were transferred into the target momentum states. We optimized our pulse times to minimize the atoms remaining in the untransferred state.

We absorption imaged the atoms after a $6.8\ \text{ms}$ TOF and the $\pm 2\hbar k_L$ atoms had traveled $\approx 203\ \mu\text{m}$. Figure 5.5 includes examples of our absorption images. Due to conservation of momentum, single scattering events are easily identified. After an elastic collision event between an atom traveling with $-2\hbar k_L$ momentum and an atom traveling with $+2\hbar k_L$ momentum, the atoms will depart with equal and opposite momenta $2\hbar k_L$ at an arbitrary angle. Therefore, the single collision s -wave scattering halo should be a spherical shell with a radius corresponding to the $\pm 2\hbar k_L$ momenta imparted from the lattice and a thickness given by $\hbar k_\epsilon$, as illustrated schematically in Fig. 5.4C.

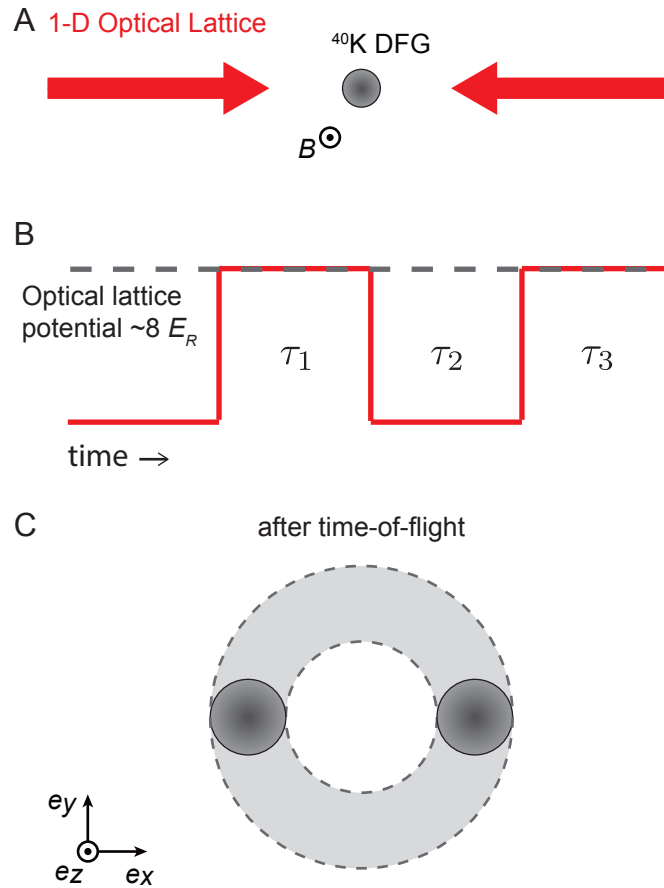


Figure 5.4: (A,B) The 1D lattice was pulsed, imparting momentum to the atoms. (C) After time of flight, the two clouds traveling along $\pm e_x$ directions have separated and the atoms that underwent a single scattering event were evenly distributed in a scattering halo around the unscattered clouds.

5.3 s -wave scattering results

5.3.1 Image processing

We optimized our signal-to-noise ratio for low atom numbers by imaging with long, high-intensity pulses [54]. Our imaging pulse was $40 \mu\text{s}$ with an intensity $0.6 I_{SAT}$. We used a probe beam approximately the size of the s -wave scattering halos to minimize interference fringes on the beam. These pulses imparted

a non-negligible velocity from the radiation pressure and Doppler shifted the atoms out of resonance with respect to the probe. We simulated this recoil induced detuning and corrected the images to count the fraction of scattered atoms in our collision experiment. An example of images before and after processing are shown in Fig. 5.5. From our simulations, we created a look-up table to go from the measured optical depth to a corrected column density along e_z . The processing constituted a $\approx 30\%$ change in the column density.

5.3.2 *s*-wave scattering halos

Our procedure for directly imaging *s*-wave scattering halos above and below the Feshbach resonance were as identical as possible. We created a spin mixture above or below the Feshbach resonance, used the two-step procedure to approach the bias field set-point, held at resonance for 3 ms, pulsed the 1-D optical lattice, and then turned off the optical dipole trap. The atoms expanded at high-field for 2 ms. For data points below the resonance, the bias field remained constant for these 2 ms before quickly going to the bias fields for imaging as represented in Fig. 5.2 field ramp A. For data points above the resonance, we held at the set-point for 1 ms and then ramped the bias field to larger bias fields to dissociate the molecules as represented in Fig. 5.2 field ramp B. We collected fifteen images at every set-point.

Figure 5.6 displays our corrected absorption images of *s*-wave scattering halos in the vicinity of a magnetically tunable Feshbach resonance. In each image, the two high-density clouds on the left and right are the atoms in the $\pm 2k_L$ momentum orders that passed through each other unscattered. The cloud in

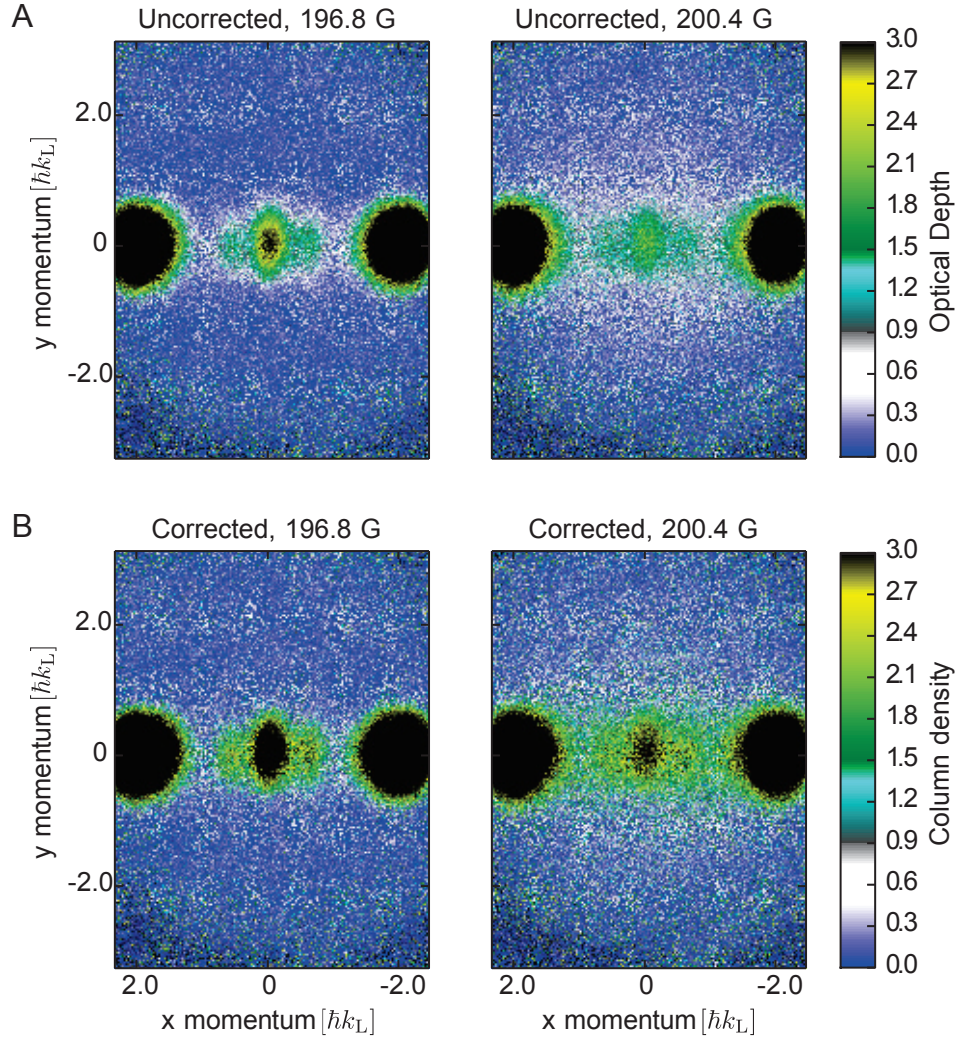


Figure 5.5: (A) Uncorrected optical depths, far from resonance (196.8 G) on the left and close to resonance (200.4 G) on the right obtained from out unprocessed absorption images. (B) Atomic column density obtained by applying corrections to raw optical depth above based on simulations [54].

the center were untransferred atoms after pulsing, and thus obtained no momentum. This cloud appears somewhat depleted closer to resonance due to scattering with atoms in the $\pm 2k_L$ momentum orders, this effect was not taken into account in our analysis. The thin spread of atoms in the radius $2\hbar k_L$ with thickness $2\hbar k_\epsilon$ were the scattered atoms.

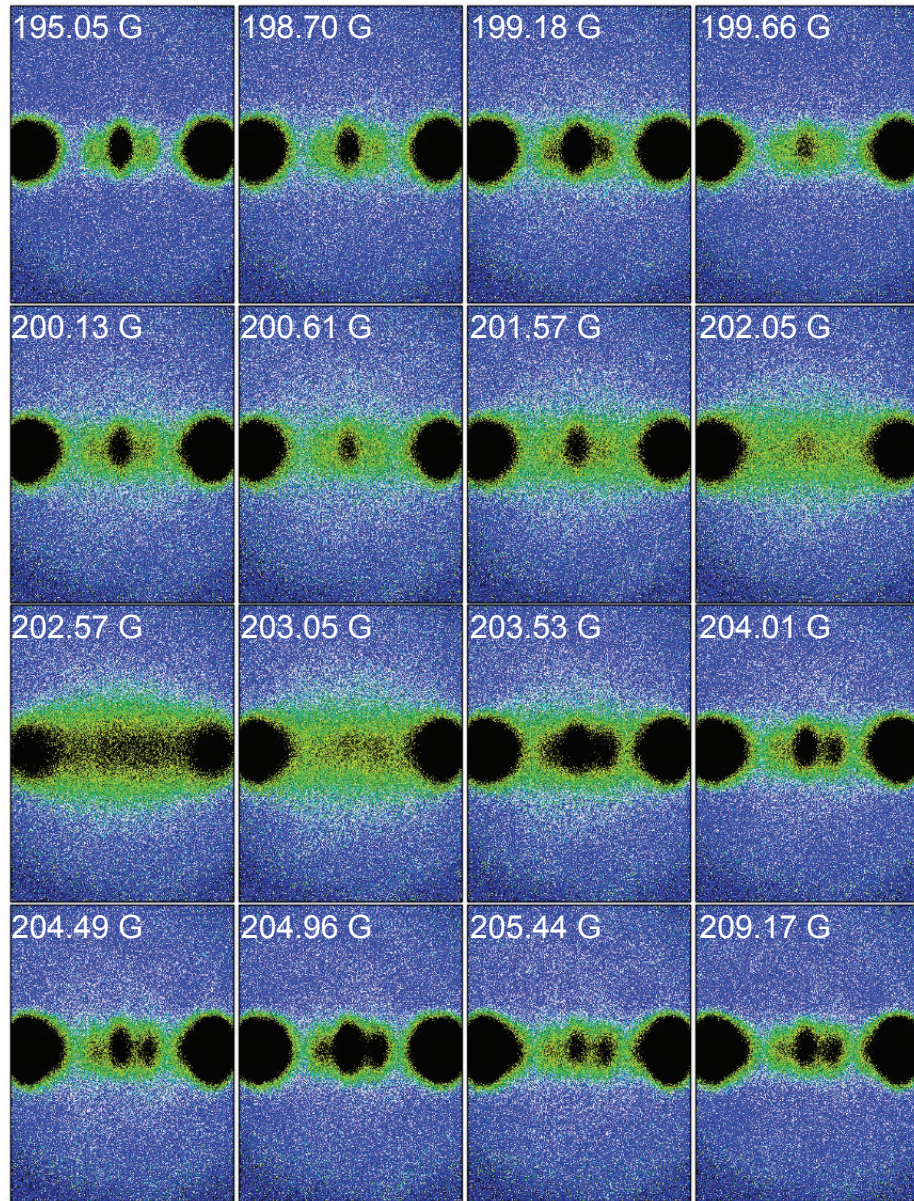


Figure 5.6: Corrected images of *s*-wave scattering halos

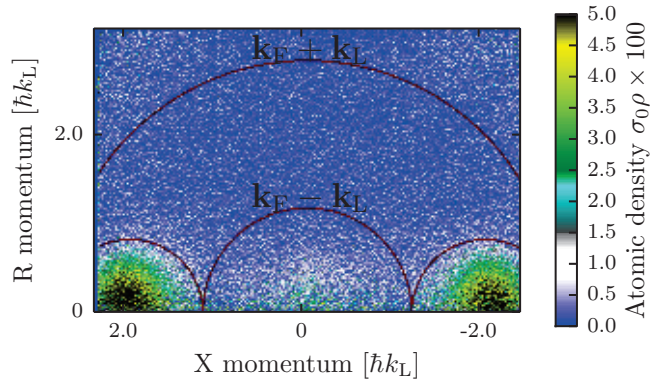


Figure 5.7: The atoms within the Fermi momentum k_F of each cloud center are in the unscattered region and counted towards the total unscattered number N_{tot} . The atoms within the radius $k_L - k_F \leq r \leq k_L + k_F$ but outside the unscattered region were counted as the number N_{scat} of single scattered atoms.

To extract the radial dependence of the 3D distribution from our 2D images, we performed an inverse Abel transform assuming cylindrical symmetry along \mathbf{e}_x , defined by the lattice [26]. We thus obtained the atomic distribution $\rho(r, \theta)$ as a function of r , the radial distance from the scattering center, and θ , the angle between r and symmetry axis \mathbf{e}_x , integrated over ϕ . We then extracted the number of atoms N_{scat} that underwent a single scattering event as a fraction of the total atom number N_{tot} for each image, as shown in Fig. 5.7. N_{scat} was the number of atoms outside the Fermi radius of the unscattered clouds, but inside the arc created by rotating the Fermi momentum k_F around the original center of the cloud (red arcs in Fig. 5.7). N_{tot} was the sum of N_{scat} and the counted atoms in the two unscattered clouds. For both the scattered and unscattered quantities, we extrapolated to include atoms that would fall outside the field of view of our camera. The undiffracted atoms were not counted as they did not contribute to the scattering halo under study.

5.3.3 Determination of Feshbach resonance magnetic field position

Since we were well below the p -wave threshold temperature and p -wave collisions are energetically forbidden, our scattering cross-section $\sigma = 4\pi a^2$ was fully defined by the s -wave scattering length a [45]. After publishing our manuscript on s -wave scattering halos in ^{40}K , a result in a higher energy scattering regime more readily imaged p -wave scattering halos because a larger fraction of the atoms scattered [126]. A single particle incident on a cloud of atoms with a surface density of N/A —where A is the cross-sectional area of the cloud and N is the number of atoms—will scatter with probability $P_{\text{scat}} = \sigma N/A$. In our case, each half $N_{\text{tot}}/2$ of the atoms was incident on the other half. Thus, the number of expected scattering events was $N_{\text{scat}} = \sigma N_{\text{tot}}^2/4A$. Assuming A was constant for all our data, we defined a fit parameter $b_0 = 4\pi a_{\text{bg}}^2/4A$, where a_{bg} is the background scattering length. We thus adapted Eqn. 3.26 to obtain the fit function

$$\frac{N_{\text{scat}}}{N_{\text{tot}}^2} = b_0 \left(1 - \frac{\Delta}{B - B_0} \right)^2 + C, \quad (5.1)$$

where B_0 is the resonant field value, Δ is the width of the resonance, and the offset C accounts for any systematic difference in the initial and final intensity images with no atoms present.

We extract $N_{\text{scat}}/N_{\text{tot}}^2$ at each bias magnetic field by plotting the measured $N_{\text{scat}}/N_{\text{tot}}$ versus the total atom number N_{tot} for each of the fifteen images at that set-point. These data were linear versus N_{tot} , and the slope and variance of this fit gave the value and uncertainty of the data plotted in Fig. 5.8. The red curve depicts a best fit of the model given in Eqn. 5.1 and the extracted parameters were $\Delta = 1.0(5)$ mT and $B_0 = 20.206(15)$ mT. For the fit, we excluded data points

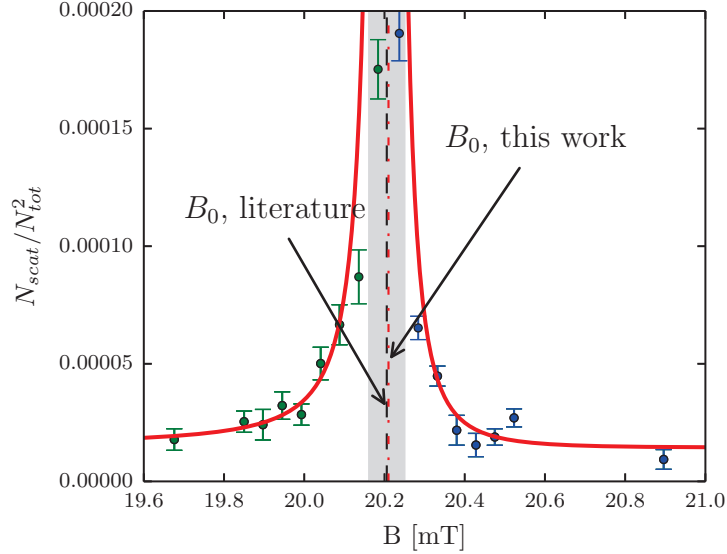


Figure 5.8: Normalized scattered population plotted versus bias field B . Green(blue) dots represent data taken coming from below(above) the resonance B_0 . The red curve depicts the line of best fit. The hydrodynamic regime is shaded in gray, and data points within that regime were excluded from the fit.

very near the resonance. In this regime, our assumption that scattered atoms only undergo a single scattering event breaks down and the atomic gas needs to be treated hydrodynamically[39]. This led to a large uncertainty on our extracted resonance width.

5.3.4 Conclusion

Our findings are in good agreement with the accepted values for the ^{40}K s -wave Feshbach resonance for the $|9/2, -9/2\rangle$ and $|9/2, -7/2\rangle$ states are $B_0 = 20.210(7)$ mT and $\Delta = 0.78(6)$ mT[111]. Although the data without the recoil induced detuning correction were $\approx 30\%$ different from the corrected data, the optimal parameters from fitting the uncorrected data were within our uncertainties from

the values listed above. The resonance location was largely unaffected by the correction, as the scattering cross-section diverges there, making it insensitive to the precise values. The width may have been affected, however the uncertainty on the fit is too large for the effect to be significant. Our imaging analysis, optimization of SNR, and our study of *s*-wave scattering halos will be useful for simulating higher-order partial waves with collisions between fermions.

In our manuscript, we noted that erbium and dysprosium DFGs [5, 90] have much higher densities than alkali DFGs and could more readily image low energy scattering halos. Recently, a result on studying dipolar interactions with scattering halos was shared on arXiv [29].

5.4 Outlook: synthetic partial waves with ^{40}K

By the end of January 2014, a constantly decreasing atom number without explanation led us to postpone experiments with ^{40}K until after we develop and install a 2-D MOT for potassium. This was after a series of unfortunate events: the October 2013 federal government shutdown, running out of potassium, potassium oven controller malfunctions, unplanned air handling outages, etc. My hope for this section is to document what we learned in combining Raman coupling and Kapitza-Dirac pulses for posterity.

5.4.1 Technique: Optical dressing then lattice pulsing

We began our attempts at simulating higher-order partial waves by optically dressing spin polarized DFGs and then pulsing the 1-D optical lattice. The plan

was to adiabatically turn on Raman coupling, wait a quarter of a trap period for the atoms to come to rest, then use the optimized Kapitza-Dirac pulses to create two clouds with opposite momenta. We tried this, but found that Kapitza-Dirac pulses excited the atoms to both the higher bands of the optical lattice and the excited band of our dressed atom state. This led to several, hard to interpret momentum orders in our absorption images. Notably, in rubidium, there was a fall off of synthetic d -wave contributions to the scattering halos for Raman coupling strengths above $6E_R$ [134]. We wanted to maximize our signal for synthetic p -wave partial waves, so we wanted Raman couplings less than $6E_R$. Consequently, our designed Kapitza-Dirac pulses for the optical lattice with potential depth $\approx 8E_R$ excited the atoms to the higher Raman band as well (the wavelengths of the 1-D optical lattice and the Raman lasers were effectively the same). Our solution to this was to modify the procedure. We would adiabatically ramp up the Raman to the desired coupling strength, wait a quarter trap period, then quickly increase the Raman coupling, apply the Kapitza-Dirac pulses, then quickly ramp back down to the Raman coupling set-point for TOF and the collisions. This method was effective at producing two optically dressed clouds with equal and opposite momenta.

First, we dress our spin polarized gas with a two-photon Raman transition that couples together the $|9/2, -9/2\rangle$ and $|9/2, -7/2\rangle$ states as discussed in Sec. 2.4.1. For the following experiments, we used laser light with wavelength $\lambda_R = 768.49$ nm, defining our recoil momentum $\hbar k_R = 2\pi\hbar/\lambda_R$ and recoil energy $E_R = \hbar^2 k_R^2 / 2m_K$. The Hamiltonian describing this coupling in the $|9/2, -9/2\rangle$, $|9/2, -7/2\rangle$ basis with the $|9/2, -9/2\rangle$ atoms at rest is

$$H_R = E_R \begin{pmatrix} k_x^2 - \delta/2 & \hbar\Omega_R/2 \\ \hbar\Omega_R/2 & (k_x - 2)^2 + \delta/2 \end{pmatrix}, \quad (5.2)$$

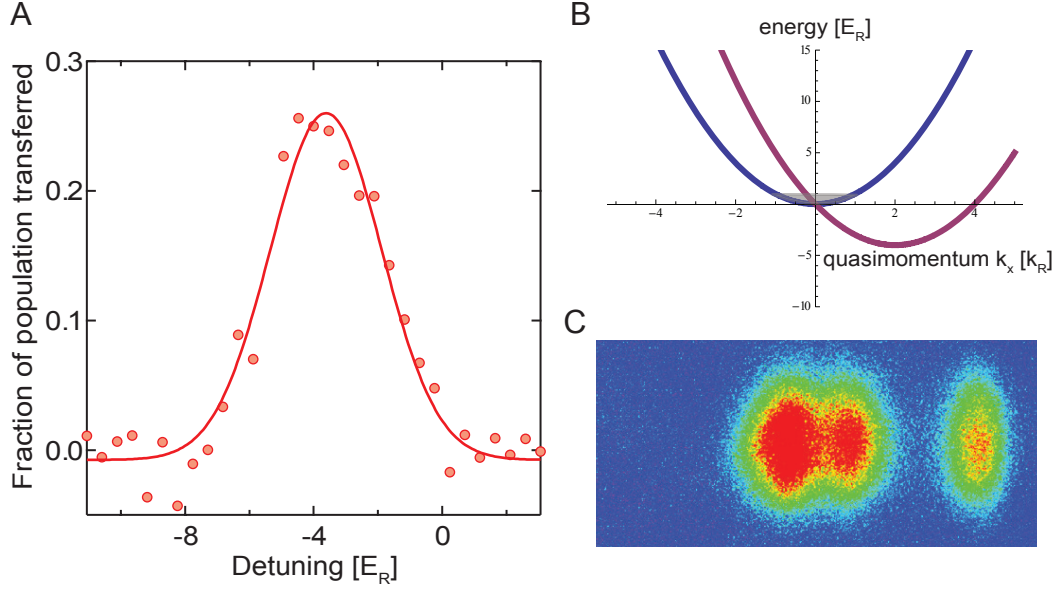


Figure 5.9: π -pulse with low Raman coupling to find $-4E_R$ detuning. (A) Fraction of population transferred versus Raman detuning found by scanning the frequency difference in the Raman beams. (B) Bare state dispersion relations at $\delta = -4E_R$. The gray line represents the Fermi energy and the shading is the momentum distribution of the atoms. (C) Absorption image of the atoms after a π -pulse at $\delta \approx 4E_R$. The momentum states around $k_x = 0$ were transferred to the different spin state.

where k_x is the quasi momentum, $\delta = \Delta\omega_R - \Delta\omega_Z$ is the detuning from the Raman resonance, and $\hbar\Omega$ is the coupling strength.

We wanted to optically dress the atoms with zero detuning δ for a given bias magnetic field. We measured our detuning by going to small coupling strengths $\hbar\Omega_R < 1$ then slicing out a narrow range of momenta to the $|9/2, -7/2\rangle$ and scanning the frequency difference $\Delta\omega_R$ in the Raman beams to determine the experiment parameters for $-4E_R$ detuning [37]. We used Raman A/C with beam waists $\approx 160 \mu\text{m}$, power $\approx 4 \text{ mW}$ and a $75 \mu\text{s}$ π -pulse. Figure 5.9 is an example of such a scan. We also show an example absorption image and the bare states for $\delta \approx -4E_R$.

To measure the sloshing in the optical trap after turning on the dressing, we

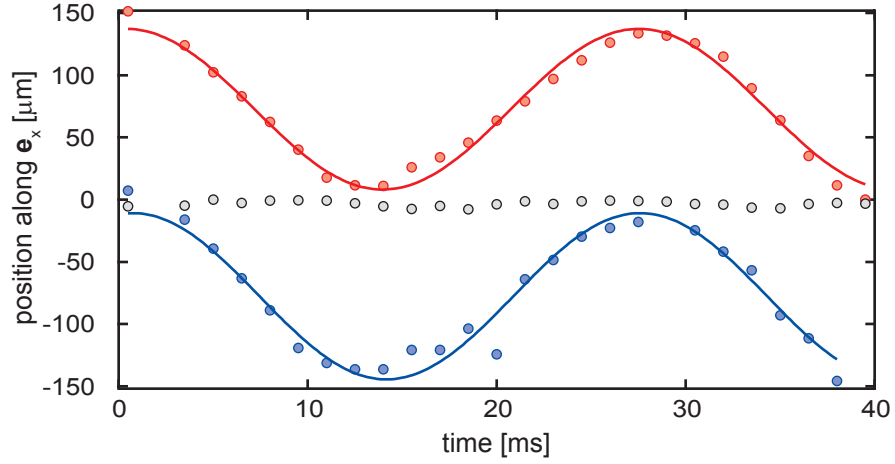


Figure 5.10: Sloshing of optically dressed ^{40}K atoms in the dipole tap. The red(blue) markers indicate the atoms were demapped into the $|9/2, -7/2\rangle$ ($|9/2, -9/2\rangle$) state. The gray markers indicate the position of atoms versus time without optical dressing.

set the frequency difference between the Raman laser beams such that $\delta = 0$. We adiabatically ramped the Raman coupling from 0 to about $7E_R$ (35 mW) in 2 ms with a linearly increasing command to the AO driver. The originally at rest $|9/2, -9/2\rangle$ would be loaded into the dressed state with $1k_R$ momentum and began to oscillate. To image the atoms, we demapped back onto the bare spin states before ramping off the Raman. During TOF, we would wait 1ms , then ramp the field by about 0.75 G in 0.5 ms before ramping off the Raman intensity in 0.5 ms. To map into the $|9/2, -9/2\rangle$ ($|9/2, -7/2\rangle$), we ramped to higher(lower) magnetic fields. The position versus time for this data is plotted in Fig. 5.10.

So, one proposed technique for seeing higher order partial waves with ^{40}K is:

1. Adiabatically ramp on Raman coupling ($\hbar\Omega < 8E_R$, about 30 mW)
2. Wait a 1/4 trap period

3. Ramp to higher Raman coupling in $50 \mu\text{s}$ ($\hbar\Omega > 8E_R$, about 65 – 70 mW)
4. Kapitza-Dirac pulses with 1-D optical lattice at $\approx 8E_R$
5. Ramp back to desired Raman coupling set-point for synthetic partial waves in $50 \mu\text{s}$
6. Allow atoms to expand and collide in TOF at Raman Coupling set-point for 1 ms
7. Demap onto one spin states by ramping the bias field 0.75 G in 0.5 ms and then Ramp down Raman intensity in 0.5 ms

This technique has the advantage that there are no losses due to the Feshbach resonance until the experiment starts. However, the disadvantage of beginning with a spin polarized gas is that it is harder to cool well and has a larger distribution of initial momentum states populated. Additionally, waiting the 1/4 trap period to begin the experiment is complicated and heats the atoms, further increasing the momentum distribution and decreasing the atom number.

5.4.2 Technique: Pulse Raman, pulse lattice, optically dress

Here, I will describe a technique we implemented partly. We successfully pulsed the Raman, then pulsed the lattices to create 2 clouds of opposite momenta and spin. If we had this pulsing technique for the s -wave scattering experiment, it would have increased our scattered signal by a factor of two. We made the decision to no longer work on ^{40}K before attempting to ramp on the Raman to optically dress the colliding atoms. I do not know what might arise when that step is implemented. We successfully implemented the pulsing sequence

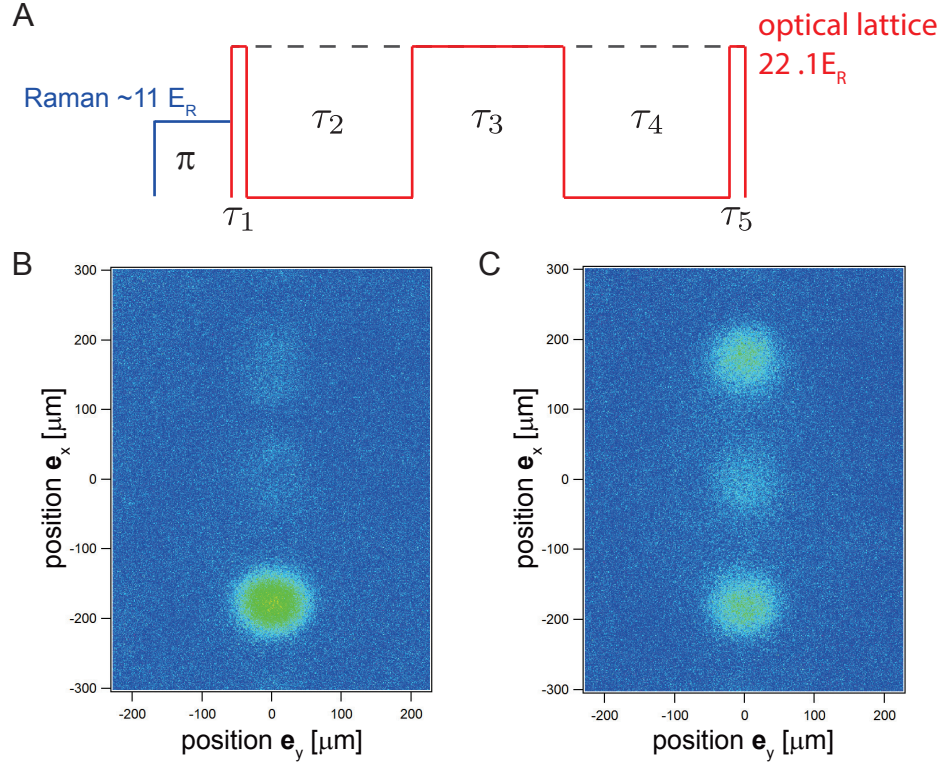


Figure 5.11: Pulse Raman, then pulse lattice. (A) Pulse sequence of light. First pulse on Raman coupling for a π -pulse, then pulse Kapitza-Dirac pulses for atoms optimized to transfer atoms with momentum $2k_R$ to a different band. (B) Absorption image of atoms after this pulse sequence with a spin polarized gas. (C) Absorption image of atoms after this pulse sequence on a spin mixture.

for both a spin polarized gas and a spin mixture. Here is our alternative pulse sequence technique:

1. Begin with spin mixture at the desired bias magnetic field
2. Apply a π -pulse at large Raman coupling ($11E_R$, 70 mW) and $\delta = 0$
3. Apply Kapitza-Dirac pulses optimized to transfer atoms with $k_x = \pm 2k_R$ and $1k_R$ width to momentum $k_x = \mp 2k_L$
4. Ramp on Raman in $\approx 50 \mu\text{s}$

We began implementing this pulse sequence with a spin polarized gas. Applying the π -pulse with the Raman gave the $|9/2, -9/2\rangle$ atoms gave them a $2k_R$ kick in the $+\mathbf{e}_x$ directions. We then used the optimized Kapitza-Dirac pulses illustrated in Fig. 5.11A and saw the atoms get a $2k_L$ kick in the $-\mathbf{e}_x$ direction. Figure 5.11B is an example absorption image of a spin polarized gas after this pulse sequence. In Fig. 5.11, we show the same pulse sequence applied to a spin mixture. This creates two clouds of opposite spin and momenta.

The advantages of this technique is there is no $1/4$ period trap wait time and spin mixtures are cooled more easily. However, we would have to consider losses due having a binary spin mixture in the vicinity of a Feshbach resonance earlier in the sequence. Additionally, the Feshbach resonance moves to higher field with Raman coupling [133], so that would be an additional complication.

CHAPTER 6

SOLITONS IN THE PRESENCE OF IMPURITIES

Solitons are spatially-localized, propagating excitations resulting from an interplay between nonlinearity and dispersion. We launched long-lived dark solitons in highly elongated ^{87}Rb Bose-Einstein condensates (BECs) and showed that a dilute background of impurity atoms in a different internal state dramatically affects the soliton. With no impurities and in one-dimension (1-D), these solitons would have an infinite lifetime, a consequence of integrability. Understanding the decay and destabilization of solitons is an outstanding problem. We contributed to understanding this problem by observing how adding impurities decreases soliton lifetime and contributes to its Brownian motion [50]. By measuring decreasing lifetime with increasing impurities, we studied how random processes destabilize solitons. Additionally, we describe the soliton's diffusive behavior using a quasi-1-D scattering theory of impurity atoms interacting with a soliton, giving diffusion coefficients consistent with experiment.

6.1 Introduction

Our BECs can be modeled by the one-dimensional (1-D) Gross-Pitaevski equation (GPE) derived in Sec. 3.3. Solitons are exact excited state solutions of the GPE. In atomic (BECs), density maxima can be stabilized by attractive interactions, i.e., bright solitons [122]; or as here, density depletions can be stabilized by repulsive interactions, i.e., dark solitons [30, 47]. For a homogeneous 1-D BEC of particles with mass m with density ρ_0 , speed of sound c , and healing

length $\xi = \hbar / \sqrt{2}mc$ the dark soliton solutions

$$\varphi(z, t) = \sqrt{\rho_0} \left[i \frac{v_s}{c} + \frac{\xi}{\xi_s} \tanh \left(\frac{z - v_s t}{\sqrt{2} \xi_s} \right) \right] \quad (6.1)$$

are expressed in terms of time t , axial position z , the soliton velocity v_s , and soliton width $\xi_s = \xi / \sqrt{1 - (v_s/c)^2}$. Such dark soliton solutions have a minimum density $\rho_0(v_s/c)^2$ and a phase jump $-2 \cos^{-1}(v_s/c)$ dependent upon the soliton velocity v_s . These solitons behave as classical objects with a negative inertial mass m_s , essentially the missing mass of the displaced atoms. This implies increasing the velocity reduces the kinetic energy, thus the addition of dissipation accelerates rather than decelerates dark solitons [101]. This can also be seen from the soliton equation of motion [49]

$$m_s \ddot{z}(t) = -\gamma \dot{z}(t) - \partial_z V + f(t) \quad (6.2)$$

where V is the axial confining potential, $\gamma \dot{z}$ is the friction force and $f(t)$ is a stochastic Langevin force. $f(t)$ is responsible for Brownian motion of the soliton and is connected to the friction coefficient γ through the fluctuation-dissipation theorem. Both can be controlled by the impurity atoms in the system.

6.2 Solitons in elongated condensates

Idealized solitons are infinitely long-lived due to the integrability of the 1-D GPE. Integrability breaking is inherent in all physical systems, for example due to the non-zero transverse extent of quasi-1-D systems. Indeed in experiments, solitons are only long-lived in highly elongated geometries [20, 130, 66], where integrability breaking is weak. Cold atom experiments have profoundly advanced our understanding of soliton instability by controllably lifting integra-

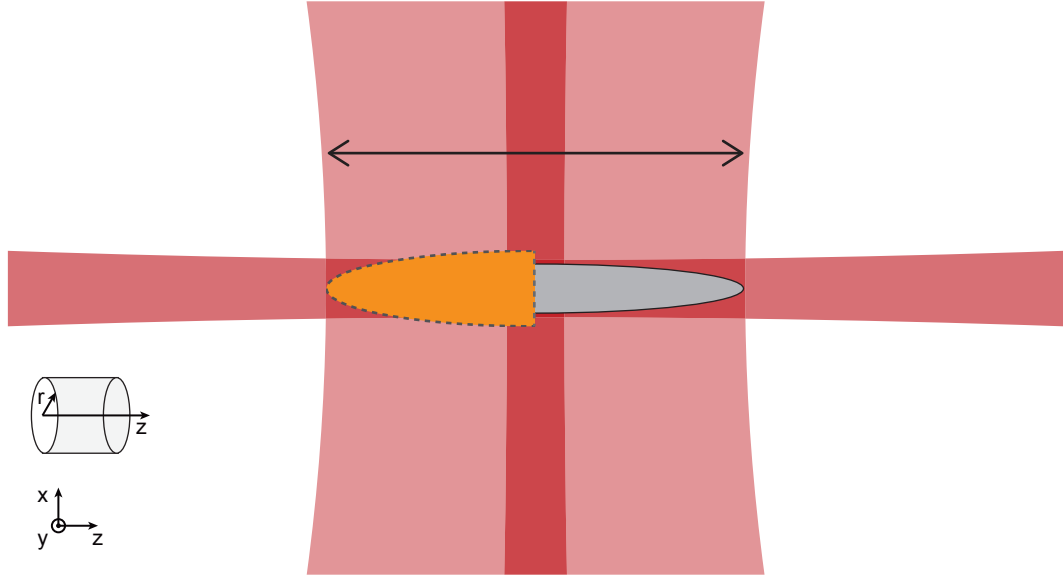


Figure 6.1: To make elongated BECs, we spatially modulated one beam of our crossed-beam optical dipole trap (ODT). Orthogonal to the plane defined by the ODT, we back-lit a razor blade to imprint a phase shift (orange) on half the condensate and launch solitons.

bility by tuning the dimensionality [6, 83]. Here, we studied the further lifting of integrability by coupling solitons to a reservoir of impurities.

6.2.1 Soliton creation and optimization.

We created BECs in the optical potential formed by a pair of crossed horizontal laser beams of wavelength $\lambda = 1064$ nm [87]. The beam traveling orthogonal to the elongated direction of the BEC was spatially dithered by modulating the frequency on an acoustic-optic modulator in the beam path at a few hundred kHz as shown in Fig. 6.1. This created a nominally flat-bottomed, time-averaged potential. We loaded into this optical potential after evaporating in a magnetic quadrupole trap. Our atoms were initially in the $|F = 1, m_F = -1\rangle$ internal state. We transferred them into the $|F = 1, m_F = 0\rangle$ internal state by ramping

a radio frequency (rf) magnetic field on ≈ 68 mG or 0.047 MHz away from resonance, linearly ramping to resonance in 5 ms, and then ramping off the rf in 5 ms. Magnetic field drifts would contribute to unwanted admixtures of atoms in the $|F = 1, m_F = -1\rangle$ and $|F = 1, m_F = +1\rangle$ states, so we actively stabilized the magnetic field before state transfer as described in Sec. 4.4.1. We prepared $N = 8(2) \times 10^5$ atoms in the $|F = 1, m_F = 0\rangle$ internal state at a temperature $T = 10(5)$ nK. To reach the extremely cold temperatures necessary to realize long lived solitons, we evaporated to the lowest dipole trap depth in which our technical stability allowed us to realize uniform BECs. In our system, number fluctuations increased at this low trap depth. Our system's $\approx 250 \mu\text{m}$ longitudinal extent was about 30 times its transverse Thomas-Fermi diameter set by the radial trap frequency $\omega_r = 2\pi \times 115(2)$ Hz and chemical potential $\mu \approx h \times 1$ kHz. We then applied a phase shift to half of a condensate by imaging a back-lit, carefully-focused razor edge with light red detuned by ≈ 6.8 GHz from the D_2 transition for $20 \mu\text{s}$ to launch long-lived dark solitons [30, 47].

6.2.2 Soliton oscillations

We absorption-imaged our solitons after a sufficiently long time-of-flight (TOF) that their initial width $\xi_s \approx 0.24 \mu\text{m}$ expanded beyond our $\approx 2 \mu\text{m}$ imaging resolution. Figure 6.2A is an image of our elongated BEC taken 2 ms after the soliton's inception. This density depletion feature had a velocity v_s in the positive \mathbf{e}_z direction and quickly decayed into several excitations including the dark soliton of interest. After a few hundred milliseconds, the additional excitations dissipated and the remaining soliton was identified. Figure 6.2B displays an image of a BEC with a dark soliton taken 0.947 s after its inception. The soliton is the

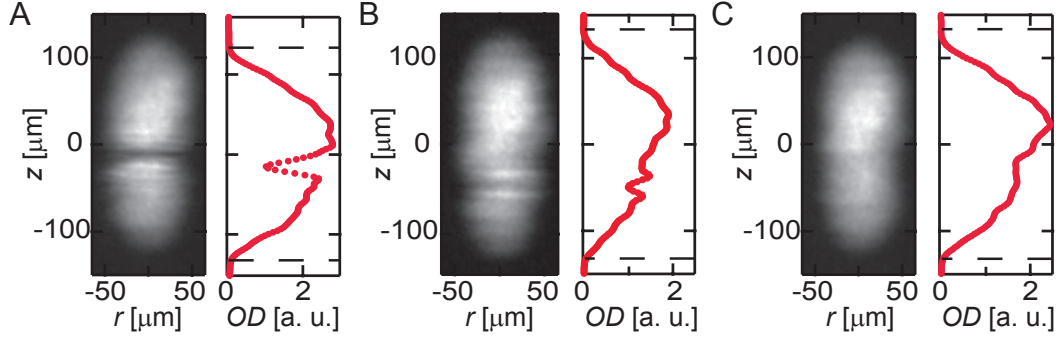


Figure 6.2: Soliton tracking. Each absorption image was taken with a 19.3ms TOF. (A) Image taken 2 ms after the phase imprint and a longitudinal density distribution obtained by averaging over the remaining transverse direction. An image and 1-D distribution taken at time $t = 0.942$ s (B) with a soliton that has $\approx 30\%$ contrast and (C) without a soliton.

easily identified density depletion sandwiched between two density enhancements. We quantitatively identified the soliton position as the minimum of the density depletion from 1-D distributions (right panels of Fig. 6.2A and B). By backtracking the soliton trajectory, we were able to distinguish the soliton even at short times where there were multiple density depletions. Often, at longer times after the phase imprint, there would be no soliton present. Figure 6.2C is an example of an image taken with an identical procedure to Fig. 6.2B but there is no soliton present.

In addition to the extremely low temperature requirements, a sharp edge was essential for creating long lived solitons. Placement of the edge was difficult. Going to a few seconds after the phase imprint and adjusting the edge position at constant intensity in the phase imprint beam was efficient for finding the soliton at the beginning of the day. We found the turning on the water cooling would shift the position of the dipole trap by a beam waist in approximately four hours after machine turn-on in the direction orthogonal to the phase imprint beam. The $\sim 10 \mu\text{m}$ difference in position of the dipole trap caused the

edge to be out of focus at the atoms. Luckily, our magnetic field lock feedback on xz images (see Ch. 4) and we could manually feedback on the dipole trap position. Alternatively, we found it helpful, but risky to leave the water cooling on overnight during data collection. Leaving on the water cooling on overnight allowed the system to be in nominal thermal equilibrium when we turned it on in the morning, giving a one hour instead of four hour warm up.

Figure 6.3A shows a series of 1-D distributions taken from time $t \approx 0$ s to 4 s after the phase imprint. These images show three salient features: (1) the soliton underwent approximately sinusoidal oscillations, (2) there was significant scatter in the soliton position, and (3) the soliton was often absent at long times. Items (2) and (3) suggests that random processes were important to the soliton's behavior. These random processes may include but are not limited to phase and density fluctuations or interactions with phonons. The soliton's position z —when present—is represented by the light pink symbols in Fig. 6.3B and the darker pink symbols mark the average position $\langle z \rangle$ for each time t . To collect data, we repeated each measurement 8 times.

6.2.3 Microwave tomography

To verify we had a soliton and not some other excitation such as a solitonic vortex, we used rf-tomography techniques to study the density profile of the atoms orthogonal to the imaging direction [83, 76]. This technique works by applying a magnetic field gradient in the direction orthogonal to the imaging plane, then scanning the frequency of a microwave (μ -wave) Blackman pulse to be in resonance with an atomic transition at different spatial locations in

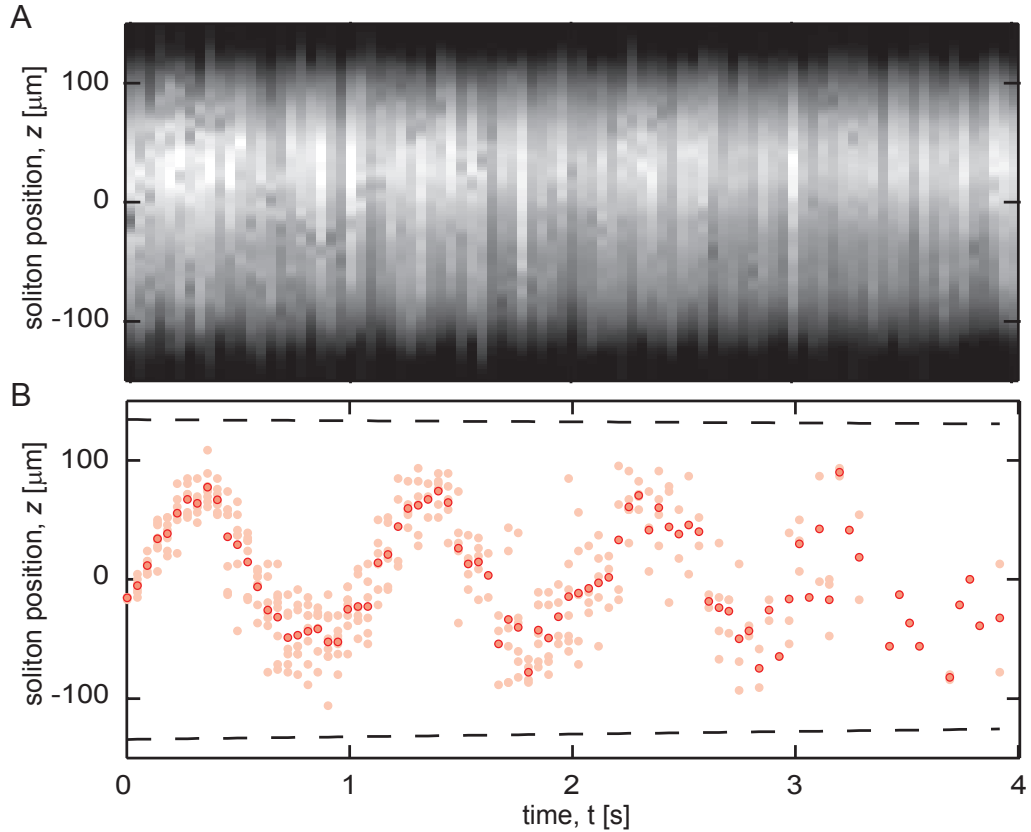


Figure 6.3: Soliton oscillations: (A), A subset of the data where each vertical slice is the density distribution obtained from a single realization of the experiment plotted versus time t . (B), The axial position z_i of the soliton (light pink) versus time t for different realizations of the experiment. Dashed lines represent the edges of the elongated condensate. The dark markers represent the average soliton position $\langle z \rangle$ at each time t .

the condensate. We opted to use an microwave pulse to transfer the atoms to a different hyperfine state. Using pulse on resonance with a different Zeeman sublevel within the same hyperfine state would have transferred the atoms to two different states instead of one because our majority atoms were in the $|F = 1, m_F = 0\rangle$ state. We turned a $2.4 \text{ mG}/\mu\text{m}$ gradient in the direction orthogonal to the imaging plane, then pulsed on a microwave field detuned from the $|F = 1, m_F = 0\rangle \rightarrow |F = 2, m_F = -1\rangle$ transition. We scanned this detuning to get the in-situ density profile in this direction. As shown in Fig. 6.4, the measured

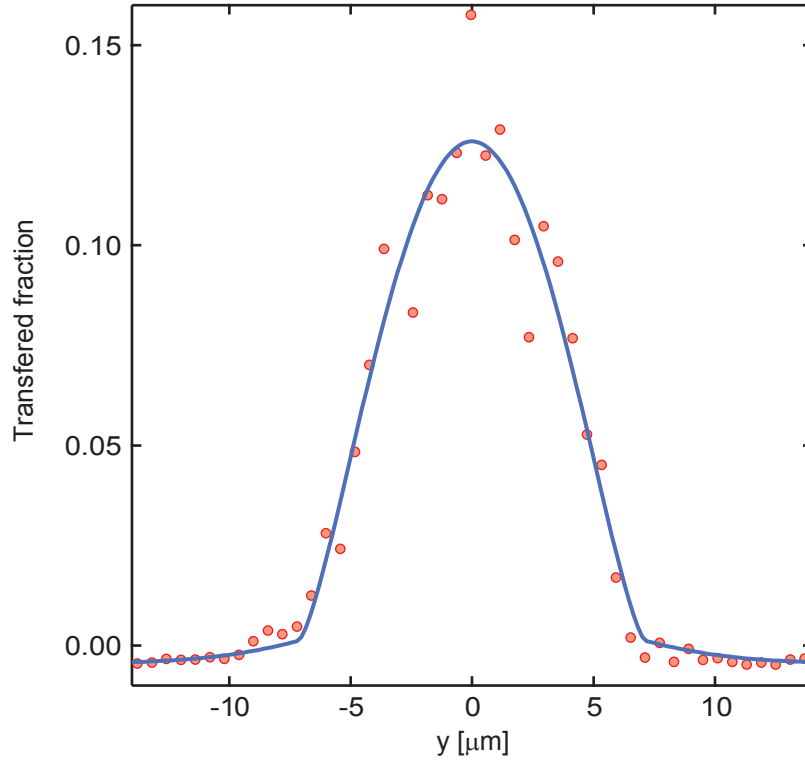


Figure 6.4: Microwave tomography of in-situ atoms. We plot the fraction of transferred atoms versus the position in the orthogonal direction. Fitting the density distribution in this direction to a 1-D Thomas-Fermi profile we find a Thomas-Fermi radius of $7.1 \pm 0.3 \mu\text{m}$.

Thomas-Fermi radius $7.1 \pm 0.3 \mu\text{m}$ in this direction is larger than the $\sim 4\text{-}5 \mu\text{m}$ we expected from our measurements of speed of sound and our atom number calibration. However, the larger Thomas-Fermi radius can be due to the gravitational sag in this direction. Comparing the trap potential to the chemical potential indicated that gravitational sag was the most likely reason for the larger radius. Figure 6.5 plots an optical potential without sag (red). The purple curve is the same optical potential with sag. When we measured trap frequencies, the gravitational sag was present. Without sag, for a given beam waist and optical power, the measured trap frequency would be larger. The pink curve represents an optical potential with sag adjusted to match the measured trap

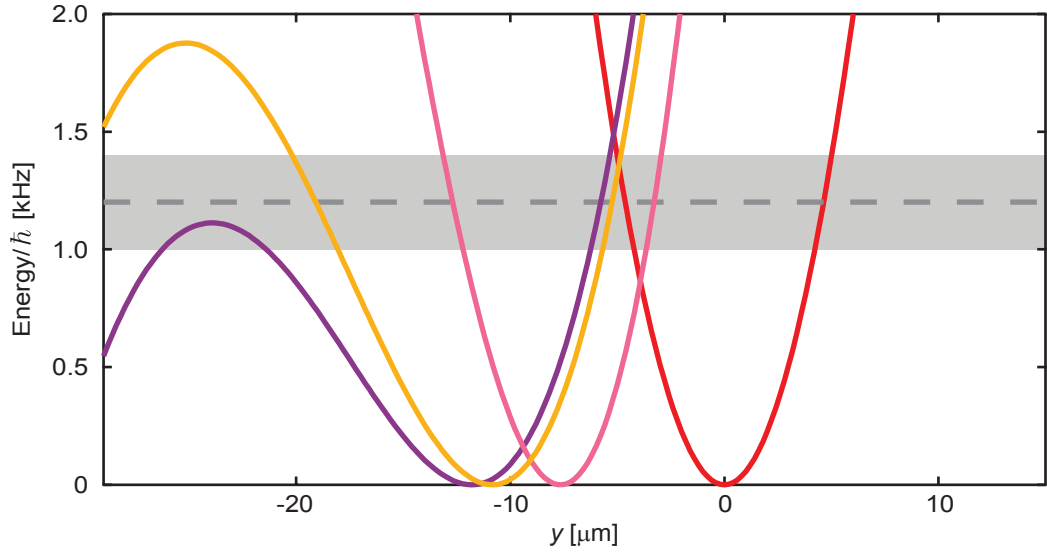


Figure 6.5: Effect of gravitational sag on optical potential. The optical potential without gravitational sag (red) was calculated from the ODT’s measured beam waist $35 \mu\text{m}$ and trap frequency $\omega_r = 2\pi \times 115(2) \text{ Hz}$. Other curves (pink,yellow,purple) include gravitational sag. The approximate chemical potential μ is included for reference.

frequency. The yellow curve was adjusted until the intersection of the optical potential with the chemical potential μ (gray) was $\approx 14 \mu\text{m}$. Because we did not measure our trap frequency as a function of power, we did not have a model for our optical potential. However, gravitational sag does have a large impact on in-situ Thomas-Fermi radii. We did convolve the Blackman window pulse we used with a Thomas-Fermi profile, but the in-situ radius from the convolved fit was consistent with the fit absent the convolution.

We used our μ -wave tomography technique to verify we had a soliton from images of our out-coupled atoms. Our resolution was set by the 1 ms pulse duration and energy shift from the applied magnetic field gradient. Our calculated resolution was $\approx 0.6 \mu\text{m}$. To ensure mean field effects during TOF did not affect our tomography of the atoms, we doubled the gradient immediately following

the pulse during TOF so that the transferred atoms expanded in a different spatial location than the majority atoms. The absorption imaged captured both the transferred and untransferred atoms. The series of images in Fig. 6.6 displays the tomography of the atoms at 1.045 s and 1.420 s after soliton inception. The transferred atoms were likely out of focus from the added field gradient leading to the odd looking soliton feature. The tomography data supported that we launched a soliton due to the density depletion not being localized in the direction orthogonal to the imaging direction. When a soliton feature was present, even at long time, our μ -wave tomography data confirms that it is a soliton, not a decay product such as a solitonic vortex or ring.

6.3 Injecting impurity atoms

Having established a procedure for creating solitons, we turned to the impact of coupling to a reservoir of impurity atoms in a different internal state, thus further breaking integrability.

6.3.1 Injection and number calibration

We controllably introduced a uniform [51] gas of N_I impurity atoms in thermal equilibrium with our BECs using an rf pulse resonant with the $|F = 1, m_F = 0\rangle$ to $|F = 1, m_F = +1\rangle$ transition prior to evaporation to degeneracy [105]. This gave impurity fractions N_I/N from 0 to 0.062 in our final BECs. We use a Blackman enveloped rf pulse at 9 G magnetic field to transfer the $|F = 1, m_F = 0\rangle$ atoms primarily to the $|F = 1, m_F = +1\rangle$ internal state [76]. We varied the impurity fraction

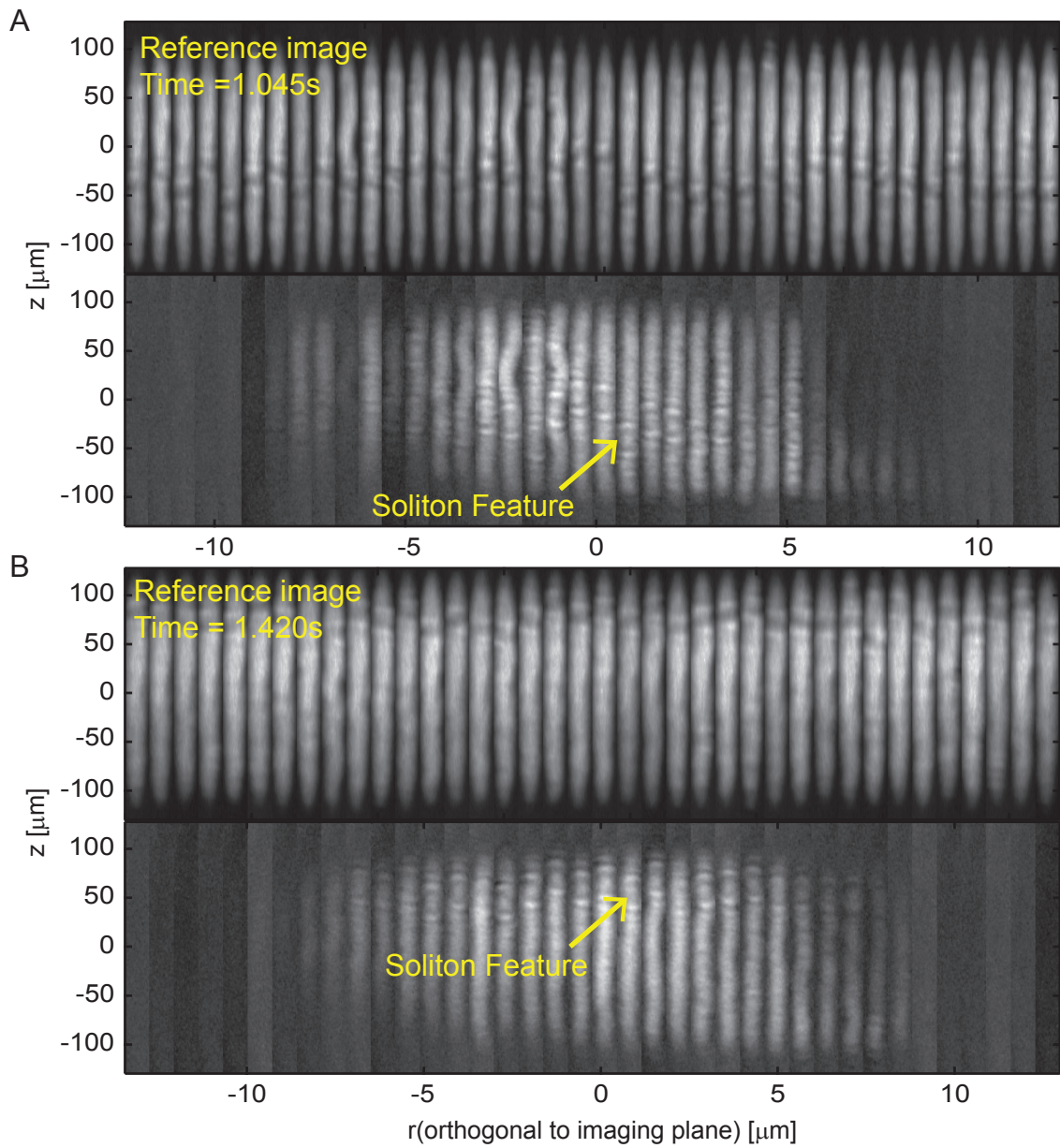


Figure 6.6: rf-Tomography of solitons. For each panel, the series of images on top are the untransferred atoms for reference. The bottom series of images represents a slice of the 3-D condensate at different z -positions using our rf-tomography techniques.

by tuning the rf amplitude. Even though the fraction of impurity atoms before evaporation determined the fraction after evaporation, they were not equal due to a preferential evaporation of the minority spin state [105].

We characterized the impurity fraction through careful calibration of our absorption imaging. First, we find the saturation intensity I_{sat} and effective saturation intensity $I_{sat}^{eff} = \alpha I_{sat}$ that characterize our imaging system [113]. We imaged an optically thin cloud of atoms, i.e. a gas above T_c , as a function of probe power to determine $I_{sat} = 2.5 \times 10^4$ in counts per pixel on the camera. We then use measurements of the probe's beam waist and power to determine the intensity at the atoms corresponding to counts on at the camera. Knowing the intensity at the atoms defines $\alpha = 5.5$ for our imaging system and we now have a corrected method to go from the optical depth in an absorption image to number of atoms.

We can also calculate our atom number by using Castin-Dum methods to calculate an in-situ Thomas-Fermi radius from a Thomas-Fermi radius after time of flight and the trap frequencies [34]. We found these methods to agree for most optical depths. The low optical depths, corresponding to low densities, is where the counting method and the Castin-Dum method differed. However we did not expect Castin-Dum to work well at low densities due to the method's dependence on chemical potential. We then used our corrected counting and a Stern-Gerlach technique during TOF to measure the relative fraction of the impurity atoms after evaporation. Typically, we prepared our spin composition above T_c . With this technique, we had some difficulty preparing the atoms only in $|F = 1, m_F = 0\rangle$ without impurities. We modified the procedure to prepare the spin state at an optical depth just below T_c . If we preformed our state prepara-

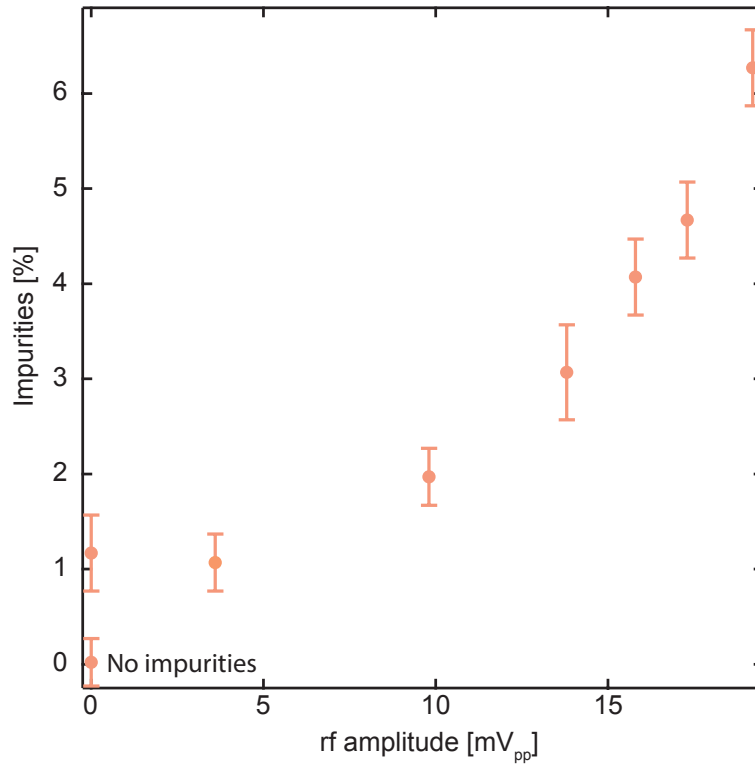


Figure 6.7: Impurities versus rf amplitude in laboratory units. The uncertainties are the standard deviation of five data points. State preparation in the majority spin state with thermal atoms led to a final state with 1.2% impurity atoms. This was overcome by preparing the no impurities sample at a slightly lower optical potential before continuing to evaporate to the final trap depth.

tion in a gas above T_c , we found that there were always 1.2% impurity atoms. This may be due to gradients across the larger extent of the thermal atoms having some atoms be out of resonance with rf fields used for state preparation.

6.3.2 Temperature measurements with impurities

Below the majority atom's condensation temperature $T_c = 350$ nK, we removed the majority atoms and fit the TOF expanded the impurity atoms to a Maxwell-Boltzmann distribution [105]. We removed the majority atoms before TOF by

pulsing on a μ -waves resonant with the $|F = 1, m_F = 0\rangle \rightarrow |F = 2, m_F = -1\rangle$ transition, then blew away the atoms with our probe resonant with the $F = 2 \rightarrow F' = 3$ optical transition. No repump light was on during this process to allow the impurity atoms to expand unperturbed. Once the temperature was below T_c for the impurity atoms, fits to a Maxwell-Boltzmann distribution give temperature estimates that can significantly underestimate the true temperature. With this method, we did observe a decrease in temperature at higher concentrations of impurity atoms consistent with data from similar experiments [105]; however, the change in temperature we observed was smaller than the uncertainty in our measurement. Fitting the small number of impurity atoms to a Bose distribution was challenging due to the signal-to-noise and the addition of another free parameter. To limit the number of free parameters, we preformed a global fit of the temperature on a few different impurity fractions and constrained the chemical potential μ to be negative. This provided an estimation of the temperature with large uncertainties. We found for our usual operating parameters and based on information from both temperature measurements, $T = 10(5)$ nK.

6.4 Solitons in the presence of impurities

6.4.1 Impact on oscillations

Figure 6.8 displays the soliton position versus time for a range of impurity fractions. Adding impurities gave two dominant effects: further increasing the scatter in the soliton position z and further decreasing the soliton lifetime. These effects manifested as a reduced fraction f_s of images with a soliton present and

an increase in the sample variance $\text{Var}(z) = \sum (z_i - \langle z \rangle)^2 / (M - 1)$ computed using the number M of measured positions z_i at each time. Additionally, the soliton oscillation frequency was slightly shifted with impurities resulting from an unintentional change in the underlying optical potential. This change also slightly reduced the BECs longitudinal extent. This is not an effect due to the presence of the impurities.

6.4.2 Impact on lifetime

The addition of impurities had a dramatic impact on the soliton lifetime. While we lack a quantitative model of the soliton's decay mechanism, there are several reasons to expect a finite lifetime. When dissipation is present, solitons accelerate to the speed of sound and disintegrate. Additionally, because our trap geometry has a finite transverse extent, quantified by the ratio $\mu/\hbar\omega_r \approx 9$, solitons can be dynamically unstable and can decay into 3-D excitations [94]. Our soliton's initial velocity $v_s \approx 0.3$ mm/s, roughly 1/5 the 1-D speed of sound $c \approx 1.4$ mm/s[137], implies it is in an unstable regime, where, as observed, it should decay [101]. Furthermore, numerical simulations show that in anharmonic traps solitons lose energy by phonon emission, accelerate, and ultimately decay [106]. All of these decay mechanisms can contribute to the soliton lifetime even absent impurities.

The added impurities act as scatterers impinging on the soliton, further destabilizing it. This effect is captured in Fig. 6.9, showing the measured survival probability f_s versus time for a range of impurity fractions. We fit the

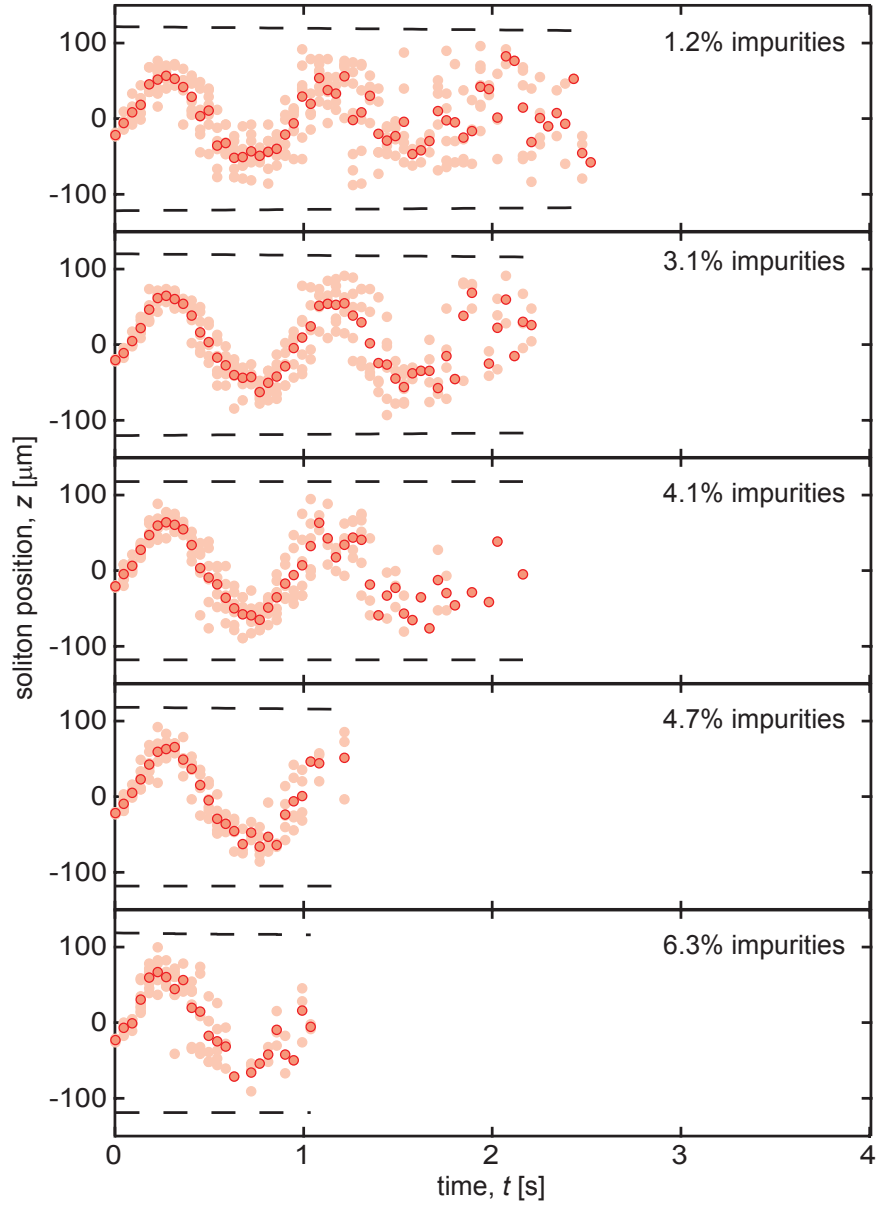


Figure 6.8: Impact of impurities. Here, we plot the position z_i of the soliton (light pink) versus time t after phase imprint for different impurity levels. The dark pink markers are the average positions $\langle z \rangle$ for each time t . Dashed lines represent the extent of the condensate on either end versus t .

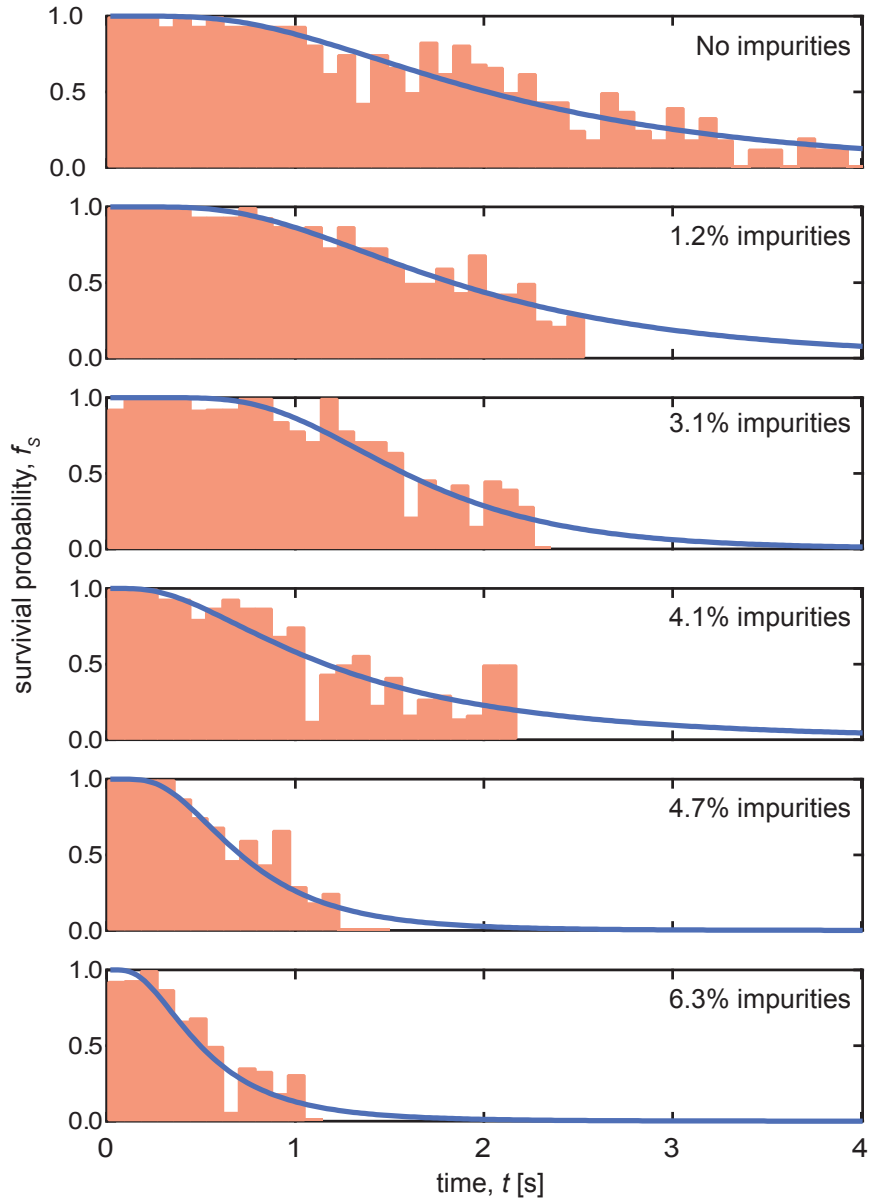


Figure 6.9: Measured survival probability. Histograms of fractional count of data with solitons f_s versus time t after phase imprint. The blue solid line is a fit to a survival function for a lognormal distribution from which we extract the lifetime τ . For each impurity fraction, we stopped collecting data when f_s fell below about 0.2.

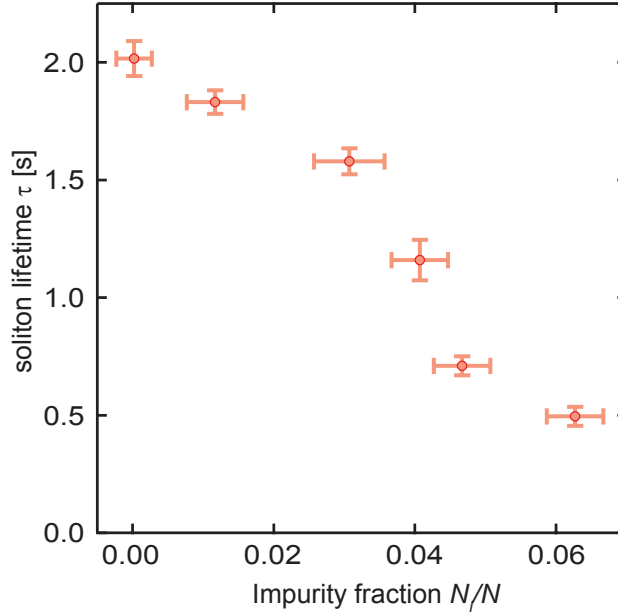


Figure 6.10: Soliton lifetime in the presence of impurities. The lifetime τ extracted from fits of the survival fraction f_s versus impurity fraction N_1/N in the condensate.

survival probability

$$f_s(t) = 1 - \frac{1}{2} \operatorname{erfc} \left[\frac{-\ln(t/\tau)}{\sqrt{2}\sigma} \right], \quad (6.3)$$

essentially the integrated lognormal distribution of decay times, suitable for decay due to accumulated random processes, to our data[41]. The survival probability $f_s(t)$ has a characteristic width parameterized by σ and reaches 1/2 at time τ which we allow us to associate τ with the soliton lifetime. Figure 6.10 shows the extracted lifetime τ versus impurity fraction N_1/N , showing a monotonic decrease. Our maximum N_1/N gives a factor of four decrease in lifetime τ .

6.4.3 Enhanced diffusion

The second important consequence of adding impurities was an increased scatter in soliton position z , reminiscent of Brownian motion. Indeed, as shown in Fig. 6.11, this scatter, quantified by $\text{Var}(z)$, increased linearly with time. We obtained the diffusion coefficients D as the slope from linear fits to these data and calculated D using a quasi-1-D scattering theory. The energy of the infinitely long 1-D system is given by the GPE energy functional

$$E[\varphi, \psi] = \int dz \frac{\hbar^2}{2m} |\nabla\varphi|^2 + \frac{\hbar^2}{2m} |\nabla\psi|^2 + \frac{g}{2} |\varphi|^2 |\varphi|^2 + \frac{g'}{2} |\varphi|^2 |\psi|^2, \quad (6.4)$$

describing the majority gas interacting with itself along with the impurities with interaction coefficients g and g' , respectively. The fields φ and ψ denote the condensate and impurity wavefunctions. Since the impurities are very dilute, we do not include interactions between impurity atoms. Impurity scattering states with momentum k_z in the rest frame of the soliton are described by the reflection coefficient

$$R(k) = \frac{1 - \cos(2\pi\lambda)}{\cosh(2\pi k_z \xi) - \cos(2\pi\lambda)}, \quad (6.5)$$

where $\lambda(\lambda - 1) = g'/g$. In ^{87}Rb , we have $g \approx g'$, giving $\lambda \approx 1.5$. The scattering problem is fully characterized by $R(k)$ and the problem is reduced to that of a classical heavy object moving through a gas of lighter particles.

We treat the soliton as a heavy classical object with a kinetic equation including a weak stochastic force due to elastic collisions with the much lighter impurity atoms. The collision integral can be expressed in Fokker-Planck form [86] with diffusion coefficient

$$D = \frac{(k_B T)^2}{B}, \quad (6.6)$$

giving $Dt = \text{Var}(x)$. Momentum diffusion is described by the transport coefficient

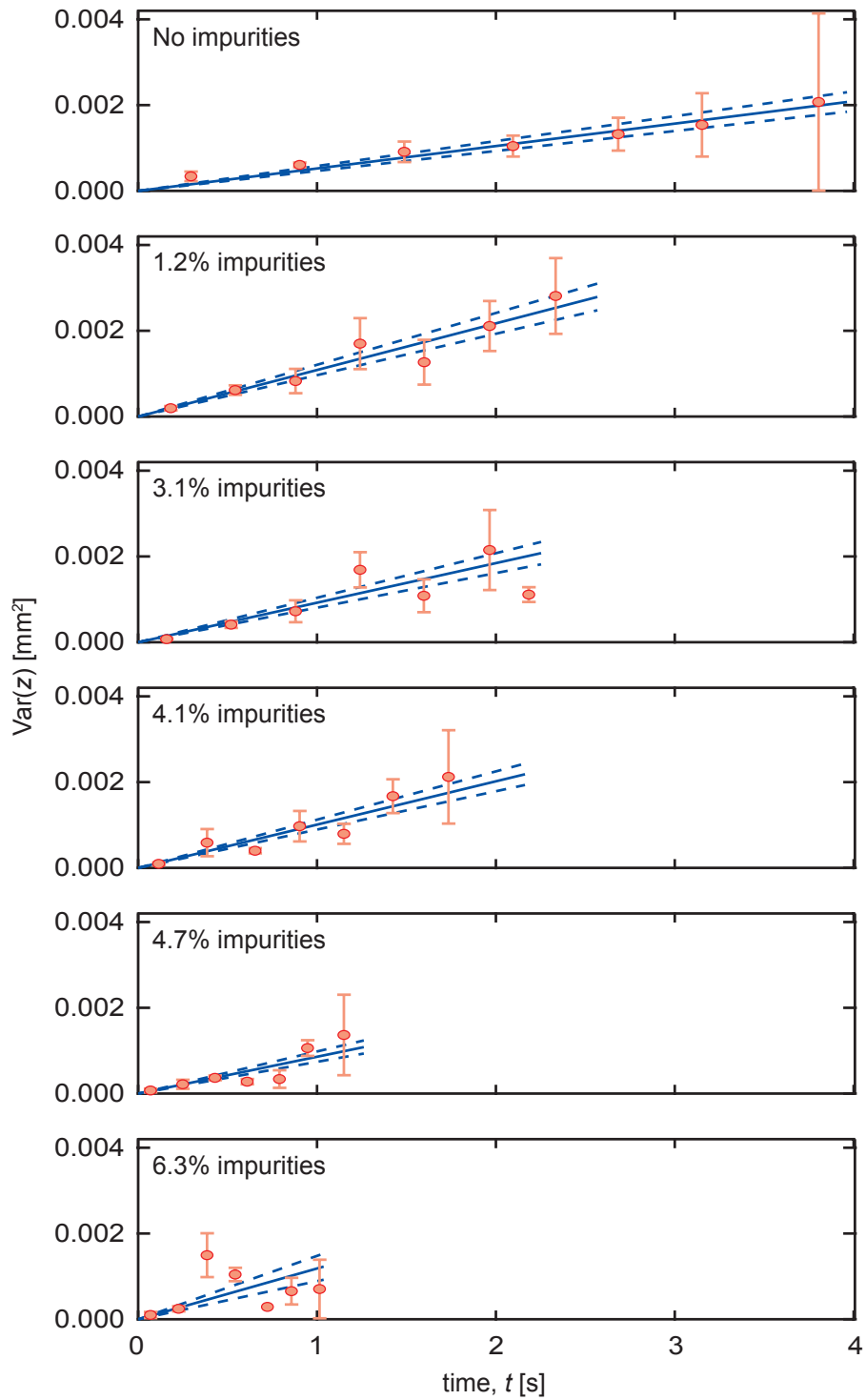


Figure 6.11: Brownian diffusion for different impurity fractions. The uncertainties in $\text{Var}(z)$ are the sample standard deviation. The slope of the linear fit is the measured diffusion D . Dashed lines represent the slope's uncertainty.

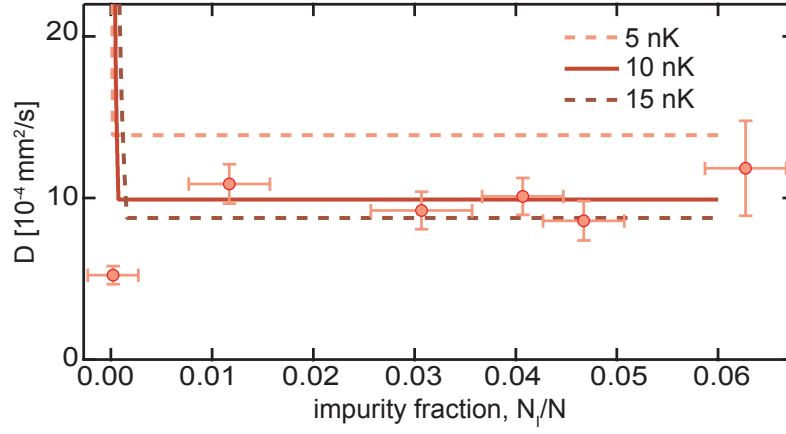


Figure 6.12: Brownian diffusion constant versus impurity fraction. The diffusion coefficient D versus impurity fraction N_1/N . The experimental results (markers) are extracted from the slope of a linear fit of the sample variance $\text{Var}(z)$ versus time t . The uncertainty in D is the uncertainty from that fit. See Sec.6.3.1 for explanation of uncertainty in N_1/N . The theory curves (line and dashed lines) are not fits.

cient [52]

$$B = 2\hbar \sum_{m,l} \int_{-\infty}^{\infty} \frac{dk_z}{2\pi} k^2 \left| \frac{\partial \epsilon}{\partial k_z} \right| R(k_z) n(\epsilon) [1 + n(\epsilon)], \quad (6.7)$$

where $\epsilon_{m,l}(k) = \hbar^2 k^2 / 2m + \hbar^2 j_{m,l}^2 / 2mR^2$ is the impurities' quasi-1D dispersion with quantized states in the radial direction, where $j_{m,l}$ is the l^{th} zero of the m^{th} Bessel function. The quantization in the radial direction is due the tight confinement in the radial direction as compared to the temperature. $n(\epsilon)$ is the Bose-Einstein distribution for impurity atoms excluding the condensed impurity atoms. We model the impurity atoms as being in a uniform potential with cylindrical volume the size of the majority condensate. $R(k_z)$ is the reflection coefficient defined in Eqn. 6.5. The term $[1 + n(\epsilon)]$ accounts for bosonic enhancement.

Figure 6.12 plots D measured experimentally (markers) and computed theoretically (solid and dashed lines) as a function of N_1/N . The quasi-1-D scattering theory accurately captures the soliton diffusion in the presence of impurities. For the theory, the abrupt change in dependence on impurity fraction is due to

the condensed impurity atoms not contributing to the soliton diffusion. Any additional impurity atoms are added to the impurity condensate, not the thermal reservoir of scatterers. In our quasi-1-D theory, the soliton is not reflectionless to phonons as in the true 1-D problem, but we did not consider them in our model. Thinking about how this may impact our results, adding more scatterers would contribute to the transport coefficient B , and since $D \propto 1/B$ the diffusion coefficient should be smaller with more scatterers. This is why our measurement of a suppressed diffusion coefficient at $N_I/N = 0$ is intriguing. With such scatterers as not reflectionless phonons, we expected some baseline diffusion coefficient at $N_I/N = 0$ to be larger than with impurities. Indeed, if the diffusion at $N_I/N = 0$ was due to technical noise in the velocity from the soliton launching technique, we would again expect a suppression of the diffusion coefficient with the addition of impurities, not enhancement. Thus, in the absence of impurities, the precise mechanism of dissipation cannot be identified within the scope of our theory and the observation of reduced diffusion remains an outstanding problem.

6.5 Conclusions and outlook

Realizing solitons in spinor systems with impurity scatterers is an exciting playground for studying integrability breaking and diffusion of quasi-classical, negative-mass objects. Our observed reduction in soliton lifetime with increasing impurity fraction is in need of a quantitative theory. For the case of no impurities there is a further open question for both theory and experiment of whether friction and diffusion can be present even in the case of preserved integrability due to non-Markovian effects, as was recently discovered for bright

solitons [49]. We began this experiment to learn about solitons. In particular, we would like to load solitons into the synthetic dimensions experiment to achieve the lofty experimental goal of chiral edge solitons. Understanding how to load solitons into systems with optical lattices or Raman coupling would be the next steps before continuing to add complexity. In this chapter, we studied how the soliton interacts with uniformly distributed atoms in a different internal spin state.

CHAPTER 7

BOSE-EINSTEIN CONDENSATES IN THE QUANTUM HALL REGIME

In this chapter, I discuss experiments in which we realized a large effective magnetic field for charge neutral atoms in a hybrid two dimensional (2-D) lattice. Our hybrid 2-D consists of a 1-D optical lattice as one dimension and an internal state of the atom as another, synthetic dimension. This specific choice of internal states of ^{87}Rb enabled single site resolution in the synthetic dimension through the use of a Stern-Gerlach pulse during time of flight (TOF). We used a two-photon Raman transition to induce tunneling in the synthetic dimension and to imprint an engineered phase onto an atom, an effective Aharonov-Bohm phase $\phi_{\text{AB}}/2\pi$. This phase fully defined an effective magnetic field. We directly imaged the eigenstates of the hybrid 2-D system with and without the synthetic magnetic flux. Then we studied dynamics by exciting coherent super positions of magnetic subbands, analogs to Hofstadter bands, and observed bulk and edge dynamics. The single site “spatial” resolution in the synthetic dimension enabled us to directly image bulk excitations, normally inaccessible in condensed matter systems, and skipping orbits of edge site excitations. This work is published in *Science* **349** (2015) concurrent with a similar technique implemented with fermionic ytterbium by Mancini *et al.* [124, 93].

7.1 Introduction

Cold atoms are highly tunable and controllable systems that can realize exotic topological states. The quintessential topological state is the quantum Hall effect, a topological insulator formed in a 2-D electron gas with an insulating bulk

and conducting, protected edge states [65]. Many groups see the realization of quantum Hall states in cold atoms as a stepping stone to creating more exotic topological states. Creating large artificial gauge fields, analogous to large magnetic fields, is one way to realize the extreme quantum limits required for quantum Hall-type effects in cold atoms. Previous, pioneering methods required large Raman laser coupling, leading to heating through spontaneous emission, and had the disadvantage of the realized effective magnetic field strength limited by the linear extent of the condensate [88]. Other experimental methods for creating large artificial gauge fields reduce the limitations imposed by spontaneous emission, but introduce other sources of heating leading to lifetimes well below 1 second. These methods include shaking optical lattices to introduce a vector potential [123, 79] and laser-assisted tunneling in a tilted optical lattice [3, 97]. Our technique presented in this chapter minimizes the required Raman laser coupling and has lifetimes due to spontaneous emission larger than 10 seconds.

7.2 Synthetic Dimensions: Particle in a Box

The tight-binding Hamiltonian

$$H_{tb} = - \sum_{j,m} [t_x |j+1, m\rangle \langle j, m| + t_s |j, m+1\rangle \langle j, m| + \text{h.c.}] \quad (7.1)$$

with hopping amplitudes t_x and t_s governs the motion of particles moving in a 2-D lattice [8] with sites labeled by j and m . We implemented a such 2-D lattice by combining a conventional optical lattice to define the long axis of our system (\mathbf{e}_x direction, with sites labeled by j , and effective tunneling strength t_x), with three sequentially coupled internal “spin” states to define the short axis of our

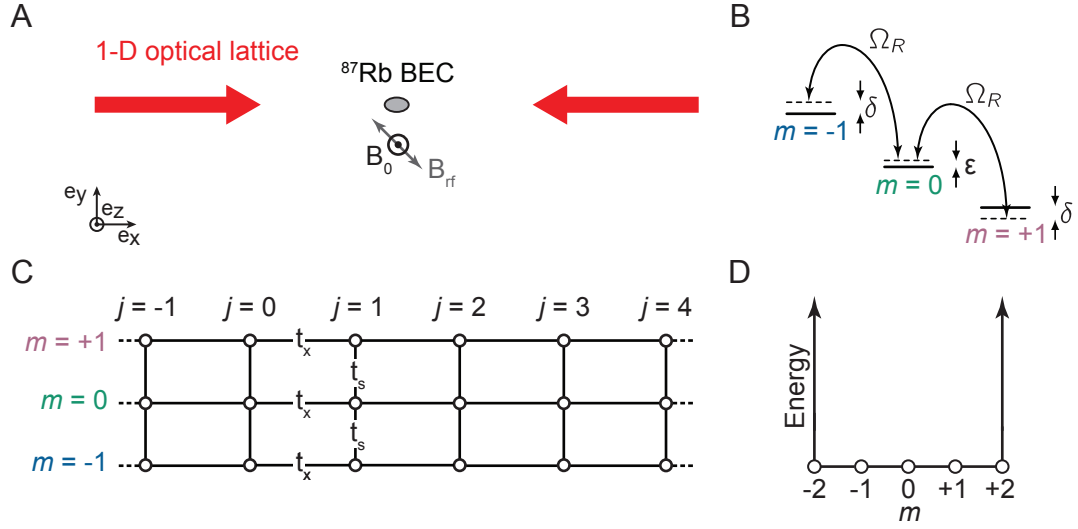


Figure 7.1: Particle in a Box with Synthetic Dimensions. (A) Experimental setup with 1-D optical lattice, bias magnetic field B_0 and oscillating rf field B_{rf} . (B) The rf field coupled the three internal states of ^{87}Rb with Rabi frequency Ω_R and detuning δ . The $m = 0$ internal state is shifted by the quadratic Zeeman shift ϵ . (C) Our 2-D hybrid lattice hopping t_x in the spatial dimension \mathbf{e}_x and t_s in the synthetic dimension \mathbf{e}_s . (D) Potential along \mathbf{e}_s can be modeled as a square well with infinite hard walls at $m = \pm 2$

system (\mathbf{e}_s direction, with just three sites labeled by $m \in \{-1, 0, +1\}$, and effective tunneling strength t_s) [23]. Figure 7.1 shows a schematic for the experimental set up, the coupling of the different internal states, and the resulting hybrid 2-D lattice. As shown in Fig. 7.1A, we used a 1-D optical lattice, formed by a pair of $\lambda_L = 1064.46$ nm laser beams counter-propagating along \mathbf{e}_x with beam waists $\approx 160 \mu\text{m} \times 135 \mu\text{m}$ for the forward beam and $\approx 126 \mu\text{m} \times 150 \mu\text{m}$ for the retro-reflection. This lattice defines the single-photon recoil momentum $\hbar k_L = 2\pi\hbar/\lambda_L$ and recoil energy $E_L = \hbar^2 k_L^2 / 2m_{\text{Rb}}$, where m_{Rb} is the atomic mass. The tunneling t_x in the spatial dimension was controlled by adjusting the intensity of the laser beams to control the potential V due to the optical dipole force. The internal “spin” states are the Zeeman sublevels of the $f = 1$ hyperfine manifold of ^{87}Rb and the tunneling between these sites is controlled by an rf magnetic field. The amplitude of this field controls the tunneling strength t_x along the

spin “direction” \mathbf{e}_s , proportional to the Rabi frequency Ω_R . The frequency of the rf field was set to be in resonance with $g\mu_B B_0/h \approx 0.817$ MHz Zeeman splitting, giving $\delta = 0.0$. The corresponding quadratic Zeeman shift additionally lowered $|m = 0\rangle$ by $\epsilon = 0.05E_L$ as shown in Fig. 7.1B. Since there are no other Zeeman sub-levels, this system effectively has an infinite repulsive potential at sites $m = -2$ and $m = +2$ as shown in Fig. 7.1D. This allows for the formation of robust edge states in the presence of an effective magnetic field, analogous to the conducting edge states discussed in Sec.2.3.2. Interestingly, the synthetic dimension \mathbf{e}_s is an exact realization of the tight-binding model with only tunneling to nearest neighboring sites and no tunneling to next to nearest neighboring sites. For the sites in the optical lattice, the tight-binding model is a very good approximation (see Sec. 2.2.1).

We began our experiments by directly imaging adiabatically loaded eigenstates of the three lowest bands of our hybrid 2-D lattice. The Hamiltonian for our system in momentum space in the $|l, m\rangle$ basis is

$$H_{rf} = E_L \begin{cases} (k_x + 2l)^2 + m\delta + (|m| - 1)\epsilon & l = l', m = m' \\ V/4 & |l - l'| = 1, m = m' \\ \hbar\Omega_R/2 & l = l', |m - m'| = 1 \\ 0 & \text{otherwise,} \end{cases} \quad (7.2)$$

where the quasimomentum k_x is in units of k_L and $-\infty < l < \infty$ is an integer. Now we find the eigenstates and eigenvalues of our 2-D lattice and plot the 6 lowest energy bands in Fig. 7.2. This was done numerically with $l_{max} = 5$, but there were not any significant quantitative differences when $l_{max} = 25$. The parameters for this simulation were $(\hbar\Omega_R, V, \delta, \epsilon) = (0.5, 6, 0.0, 0.05)E_L$. The band structure of our hybrid 2-D lattice is similar to the band structure for a 1-D periodic potential,

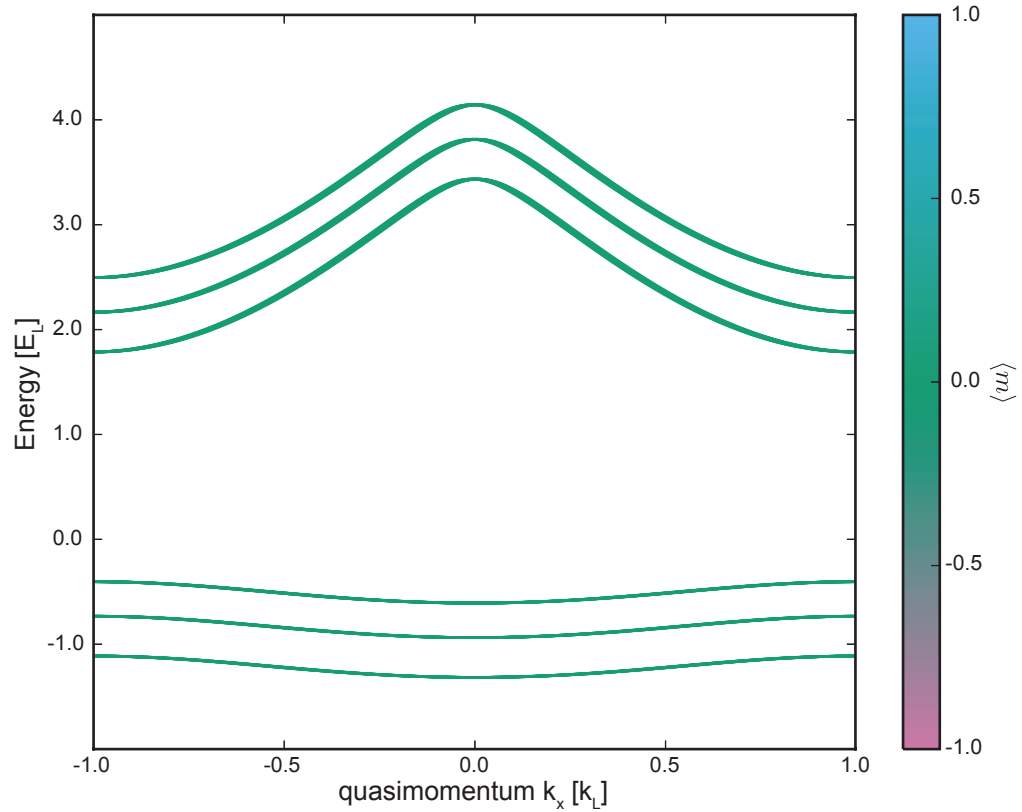


Figure 7.2: Bloch bands for hybrid 2-D lattice as a function of quasimomentum k_x in the \mathbf{e}_x dimension

however, each band in our system now has 3 subbands. The colorbar represents the magnetization $\langle m \rangle$ in each subband. Because $\delta = 0$, the bands and subbands all have the same magnetization $\langle m \rangle = 0$. Adjusting the detuning δ changes $\langle m \rangle$ for the lowest and highest energy subbands within a band by adjusting which m site has the lowest or highest energy.

We now load our atoms into these different magnetic subbands. We can do this by initializing the atoms in different m states within the $f = 1$ hyperfine manifold, then adiabatically turning on our hybrid 2-D lattice. We initialize our BECs, confined in our typical crossed-beam optical dipole trap, with trap fre-

quencies $(\omega_x, \omega_y, \omega_z)/2\pi = (50, 40, 110)$ Hz, into one of three internal $|m\rangle$ states with a bias magnetic field $B_0\mathbf{e}_z$. To load into the ground, 1st and 2nd excited subband, we initialized our BEC in the $m = +1, 0, -1$ Zeeman sublevel, respectively. Then, we adiabatically loaded into the lowest band of the optical lattice by linearly increasing the optical potential from 0 to $63 \sim 6E_L$ in 200 ms. The lattice depth $V \approx 6E_L$ (about 63 mW) gave a hopping strength $|t_x| \approx 0.05E_L$ along \mathbf{e}_x . To turn on hopping in the synthetic dimension, we would linearly ramp the magnetic field to $(B_0 - 0.06B_0)\mathbf{e}_z$, and then linearly ramp on an rf magnetic field. Then we would linearly ramp the magnetic field back to resonance $B_0\mathbf{e}_z$ in 250ms, adiabatically turning on tunneling in the synthetic dimension.

After preparation, we used a measurement procedure common to all experiments in this chapter: we simultaneously removed all potentials and coupling fields ($t_{\text{off}} < 1 \mu\text{s}$), which returned the atoms to bare spin and momentum states. The atomic cloud expanded for a ≈ 18 ms time-of-flight (TOF) period. During TOF a 2 ms magnetic gradient pulse was applied, Stern-Gerlach separating the three $|m\rangle$ states. The resulting 2-D column density was recorded using standard absorption imaging techniques, giving the normalized momentum distributions $n_m(k_x)$ with perfect single lattice site resolution along \mathbf{e}_s as shown in Fig. 7.3A. The site-resolved fractional population distributions for each image are displayed next to their corresponding absorption image in Fig. 7.3B.

First, we loaded into the ground subband by initializing the BEC in the $|m\rangle = +1$ internal state which has the lowest energy in a bias magnetic field $B_0\mathbf{e}_z$. The top panel in Fig. 7.3A shows typical data for this procedure. Note, the fractional population $n_m = \int dk_x n_m(k_x)$ resembles (Fig. 7.3B) that of a particle in a discretized box along \mathbf{e}_s , while the momentum distributions, typical for atoms

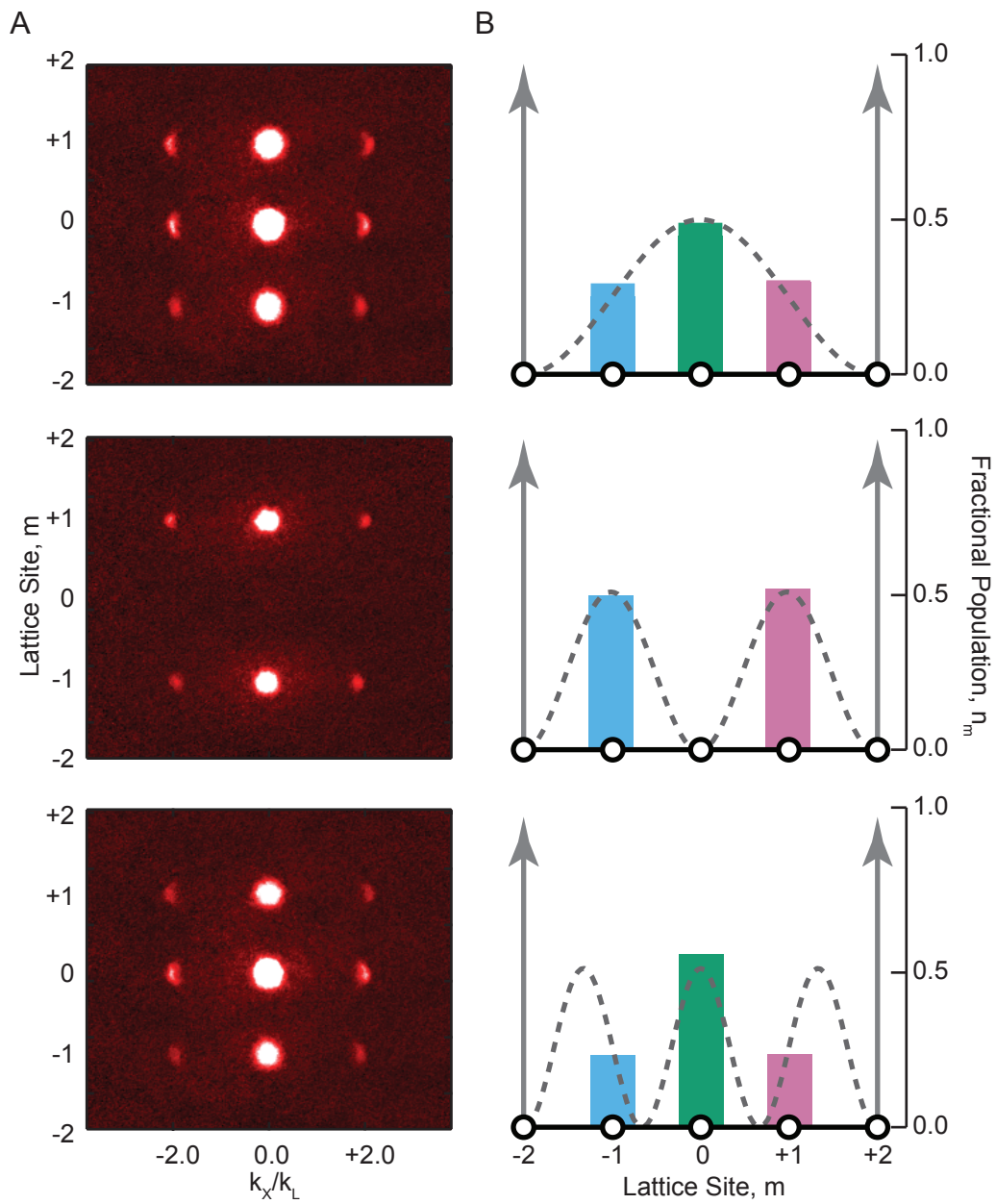


Figure 7.3: Particle in a box along e_s data. (A) Absorption images with momentum resolution in e_x and site resolution in e_s . (B) Fractional population n_m for the ground, 1st and 2nd excited subbands vs lattice site in e_s . The gray dashed line is the probability density for a particle in a box with infinitely hard potential indicated by the solid gray arrows.

in an optical lattice [59], have the same profile for each m site. This demonstrates that the two directions are uncoupled. The grey dashed lines in Fig. 7.3B are the particle in a box wave probability densities:

$$\begin{aligned} |\Psi_1(q_m)|^2 &= \sin\left(\frac{\pi q_m}{2}\right) \\ |\Psi_2(q_m)|^2 &= \cos(\pi q_m) \\ |\Psi_3(q_m)|^2 &= \sin\left(\frac{3\pi q_m}{2}\right), \end{aligned} \tag{7.3}$$

which can be found in any quantum mechanics text book. q_m is a non-integer position coordinate along \mathbf{e}_s in units of lattice site m for purposes of plotting. Then, we initialized the BEC in the $|m\rangle = 0$ and -1 internal state and adiabatically loaded following the same procedure. For the three lowest subbands of our system, we measured the momentum distribution along \mathbf{e}_x and the corresponding probability density for a particle in a box along \mathbf{e}_s .

7.3 Synthetic Flux: Quantum Hall Ribbon

Now, we will introduce complex hopping into our hybrid 2-D lattice by using two-photon Raman transitions instead of an rf magnetic field to enable hopping in the synthetic m direction. The Raman lasers with wavelength λ_R co-propagated with the 1-D optical lattice (Fig. 7.4A) and introduced a phase to the wavefunction of the atom as it hopped from site to site directly proportional to the ratio λ_L/λ_R . This acquired phase is an effective Aharonov-Bohm phase $\phi_{AB}/2\pi$ and fully defines the effective magnetic field. For the wavelengths of light we choose $\phi_{AB}/2\pi \approx 4/3$ around each plaquette corresponding to a field of $\sim 20,000$ T in material with typical lattice constant $a \sim 5$ Å. By introducing this complex hopping into our hybrid 2-D lattice, we engineered a system that

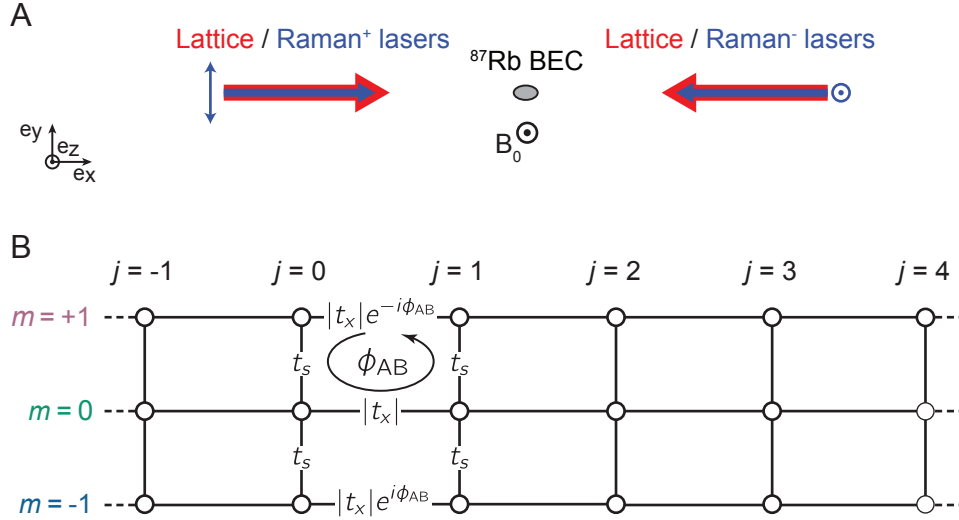


Figure 7.4: Experimental schematic for hybrid 2-D lattice with flux. (A) Two orthogonally-polarized Raman lasers co-propagate with the 1-D optical lattice and induce tunneling t_s . (B) The wavelength mismatch between the lattice and the Raman lasers introduces a complex hopping along t_x creating an effective Aharonov-Bohm phase ϕ_{AB} .

is described by the Harper-Hofstadter Hamiltonian for a charged particle in a 2-D lattice.

7.3.1 The Harper-Hofstadter Hamiltonian

The Harper-Hofstadter Hamiltonian

$$H_{HH} = - \sum_{j,m} \left[t_x |j+1, m\rangle \langle j, m| + t_s |j, m+1\rangle \langle j, m| + \text{h.c.} \right] \quad (7.4)$$

with complex hopping amplitudes t_x and t_s governs the motion of charged particles moving in a 2-D lattice [64, 68] with sites labeled by j and m , the situation which we engineered for our neutral atoms. Analogous to the Landau gauge in continuum systems, we describe our experiment with real t_s (no phase), and with complex $t_x = |t_x| \exp(-i\phi_{AB}m)$ dependent on m . As shown in Fig. 7.4B, the

sum of the tunneling phases around any individual plaquette is ϕ_{AB} .

7.3.2 Eigenstates of the Harper-Hofstadter Hamiltonian

To find the eigenstates of the Harper-Hofstadter Hamiltonian, we again write our Hamiltonian as a matrix in the $|l, m\rangle$ basis for our hybrid 2-D lattice. Similar to controlling magnitude of the rf field, the intensity in the Raman lasers gave a laboratory tunable effective tunneling strength $|t_s| \sim |t_x|$ along the spin “direction” \mathbf{e}_s , proportional to the Rabi frequency Ω_R . However, now there are $2\hbar k_R$ momentum imparted by these transitions and this results in a spatially periodic phase factor $\exp(i2k_R x) = \exp(i\phi_{AB} j)$ [35]. The sign of ϕ_{AB} was controlled by the relative detuning of the Raman lasers. Consequently, our Hamiltonian is

$$H_{HH} = E_L \begin{cases} (k_x + 2l + 2m\phi_{AB})^2 + m\delta + (|m| - 1)\epsilon & l = l', m = m' \\ V/4 & |l - l'| = 1, m = m' \\ \hbar\Omega_R/2 & l = l', |m - m'| = 1 \\ 0 & \text{otherwise.} \end{cases} \quad (7.5)$$

Figure 7.5 plots the numerical simulation of the 3 lowest magnetic subbands with the parameters $(\hbar\Omega_R, V, \delta, \epsilon) = (0.2, 6, 0.0, 0.05)E_L$. There are two very noticeable differences between this band structure with flux and the other without flux. First, the magnetization is no longer the same for each subband. Instead the magnetization depends on the quasimomentum k_x . Second, the lowest band now has 3 local minima. This will be essential for imaging localized edge states. In IQHE systems these states would govern the conductivity, but as individual eigenstates they exhibit no time-dependence. We will now load into the ground band of our Hamiltonian. In contrast to the previous Hamiltonian, initializing

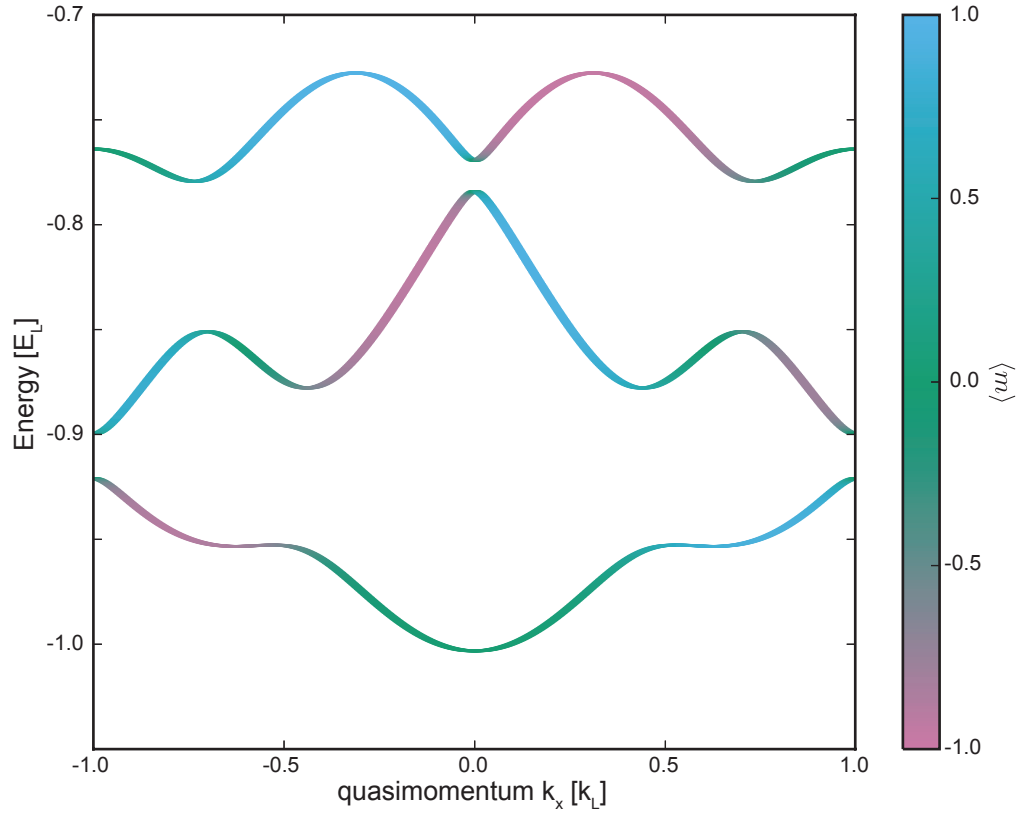


Figure 7.5: Bloch bands for hybrid 2-D lattice with magnetic flux as a function of quasimomentum k_x in the \mathbf{e}_x dimension.

the states into the different Zeeman sublevels no longer adiabatically loads into the different sublevels. Now, the different states will load into the bulk or edge states for initializing in the $m = 1$ or $m = \pm 1$ states, respectively.

The two counter-propagating $\lambda_R = 790.04$ nm Raman lasers along \mathbf{e}_x have orthogonal polarization, wave-vector $k_R = \pm 2\pi/\lambda_R$ and beam waist $\approx 175 \mu\text{m}$, as shown in Fig. 7.4A. These lasers counter-propagated at an angle $\theta = 0.75^\circ$ away from \mathbf{e}_x established by the 1-D lattice, effectively reducing k_R by $\approx 1 \times 10^{-4}$ and introducing a quadratic Zeeman like term with strength $-0.001E_L$. Both of these effects are negligible in our experiment. The Raman lasers' relative phase

was actively stabilized so the phase noise in the Raman beams did not translate to the phase imparted to the atoms (see Sec. 4.3.3). To adiabatically load the ground band, we once again ramped on the 1-D optical lattice from $0E_L$ to $6E_L$ in 200 ms. Due to the next higher subband being $4E_L$ away, we could ramp the Raman lasers on resonance from $0E_L$ to $0.2E_L$ (about 1 mW) in 10 ms and adiabatically load the ground band of our system.

We directly imaged the three eigenstates of the ground Hofstadter band along \mathbf{e}_s for both positive (Fig. 7.6A,B) and negative (Fig. 7.6C,D) flux. The data in Fig. 7.6, with $\phi_{AB} \neq 0$, are qualitatively different as a function of both k_x and m . In k_x for positive flux, the zero order of the 1-D optical lattice for the $m = +1$ is shifted by $2(k_R - k_L)$ relative to the $m = 0$ site. In m , the occupation no longer resembles the distribution expected from a particle in a box.

These differences can be understood in analogy with a 2-D electron in a perpendicular magnetic field, confined in one dimension with hard walls. Along the confined direction the wavefunction is localized to the scale of the magnetic length $\ell_B = \sqrt{\hbar/qB}$, with center position at $k_x \ell_B^2$ in the bulk. Even though the magnetic length is a continuum concept, estimating it for our system is useful for conceptualizing the localized edge eigenstates. Since all physics is 2π periodic in the acquired phase, our flux $\phi_{AB}/2\pi \approx 4/3$ is equivalent to $\phi_{AB} \approx 2\pi/3$. In our system the magnetic length $\ell_B^* = \sqrt{3/2\pi} \approx 0.7$ in units of lattice period is of order unity. The analogue of the wavefunction's localization is observed by comparing the significantly narrowed the bulk state (Fig. 7.6, middle row) with $\phi_{AB} \neq 0$ to the $\phi_{AB} = 0$ case (Fig. 7.3, top row). Continuing the analogy, for large $|k_x|$, the electron becomes localized near the edges. For data initialized in the $m = \pm 1$ site, we observed the appearance of states localized at the sys-

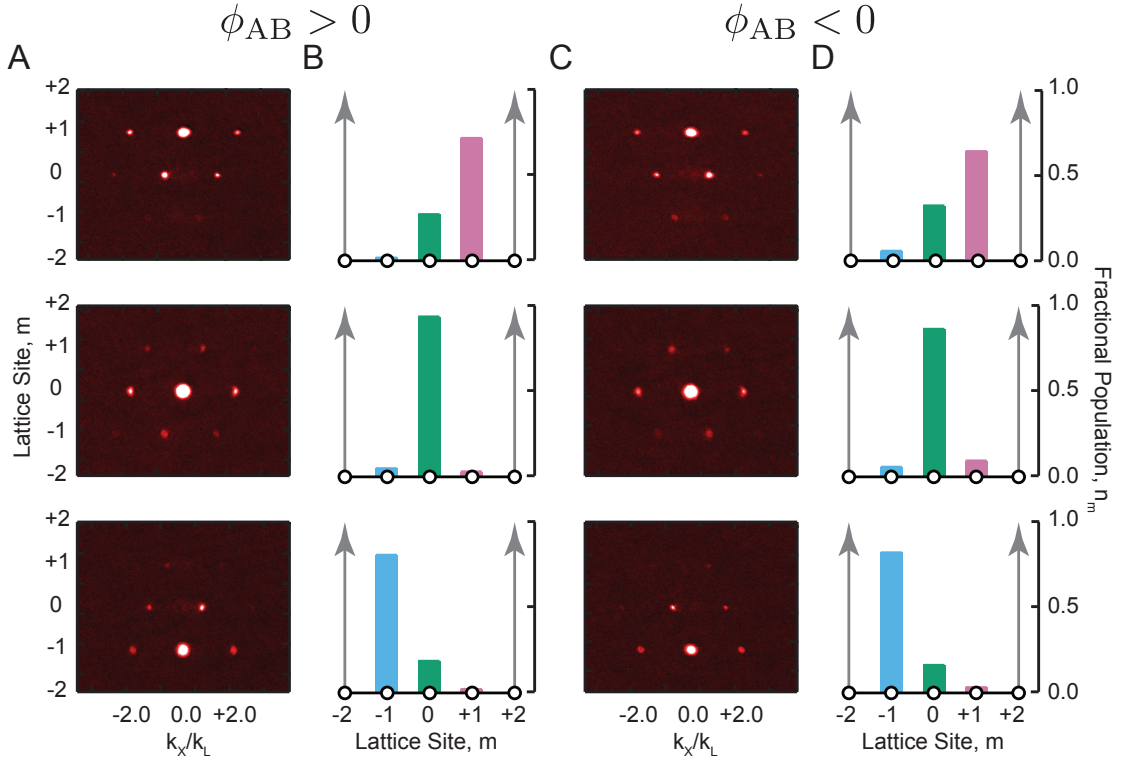


Figure 7.6: Eigenstates for positive and negative flux. (A,C) Absorption images with momentum resolution in \mathbf{e}_x and site resolution in \mathbf{e}_s for positive and negative flux. (B,D) Fractional population n_m for positive and negative flux. The eigenstates are localized on the edges and on the bulk.

tem's edges (Fig. 7.6 top and bottom row), which are completely absent for the ground band when $\phi_{AB} = 0$. These localized edge states are the analogue to the current carrying edge states in fermionic IQHE systems. In contrast, localized bulk states correspond to closed cyclotron orbits.

7.4 Dynamic Hall effect

Next, we loaded our systems into the bulk ($m = 0$ site) with $t_s = 0$ with $\delta \approx 0$, and then abruptly turned on t_s , allowing tunneling along \mathbf{e}_s . Consequently, the

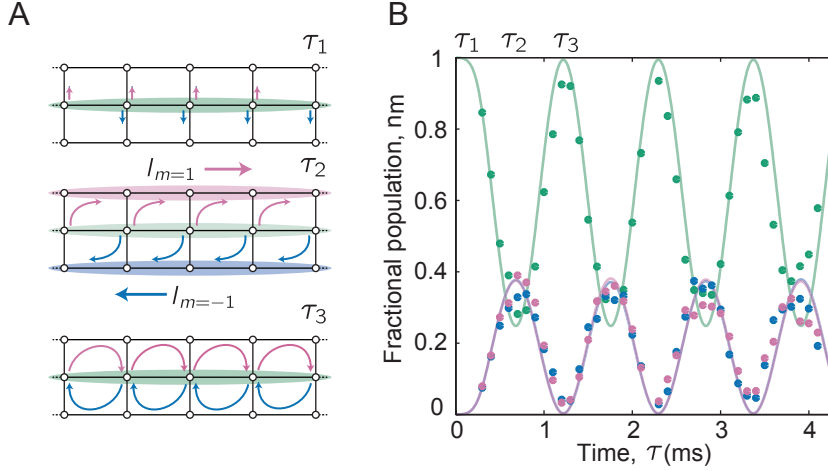


Figure 7.7: Chiral Current in Quantum Hall Strip. (A) The tunneling in \mathbf{e}_s was rapidly turned on so the atoms began to coherently tunnel and feel a force perpendicular to their motion. This created edge currents $I_{m=\pm 1}$. (B) The coherent Rabi flops between sites m for ≈ 2.4 mW in the Raman beams. The solid curves are generated by evaluating our full Hamiltonian with best fit parameters $(\hbar\Omega_R, V, \delta, \epsilon) = (0.73, 6, 0.001, 0.05)E_L$.

resulting state consisted of coherent superpositions of magnetic subband eigenstates with crystal momentum $q_x/k_L = -m\phi_{AB}/\pi$. When $\phi_{AB} \neq 0$, atoms coherently tunneling along \mathbf{e}_s experienced an associated Lorentz force along \mathbf{e}_x . This motion along m drove transverse, i.e. Hall, edge currents $I_{m=\pm 1}(\tau) = n_m(\tau)\langle v_m \rangle$ along \mathbf{e}_x (Fig. 7.7A), where $\langle v_m \rangle$ is the mean velocity of atoms on site m along \mathbf{e}_x .

Figure 7.7 displays these dynamics and how balanced populations oscillated in and out of the the originally empty $m = \pm 1$ sites as a function of time τ . At time $\tau_1 = 0$, we linearly ramped $\hbar\Omega_R$ from $0E_R$ to a set-point in $300 \mu s$. We varied $\hbar\Omega_R$ from $0.2E_R$ to $0.9E_R$ (about 0.9 mW to 3 mW) changing the tunneling anisotropy t_s/t_x from about one to three. The shortened time scale was adiabatic with respect to the $\approx 5E_L$ band spacing in the 1-D optical lattice, yet nearly instantaneous with respect to the $\approx 4t_x$ magnetic band width. At τ_2 the maximum fractional population of atoms tunneled to the edges, acquired a transverse ve-

locity and contributed maximally to our defined a chiral current $\mathcal{I} = I_1 - I_{-1}$. The transverse velocity was controlled by two parameters: ϕ_{AB} set the crystal momentum acquired while tunneling, and t_x gave the natural unit of velocity $2t_x/\hbar k_L$. At τ_3 , the atoms tunnel back to the bulk state and $\mathcal{I} = 0$.

We confirmed the system's chirality by inverting ϕ_{AB} and verifying that \mathcal{I} changed sign. Additionally, we repeated the experiment with $\phi_{AB} = 0$, and observed no chiral current. Because the transverse velocity for the atoms was symmetric ($\langle v_{+1} \rangle = -\langle v_{-1} \rangle$), \mathcal{I} oscillated in phase with the fractional populations in the edges $\langle |m| \rangle$ V as shown in Fig. 7.8A. We extracted a slope S from linear fits to \mathcal{I} dependence on $\langle |m| \rangle$. Figure 7.8B displays an example of this linear fit for positive, negative and zero flux. The small offset is due to a non-zero turn on time for tunneling in \mathbf{e}_s and is correctly predicted by our theory. The peak edge current \mathcal{I}_{\max} strongly depends on t_s/t_x (Fig. 7.8C), increasing from zero then reaching saturation when all the atoms are no longer in the bulk, but on the edges. This dependence and saturation of the chiral current on the tunneling anisotropy t_s/t_x is reminiscent of the optical lattice experiments in Ref. [10]. For small t_s/t_x , few atoms tunneled to the edges, giving a correspondingly small \mathcal{I}_{\max} . As t_s/t_x increased \mathcal{I}_{\max} was bounded its value with all the atoms contributing to the current on the edges [70]. In contrast, S , essentially constant in t_s/t_x as shown by the inset in Fig. 7.8C. The slight downward curvature in our theoretical model, plotted by the grey curve, evidences 5%-level corrections proportional to $|t_s|^2$ to the tight binding model, owing to mixing with excited Bloch bands of the 1-D optical lattice.

The linear dependence of the chiral current on m demonstrates a new kind of dynamic Hall effect. We can measure this bulk property due to simultaneously

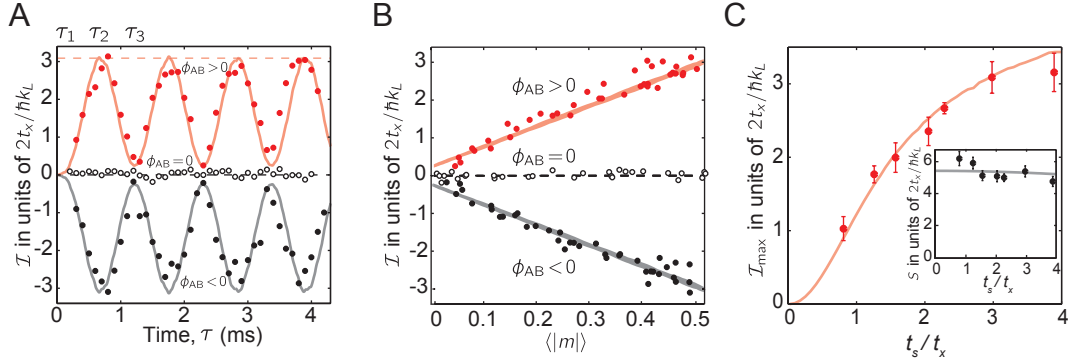


Figure 7.8: Dynamic Hall effect. Data shown in red, black, and empty circles are taken for positive, negative, and zero ϕ_{AB} , respectively. Our theory (solid or dashed curves) uses parameters determined from Fig. 7.7B for $\phi_{AB} \neq 0$, giving $t_s = 0.14E_L$. (A) We observed in-phase oscillation of \mathcal{I} and the combined $m = \pm 1$ populations $\langle |m| \rangle$. The pink dashed line shows how we extracted \mathcal{I}_{\max} . (B) The chiral current $\mathcal{I} = I_1 - I_{-1}$ had the same sign as ϕ_{AB} and was linear in $\langle |m| \rangle$. (C) The chiral current saturated in tunneling anisotropy t_s/t_x , but the slope of \mathcal{I} was essentially constant in t_s/t_x (inset).

resolving the momentum along \mathbf{e}_x and site m in our TOF images. Although this bulk property is hard to access in condensed matter systems due to the symmetry of the produced current and the dominant edge properties, this behavior should still exist.

7.5 Edge magnetoplasmons: skipping orbits

Edge magnetoplasmons are superpositions of edge eigenstates in different Landau levels [81, 9], or here magnetic bands. We launched these excitations and recorded their full motion, including a chiral drift along the system's edge and an underlying skipping motion, on either edge. Figure 7.9 illustrates this motion starting from $m = -1$. The potential was tilted along \mathbf{e}_s , such that the initially occupied site was at the potential minimum (Fig. 7.9B). We used our simulations of our full Hamiltonian to specify what detuning δ and Raman coupling

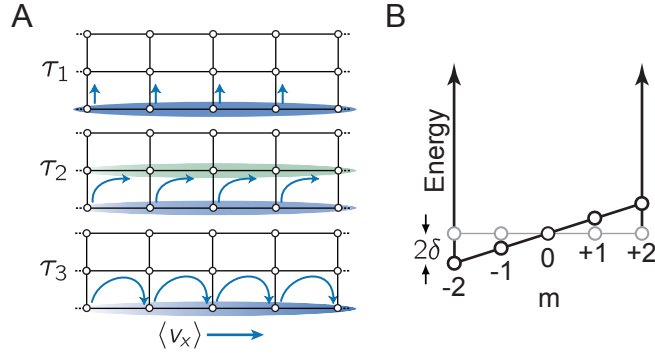


Figure 7.9: Schematic of Skipping Orbits. (A) As atoms tunneled from the $m = -1$ edge to the bulk, they began their orbit. Before finishing the orbit, they encounter the infinitely hard edge of the system and reflect off it. This leads to a chiral drift along the edge. (B) The non-zero detuning δ tilts the potential.

strength $\hbar\Omega$ would create the large enough orbits to image easily. Our modeling of the full Hamiltonian, which does not include interactions, was more consistent with experiment at smaller atom numbers. Also based on our simulations, we decided to operate a larger quadratic Zeeman shift to more easily image the skipping orbits, therefore we changed our bias field B_0 . Thus, our Raman coupling was detuned from the $g\mu_B B_0/h \approx 1.35$ MHz Zeeman splitting by a nonzero δ and tilted the lattice along \mathbf{e}_s as shown in Fig. 7.9. The corresponding quadratic Zeeman shift additionally lowered $|m = 0\rangle$ by $\epsilon = 0.13E_L$. We loaded our systems on to either edge in m with $t_s = 0$, and then abruptly turned on t_s , allowing tunneling along \mathbf{e}_s . The abrupt turn-on resulted in either edge state consisting of coherent superpositions of magnetic band eigenstates with crystal momentum $q_x/k_L = -m\phi_{AB}/\pi$, which began to coherently tunnel along \mathbf{e}_s and experienced an associated Lorentz force along \mathbf{e}_x . These atoms then became cold-atom analogues to edge magnetoplasmons: they began cyclotron orbits, were reflected from the hard wall, and skipped down one edge or the other.

In Fig. 7.10, we plot the time evolving average position $\langle m(\tau) \rangle$ along \mathbf{e}_s

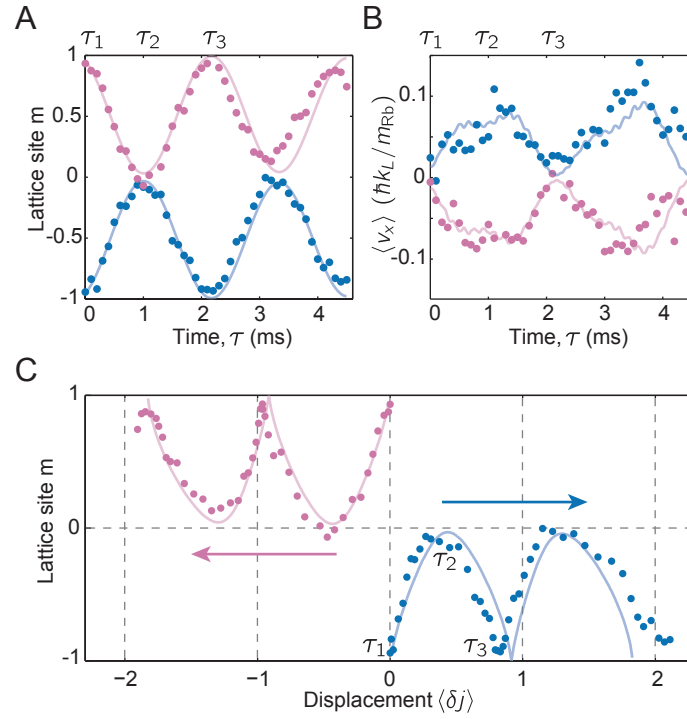


Figure 7.10: Skipping Orbits. Data shown in pink/blue solid circles are for systems initialized on $m = 1$ ($m = -1$). (A) Average position in m and (B) velocity $\langle v_x \rangle$ along \mathbf{e}_x versus time τ . (C) Displacement in m versus displacement along \mathbf{e}_x shows a skipping orbit trajectory.

and velocity $\langle v_x(\tau) \rangle = \sum_m I_m$ along \mathbf{e}_x for excitations on both edges. $\langle v_x(\tau) \rangle$ evolved periodically in time but with opposite velocities for the different edges. The solid curves are numerical simulations using parameters $(\hbar\Omega_R, V, \delta, \epsilon) = (0.58, 5.2, \pm 0.087, 0.13)E_L$. The spatial trajectories are illustrated in Fig. 7.10 C, where we obtained the displacement $\langle \delta j(\tau) \rangle$ by directly integrating $\langle v_x(\tau) \rangle / a$, where $a = \lambda_L/2$ is the lattice period. These data clearly show edge magnetoplasmons with their chiral longitudinal motion, and constitute the first experimental observation of their edge localization and transverse skipping motion.

7.6 Conclusions and Outlook

We engineered a 2-D lattice with square geometry for ^{87}Rb Bose-Einstein condensates in which we directly controlled the acquired phases as atoms traversed the lattice, giving a tunneling phase $\phi_{\text{AB}}/2\pi \approx 4/3$ around each plaquette. Aharonov-Bohm phases of order unity are only possible in engineered materials [53, 71], or in atomic [74, 3, 97, 79, 4, 93] and optical [62] settings. These phases take the place of the Aharonov-Bohm phases produced by true magnetic fields and suffice to fully define the effective magnetic field. With our hard-wall potential, a realization of the Laughlin charge pump [84] is straightforward: as particles accelerate along \mathbf{e}_x , mass moves from one edge to the other in the orthogonal direction \mathbf{e}_y . My colleague Dina Genkina is currently implementing the Laughlin charge pump in the lab. We are also set up to extend our technique to periodic boundary conditions, coupling together the $|m = \pm 1\rangle$ states. Another colleague Ben Stuhl began implementing this experiment before moving out west. The implementation of periodic boundary conditions should produce systems exhibiting a fractal Hofstadter spectrum [35], even given a three-site extent along \mathbf{e}_y . Going beyond conventional condensed matter realities, the flexibility afforded by directly laser-engineering the hopping enables the creation of Möbius strip geometries: topological systems with just one edge [24].

CHAPTER 8

PHYSICS, WE HAVE A PROBLEM: SEXUAL HARASSMENT

In this chapter, I present the results from a pre- and post conference evaluation survey of the American Physical Society (APS) Conferences for Undergraduate Women in Physics (CUWiP). Forty-eight percent (252/521) of the respondents reported ‘Sometimes’ or ‘Often’ observing sexual harassment in physics. Forty-nine percent (255/522) of the respondents reported having personally experienced sexual harassment in physics. We also found strong correlations among experienced harassment, frequency of observed harassment and perception of serious, unresolved gender issues in physics. Lastly, reporting more frequent observations and personally experiencing sexual harassment were correlated with a lower GPA in physics courses. These results are part of an ongoing study on participants’ career plans, attitudes, and prior experiences with physics to improve undergraduate physics education and the CUWiP experience for future students. I joined the collaboration in June 2015 after advocating for the addition of questions pertaining to sexual harassment in physics.

8.1 Introduction

The term “sexual harassment” was coined in response to the behavior of a physics professor at Cornell University [12]. This is the story of Carmita Wood, an administrative assistant at Wilson Synchrotron Laboratory. Wood was in her mid-forties and a mother of four in June of 1974 when she was forced to quit her job. Wood developed severe physical pain from the constant stress of fending off the professor’s advances such as physically accosting her or mimicking

masturbation in her presence. When the professor went on a one year leave of absence, the pain went away. In anticipation of his return and the return to daily stresses of harassment, Wood quit. She was denied unemployment benefits for voluntarily leaving her job. For legal assistance and support, she approached Lin Farley, a lecturer in the Women's Section of Cornell University's Human Affairs Program. Ultimately, Wood lost the appeal, but a movement against sexual harassment in the workplace was born [27, 12, 96].

Recently, several high profile cases of sexual harassment in academia have been brought to light in the fields of anthropology [14], astronomy [135] and biology [63]. These cases have indicated the need for academic communities to address issues of sexual harassment in their professional spheres. Many climate studies have been underway in anthropology [40] and astronomy [114]. In the field of physics, the APS ad-hoc committee on lesbian, gay, bisexual, transgender (LGBT) Issues recently released a report on a professional climate survey of the members of the LGBT community in physics [11]. In this report, the female survey participants reported experiencing exclusionary behavior—defined as behavior that shuns, ignores or harasses a person—at three times the rate of male participants. Additionally, a qualitative study of female graduate students' experiences in physics found that a majority of its participants experienced microaggressions—subtle insults or slights—and several reported experiencing more traditional hostile sexism [19]. We complement these climate and qualitative studies by measuring the extent to which female undergraduates experience and observe sexual harassment in physics.

To explore the ways sexual harassment may impact female undergraduates, we offer three hypotheses: (1) Sexual harassment occurs in physics contexts—

defined as in research labs, instructional settings, department or student organization events—and the degree to which respondents directly experience and observe sexual harassment will be correlated to each other, (2) reporting that one believes that there are serious gender issues to be reconciled in physics will be positively correlated with both experienced and observed harassment, and (3) reported GPA from physics courses will be negatively correlated with experienced and observed harassment.

8.2 Methods

In this section, I detail the methods for our internet-based survey ($n = 522$) of attendees of the American Physical Society (APS) Conferences for Undergraduate Women in Physics (CUWiP). I will discuss our participant recruitment and demographics. Then, I will discuss the question design and present the questions in their full text. Notably, we were able to survey a large proportion of the female undergraduate physics majors in the United States.

8.2.1 Ethics Statement

Participation was voluntary and informed consent was obtained from all survey participants. We obtained approval for human subjects research with minimal risk from the University of Maryland College Park Institutional Review Board (project [505475-11]). In addition, I obtained an exemption (Protocol ID# 1601006083) from Cornell University's Office of Research Integrity and Assurance.

8.2.2 Participant Recruitment

CUWiP are a continuation of a grass-roots collaborative effort of physicists from around the country that has provided conferences annually since 2006. The goals of the CUWiP effort are to increase retention and improve career outcomes of undergraduate women in physics. As part of the effort to measure the impact of the conference goals, online pre- and post-conference assessment surveys are administered annually. In 2016, there were 1088 attendees at CUWiP. These attendees were predominantly undergraduate female physics majors. In 2014, 1341 women graduated with a Bachelor's degree in physics [1]. Estimating the number of female undergraduates majoring in physics by multiplying the number of Bachelor's in a year by four, there are approximately 5,400 female physics majors in the United States (U. S.). The demographic breakdown will be discussed in the next section. If we solely look at the number of the attendees compared to the number of female physics majors, we have the possibility of sampling about 19% of the female physics majors in the US.

By recruiting our survey participants from this population, we have the potential to collect responses from a large fraction of the undergraduate women in physics in the U. S. Additionally, by including our questions about observed and experienced harassment on a post conference evaluation survey, the results will have a different response bias than typical climate or sexual harassment surveys. So far, field specific surveys have used snowball methods, where participants recruited other participants and the survey was advertised at conferences and through social media. These snowball climate surveys can have selection bias, e.g. introduced through participants forwarding the survey to members of the community who have disclosed negative experiences, and response bias,

e.g. people who have been harassed may be both more or less likely to respond to a survey on sexual harassment. There were no repeat survey participants because each participant had a unique identifier.

8.2.3 Participant Demographics

For our study, we focused on the sample of the (890) self-identified female undergraduates of the (1088) total CUWiP attendees in January 2016. Out of the female undergraduate attendees, 524 took the post survey and $n = 522$ responded to the questions on sexual harassment. Comparing the demographics of our sample to the population of female physics undergraduates is difficult because the collection of the racial demographics of our sample was more flexible than the demographic data on undergraduate physics students, i.e. our survey allowed for more choice than usual demographic data. All demographic questions were asked on the pre-survey (Table 8.2). The participants were asked if they were Hispanic or Latino(a). Separately, they were asked with which racial groups they identified and informed they could mark all that apply with options Black, White, Asian, Native American or Alaskan Native (NAAN), Native Hawaiian or Pacific Islander (NHPI) or Other. Other had an option for the participant to self-identify. In contrast, the demographic data on students earning their Bachelor's degree in physics has these inquiries as one question, and if a student is Hispanic or a Temporary resident, any additional information about their racial identity is not reported. Furthermore, the data does not include which racial groups multi-racial students identify. These differences in demographic data collection could lead to significant differences of the proportion of students reported in different racial groups.

To assess whether our results give us insight into the female undergraduates' experiences with sexual harassment, we first compare the largest demographic group easily identified through both methods of collection. Sixty-eight percent (601/890) of the female, undergraduate CUWiP attendees identified as white and non-Hispanic/Latina. This is consistent with the 68% (911/1341) white, non-Hispanic women who earned Bachelor's degrees in 2014 [1]. If we exclude the women who identified in multiple racial groups from the count, the attendees included closer to 62% (554/890) white, non-Hispanic women. We cannot know how the women who self-identified as multi-racial or white, Hispanic would have reported their race/ethnicity if they were only given one option. The data indicates that the vast majority of our sample is white and non-Hispanic, similar to the reported population of women earning Bachelor's degrees in Physics. The demographics of the self-identified female undergraduates were sufficiently heterogeneous with respect to the remaining demographic characteristics of the women earning Bachelor's degrees in physics that there is a good basis for the generality of our results. Table displays the demographic data of our sample, the CUWiP attendees and women who Bachelor's degrees in physics at U. S. institutions. For our data, participants are counted in all groups with which they identified. Due to difference in data collection, we cannot differentiate if we are oversampling under-represented minority (URM) female undergraduates or if the additional flexibility of our demographic data collection is the explanation for the demographic differences between the attendees and the degree earners.

We compared the demographics of the female undergraduate CUWiP attendees (890) to our sample ($n = 522$)—the participants who responded to the sexual harassment questions on the post-survey—to examine the response bias. About

Race or Ethnicity	Sample	%	Attendees	%	Degrees [†]	%
Total	522	100	890	100	1341	100
URM	174	19.6	97	18.6	146	10.8
Hispanic or Latina	131	14.7	75	14.4	86	6.4
Black	19	3.6	36	4.0	54	4.0
NAAN	12	2.2	17	1.9	4	0.3
NHPI	2	0.4	9	1.0	2	0.1
White	419	80.2	691	77.6	–	–
w/o Hispanic or Latina	365	69.9	601	67.5	–	–
and w/o multi-racial	338	64.8	554	62.2	911	67.9
Asian	77	14.8	149	16.7	89	6.6
Other	16	3.1	24	2.7	54	4.0
Multi-racial	39	7.5	64	7.2	49	3.7

Table 8.1: Racial/Ethnic Groups of our sample of and total female, undergraduate CUWiP attendees, and Bachelor’s degrees in physics earned by women at U. S. institutions in 2014 [1]. [†]This demographic data was collected with slightly different racial and ethnic groups, and only allowed for an individual to be identified in one.

15% (131/890, 75/522) of our selected population and sample reported identifying as Hispanic/Latina and about 1% (13/890, 6/522) did not specify. A majority 66% (342/522) of our sample specified being in their 3rd, 4th or 5th year of college and the remaining 34% (180/522) specified being in their 1st or 2nd year of college. This is consistent with the overall selected population’s year in college demographics: 65% (582/890) and 35% (308/890), respectively. Ninety-four percent of both the female CUWiP attendees (834/890) and the participants in our sample (492/522) intend to complete a Bachelor’s degree in physics. There are no large shifts in demographics from the demographic data about CUWiP attendees to the sample in which we measured observations and experiences of sexual harassment.

8.2.4 Survey Design

The results in this study derive from two questions on the pre-survey administered at the time of conference registration and two questions on the post-conference survey after the conference was completed. Both surveys were administered online. The pre-survey question on belief in gender issues was asked after inquiring about the participant's career plans and in a section inquiring about their physics attitudes and experiences. The question on the participant's physics GPA was in this section as well. Both of these questions came before inquiring about the participant's demographic data. Both of these questions were asked before the participants attended the conference as shown in Table 8.2. Additionally, the GPA inquiry was on a pre-survey which was administered prior to the post survey with the questions on sexual harassment, hence our participants were not primed by the sexual harassment questions to report a lower physics GPA.

The two questions on the post-survey asked about the frequency at which the participant observed harassing behavior and whether the participant had personally experienced this behavior limited to a context associated with physics (Table 8.3). These questions were adapted from question 31 and 32 on the climate survey of academic field work in anthropology [40]. We do not ask about harassment through direct query, but rather describe behavioral experiences and ask about frequency and whether or not the participant was personally targeted. This is the preferred method for studying sexual harassment because people's perceptions about sexual harassment change over time. Additionally, a study on two private sector organizations and one university found that regardless of whether a woman labeled her experiences as

12. Other than representation (i.e. numbers participating), do you feel that there are serious gender issues in physics? Not at all 0 1 2 3 4 Very much so

14. What year are you in college?

- First year
- Second year
- Third year
- Fourth year
- Fifth year
- Graduate Student
- Faculty

15. Which of the following physics courses (or equivalent) have you taken and completed in college? Mark all that apply.

- Intro Physics I
- Intro Physics II
- Modern Physics
- Classical Mechanics (not intro)
- Thermodynamics (Stat. Mech.)
- Electromagnetism I
- Electromagnetism II
- Quantum Mechanics I
- Quantum Mechanics II

16. What is your approximate average GPA (4=A, 3=B, 2=C, 1=D, 0=F) in these physics courses-please enter a number(decimals allowed)?

20. Are you Female or Male?

- Female
- Male
- Other:.....

21. Are you Hispanic or Latino(a)?

- No
- Yes

22. With which racial group(s) do you identify? (*For multi-racial, mark all that apply*)

- Black
- White
- Asian
- Native American or Alaskan
- Native
- Native Hawaiian or Pacific Islander
- Other:.....

Table 8.2: Pre-survey Questions

<p>16. With what frequency do you observe or hear about individuals making inappropriate or sexual remarks, comments about physical beauty, cognitive sex differences, or jokes in a context associated with physics (e.g. in research labs, instructional settings, department or student organization events)? These may come from other students, high school teachers, instructors or professors.</p> <ul style="list-style-type: none"> • Never • Rarely • Sometimes • Often <p>17. Have you ever personally experienced inappropriate or sexual remarks, comments about physical beauty, cognitive sex differences, or jokes in a context associated with physics?</p> <ul style="list-style-type: none"> • Yes • No • I don't know
--

Table 8.3: Post-survey Questions

sexual harassment, she experiences similar psychological, work and health consequences [91]. A study on both men and women in the military strongly replicated these results [100] suggesting they are quite generalizable. Furthermore this study found that negative outcomes were more related to frequency of the sexually harassing behavior rather than labeling the behavior as “sexual harassment”.

8.2.5 Enumeration and Analysis

Identifying correlations required us to enumerate the responses to the sexual harassment questions. For post-survey question 16, we note the ordinal response

has four levels, increasing with frequency. We set 'Never'= 1, 'Rarely'=2, 'Sometimes'=3, and 'Often'=4. Because the response is ordinal, we note we should not assume a linear relationship with other variables. We use a Spearman's Rank correlation ρ_S test to look for correlations between the observed response and our other variables of experienced, belief in gender issues and GPA. For the experienced question, we excluded the 'I don't know' responses from the analysis, because there is not a clear placement relative to 'Yes' and 'No'. We set 'Yes'=1 and 'No'=2. The responses to the question about belief in gender issues in physics was already enumerated as it is an anchored Likert-type scale from 'Not at all' (0) to 'Very much so' (4). GPA was already enumerated as well, however it saturates at 4.0. To test for correlations between the experienced response and belief in gender issues or GPA, we used a Pearson's product-moment correlation ρ_P due to the variables all qualifying as an interval scale.

8.3 Results and Discussion

8.3.1 Female undergraduate physics majors experience and observe sexual harassment

Forty-eight percent (252/521) of respondents report they observed harassment 'Sometimes' or 'Often' in a context associated with physics (Fig. 8.1A). Forty-nine percent (255/522) of the respondents reported being the target of sexual harassment (Fig. 8.1B). These results support our hypothesis that sexual harassment occurs in contexts associated with physics.

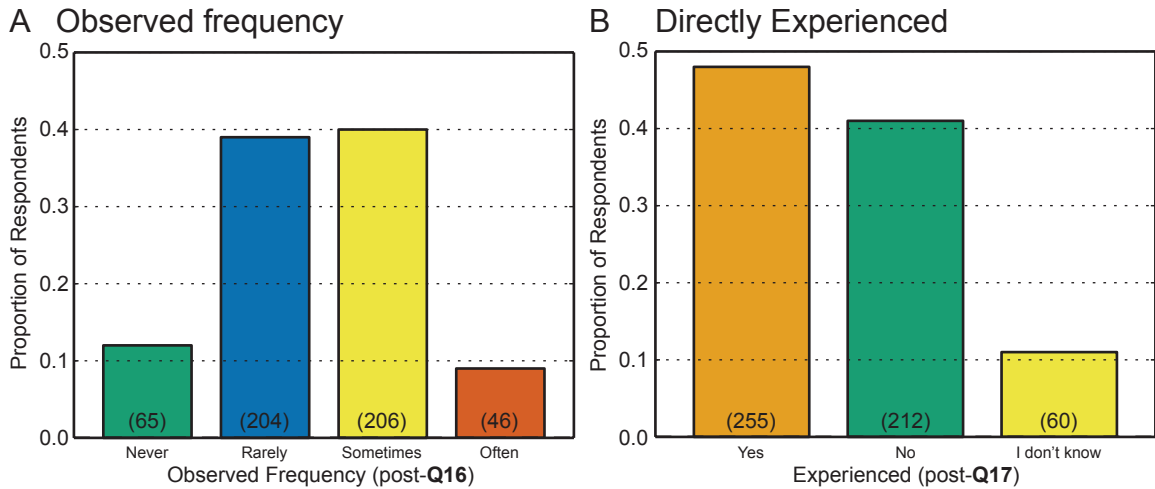


Figure 8.1: Observed and experienced sexual harassment in physics

We predicted prevalence because women in male-dominated occupations report experiencing sexual harassment at higher rates than women in female-dominated ones [21]. The 49% of our respondents reporting observations of sexual harassment is similar in magnitude to the 38% (184/481) of female participants who reported observations of sexual or inappropriate comments occurring ‘Regularly’ or ‘Often’ at scientific field sites [40], despite varying methodologies. Our data provides compelling evidence that students are experiencing sexual harassment in physics contexts. For reference on the collegiate experience, the American Association of Universities conducted a climate survey on Sexual Assault and Sexual Misconduct and found 61.9% of that sample of female students ($n = 55,552$) experienced sexual harassment on campus [32]. More broadly, a recent meta-analysis of incident rates of work-related sexual harassment studies with probability sampling and behavioral experiences survey methods reported 58% of women (excluding studies on students) in academic samples and 69% of women in military samples reported having experienced harassing behaviors [72].

Our survey questions solely focused on gender, not on any intersection of gender and other marginalized identities, eg. race or ability. Additionally, we only analyzed the data in the context of the female students due to the small representation of the responses from other genders. It is important to remember that people with additional marginalized identities often face more harassment and discrimination. As shown in Fig. 8.2, we did explore if belonging to a racial group increased or decreased the likelihood of reporting observed or experienced sexual harassment. An exact Fisher’s test performed on each

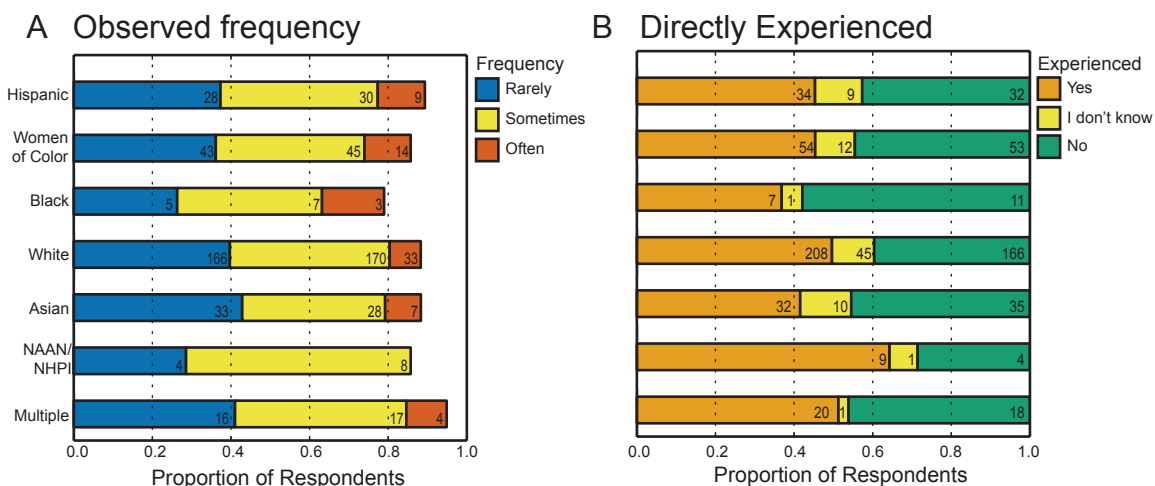


Figure 8.2: Sexual harassment in physics reported by female undergraduate physics majors by their race and ethnicity.

racial sub group and on Women of Color–female participants identifying with any non-white racial group–as compared to the rest of the female participants had no statistically significant difference among racial groups. This is consistent with a study on $n = 208$ women faculty scientists, which found no different between the rates of reported sexual harassment among white women and Women of Color [117]. However, an intersectional bias study of $n = 557$ female STEM faculty found that through direct query–inquiring whether the participant had been sexual harassed on the survey–white women (37.2%) were the

most likely to report sexual harassment, as compared to Asian women (25%), Latinas (21.9%) and Black women (12.5%) [132].

Prevalent sexual harassment in physics may be indicative of a deeper cultural problem surrounding women in physics. Male attitudes about women in science have been studied through measured gender bias in their evaluations of women in science. For example, elite male life sciences faculty employ fewer women [118], male biology students have a strong male bias when evaluating the knowledge of their peers [61], and male students rate female high school science teachers significantly lower than their male counterparts on evaluations in biology, chemistry, and physics [108]. Furthermore, women can also show bias against women in science, particularly in the physical sciences. In the same study that found a male bias in male student evaluation of high school science teachers, female students did not show a gender bias on evaluations in biology and chemistry, but did in physics [108]. This gender bias may be illustrating the impact on both male and female students of deep-seated cultural stereotypes about women in physics. Knowing more about the attitudes about women in physics in different educational environments and rates of sexual harassment in those environments would be a potential future study.

8.3.2 Correlations with belief in serious gender issues in physics and physics GPA

We found a strong relationship with those who directly experience and those who frequently observe sexual harassment ($\rho_S = -0.503$, $N = 462$, $p < 0.0001$). In Fig. 8.3, the respondents ($N = 521$) are grouped based on their responses to the

experienced question and calculated the percentages each group that responded 'Never', 'Rarely', 'Sometimes' or 'Often' to the inquiry about frequency of observation. The area of the circles is proportional to the percentage of responses in each 'Yes', 'I don't know' or 'No' subgroup. Even though the 'I don't know' responses were not included in the correlation test, overall their responses were less extreme than the whole population and were fairly evenly balanced between 'Rarely' and 'Sometimes'. The strong correlation is visible.

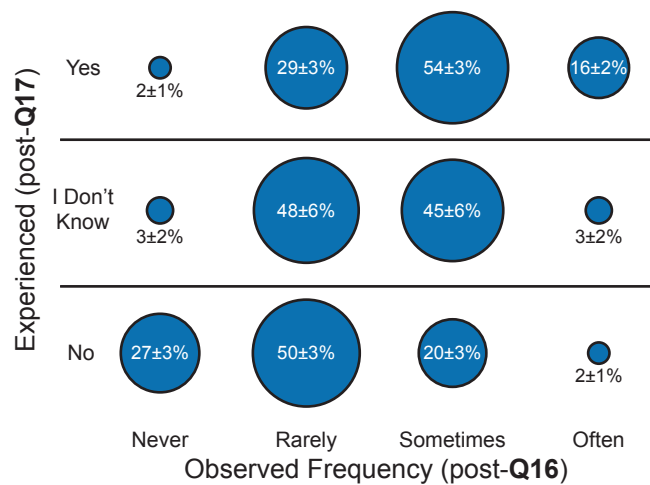


Figure 8.3: Experienced versus frequency of observed sexual harassment. The uncertainties are the standard error.

One explanation for correlation between observed and experienced harassment can be because higher levels of sexual harassment occur where such behavior is perceived as being tolerated [100]. Another explanation could be that certain women galvanize more sexual harassment than others. To be viewed as competent physicists, some women distance themselves from their gender and gender-roles [56]. An experimental psychology paper exploring the cause of sexual harassment found that women who violate feminine ideals and work in male-dominated fields are the most likely to be sexually harassed to punish them for being gender-role deviant [21]. So a woman distancing herself

from her gender-roles to be viewed as a competent physicist, then becomes more likely to be sexually harassed for being gender-role deviant. This trade-off between these two ideas of being feminine or competent is referred to as the tightrope [132]. Understanding the causes of this correlation is beyond the scope of the current study.

This correlation is unlikely to be due to some women being “more sensitive” than others. The idea that the prevalence of sexual harassment is overestimated due to women “whining” has been widely refuted [72, 91, 100]. A meta-analysis study compared the reporting of sexual harassment at work to the reporting of experiencing harassing behaviors at work, the labeling of sexual harassment was half the reports of harassing behavior [72]. A study in the military found that negative occupational, psychological and health outcomes correlate more with frequency of experiences with unwanted sexual behavior than labeling such behavior as sexual harassment [100]. These studies and others provide evidence against the so-called “whiner” hypothesis.

We found a medium correlation ($\rho_S = 0.350, N = 517, p < 0.0001$) between frequency of observed sexual harassment and belief in gender issues in physics (Fig. 8.4A). We found a medium correlation ($\rho_P = -0.293, N = 457, p < 0.0001, 95\%CI = [-0.375, -0.207]$) test between experienced sexual harassment and belief in gender issues in physics (Fig. 8.4B). Figure 8.4 is a box-and-whisker plot. Dividing the data into four equal parts (quartiles), the box represents the middle half of the data. The whiskers are the minimum and the maximum of the data, where outliers are represented by points. The thick vertical line is the median of the data. The box represents Our hypothesized correlation between belief in gender issues in physics and observed frequency and experienced sexual

harassment was supported. Notably, in the military study about the impact of labeling behavior as sexual harassment, the variable most related to whether or not participants labeled the behavior as sexually harassing was whether or not the participant viewed sexual harassment as a serious societal problem [100].

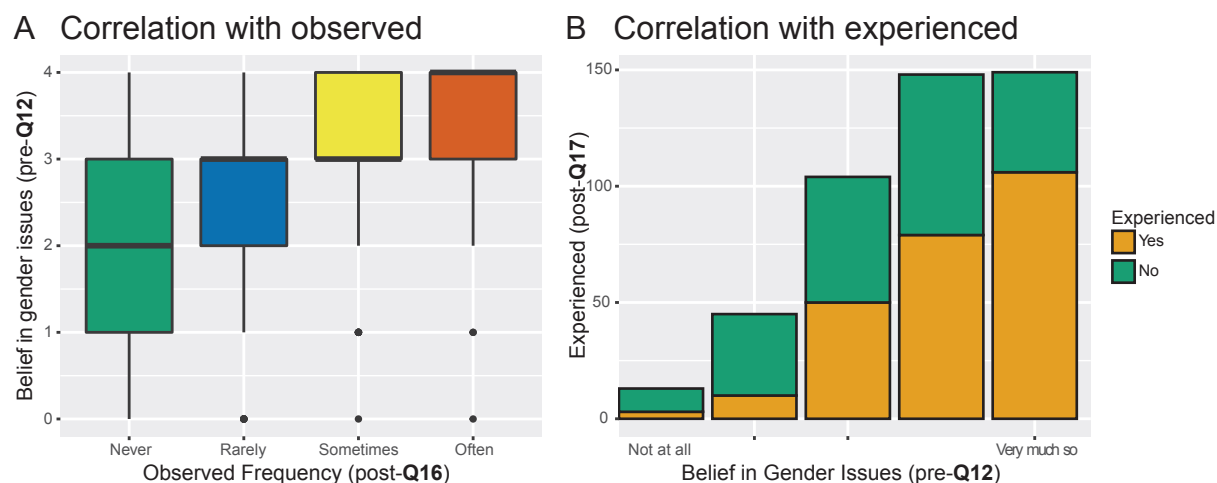


Figure 8.4: Correlation between belief in unresolved gender issues in physics and either frequency of observation or personally experienced sexual harassment in physics. (A) Belief in gender issues in physics versus frequency of observations of sexual harassment. (B) Number of participants who responded explicitly to whether they had experienced sexual harassment versus belief in gender issues in physics.

We found a significant correlation ($\rho_S = -0.153, N = 500, p < 0.001$) between reported physics GPA and observations of sexual harassment (Fig. 8.5A). We also found a significant correlation ($\rho_P = 0.141, N = 441, p < 0.003, 95\%CI = [0.048, 0.231]$) between physics GPA and directly experienced harassment (Fig. 8.5B). These correlations support our hypothesis about correlations between a lower physics GPA and experienced and more frequently observed sexual harassment. This can be due to interactions with sexist men engaging stereotype threat for female students [89]. People typically hold different stereotypes about women than about successful scientists [33], thus observing and ex-

periencing sexual harassment could increase stereotype threat and impact the student's performance in physics. The difference in the median physics GPA of the students responding 'Often' compared to the students responding 'Never' is significant for students applying to physics PhD programs due to the exponential dependence of acceptance on GPA [92].

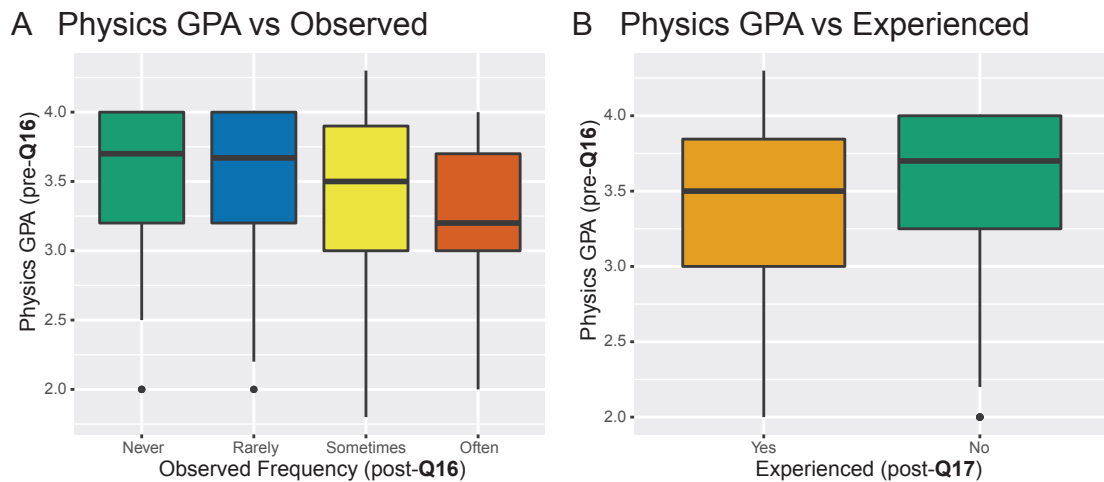


Figure 8.5: Correlation between physics GPA and either frequency of observation or personally experienced sexual harassment in physics. (A) Physics GPA in completed physics courses versus frequency of observations of sexual harassment. (B) GPA in completed physics courses versus personally experienced sexual harassment.

8.3.3 Study Limitations

For this study, there was not an equal probability of selecting any undergraduate female physics majors. By selecting from CUWiP, we may only be sampling women with strong support to continue in their physics careers. Our questions are cumulative over the participant's entire experience associated with physics, so we cannot differentiate between high school experiences and collegiate experiences and found an almost linear increase in observed and experienced ha-

harassment versus year in college and number of physics courses completed. Currently, we only reported on correlations in our data. For example, participants who believe gender issues are a serious problem in physics may also be more likely to report observed and experienced harassment based on gender.

8.4 Outlook and Moving Forward

Our results indicate experienced and observed sexual harassment are correlated in this sample, and that those in this sample who observe or experience sexual harassment also tend to believe that serious gender issues are relevant to the field of physics. The correlation between sexual harassment and physics GPA, though weaker, could also have a dramatic impact on female students' professional role confidence and their decisions to continue to pursue a career in physics. Recently, a longitudinal study on women's building of professional identity while earning a Bachelor's degree in engineering found many of the female participants experienced hostile sexism, sexual harassment, and isolation in their summer internships. These interactions during a professional training lead them to question engineering being the right "fit" for them [116]. Experiencing and observing sexual harassment may have a similar effect on young female physicists. Both experiencing a lack of fit and a depressed physics performance could be how sexual harassment affects underrepresentation of women in physics.

Discussions of underrepresentation of women in science during high school can have a positive effect on female students' persistence in physics [67]. Bystander intervention programs to prevent sexual violence towards women typ-

ically involve students discussing sexism and socialized gender-roles and how these concepts support a rape-prone culture and how to use social pressure to positively intervene in potentially harmful situations [17]. In recent psychology studies, these programs effectively increase intervention tendencies and reduce attitudes that support rape culture for both male and female students [15]. Furthermore, a survey of female science faculty found that effective chair leadership could mitigate the negative job outcomes due experiences of sexual harassment and gender discrimination [117]. Moving forward, we hope the evidence on the prevalence of sexual harassment compels the physics community to raise awareness of sexual harassment, create guidelines for respectful behavior and implement anti-harassment and bystander intervention training for all members of the community while evaluating the effectiveness of these programs. This will take strong leadership to steer the community towards addressing the chilly climate experienced by many undergraduate women in a quantitative, visible manner.

APPENDIX A
NONDESTRUCTIVE IMAGING OF AN ULTRACOLD LATTICE GAS

Nondestructive imaging of an ultracold lattice gas

Y. S. Patil, S. Chakram, L. M. Aycocock, and M. Vengalattore*

Laboratory of Atomic and Solid State Physics, Cornell University, Ithaca, New York 14853, USA

(Received 22 April 2014; published 24 September 2014)

We demonstrate the nondestructive imaging of a lattice gas of ultracold bosons. Atomic fluorescence is induced in the simultaneous presence of degenerate Raman sideband cooling. The combined influence of these processes controllably cycles an atom between a dark state and a fluorescing state while eliminating heating and loss. Through spatially resolved sideband spectroscopy following the imaging sequence, we demonstrate the efficacy of this imaging technique in various regimes of lattice depth and fluorescence acquisition rate. Our work provides an important extension of quantum gas imaging to the nondestructive detection, control, and manipulation of atoms in optical lattices. In addition, our technique can also be extended to atomic species that are less amenable to molasses-based lattice imaging.

DOI: [10.1103/PhysRevA.90.033422](https://doi.org/10.1103/PhysRevA.90.033422)

PACS number(s): 37.10.Jk, 03.67.-a, 03.75.Lm, 67.85.Hj

I. INTRODUCTION

The creation, control, and manipulation of ultracold atomic gases in tailored optical potentials has spurred enormous interest in harnessing these mesoscopic quantum systems for the realization of ultracold analogs of correlated electronic materials [1,2], studies of nonequilibrium dynamics in isolated quantum many-body systems [3], and quantum metrology [4]. The dilute nature of these gases and the weak interactions impose stringent restrictions on the energy, entropy, and means of manipulating and probing these systems. This has led to the development of techniques to cool and image these gases at ever increasing levels of precision and resolution. In this context, the *in situ* imaging of lattice gases at high spatial resolution has emerged as a powerful tool for the study of Hubbard models [5–8] and quantum information processing [9].

In this article, we demonstrate a two-photon imaging technique for ultracold lattice gases. The scheme relies on extracting fluorescence from the atoms while simultaneously cooling them to the lowest band of the lattice via Raman sideband cooling (RSC) [10–12]. Through a combination of sideband spectroscopy and time-of-flight measurements, we demonstrate broad regimes of fluorescence acquisition rates and lattice depths for which the imaging scheme preserves the spatial location and also retains the atoms in the ground vibrational state. As a result, this imaging scheme enables the imaging of atoms in shallow lattices with high fidelity. In addition, the two-photon scheme is less sensitive to details of atomic structure thereby permitting its extension to atomic species less amenable to molasses-based imaging.

II. IMPLEMENTATION OF THE IMAGING TECHNIQUE

The principle of the imaging sequence is depicted in Fig. 1. Raman sideband cooling is employed to cool individual atoms within an optical lattice to the lowest vibrational band while simultaneously pumping the atoms to the high field seeking state. In the case of ^{87}Rb atoms used in our study, this state is denoted by $|g\rangle = |F = 1, m_F = 1; \nu = 0\rangle$, where ν is the

vibrational state of the atom within a lattice site. Importantly, this state is a dark state with respect to the optical fields used for Raman cooling. As such, the atoms do not emit any fluorescence while in this ground state. Fluorescence is induced in these atoms by shining a circularly polarized (σ_-) beam resonant with the $F = 1 \rightarrow F' = 0$ (D2) transition. Simultaneous use of RSC mitigates the increase in temperature caused by this fluorescence beam by cycling the atoms back to $|g\rangle$. Due to this cycling, fluorescence can be repeatedly extracted from the atomic distribution while leaving the atom in its original state.

For the studies described below, we use three-dimensional (3D) optical lattices that are typically detuned $2\pi \times 160$ GHz from the $F = 1 \rightarrow F'$ (D2) transition of ^{87}Rb . The lattice provides both the confining potential as well as the coherent two-photon coupling required for sideband cooling [13]. In the absence of RSC, we measure a heating rate of 11 nK/ms due to the photon scattering from the near-resonant lattice. While this does not pose a limitation for the studies described in this work, this heating can be significantly reduced by employing separate optical fields to provide the lattice confinement and the Raman coupling.

Atoms are loaded into this lattice and initialized in the ground state $|g\rangle$ by a 10 ms period of RSC. Based on measurements of the atomic density within the lattice, we estimate filling fractions on the order of $f = 0.20$ – 0.25 . The average vibrational occupation number is measured using sideband spectroscopy to be $\langle n \rangle \leq 0.01$ for the entire range of lattice depths studied here. Fluorescence images are acquired by switching on the fluorescence beam at a variable intensity. The images are acquired within exposure times of up to 30 ms following which the number of atoms and temperature of the atomic distribution are measured using a combination of time-of-flight absorption imaging and sideband spectroscopy.

We perform sideband spectroscopy to accurately quantify local changes in temperature due to fluorescence imaging. For this, we employ a pair of counterpropagating beams detuned $2\pi \times 7.5$ GHz from the $F = 1 \rightarrow F'$ (D2) transition of ^{87}Rb . The beams are focused to an approximate waist of $8 \mu\text{m}$. The measured sideband asymmetry [14] allows a local extraction of the vibrational occupation number (Fig. 2). An oblique orientation of these beams with respect to the lattice coordinates ensures sensitivity of the sideband spectra

*mukundv@cornell.edu

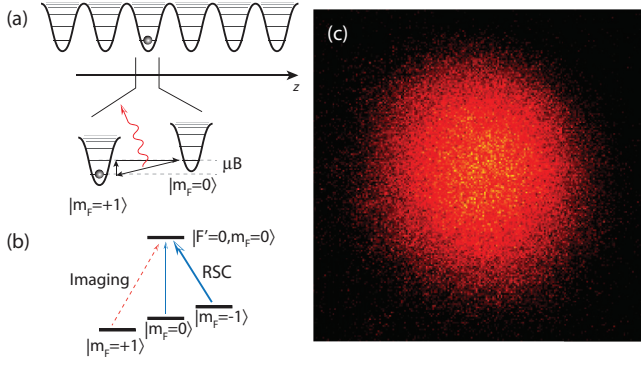


FIG. 1. (Color online) (a) Lattice imaging scheme: An atom within a lattice site is cooled to the ground state $|g\rangle \equiv |F=1, m_F=+1; \nu=0\rangle$ via RSC. An auxiliary imaging beam promotes the atom out of this state to a fluorescing state, which is subsequently cooled back to $|g\rangle$. Repeated cycles of this process extract fluorescence from the atom while continually restoring the atom to $|g\rangle$; (b) The near-resonance optical fields used in the imaging sequence. A cooling beam (RSC) with σ_+ and π components cools and optically pumps the atom into the dark state $|g\rangle$. A σ_- beam induces fluorescence by bringing the atom out of the dark state. (c) Raman fluorescence image of a gas of 1.5×10^6 atoms obtained within 15 ms. The field of view is $250 \mu\text{m} \times 250 \mu\text{m}$.

to atomic motion in all three dimensions. The two-photon pulses are typically $500 \mu\text{s}$ in duration with typical pump (probe) powers of $10 \mu\text{W}$ (20 nW). We have verified that the vibrational occupation number extracted from the sideband spectra is consistent with temperatures measured by time-of-flight imaging following a rapid ($< 1 \mu\text{s}$) extinction of the lattice [15]. Also, the observed width of the sidebands is consistent with our estimate of the coherent Raman coupling induced by the near-resonant lattice.

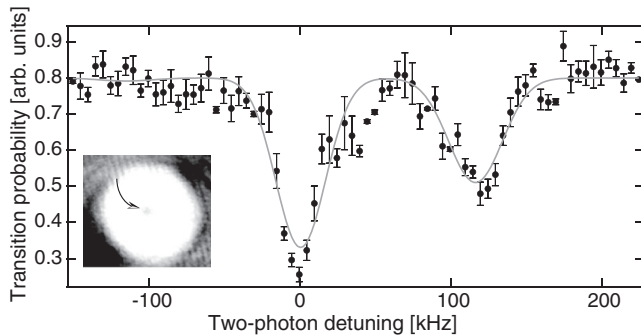


FIG. 2. Spatially resolved sideband spectroscopy of the lattice gas following the imaging sequence yielding $\langle n \rangle = 0.01^{+0.03}_{-0.01}$. Inset: A time-of-flight absorption image of the ultracold gas following an intense interrogation pulse at the two-photon resonance. The divot near the center of the atomic distribution shows the location and relative size of the beams used for sideband spectroscopy. The field of view is $600 \mu\text{m} \times 600 \mu\text{m}$.

III. DISCUSSION

Our imaging scheme, as constructed, relies on the competition between two processes: atomic fluorescence at a rate Γ_f that yields spatial information about the atomic distribution, and RSC at a cooling rate Γ_{RSC} that serves to cool the atoms back to the ground state within each lattice site. While the former depends solely on the intensity of the fluorescence beam, the latter is given by $\Gamma_{\text{RSC}} \sim \Gamma_{\text{opt}} \times \Omega_R^2 / (\Gamma_{\text{opt}}^2 + 2\Omega_R^2)$ where Ω_R is the coherent Raman coupling between the states $|m_F, \nu\rangle$ and $|m_F - 1, \nu - 1\rangle$, and Γ_{opt} is the rate of optical pumping to the $|m_F = +1\rangle$ state [16]. As the fluorescence rate is increased significantly beyond the cooling rate, atoms can be promoted to higher bands within the lattice and can tunnel to neighboring sites. In addition to modifying the atomic distribution, such tunneling can also lead to multiply occupied lattice sites and subsequent loss due to light-induced collisions.

To identify the regimes of imaging where the scheme is nondestructive, we use light-induced collisional loss as a diagnostic tool to monitor atomic tunneling across lattice sites. Further, in order to clearly demarcate atomic dynamics due to the fluorescence pulse from that due to RSC, we employ a pulsed imaging sequence wherein the fluorescence pulse and RSC are employed in rapid succession with a variable duty cycle. As expected, the average vibrational occupation number measured at the end of the fluorescence pulse grows with increasing fluorescence rate [Fig. 3(a)]. However, RSC is very efficient at cooling the atoms back to the ground state at the end of each cycle. At the end of each RSC cycle, we measure average vibrational occupation numbers (~ 0.01) that are, within our measurement uncertainty, indistinguishable from those measured in the absence of the fluorescence pulse (Fig. 2). The typical measured RSC cooling rates of $13 \mu\text{K/ms}$ are also consistent with that estimated based on the intensities of the lattice and optical pumping beams.

While simultaneous cooling during fluorescence acquisition leaves the final vibrational occupation unaltered, the transient increase in temperature during the fluorescence pulse can cause tunneling of atoms to neighboring lattice sites. This tunneling rate depends sensitively on both the average vibrational occupation number as well as the lattice depth U_0 , typically parametrized in units of the recoil energy $E_r = \hbar^2 k^2 / 2m$. At low rates of fluorescence acquisition [17], we observe that the total number of atoms is left unchanged subsequent to the imaging sequence indicating a negligible level of tunneling across sites. Beyond a certain fluorescence rate $\Gamma_{f, \text{max}}$, we observe two-body loss indicating the onset of tunneling of atoms [Fig. 3(b)]. As indicated by the rapid decrease of atoms for fluorescence rates past this maximal value, two-body loss is a very sensitive measure of the tunneling rates induced by the imaging sequence (see also Refs. [18,19]). The temporal evolution of the atom number following a brief, intense fluorescence pulse indicates that RSC cools and binds the atoms to the ground state of a lattice site within $100 \mu\text{s}$ [see inset of Fig. 3(b)], again consistent with measurements of the cooling rate.

We have performed Monte Carlo simulations of the imaging process that accurately capture the sensitivity of two-body loss to tunneling events and the threshold behavior arising from the competition of imaging, RSC, and tunneling. For the

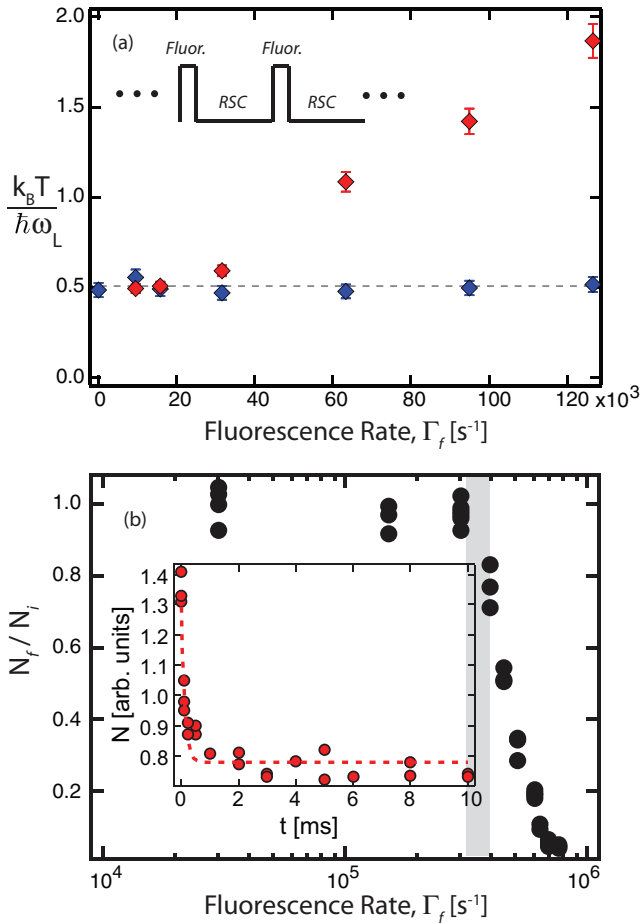


FIG. 3. (Color online) Regimes of fluorescence acquisition rates for non-destructive imaging. (a) Measured temperature of the lattice gas in a pulsed imaging sequence, in units of the vibrational frequency ω_L . The temperature during the fluorescence pulse grows (red) with increasing fluorescence rates while RSC rapidly cools the atoms back to the ground state (blue). (b) Measured atom number following the imaging sequence. At low fluorescence rates, the atom number is conserved indicating negligible levels of tunneling across sites. As the fluorescence rate is increased, the increasing temperature during the fluorescence pulse causes tunneling followed by light-induced loss. The shaded area represents the critical fluorescence rate for the onset of tunneling as identified by our measurements of light-induced loss. Inset: Evolution of atom number immediately following an intense fluorescence pulse ($\Gamma_f = 6 \times 10^5 \text{ s}^{-1}$) shows that RSC quickly (within $100 \mu\text{s}$) binds the atoms to the ground state of a lattice site thereby drastically suppressing tunneling.

filling fractions used in this work (0.20–0.25), the measured critical fluorescence rate, $\Gamma_{f, \text{max}}$, as identified by the onset of light-induced loss, is within 20% of the critical fluorescence rate for the onset of tunneling. We further find that the filling fraction needs to be reduced by more than an order of magnitude before there is a significant probability of tunneling events that do not lead to measurable loss. These findings justify the correspondence between the onset of tunneling in the lattice gas and our measured onset of two-body loss.

Similar considerations apply to the imaging of atoms in shallow optical lattices (Fig. 4). In this case, the rates of

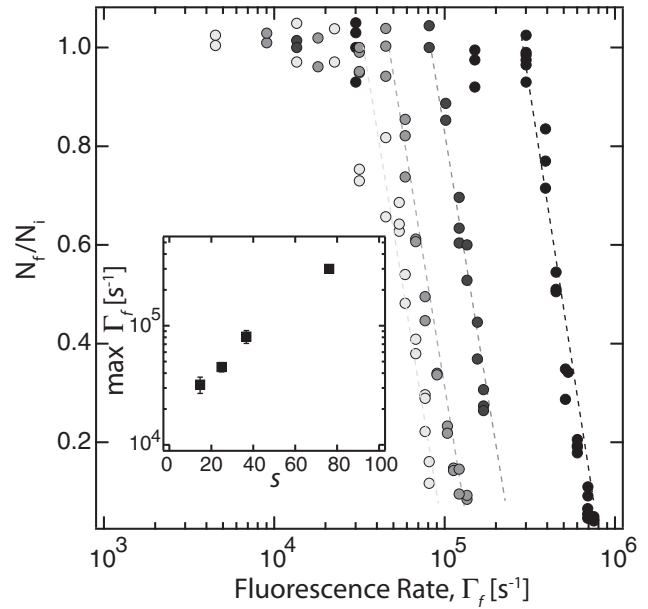


FIG. 4. The fraction of atoms remaining after the imaging sequence (N_f/N_i) vs fluorescence rates for lattice depths of $U_0/E_r = 14.6, 24.9, 36.7$ and 76.2 (left to right). Inset: An estimate of the maximum fluorescence acquisition rate $\Gamma_{f, \text{max}}$ per atom vs $s = U_0/E_r$.

tunneling grow exponentially with decreasing lattice depth [20,21]. This leads to a reduction of the maximal fluorescence rates that can be used while constraining atomic motion. As expected, an estimate of this maximum allowable fluorescence rate shows an exponential decrease with lower lattice depths (see inset of Fig. 4). Importantly, we see that fluorescence acquisition rates greater than 10^4 photons/s per atom are possible even for lattice depths around 15 recoil energies. This makes possible the use of this imaging technique to study lattice gases in regimes where coherent tunneling of atoms within the lowest band occurs on experimentally relevant time scales. In addition, it augurs the intriguing possibility of using this imaging scheme to influence or exert spatial control over such coherent tunneling processes. Nondestructive imaging of atoms in even lower lattice depths could be made possible by increasing the Raman cooling rates and operating at lower fluorescence acquisition rates.

At the lowest lattice depths, possible limitations to our imaging scheme include the reduced fidelity of RSC due to a lower Lamb-Dicke parameter and off-resonant Raman coupling to higher vibrational bands, an increased susceptibility to photon reabsorption heating [22], and faster rates of tunneling to neighboring lattice sites. As we show in Fig. 4, these limitations can be overcome by a suitable choice of fluorescence acquisition rate and Raman cooling rates. Already, the lowest lattice depth ($s \sim 15$) for which we demonstrate nondestructive imaging is more than two orders of magnitude below that required for molasses-based lattice imaging.

IV. CONCLUSIONS

In summary, we demonstrate a nondestructive imaging technique for ultracold atoms confined in an optical lattice.

The imaging technique is based on extracting fluorescence while simultaneously cooling the atoms to the ground state of the lattice via Raman sideband cooling. Using a combination of sideband spectroscopy and time-of-flight imaging, we demonstrate a large operational regime of fluorescence acquisition rates and lattice depths for which the imaging scheme preserves the spatial location of the atoms while leaving them in the ground vibrational state. At the largest rates of fluorescence acquisition ($\sim 10^6$ photons/s/atom) and the lowest lattice depths, the main loss mechanism occurs due to tunneling of atoms to occupied lattice sites followed by rapid light-induced loss. By using the light-induced loss as a diagnostic measure of tunneling, we show that this limitation can be alleviated by a suitable choice of fluorescence and Raman cooling rates. That said, we note that the imaging scheme demonstrated here does lead to light-induced loss in lattice sites occupied by multiple atoms. In this regard, it is similar to molasses-based imaging in its sensitivity to the parity of lattice occupancy.

Our imaging technique represents a powerful extension of lattice imaging to the nondestructive control and measurement of lattice gases. As such, it is an enabling technique to extend concepts of single-particle quantum control to the context of strongly correlated many-body systems. This scheme also permits the continuous monitoring of the out-of-equilibrium

dynamics of ultracold lattice gases. We also note that while used primarily as a diagnostic tool here, spatially resolved coherent two-photon processes such as the setup used for sideband spectroscopy in our work, can also be used for subdiffraction limited quantum control of the lattice gas [23,24]. Lastly, our imaging scheme is also extendable to atomic species that are less amenable to molasses-based lattice imaging as well as to lattice geometries [25] where molasses-based imaging can be stymied by local polarization gradients.

ACKNOWLEDGMENTS

This work was supported by the ARO MURI on Non-equilibrium Many-body Dynamics (63834-PH-MUR), the DARPA QuASAR program through a grant from the ARO and the Cornell Center for Materials Research with funding from the NSF MRSEC program (DMR-1120296). L.M.A. acknowledges support from a NSF graduate research fellowship. M.V. acknowledges support from the Alfred P. Sloan Foundation. M.V. conceptualized the imaging scheme; M.V., S.C., and L.M.A. contributed to the development of the apparatus; Y.S.P. and M.V. performed the experiments, the data analysis and the simulations; M. V. wrote the paper with help from Y.S.P. and S.C.

-
- [1] M. Lewenstein, A. Sanpera, V. Ahufinger, B. Damski, A. Sen, and U. Sen, *Adv. Phys.* **56**, 243 (2007).
- [2] I. Bloch, J. Dalibard, and W. Zwerger, *Rev. Mod. Phys.* **80**, 885 (2008).
- [3] A. Polkovnikov, K. Sengupta, A. Silva, and M. Vengalattore, *Rev. Mod. Phys.* **83**, 863 (2011).
- [4] B. J. Bloom, T. L. Nicholson, J. R. Williams, S. L. Campbell, M. Bishof, X. Zhang, W. Zhang, S. L. Bromley, and J. Ye, *Nature (London)* **506**, 71 (2014).
- [5] W. S. Bakr, J. I. Gillen, A. Peng, S. Fölling, and M. Greiner, *Nature (London)* **462**, 74 (2009).
- [6] N. Gemelke, X. Zhang, C. L. Hung, and C. Chin, *Nature (London)* **460**, 995 (2009).
- [7] P. Würtz, T. Langen, T. Gericke, A. Koglbauer, and H. Ott, *Phys. Rev. Lett.* **103**, 080404 (2009).
- [8] J. F. Sherson, C. Weitenberg, M. Endres, M. Chaneau, I. Bloch, and S. Kuhr, *Nature (London)* **467**, 68 (2010).
- [9] K. D. Nelson, X. Li, and D. S. Weiss, *Nature Phys.* **3**, 556 (2007).
- [10] V. Vuletić, C. Chin, A. J. Kerman, and S. Chu, *Phys. Rev. Lett.* **81**, 5768 (1998).
- [11] S. E. Hamann, D. L. Haycock, G. Klose, P. H. Pax, I. H. Deutsch, and P. S. Jessen, *Phys. Rev. Lett.* **80**, 4149 (1998).
- [12] D. J. Han, S. Wolf, S. Oliver, C. McCormick, M. T. DePue, and D. S. Weiss, *Phys. Rev. Lett.* **85**, 724 (2000).
- [13] A. J. Kerman, V. Vuletić, C. Chin, and S. Chu, *Phys. Rev. Lett.* **84**, 439 (2000).
- [14] C. Monroe, D. M. Meekhof, B. E. King, S. R. Jefferts, W. M. Itano, D. J. Wineland, and P. Gould, *Phys. Rev. Lett.* **75**, 4011 (1995).
- [15] For very large atom numbers ($\sim 10^8$) where the atomic cloud size is commensurate with that of the lattice waist, the time-of-flight measurements indicate slightly elevated temperatures in comparison to that extracted from the local sideband spectra. This is presumably due to the inhomogeneous variation of lattice frequencies across the atomic distribution and a reduced efficacy of RSC for atoms on the periphery. In such cases, we rely on the sideband spectra for a more reliable estimate of the temperature.
- [16] C. Cohen-Tannoudji, J. Dupont-Roc, and G. Grynberg, *Atom Photon Interactions* (Wiley-Interscience, New York, 1998).
- [17] The fluorescence rate is calibrated by the measured rate of Raman fluorescence acquired by the camera, and a geometrical estimate of the numerical aperture of our imaging system. This calibration is very close to the rate estimated from the measured intensity and detuning of the fluorescence beam.
- [18] N. Syassen, D. M. Bauer, M. Lettner, T. Volz, D. Dietze, J. J. Garcia-Ripoll, J. I. Cirac, G. Rempe, and S. Dürr, *Science* **320**, 1329 (2008).
- [19] B. Yan, S. A. Moses, B. Gadway, J. P. Covey, K. R. A. Hazzard, A. M. Rey, D. S. Jin, and J. Ye, *Nature (London)* **501**, 521 (2013).
- [20] D. Jaksch, C. Bruder, J. I. Cirac, C. W. Gardiner, and P. Zoller, *Phys. Rev. Lett.* **81**, 3108 (1998).
- [21] W. Zwerger, *J. Opt. B* **5**, S9 (2003).
- [22] S. Wolf, S. J. Oliver, and D. S. Weiss, *Phys. Rev. Lett.* **85**, 4249 (2000).
- [23] K. S. Johnson, J. H. Thywissen, N. H. Dekker, K. K. Berggren, A. P. Chu, R. Younkin, and M. Prentiss, *Science* **280**, 1583 (1998).
- [24] A. V. Gorshkov, L. Jiang, M. Greiner, P. Zoller, and M. D. Lukin, *Phys. Rev. Lett.* **100**, 093005 (2008).
- [25] P. Windpassinger and K. Sengstock, *Rep. Prog. Phys.* **76**, 086401 (2013).

APPENDIX B
VISUALIZING EDGE STATES WITH AN ATOMIC BOSE GAS IN THE
QUANTUM HALL REGIME

QUANTUM SIMULATION

Visualizing edge states with an atomic Bose gas in the quantum Hall regime

B. K. Stuhl,^{1*} H.-I. Lu,^{1*} L. M. Ayccock,^{1,2} D. Genkina,¹ I. B. Spielman^{1†}

Bringing ultracold atomic gases into the quantum Hall regime is challenging. We engineered an effective magnetic field in a two-dimensional lattice with an elongated-strip geometry, consisting of the sites of an optical lattice in the long direction and of three internal atomic spin states in the short direction. We imaged the localized states of atomic Bose-Einstein condensates in this strip; via excitation dynamics, we further observed both the skipping orbits of excited atoms traveling down the system's edges, analogous to edge magnetoplasmons in two-dimensional electron systems, and a dynamical Hall effect for bulk excitations. Our technique involves minimal heating, which will be important for spectroscopic measurements of the Hofstadter butterfly and realizations of Laughlin's charge pump.

In solids, the quantum Hall effects represent an extreme quantum limit, at which a system's behavior defies description by classical physics. The integer quantum Hall effect (IQHE) for two-dimensional (2D) electronic systems in magnetic fields (1) was the first topo-

logical insulator (2): a bulk insulator with conducting edge states, always present in finite-sized topological systems, which produce the IQHE's signature quantized Hall resistance (3).

In classical systems, the magnetic field acts entirely through the Lorentz force, whereas in quantum systems, a particle with charge q in a uniform field B additionally acquires an Aharonov-Bohm phase $\phi_{AB}/2\pi = AB/\Phi_0$, after its path encircles an area A normal to B . (Here, $\Phi_0 = 2\pi\hbar/q$ is the flux quantum, and $2\pi\hbar$ is Planck's constant.) We generated an effective magnetic field in a system of cold

atoms, following (4), which yielded an elongated 2D square lattice formed from the sites of an optical lattice in the long direction and three internal atomic spin states in the short direction (a synthetic "spatial" dimension). We directly controlled the phases acquired as atoms traversed the lattice, creating an aggregate tunneling phase $\phi_{AB}/2\pi \approx 4/3$ around each lattice plaquette. These phases take the place of the Aharonov-Bohm phases produced by true magnetic fields and suffice to fully define the effective magnetic field. Aharonov-Bohm phases of order unity in the Harper-Hofstadter Hamiltonian, currently realized in engineered materials (5, 6) and in atomic (7–12) and optical (13) settings, fragment the low-field Landau levels into the fractal energy bands of the Hofstadter butterfly (14). Such Hofstadter bands are generally associated with a nonzero topological index, the Chern number (3).

Topologically nontrivial bulk properties are reflected by the presence of edge channels, composed of edge states, with quantized conductance. In fermionic systems, the number of edge channels is fixed by the aggregate topological index of the filled bands (2, 3, 15); this ultimately gives rise to phenomena such as the IQHE for electrons. Conceptually, the constituent edge states can be viewed as skipping orbits (2, 16, 17): In the presence of a strong magnetic field, nascent cyclotron orbits near the boundary reflect from the hard wall before completing a revolution, leading to skipping trajectories that follow the system's boundary. In contrast, localized bulk states correspond to closed cyclotron orbits.

By applying large effective fields to atomic Bose-Einstein condensates (BECs), we directly imaged individual, deterministically prepared bulk and edge eigenstates. In IQHE systems, these states

¹Joint Quantum Institute (JQI), National Institute of Standards and Technology (NIST) and University of Maryland, Gaithersburg, MD 20899, USA. ²Department of Physics, Cornell University, Ithaca, NY 14850, USA. *These authors contributed equally to this work. †Corresponding author. E-mail: ian.spielman@nist.gov

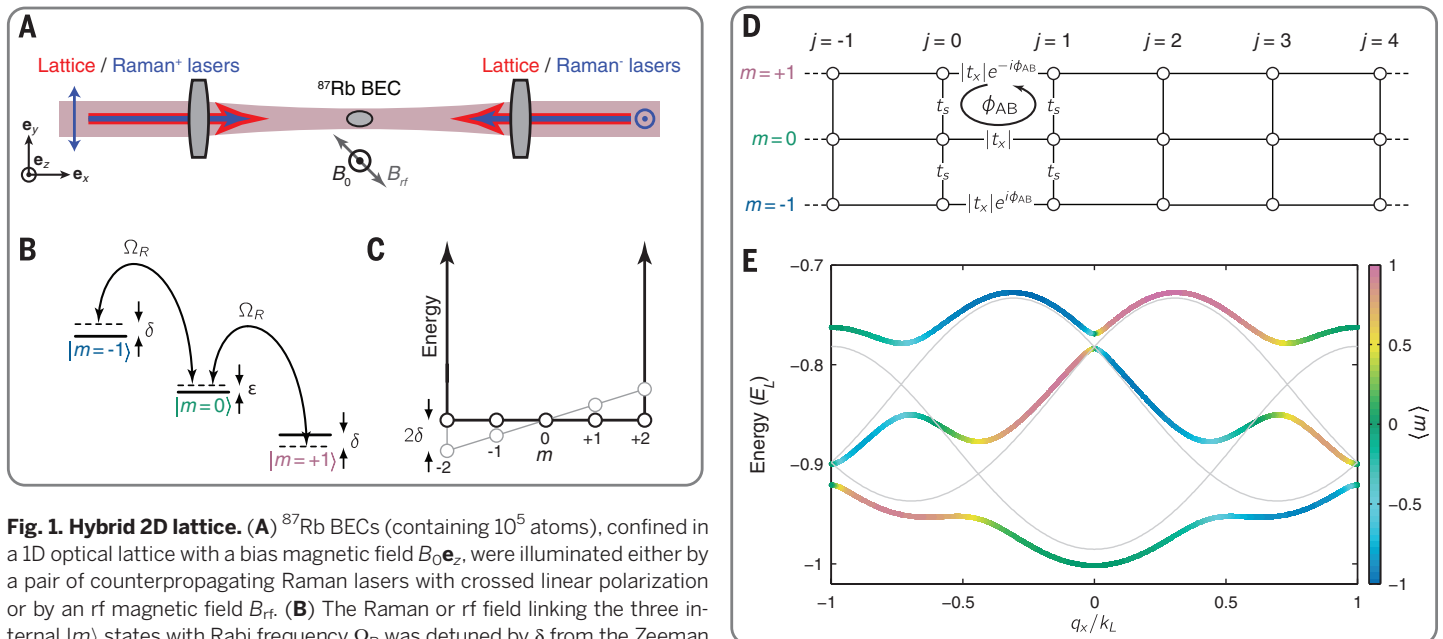


Fig. 1. Hybrid 2D lattice. (A) ⁸⁷Rb BECs (containing 10^5 atoms), confined in a 1D optical lattice with a bias magnetic field $B_0 \mathbf{e}_z$, were illuminated either by a pair of counterpropagating Raman lasers with crossed linear polarization or by an rf magnetic field B_{rf} . (B) The Raman or rf field linking the three internal $|m\rangle$ states with Rabi frequency Ω_R was detuned by δ from the Zeeman splitting ($g\mu_B B_0/h \approx 0.817$ MHz or 1.35 MHz; g , the Landé g -factor; h , Planck's constant). The corresponding quadratic Zeeman shift lowered $|m=0\rangle$ by $\epsilon = 0.05E_L$ (for the data in Fig. 3) or $0.13E_L$ (for the data in Fig. 4). The Raman lasers' relative phases were actively stabilized at a beam combiner adjacent to the optical-lattice retroreflection mirror (24). (C) The lattice along \mathbf{e}_s can be considered as a square well with hard walls at $m = \pm 2$, for which $\delta \neq 0$ tilts the potential. (D) The 2D lattice structure, where the nonspatial dimension is built from the internal states $|m\rangle$, with an effective magnetic flux per plaquette of $\Phi/\Phi_0 = \phi_{AB}/2\pi$. (E) The three lowest magnetic bands (rainbow colors), computed for our full lattice without making the tight-binding approximation, with parameters $(\hbar\Omega_R, V, \delta, \epsilon) = (0.141, 6, 0, 0.05)E_L$. The pale curves represent computations for $\hbar\Omega_R = 0$.

would govern the conductivity, but as individual eigenstates, they exhibit no time dependence. The corresponding dynamical entities are edge magnetoplasmons, consisting of superpositions of edge eigenstates in different Landau levels (18, 19) or, in this case, magnetic bands. We launched these excitations and recorded their full motion, observing both a chiral drift along the system's edge and the underlying skipping motion.

The Harper-Hofstadter Hamiltonian

$$H = - \sum_{j,m} [t_x |j+1, m\rangle \langle j, m| + t_s |j, m+1\rangle \langle j, m| + \text{h.c.}] \quad (1)$$

governs the motion of charged particles moving in a 2D lattice (14, 20)—i.e., the situation that we engineered for our neutral atoms—with complex hopping amplitudes t_x (long direction) and t_s (short direction) and sites labeled by j and m (h.c., Hermitian conjugate). Analogous to the Landau gauge in continuum systems, we describe our ex-

periment with real t_s (no phase) and with complex $t_x = |t_x| \exp(-i\phi_{AB} m)$, dependent on m . The sum of the tunneling phases around any individual plaquette is ϕ_{AB} (Fig. 1D).

We created a 2D lattice by combining a conventional optical lattice (21) to define the long axis of our system (\mathbf{e}_x direction, sites labeled by j) with three sequentially coupled internal spin states to define the short axis (\mathbf{e}_s direction, three sites labeled by $m \in \{-1, 0, +1\}$); in parallel to the work described here, an analogous scheme has been realized for fermionic ytterbium (12). This system effectively has an infinite repulsive potential for $|m| \geq 2$ (Fig. 1C), allowing for the formation of robust edge states. In each band of our engineered lattice (Fig. 1E), the momentum along \mathbf{e}_x specifies the position in \mathbf{e}_s (denoted by color on the curves), as for 2D electrons in Landau levels.

We used ^{87}Rb BECs in the $f = 1$ ground-state hyperfine manifold (22), confined in an optical dipole potential from two 1064-nm laser beams aligned along \mathbf{e}_x and \mathbf{e}_y , with trap frequencies $(\omega_x, \omega_y, \omega_z)/2\pi = (50, 40, 110)$ Hz (Fig. 1, A and B). We adiabatically (23) loaded these BECs onto the

sites of the 1D optical lattice, formed by a pair of laser beams (wavelength, $\lambda_L = 1064.46$ nm) counterpropagating along \mathbf{e}_x . The motion of atoms along \mathbf{e}_y and \mathbf{e}_z within each 2D layer formed by the 1D optical lattice was largely unaltered by the presence of the lattice, which only affected motion along \mathbf{e}_x . The lattice lasers' wavelength defines the single-photon recoil momentum $\hbar k_L = 2\pi\hbar/\lambda_L$ and recoil energy $E_L = \hbar^2 k_L^2 / 2m_{\text{Rb}}$, where \hbar is the reduced Planck's constant, and m_{Rb} is the atomic mass. The lattice depth $V \approx 6E_L$ gave a hopping strength $|t_x| \approx 0.05E_L$ along \mathbf{e}_x .

We then coupled the three $|m\rangle$ sublevels, either with two-photon Raman transitions or with a radio-frequency (rf) magnetic field. The Raman lasers ($\lambda_R = 790.04$ nm) also counterpropagated approximately along \mathbf{e}_x (24), with wavenumber $k_R = \pm 2\pi/\lambda_R$; the rf coupling effectively had a k_R of 0. Either field produced a laboratory-tunable effective tunneling strength $|t_s| \sim |t_x|$ along \mathbf{e}_s , proportional to the Rabi frequency Ω_R . The $2\hbar k_R$ momentum imparted from these transitions resulted in a spatially periodic phase factor $\exp(i2k_R x) = \exp(i\phi_{AB} j)$ accompanying the change in m , where $\phi_{AB}/2\pi = k_R/k_L \approx \pm 4/3$ for Raman coupling, and $\phi_{AB}/2\pi = 0$ for rf coupling (25, 4). The sign of ϕ_{AB} was controlled by reversing the relative detuning of the Raman lasers (Fig. 1, A and B), effectively swapping the laser directions.

Figure 1E shows the band structure for our system, featuring the three Hofstadter bands expected for $\phi_{AB}/2\pi \sim 4/3$, with our boundary conditions. The system is most easily understood after making the local gauge transformation $|j, m\rangle \rightarrow \exp(-i\phi_{AB} j m) |j, m\rangle$, which transfers the Peierls phase from t_s into t_x . This fully maps our system to Eq. 1 and results in an effective flux $\Phi/\Phi_0 = \phi_{AB}/2\pi$ per plaquette (Fig. 1D).

We began our experiments by directly imaging adiabatically loaded eigenstates of the ground Hofstadter band with either $\phi_{AB}/2\pi = 0$ or $\phi_{AB}/2\pi \approx 4/3$, in an isotropic lattice with $|t_x| \approx |t_s|$. After preparation, we used a measurement procedure common to all experiments: We simultaneously removed all potentials and coupling fields (with a turnoff time $t_{\text{off}} < 1 \mu\text{s}$), which returned the atoms to bare spin and momentum states. The atomic cloud expanded for an ~ 18 -ms time-of-flight (TOF) period (21). During TOF, a 2-ms magnetic gradient pulse was applied, and Stern-Gerlach spin separation was used to separate the three $|m\rangle$ states. The resulting 2D column density was recorded using standard absorption imaging techniques, giving the normalized momentum distributions $n_m(k_x)$ with perfect single-lattice site resolution along \mathbf{e}_s .

Figure 2A shows typical data for $\phi_{AB} = 0$, under which conditions we adiabatically loaded the BEC into the ground state and observed $n_m(k_x)$. The fractional population $n_m = \int dk_x n_m(k_x)$ (Fig. 2B) resembles that of a particle in a discretized box along \mathbf{e}_s , whereas the momentum distributions, typical for atoms in an optical lattice (26), have the same profile for each m site. This demonstrates that the two directions are uncoupled at $\phi_{AB} = 0$.

The data in Fig. 2, C to E, for which $\phi_{AB} \neq 0$, are qualitatively different as a function of both k_x

Fig. 2. Adiabatically loaded eigenstates.

(Left panels) Site-resolved normalized momentum distributions $n_m(k_x)$ obtained by absorption imaging. (Right panels) Fractional population n_m . (A and B) Atoms loaded into the single ground state present for $\phi_{AB} = 0$ show the expected separable behavior along \mathbf{e}_x and \mathbf{e}_s . (C to H) Atoms loaded into the upper-edge, bulk, and lower-edge states (top, middle, and bottom panels, respectively) present for $\phi_{AB}/2\pi \approx 4/3$ demonstrate the coupling between \mathbf{e}_x and \mathbf{e}_s and the localization along \mathbf{e}_s .

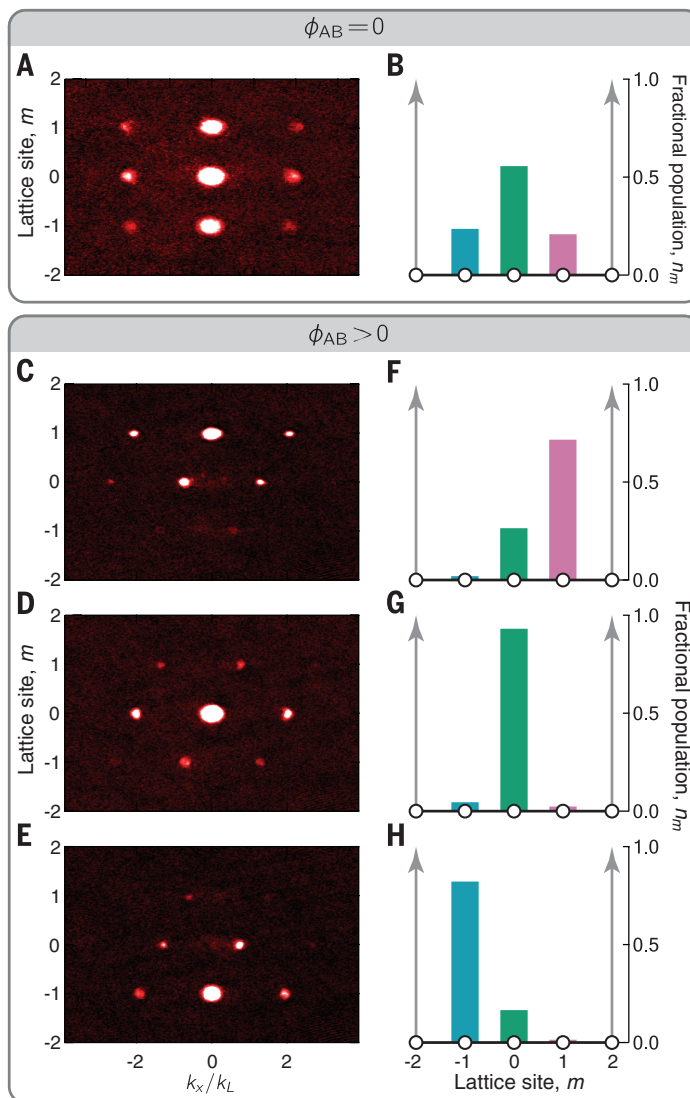
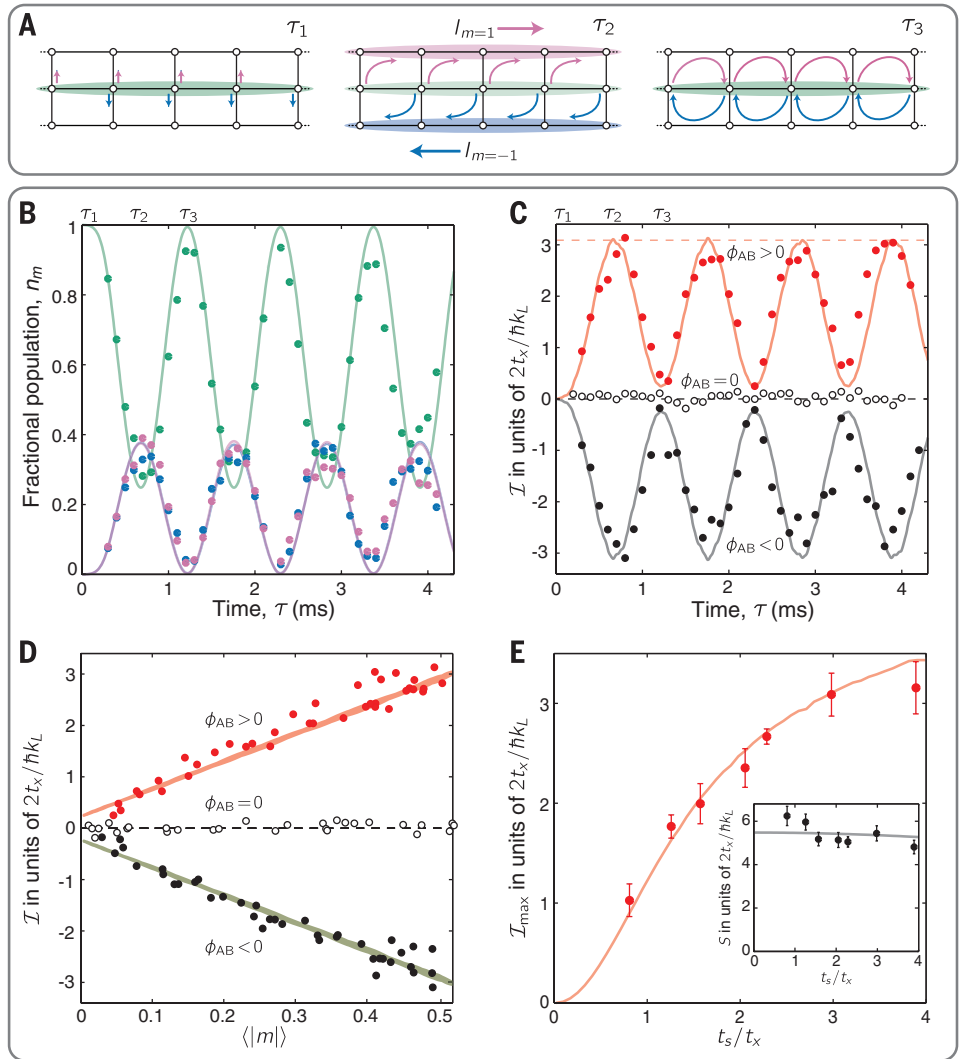


Fig. 3. Chiral edge currents. (A) Schematic of system dynamics: A system prepared on site $m = 0$ at time $\tau_1 = 0$ obtains a chiral edge current at τ_2 , which returns to zero at τ_3 . (B) Measured fractional population versus time for atoms initialized on $m = 0$ at time $\tau = 0$. The dynamics are the same for positive and negative values of ϕ_{AB} . Colors in (A) and (B) correspond to m sites, as in Figs. 1 and 2. (C) Chiral edge current \mathcal{I} versus time. Data shown in red, black, and open circles correspond to positive, negative, and zero values of ϕ_{AB} , respectively. (D) \mathcal{I} plotted against $\langle |m| \rangle$. The solid curves (theory) use parameters $(\hbar\Omega_R, V, \delta, \epsilon) = (0.52, 6, 0.001, 0.05)E_L$, determined from the data in (B) for $\phi_{AB} \neq 0$ and giving $t_s = 0.14E_L$, and parameters $(\hbar\Omega_R, V, \delta, \epsilon) = (0.33, 6, -0.01, 0.05)E_L$ for $\phi_{AB} = 0$. (E) Maximum edge current versus asymmetry (t_s/t_x). (Inset) Slope S [taken from data as in (D)] is nearly independent of t_s/t_x .



and m . These differences can be understood by analogy with a 2D electron system in a perpendicular magnetic field, confined in one dimension with hard walls. Along the confined direction, the wavefunction is localized to the scale of the magnetic length $\ell_B = \sqrt{\hbar/qB}$, with the center position at $k_x \ell_B^2$ in the bulk state, and where $\hbar k_x$ is the electron's canonical momentum. At large $|k_x|$, the electron becomes localized near the edges, lifting the degeneracy of the otherwise macroscopically degenerate Landau levels. Each of these points has an analog in our observations (Fig. 1E and Fig. 2, F to H). In our system, the magnetic length $\ell_B \sim \sqrt{3/2\pi} \approx 0.7$, in units of lattice period, was of order unity (23); this considerably narrowed the bulk state (Fig. 2G), as compared with conditions in which $\phi_{AB} = 0$ (Fig. 2B). In addition, we observed the appearance of states that were localized at the system's edges (Fig. 2, F and H), which were completely absent when $\phi_{AB} = 0$. These localized edge states are the analog to the current-carrying edge states in fermionic IQHE systems (27).

Having described the static properties of this system, we now turn to dynamics. We loaded our system onto different m sites with $t_s = 0$ and then

abruptly (24) turned on t_s , allowing tunneling along \mathbf{e}_x . The resulting initial states all consisted of coherent superpositions of magnetic-band eigenstates with crystal momentum $q_x/k_L = -m\phi_{AB}/\pi$, which began to coherently tunnel along \mathbf{e}_x , and to move along \mathbf{e}_x as a result of the associated Lorentz force. Atoms initialized on the bulk $m = 0$ site exhibited a dynamic Hall effect. Those starting on the edge sites became cold-atom analogs to edge magnetoplasmons: They began cyclotron orbits, were reflected from the hard wall, and skipped down one edge or the other.

The dynamics of atoms initialized in the bulk state (on the $m = 0$ site) are presented in Fig. 3. As schematically illustrated in Fig. 3A and plotted in Fig. 3B, a balanced population oscillated in and out of the originally empty $m = \pm 1$ sites, as a function of time τ . When $\phi_{AB} \neq 0$, this motion drove transverse (i.e., Hall) edge currents $I_{m=\pm 1}(\tau) = n_m(\tau) \langle V_m \rangle$ along \mathbf{e}_x (Fig. 3A), where $\langle V_m \rangle$ is the mean velocity of atoms on site m along \mathbf{e}_x .

A chiral current $\mathcal{I} = I_1 - I_{-1}$ developed, with its overall sign following that of ϕ_{AB} (Fig. 3C). As atoms tunneled to the edges, they acquired a transverse velocity controlled by two parameters: ϕ_{AB} determined the crystal momentum

acquired while tunneling, and t_x set the natural unit of velocity $2t_x/\hbar k_L$. This led to the observed in-phase oscillation of \mathcal{I} and the combined $m = \pm 1$ populations $\langle |m| \rangle$.

This synchronous oscillation implies a linear dependence of \mathcal{I} on $\langle |m| \rangle$, the slope S of which is plotted in red and black symbols in Fig. 3D. We confirmed the system's chirality by inverting ϕ_{AB} and verifying that S changed in sign. For comparison, we repeated the experiment with $\phi_{AB} = 0$ and observed no chiral current (open symbols). These data are in good agreement with our theory (solid curves in Fig. 3D), which uses parameters obtained from fits to Fig. 3B (24).

The dependence of the chiral current on the tunneling anisotropy t_s/t_x (Fig. 3E) is reminiscent of the optical lattice experiments in (28). The chiral current remained linear in $\langle |m| \rangle$, with an essentially constant slope $S \approx 2t_x \lambda_1 \sin(\phi_{AB})/\hbar$; this demonstrates a dynamic Hall effect (29) governed by the magnetic flux and the optical lattice strength and period (24). In contrast, the peak edge current \mathcal{I}_{\max} (pink dashed line in Fig. 3C) strongly depends on t_s/t_x (Fig. 3E), increasing from zero and then reaching saturation. For small t_s/t_x , few atoms tunneled, giving a correspondingly small

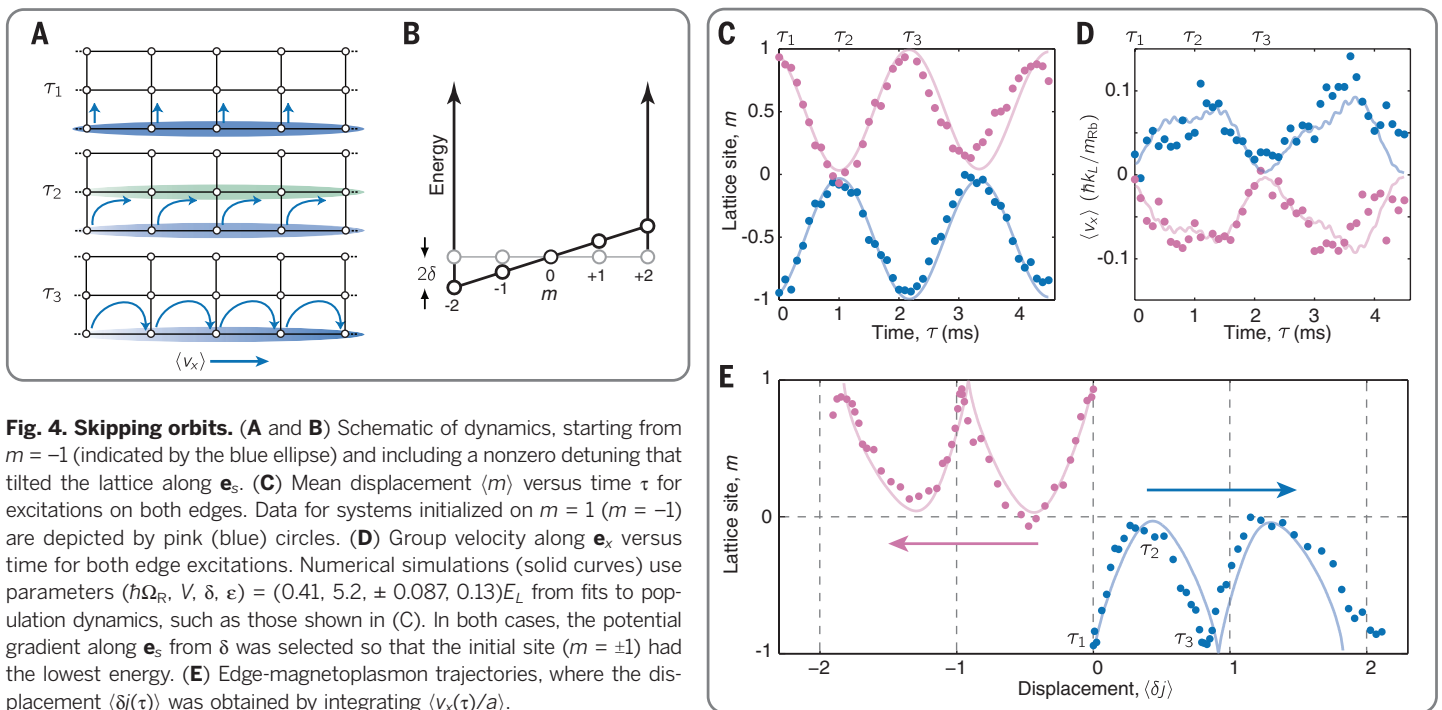


Fig. 4. Skipping orbits. (A and B) Schematic of dynamics, starting from $m = -1$ (indicated by the blue ellipse) and including a nonzero detuning that tilted the lattice along \mathbf{e}_s . (C) Mean displacement $\langle m \rangle$ versus time τ for excitations on both edges. Data for systems initialized on $m = 1$ ($m = -1$) are depicted by pink (blue) circles. (D) Group velocity along \mathbf{e}_x versus time for both edge excitations. Numerical simulations (solid curves) use parameters $(\hbar\Omega_r, V, \delta, \epsilon) = (0.41, 5.2, \pm 0.087, 0.13)E_L$ from fits to population dynamics, such as those shown in (C). In both cases, the potential gradient along \mathbf{e}_s from δ was selected so that the initial site ($m = \pm 1$) had the lowest energy. (E) Edge-magnetoplasmon trajectories, where the displacement $\langle \delta j(\tau) \rangle$ was obtained by integrating $\langle v_x(\tau) \rangle$.

\mathcal{I}_{\max} ; as t_s/t_x increased, \mathcal{I}_{\max} began to saturate as essentially all atoms tunneled (27).

We then shifted our focus from bulk excitations to edge excitations, which we studied by launching edge magnetoplasmons, or superpositions of edge states across magnetic bands with crystal momentum $q_x/k_L = \mp\phi_{AB}/\pi$. We created them on either edge, with the potential tilted along \mathbf{e}_s (Fig. 4, A and B), so that the initially occupied site was at the potential minimum. The time-evolving average position $\langle m(\tau) \rangle$ along \mathbf{e}_s and the velocity $\langle v_x(\tau) \rangle = \sum_m I_m$ along \mathbf{e}_x are shown in Fig. 4, C and D. Data shown in pink and blue solid circles are for initial sites $\langle m(\tau = 0) \rangle = \pm 1$, both of which evolved periodically in time but with opposite velocities. The spatial trajectories are illustrated in Fig. 4E; we obtained the displacement $\langle \delta j(\tau) \rangle$ by directly integrating $\langle v_x(\tau)/a \rangle$, where $a = \lambda_L/2$ is the lattice period. These data show edge magnetoplasmons with their chiral longitudinal motion and constitute an experimental observation of their edge localization and transverse skipping motion.

This and related approaches (12) have a practical advantage over other techniques for creating artificial gauge fields, in that minimal Raman-laser coupling is required [typically 10 to 50 times less than in previous experiments using Raman coupling (30)], thereby minimizing heating from spontaneous emission and enabling many-body experiments that require negligible heating rates. Lifetimes from spontaneous emission with this technique are in excess of 10 s (corresponding to a heating rate of $<10^{-3} t_x/2\pi\hbar$), whereas other approaches for creating large artificial gauge fields have lifetimes well below 1 s (8–10, 31).

The experiments described here used nearly pure BECs, either in adiabatically prepared eigen-

states or evolving after sudden changes to the Hamiltonian. In the former case, interactions did not affect our measurements, whereas in the latter case, collisions during the dynamical evolution gradually populated additional states and contributed to considerable dephasing within 10 ms. Because our approach of using the internal atomic spin states as lattice sites involves different “synthetic sites” residing in the same location in space, the interactions between atoms are anisotropic—short-ranged along \mathbf{e}_x but long-ranged along \mathbf{e}_s . In (32), it was shown theoretically that even such anisotropic systems can support fractional quantum Hall states.

With our hard-wall potential, a realization of the Laughlin charge pump (33) is straightforward: As particles accelerate along \mathbf{e}_s , mass moves from one edge to the other in the orthogonal direction \mathbf{e}_x . Extending our technique to periodic boundary conditions—i.e., coupling the $|m = \pm 1\rangle$ states—should produce systems exhibiting a fractal Hofstadter spectrum (4), even with only a three-site extent along \mathbf{e}_s . Going beyond conventional condensed-matter realities, the flexibility afforded by directly laser-engineering the hopping enables the creation of Möbius strip geometries, or topological systems with only one edge (34).

REFERENCES AND NOTES

- K. von Klitzing, G. Dorda, M. Pepper, *Phys. Rev. Lett.* **45**, 494–497 (1980).
- M. Z. Hasan, C. L. Kane, *Rev. Mod. Phys.* **82**, 3045–3067 (2010).
- D. J. Thouless, M. Kohmoto, M. P. Nightingale, M. den Nijs, *Phys. Rev. Lett.* **49**, 405–408 (1982).
- A. Celi et al., *Phys. Rev. Lett.* **112**, 043001 (2014).
- M. C. Geisler et al., *Phys. Rev. Lett.* **92**, 256801 (2004).
- B. Hunt et al., *Science* **340**, 1427–1430 (2013).
- D. Jaksch, P. Zoller, *New J. Phys.* **5**, 56 (2003).
- M. Aidelsburger et al., *Phys. Rev. Lett.* **111**, 185301 (2013).
- H. Miyake, G. A. Siviloglou, C. J. Kennedy, W. C. Burton, W. Ketterle, *Phys. Rev. Lett.* **111**, 185302 (2013).

- G. Jotzu et al., *Nature* **515**, 237–240 (2014).
- M. Aidelsburger et al., *Nat. Phys.* **11**, 162–166 (2015).
- M. Mancini et al., *Science* **349**, 1510–1513 (2015).
- M. Hafezi, S. Mittal, J. Fan, A. Migdall, J. M. Taylor, *Nat. Photonics* **7**, 1001–1005 (2013).
- D. R. Hofstadter, *Phys. Rev. B* **14**, 2239–2249 (1976).
- W. Beugeling, N. Goldman, C. Morais Smith, *Phys. Rev. B* **86**, 075118 (2012).
- M. Büttiker, *Phys. Rev. B* **38**, 9375–9389 (1988).
- G. Montambaux, *Eur. Phys. J. B* **79**, 215–224 (2011).
- K. Kern, D. Heitmann, P. Grambow, Y. H. Zhang, K. Ploog, *Phys. Rev. Lett.* **66**, 1618–1621 (1991).
- R. C. Ashoori, H. L. Stormer, L. N. Pfeiffer, K. W. Baldwin, K. West, *Phys. Rev. B* **45**, 3894–3897 (1992).
- P. G. Harper, *Proc. Phys. Soc. A* **68**, 879–892 (1955).
- O. Morsch, M. Oberthaler, *Rev. Mod. Phys.* **78**, 179–215 (2006).
- Y.-J. Lin, A. R. Perry, R. L. Compton, I. B. Spielman, J. V. Porto, *Phys. Rev. A* **79**, 063631 (2009).
- Because all physics is 2π -periodic in the acquired phase, our flux $\phi_{AB}/2\pi \approx 4/3$ is equivalent to $\phi_{AB} \approx 2\pi/3$. For the purpose of estimating the magnetic length, which is a continuum concept, it is suitable to use $l_B^* \approx \sqrt{3}/2l_B$.
- Materials and methods are available as supplementary materials on Science Online.
- O. Boada, A. Celi, J. I. Latorre, M. Lewenstein, *Phys. Rev. Lett.* **108**, 133001 (2012).
- M. Greiner, I. Bloch, O. Mandel, T. Hänsch, T. Esslinger, *Phys. Rev. Lett.* **87**, 160405 (2001).
- D. Hügél, B. Paredes, *Phys. Rev. A* **89**, 023619 (2014).
- M. Atala et al., *Nat. Phys.* **10**, 588–593 (2014).
- L. J. LeBlanc et al., *Proc. Natl. Acad. Sci. U.S.A.* **109**, 10811–10814 (2012).
- Y. J. Lin, R. L. Compton, K. Jiménez-García, J. V. Porto, I. B. Spielman, *Nature* **462**, 628–632 (2009).
- J. Struck et al., *Phys. Rev. Lett.* **108**, 225304 (2012).
- A. Petruscu, K. Le Hur, *Phys. Rev. B* **91**, 054520 (2015).
- R. Laughlin, *Phys. Rev. B* **23**, 5632–5633 (1981).
- O. Boada, A. Celi, J. Rodríguez-Laguna, J. I. Latorre, M. Lewenstein, *New J. Phys.* **17**, 045007 (2015).

ACKNOWLEDGMENTS

This work was partially supported by the Army Research Office’s Atomtronics Multidisciplinary University Research Initiative (MURI), the Air Force Office of Scientific Research’s Quantum

Matter MURI, NIST, and NSF (through the Physics Frontier Center at the JQI). B.K.S. is a NIST–National Research Council Postdoctoral Research Associate. L.M.A. was supported by the NSF Graduate Research Fellowship Program. All authors except I.B.S. contributed to the data collection effort. B.K.S. and L.M.A. configured the apparatus for this experiment. H.-I.L. led the team on all aspects of the edge-current and skipping-orbit measurements. H.-I.L., L.M.A., and B.K.S. analyzed data. B.K.S.,

H.-I.L., L.M.A. and I.B.S. performed numerical and analytical calculations. All authors contributed to writing the manuscript. I.B.S. proposed the initial experiment.

SUPPLEMENTARY MATERIALS

www.sciencemag.org/content/349/6255/1514/suppl/DC1
Materials and Methods

Supplementary Text
Fig. S1
Reference (35)
Database S1

9 February 2015; accepted 28 July 2015
10.1126/science.aaa8515

NANOMATERIALS

Atomically thin two-dimensional organic-inorganic hybrid perovskites

Letian Dou,^{1,2*} Andrew B. Wong,^{1,2*} Yi Yu,^{1,2,3*} Minliang Lai,¹ Nikolay Kornienko,^{1,2} Samuel W. Eaton,¹ Anthony Fu,^{1,2} Connor G. Bischak,¹ Jie Ma,² Tina Ding,^{1,2} Naomi S. Ginsberg,^{1,2,4,5,6} Lin-Wang Wang,² A. Paul Alivisatos,^{1,2,5,7} Peidong Yang^{1,2,5,7†}

Organic-inorganic hybrid perovskites, which have proved to be promising semiconductor materials for photovoltaic applications, have been made into atomically thin two-dimensional (2D) sheets. We report the solution-phase growth of single- and few-unit-cell-thick single-crystalline 2D hybrid perovskites of $(\text{C}_4\text{H}_9\text{NH}_3)_2\text{PbBr}_4$ with well-defined square shape and large size. In contrast to other 2D materials, the hybrid perovskite sheets exhibit an unusual structural relaxation, and this structural change leads to a band gap shift as compared to the bulk crystal. The high-quality 2D crystals exhibit efficient photoluminescence, and color tuning could be achieved by changing sheet thickness as well as composition via the synthesis of related materials.

The organic-inorganic hybrid perovskites, especially $\text{CH}_3\text{NH}_3\text{PbI}_3$, have recently been used in solution-processable photovoltaic devices that have reached 20% power conversion efficiency (1–4). These layered materials have a general formula of $(\text{RNH}_3)_2(\text{CH}_3\text{NH}_3)_{m-1}\text{A}_m\text{X}_{3m+1}$, where R is an alkyl or aromatic moiety, A is a metal cation, and X is a halide. The variable m indicates the number of the metal cation layers between the two layers of the organic chains (5–11). In the extreme case where $m = \infty$, the structure becomes a three-dimensionally bonded perovskite crystal with a structure similar to BaTiO_3 . In the opposite extreme where $m = 1$, the structure becomes an ideal quantum well with only one atomic layer of AX_4^{2-} separated by organic chains, in which the adjacent layers are held together by weak van der Waals forces.

This arrangement is fundamentally different from transition metal dichalcogenides, in which one layer of the metal ions is sandwiched between two hexagonal layers of S or Se atoms, affording a rigid backbone. In contrast, the lay-

ered hybrid perovskites normally have a tetragonal or orthorhombic structure and are inherently more flexible and deformable (5–11). By varying the value of m , the thickness and the related optoelectronic properties of the quantum well can be tuned. To date, many organic amines, metal cations (Cu^{2+} , Mn^{2+} , Cd^{2+} , Ge^{2+} , Sn^{2+} , Pb^{2+} , Eu^{2+} , etc.) and halides (Cl, Br, and I) have been used to construct such layered materials ($m = 1 \sim 3$), and their corresponding optoelectronic properties have been well studied (12–15). Previous reports have claimed that the organic layers effectively isolate the two-dimensional (2D) quantum wells in each layer from electronic coupling, if the organic chain is longer than propyl amine (16). This means that the properties of the atomically thin 2D quantum well should be the same as those of the bulk layered material (microscopic crystal, powder, or film). This hypothesis, as well as the technical difficulty of separating individual layers, has probably delayed investigation of free-standing single layers of such 2D materials. Very recently, attempts to obtain ultrathin 2D perovskite samples by spin coating, chemical vapor deposition, or mechanical exfoliation methods have been made with limited success (17–19).

Here we report the direct growth of atomically thin 2D hybrid perovskites $[(\text{C}_4\text{H}_9\text{NH}_3)_2\text{PbBr}_4]$ and derivatives from solution. Uniform square-shaped 2D crystals on a flat substrate with high yield and excellent reproducibility were synthesized by using a ternary co-solvent. We investigated the structure and composition of individual 2D crystals using transmission electron microscopy (TEM), energy-dispersive spec-

troscopy (EDS), grazing-incidence wide-angle x-ray scattering (GIWAXS), and Raman spectroscopy. Unlike other 2D materials, a structural relaxation (or lattice constant expansion) occurred in the hybrid perovskite 2D sheets that could be responsible for emergent features. We investigated the optical properties of the 2D sheets using steady-state and time-resolved photoluminescence (PL) spectroscopy and cathodoluminescence microscopy. The 2D hybrid perovskite sheets have a slightly shifted band edge emission that could be attributed to the structural relaxation. We further demonstrated that the as-grown 2D sheets exhibit high PL quantum efficiency as well as wide composition and color tunability.

A structural illustration of a monolayer 2D perovskite (Fig. 1A) shows the case with six Br atoms surrounding each Pb atom, and the four in-plane Br atoms are shared by two octahedrons, forming a 2D sheet of PbBr_4^{2-} . The negative charges are compensated for by the butylammonium that caps the surfaces of the 2D sheet. This structure is amenable to facile solution synthesis. The ionic character of such materials is stronger than the transition metal disulfides and diselenides, and the bulk solid is soluble in polar organic solvents such as dimethylformamide (DMF) (20). To grow 2D sheets, a very dilute precursor solution was dropped on the surface of a Si/SiO₂ substrate and dried under mild heating [see the supplementary materials (21)]. A DMF and chlorobenzene (CB) co-solvent was initially investigated, because CB helps to reduce the solubility of $(\text{C}_4\text{H}_9\text{NH}_3)_2\text{PbBr}_4$ in DMF and promote crystallization. Because CB has a similar boiling point and evaporation rate as DMF, the drying of the solvents and the crystallization process were uniform across the whole substrate.

We examined the products of this reaction by optical microscopy and atomic force microscopy (AFM), but instead of monolayers, thick particles with random shapes formed on the substrate (fig. S1). Hybrid perovskites have limited solubility in acetonitrile, and the solvent has been used previously for making microscopic hybrid perovskite single crystals (22). In this case, acetonitrile evaporates more quickly and helps induce the formation of the ultrathin 2D hybrid perovskite sheets. When acetonitrile was combined with DMF and CB, uniform square sheets grew on the substrate (Fig. 1B). The edge length of the square crystals ranged from 1 to 10 μm , with an average of 4.2 μm (the size distribution statistics can be found in fig. S2). The detailed synthetic procedure and discussion of the role of each solvent can be found in the supplementary text (21).

¹Department of Chemistry, University of California, Berkeley, CA 94720, USA. ²Materials Sciences Division, Lawrence Berkeley National Laboratory, Berkeley, CA 94720, USA. ³School of Physical Science and Technology, ShanghaiTech University, Shanghai, 201210, China. ⁴Department of Physics, University of California, Berkeley, CA 94720, USA. ⁵Kavli Energy NanoScience Institute, Berkeley, CA 94720, USA. ⁶Physical Biosciences Division, Lawrence Berkeley National Laboratory, Berkeley, CA 94720, USA. ⁷Department of Materials Science and Engineering, University of California, Berkeley, CA 94720, USA.

*These authors contributed equally to this work. †Corresponding author. E-mail: p_yang@berkeley.edu

APPENDIX C

**FESHBACH ENHANCED S-WAVE SCATTERING OF FERMIONS: DIRECT
OBSERVATION WITH OPTIMIZED ABSORPTION IMAGING**



PAPER

Feshbach enhanced s -wave scattering of fermions: direct observation with optimized absorption imaging

OPEN ACCESS

RECEIVED

30 September 2015

REVISED

20 November 2015

ACCEPTED FOR PUBLICATION

24 November 2015

PUBLISHED

17 December 2015

Content from this work may be used under the terms of the [Creative Commons Attribution 3.0 licence](#).

Any further distribution of this work must maintain attribution to the author(s) and the title of the work, journal citation and DOI.

D Genkina^{1,4}, L M Aycock^{1,2,4}, B K Stuhl¹, H-I Lu¹, R A Williams³ and I B Spielman¹¹ Joint Quantum Institute, National Institute of Standards and Technology, and University of Maryland, Gaithersburg, MD 20899, USA² Physics Department, Cornell University, Ithaca, NY 14850, USA³ National Physical Laboratory, Hampton Road, Teddington, Middlesex, TW11 0LW, UK⁴ These authors contributed equally to the work.E-mail: ian.spielman@nist.gov

Keywords: quantum gases, atomic physics, Feshbach resonances, absorption imaging

Abstract

We directly measured the normalized s -wave scattering cross-section of ultracold ^{40}K atoms across a magnetic-field Feshbach resonance by colliding pairs of degenerate Fermi gases (DFGs) and imaging the scattered atoms. We extracted the scattered fraction for a range of bias magnetic fields, and measured the resonance location to be $B_0 = 20.206(15)$ mT with width $\Delta = 1.0(5)$ mT. To optimize the signal-to-noise ratio (SNR) of atom number in scattering images, we developed techniques to interpret absorption images in a regime where recoil induced detuning corrections are significant. These imaging techniques are generally applicable to experiments with lighter alkalis that would benefit from maximizing SNR on atom number counting at the expense of spatial imaging resolution.

1. Introduction

Feshbach resonances are widely used for tuning the interaction strength in ultracold atomic gases. In degenerate Fermi gases (DFGs), the tunability of interactions provided by Feshbach resonances has allowed for studies of the creation of molecular Bose–Einstein condensates (BECs) [1–3] as well as observation of the phase transition from the Bardeen–Cooper–Schrieffer (BCS) superconducting regime to the BEC regime at sufficiently low temperatures [4–7]. Conversely, measuring interactions as a function of controlled parameters can be used to characterize a Feshbach resonance.

A Feshbach resonance occurs when a diatomic molecular state energetically approaches the two-atom continuum [8, 9]. For a magnetic-field Feshbach resonance, a bias magnetic field defines the relative energy of the free atomic states in two hyperfine sublevels and the molecular state. Consequently, the Feshbach resonance can be accessed by changing the bias field. In cold atomic systems where only s -wave channels contribute to scattering, the interactions are entirely characterized by the scattering length a . In the simple case where there are no inelastic two-body channels, such as for the ^{40}K resonance discussed in this work, the effect of the resonance on the scattering length between two free atoms is [8]

$$a(B) = a_{\text{bg}} \left(1 - \frac{\Delta}{B - B_0} \right), \quad (1)$$

where a_{bg} is the scattering length far from any resonance (background scattering length), Δ is the width of the resonance, and B_0 is the field value at which the resonance occurs.

The exact value of the resonant field B_0 is difficult to calculate analytically and is commonly computed via numerical models based on experimental input parameters [10–12] or determined experimentally [13, 14]. Many experimental techniques have been used to characterize Feshbach resonances. These include the observation of atom loss due to three-body inelastic scattering, measurement of re-thermalization timescales, and anisotropic expansion of a cloud upon release from a confining potential, which infer the elastic scattering cross section from collective behavior of the cloud [15–17]. More recently, precise measurements of the

molecular binding energy have been performed, which can be used in conjunction with theoretical modeling to extract the scattering cross section [18, 19].

Here direct scattering was the primary probe of the location and width of a Feshbach resonance. We collided pairs of DFGs and imaged the resulting *s*-wave scattered atoms as a function of bias magnetic field. This allowed us to observe the enhancement in scattering without relying on proxy effects. We measured the fraction of atoms scattered during the collision at different bias magnetic fields and deduced the location and width of the resonance.

In contrast to BECs, where scattering halos are readily imaged [20–22], the density of Fermi clouds is typically ≈ 100 times less than that of BECs⁵, making it necessary to enhance the strength of inter-atomic interactions to directly detect the scattered atoms. In our dilute DFGs, even with the resonant enhancement of the scattering cross section, only a small fraction of the atoms was scattered. Using typical absorption imaging, direct detection of scattered atoms was difficult due to detection uncertainty that particularly affected regions of low atomic density. To optimize the signal-to-noise ratio (SNR) for low atom numbers, we absorption imaged with fairly long, high-intensity pulses—a non-standard regime—which imparted a non-negligible velocity and therefore Doppler shift to the atoms. Simulation of the absorption imaging process was necessary for an accurate interpretation of these images. Using the simulation-corrected images, we extracted the fraction of atoms scattered in our collision experiment.

This paper is divided into two parts. First, we study absorption imaging in the presence of a significant time-dependent Doppler shift and show how we use our results to interpret data. Second, we describe our *s*-wave scattering experiment and extract a measure of the location and width of the Feshbach resonance in ^{40}K .

2. Absorption imaging in the presence of strong recoil induced detuning

Absorption imaging measures the shadow cast by an atomic ensemble in an illuminating probe laser beam with angular frequency ω_L . This imaging technique relies on optical transitions between ground and excited atomic states. Such atomic transitions have an energy difference $\hbar\omega_0$, and a natural transition linewidth Γ . When interacting with a laser field an atom scatters photons from the field into the vacuum modes. In the two-level atom approximation, the rate of scattering is [25]

$$\gamma_{\text{sc}} = \frac{\Gamma}{2} \frac{\tilde{I}}{1 + 4\tilde{\delta}^2 + \tilde{I}}, \quad (2)$$

where $\tilde{I} = I/I_{\text{sat}}$ is the laser intensity in units of the saturation intensity, and $\tilde{\delta} = \delta/\Gamma$ is the detuning $\delta = \omega_L - \omega_0$ in units of the natural linewidth.

An absorption image is obtained by shining an on- or near-resonant probe beam (generally $\tilde{\delta} \ll 1$) onto the atomic cloud. Some of the light is scattered by the atoms, and the shadow cast by the atoms in the probe beam, $\tilde{I}_f(x, y)$, is imaged onto a camera, as depicted in figure 1(a) (top). The probe light is reapplied with the atoms absent to calibrate the intensity $\tilde{I}_0(x, y)$ of light unaffected by the atoms (bottom).

Consider the light as it travels along the imaging axis \mathbf{e}_z through a 3D atomic density profile $\rho(x, y, z)$. We focus on a single pixel of the camera: sensitive to a single column of atoms $\rho(z)$, integrated in *x* and *y* over the pixel, giving a single value of \tilde{I}_0 and \tilde{I}_f . Every atom scatters light according to equation (2). Therefore, the atoms further along the imaging axis \mathbf{e}_z experience a reduced optical intensity due to attenuation of the laser field by the other atoms (figure 1(b)). The intensity change from scattering as a function of *z* is

$$\frac{d\tilde{I}(z)}{dz} = -\hbar\omega_L\rho(z)\gamma_{\text{sc}}(z) = -\rho(z)\sigma_0\frac{\tilde{I}(z)}{1 + 4\tilde{\delta}^2 + \tilde{I}}, \quad (3)$$

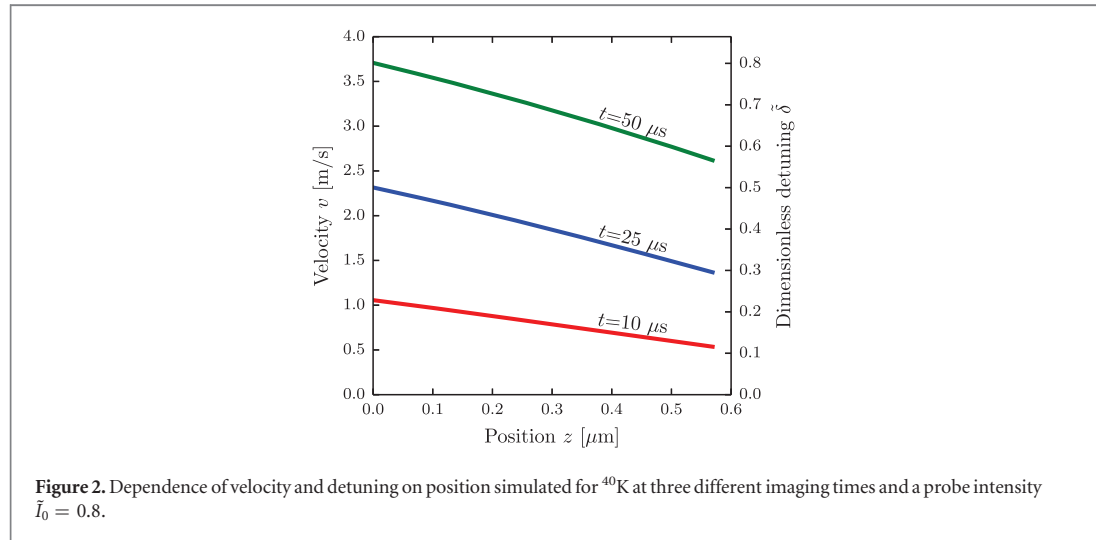
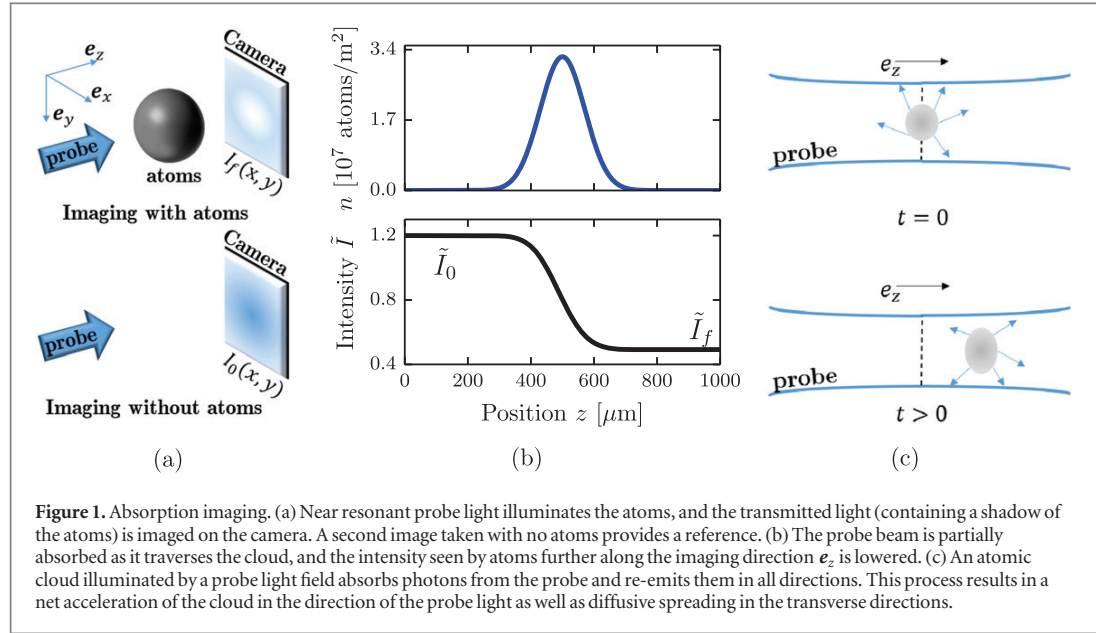
where σ_0 is the resonant scattering cross section. Integrating this equation [26] yields a straightforward relation between the observed intensities \tilde{I}_0 and \tilde{I}_f and the atomic column density $n = \int \rho(z) dz$:

$$\sigma_0 n = -\left(1 + 4\tilde{\delta}^2\right) \ln\left(I_f/I_0\right) + \tilde{I}_0 - \tilde{I}_f. \quad (4)$$

We call the column density deduced from this relation $\sigma_0 n^{(1)}$. When the probe intensity is much smaller than the saturation intensity, $\tilde{I}_0 \ll 1$, and the probe light is on resonance, $\tilde{\delta} = 0$, the right-hand side of equation (4) reduces to the optical depth, defined as $\text{OD} = -\ln(I_f/I_0)$ [26], giving the simple relationship $\sigma_0 n^{(0)} = \text{OD}$. In all other regimes, the optical depth is not constant and depends on the probe intensity and imaging time.

Equations (3), (4) neglect the atomic recoil momentum and the resulting Doppler shift [27]. When an atom absorbs a photon from the laser light field it acquires a momentum kick $\hbar k_r$ in the \mathbf{e}_z direction. The associated recoil velocity is $v_r = \hbar k_r/m$, where *m* is the atomic mass and $\hbar k_r = h/\lambda$ is the recoil momentum from the laser with wavelength λ . Each re-emitted photon imparts a similar recoil momentum \mathbf{p}_e , but over many scattering

⁵ This is not the case for recently realized erbium and dysprosium DFGs [23, 24], where strong dipolar interactions are present.

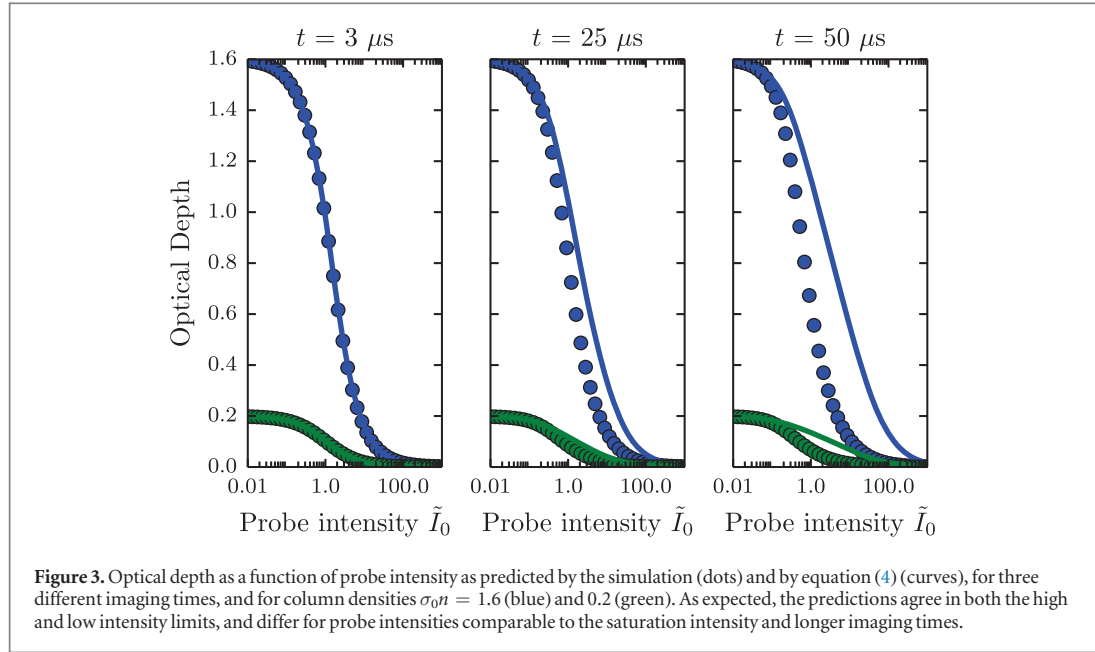


events this momentum distribution averages to zero. Therefore the atom will only acquire an average velocity per photon v_r along \mathbf{e}_z . The variance of \mathbf{p}_e , however, is not zero, allowing the atoms to acquire some momentum transverse to the laser field. While we ignore this correction, it results in the reduction of spatial resolution in the final image and its effect on the atomic cloud is pictured in figure 1(c).

The average atomic velocity parallel to the light field after scattering N photons is Nv_r and the laser frequency as seen by the atoms is Doppler shifted $\delta = k_r Nv_r$ from resonance. After an atom scatters $N_{\text{photons}} = \Gamma/2k_r v_r$, it gets Doppler detuned by half a linewidth. For a probe intensity of $\tilde{I}_0 = 1$, the time it takes a single atom to scatter on average that many photons is given by $t_{\text{recoil}} = N_{\text{photons}}/\gamma_{\text{sc}} = 2/k_r v_r$. For ^{40}K atoms imaged on the D2 transition, the case relevant for our experiment, $N_{\text{photons}} = 178$ and $t_{\text{recoil}} = 18.76 \mu\text{s}$ —for imaging times longer than that the recoil induced detuning correction cannot be neglected. Furthermore, this detuning varies both with imaging time t and with distance along the propagation direction \mathbf{e}_z (figure 2). Thus, the laser's spatially varying intensity profile in the atomic cloud also depends on time:

$$\frac{d\tilde{I}(t, z)}{dz} = -\sigma_0 \rho(t, z) \frac{\tilde{I}(t, z)}{1 + 4\tilde{\delta}(t, z)^2 + \tilde{I}(t, z)}. \quad (5)$$

Assuming that the atoms do not move significantly during the imaging time (we will remove this assumption shortly), the dimensionless detuning is



$$\tilde{\delta}(t, z) = \frac{k_r v_r}{2\sigma_0 \rho(t, z)} \int_0^t \frac{d\tilde{I}(z, \tau)}{dz} d\tau; \quad (6)$$

the relationship between the atomic density and the observed intensities is no longer straightforward. Perturbative treatments of these equations also prove insufficient (see appendix A.1).

2.1. Simulation

To obtain a relationship between the atomic density and the observed intensities in this non-standard regime, we numerically simulated the imaging process, including the recoil induced detuning. We used parameters relevant to our experiment—the D2 transition of ^{40}K , with $\lambda = 766.701$ nm, $\Gamma/2\pi = 6.035$ MHz, $v_r = 1.302$ cm s $^{-1}$ and $I_{\text{sat}} = 1.75$ mW cm $^{-2}$ [28]. The simulation obtained \tilde{I}_f as a function of imaging time t , atomic density $\sigma_0 n$, and probe intensity \tilde{I}_0 .

We performed two versions of this simulation. First, we took a simplistic approach where the spatial distribution of atoms did not change appreciably during the imaging time: $vt \ll I_0/(\hbar\omega_L\gamma_{\text{sc}}\rho)$ —the stationary assumption. Starting with a Gaussian density profile, we numerically integrated equations (5) and (6) and obtained a simulated optical depth for a range of input probe intensities and atomic column densities. We used the results of this simulation to check the self-consistency of the stationary atom assumption and found it to be invalid (see appendix A.2).

To account for the changing atomic distribution during the imaging pulse, we numerically simulated the classical kinetics of atoms subject to the recoil driven optical forces, and obtained a dynamics adjusted version of the simulated optical depth. We compared the optical depths predicted by each of the two simulations in the parameter range $0.3 \leq t \leq 100$ μs , $0.01 \leq \tilde{I}_0 \leq 50$ and $0.01 \leq \sigma_0 n \leq 2$ and found that the predicted optical depths were hardly changed by including the full time evolution (see appendix A.3). Thus, for the purposes of deducing the atomic density from experimental optical depths, the stationary atom simulation is sufficient in the experimentally relevant parameter regime we explored. However, since there is no *a priori* reason why this should be sufficient, it is possible that for some range of experimental optical depths or imaging times this correction is significant, or that it has some impact on the acquired transverse velocity of the atoms—an effect not considered in our simulations. Furthermore, we simulated a range of initial density profiles $\rho(z)$, and found their impact on the simulated OD to be negligible—the only observable is the integrated atomic density n , and 3D atomic densities cannot be reconstructed.

Figure 3 illustrates the effect of the recoil induced detuning correction as obtained from our simulations. In the limit of low probe intensity, $\tilde{I}_0 \ll 1$, the atomic velocities are hardly changed and the recoil induced detuning correction is negligible. In the limit of high probe intensity $\tilde{I}_0 \gg \tilde{\delta}$, even far detuned atoms will scatter light at their maximum rate and the overall absorption will again be unaffected by the correction. In the intermediate regime, there is a significant deviation between the optical depth predicted by equation (4) and the simulated optical depth, and this deviation becomes stronger with longer imaging times.

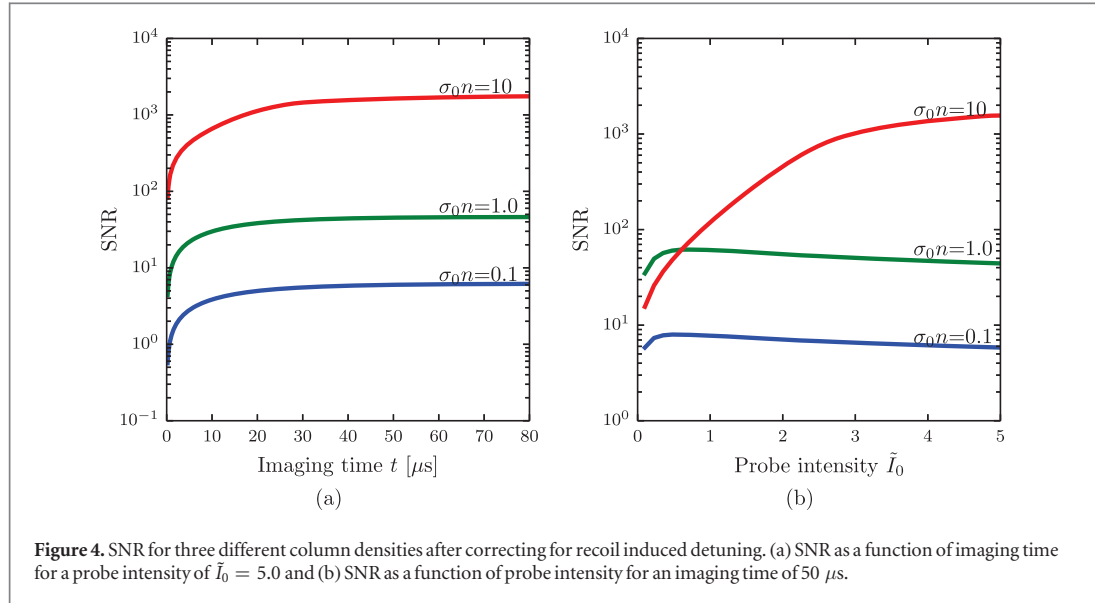


Figure 4. SNR for three different column densities after correcting for recoil induced detuning. (a) SNR as a function of imaging time for a probe intensity of $\tilde{I}_0 = 5.0$ and (b) SNR as a function of probe intensity for an imaging time of $50 \mu\text{s}$.

This simulation provided us with a correction procedure to interpret experimentally observed \tilde{I}_f and \tilde{I}_0 . For a given imaging time, the simulation predicted a final intensity as a function of probe intensity and atomic column density. We inverted this prediction to obtain an atomic column density given our observed intensities. For interpreting experimental images, we used the optical depths predicted by the traveling atom simulation, OD^{sim} .

2.2. SNR optimization

We added shot noise to our simulation and established optimal imaging parameters to maximize the SNR of this detection scheme. We considered Poisson noise on the detected arriving photons (i.e., photoelectrons) in both the initial and final images I_0 and I_f with standard deviation proportional to $\sqrt{q_e N_p}$, where q_e is the quantum efficiency of the camera (0.66 for our camera) and N_p is the photon number. We then propagated the shot noise in the two images using standard error propagation techniques through the correction scheme described in section 2.1 to obtain the uncertainty in a deduced column density, $\delta_{\sigma_0 n}$. We define the SNR as $\sigma_0 n / \delta_{\sigma_0 n}$.

As seen in figure 4(a), after about $40 \mu\text{s}$ extending the imaging time no longer yields appreciable improvement in SNR. Imaging for $40 \mu\text{s}$ as opposed to $10 \mu\text{s}$, where the uncorrected model is appropriate, improves the SNR by a factor of 1.5. We therefore performed the experiments described in the second section at $40 \mu\text{s}$ imaging time. Figure 4(b) shows that the optimal probe intensity varies with the atomic column density. For low atom numbers, $\sigma_0 n \approx 0.1$, a probe intensity of $\tilde{I}_0 \approx 0.6$ is best. However, in our experiment the probe intensity had a Gaussian profile and was not uniform over the whole image. The typical probe intensities used in our experiments varied over the $\tilde{I}_0 = 0.1$ – 0.7 range.

2.3. Calibration of saturation intensity

The calibration of the observed signal in units of the saturation intensity is crucial to our measurement of the column densities. Our absorption images were taken using a charge-coupled device camera. For each pixel, the camera returned an integer number of counts proportional to the radiant fluence seen by that pixel. However, the proportionality constant depended on many factors, such as the quantum efficiency of the camera, the electronic gain during the readout process and losses in the imaging system. One way to determine this proportionality constant is to experimentally calibrate the saturation intensity in counts per unit time.

To calibrate the saturation intensity in camera counts per unit time, we took absorption images of the atoms at three different imaging times (40 , 100 , and $200 \mu\text{s}$) with varying probe intensities. For each image we obtained \tilde{I}_0 and \tilde{I}_f in counts per microsecond by averaging over a few pixels in a region of constant atomic column density. We then simultaneously fit our simulated optical depth OD^{sim} to this full data set, with the atomic density $\sigma_0 n$ and I_{sat} in counts per microsecond as free parameters. As seen in figure 5, the model produced a good fit to the experimental data, and provided a calibration of the saturation intensity for our experiment.

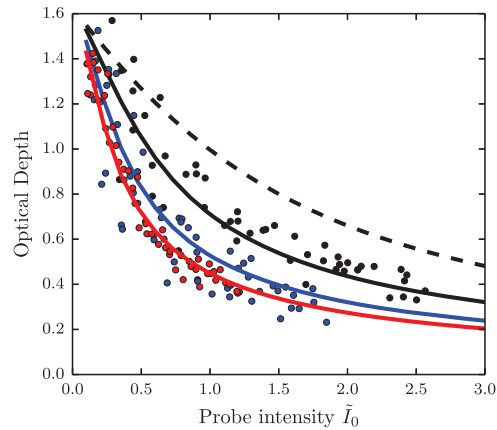


Figure 5. The optical depth as a function of probe intensity for three imaging times: $t = 40 \mu\text{s}$ (black), $t = 75 \mu\text{s}$ (blue), $t = 100 \mu\text{s}$ (red). The dots represent experimental data and the curves represent the best fit of simulated data. The optimal fit parameters pictured are a $\sigma_0 n$ of 1.627(5) and saturation intensity of 29(7) counts/ μs . The dashed curve represents the theoretical prediction without recoil induced detuning corrections.

3. s-wave scattering experiment

For our measurement of the Feshbach resonance location and width, we collided two counter-propagating ^{40}K clouds in a spin mixture of $|F = 9/2, m_F = -9/2\rangle$ and $|F = 9/2, m_F = -7/2\rangle$ hyperfine states and observed the resulting s -wave halo of scattered atoms. We measured the dependence of the scattered atomic fraction on the bias magnetic field in the vicinity of the Feshbach resonance. We used this data to extract the location of the resonance at 20.206(15) mT with width 1.0(5) mT, consistent with the accepted values of 20.210(7) mT and 0.78(6) mT [7].

3.1. Experimental procedure

Our experiment is a hybrid ^{40}K and ^{87}Rb apparatus, previously described in [29–31]. Initially, we prepared a spin polarized $|F = 9/2, m_F = -9/2\rangle$ DFG of $\approx 4 \times 10^5$ atoms of ^{40}K at a temperature of $T \approx 0.4 T_F$, where T_F is the Fermi temperature, in a crossed optical dipole trap with frequencies $(\omega_x, \omega_y, \omega_z)/2\pi = (39, 42, 124)$ Hz (see appendix B).

To map out the entire Feshbach resonance without the added losses associated with going through the resonance [8], we needed to create equal spin mixtures of $|F = 9/2, m_F = -9/2\rangle$ and $|F = 9/2, m_F = -7/2\rangle$ on either side of the resonance. We ramped the bias magnetic field to 19.05 mT (21.71 mT) and turned on a 42.42 MHz (47.11 MHz) rf field⁶ resonant with the Zeeman splitting between the two states when preparing the mixture below (above) the Feshbach resonance. We then sinusoidally modulated the bias field at 125 Hz for 0.5 s, with a 0.14 mT amplitude, producing an equal mixture of the two hyperfine states. The depolarization allowed the fermions to re-thermalize, allowing us to further evaporate in the dipole trap [32]. These hyperfine states of ^{40}K were then used to study their Feshbach resonance.

After evaporation, we ramped the bias field in a two-step fashion to the desired field value near the Feshbach resonance. The two-step procedure was designed to allow us to approach the set-point quickly and avoid additional losses. This procedure used two sets of Helmholtz coils—large coils that provided the majority of the bias field but had a long inductive timescale, and smaller coils only capable of generating 0.59 mT of bias, but with a shorter inductive timescale. We approached the field using the large coils to bring the magnetic field to a set-point 0.59 mT above or below the intended bias field. We held the atoms at this field for 100 ms to allow the eddy currents induced by the large coils to settle, and then used the smaller coils to quickly change the bias field the remaining 0.59 mT. For all set-points, the data was taken approaching from both above and below the Feshbach resonance⁷.

Once at the intended bias field, we split the cloud into two spatially overlapping components with opposite momenta and observed scattering as they separated. These counterpropagating components were created using Kapitza-Dirac pulses of a 1D retro-reflected near-resonant optical lattice ($\lambda_L = 766.704$ nm) with $8E_L$ depth, where $E_L = \hbar^2 k_L^2 / 2m_K$ is the lattice recoil energy and $\hbar k_L = 2\pi\hbar/\lambda$ is the recoil momentum. We rapidly pulsed

⁶The rf intensity at these frequencies was too low for us to calibrate the coupling strength.

⁷An extra data point was taken on each side far from the resonance using only one approach.

this lattice on and off with a double-pulse protocol [33]. The pulse sequence was optimized to transfer most of the atoms into the $\pm 2\hbar k_L$ momentum states. Since the initial Fermi gas had a wide momentum spread (here, $2\hbar k_L \approx 2.5\hbar k_F$, where k_F is the Fermi momentum), and the lattice pulsing is a momentum dependent process [34], not all the atoms were transferred into the target momentum states. We optimized our pulse times to minimize the atoms remaining in the zero momentum state.

We then released the atoms from the trap and allowed 1 ms for the two opposite momentum states to pass through each other while interacting at the magnetic field set-point. For data taken approaching the set-point from below, we then ramped down the field and imaged the atoms. For data taken approaching the set-point from above, molecules may have been created when crossing the Feshbach resonance. Therefore, we first ramped the field up to a point above the resonance to dissociate any molecules that were created and then quickly ramped the field back down and imaged the atoms. After a total time-of-flight $t_{\text{TOF}} = 6.8$ ms, we used a 40 μs imaging pulse with $\tilde{I}_0 \approx 0.6$ at the center of the probe laser, chosen for SNR optimization as described in section 2.2.

3.2. Magnetic field calibration

The magnetic fields produced by our coils in the regime of interest were independently calibrated by rf-spectroscopy on the $|F = 9/2, m_F = -9/2\rangle$ to $|F = 9/2, m_F = -7/2\rangle$ transition. We prepared a spin polarized state and ramped the large coils to variable set-points. We then illuminated the atoms with a rf field with frequency ν_{rf} and performed adiabatic rapid passage (ARP) by ramping the smaller coils 0.0284 mT in 250 ms. We applied a Stern–Gerlach pulse and imaged the atoms to measure the fractional population in the $|F = 9/2, m_F = -9/2\rangle$ and $|F = 9/2, m_F = -7/2\rangle$ states. We fit the fractional population as a function of current to a Gaussian function⁸. The center of the Gaussian corresponded to the resonant magnetic field, which was produced by the high inductance coil setpoint plus half the ARP, 0.0142 mT, with an uncertainty given by the Gaussian width. We used the Breit–Rabi formula to determine the resonant field value at ν_{rf} . We did this for five different rf frequencies, and acquired a field calibration with an uncertainty of 0.004 mT, which was included in the listed uncertainty on our measured value of B_0 .

3.3. Methods

We first processed the *s*-wave scattering images by comparing the observed OD to simulations taking into account the recoil induced detuning as described in section 2. An example of images before and after processing are shown in figure 6. The processing constituted a $\approx 30\%$ change in the column density.

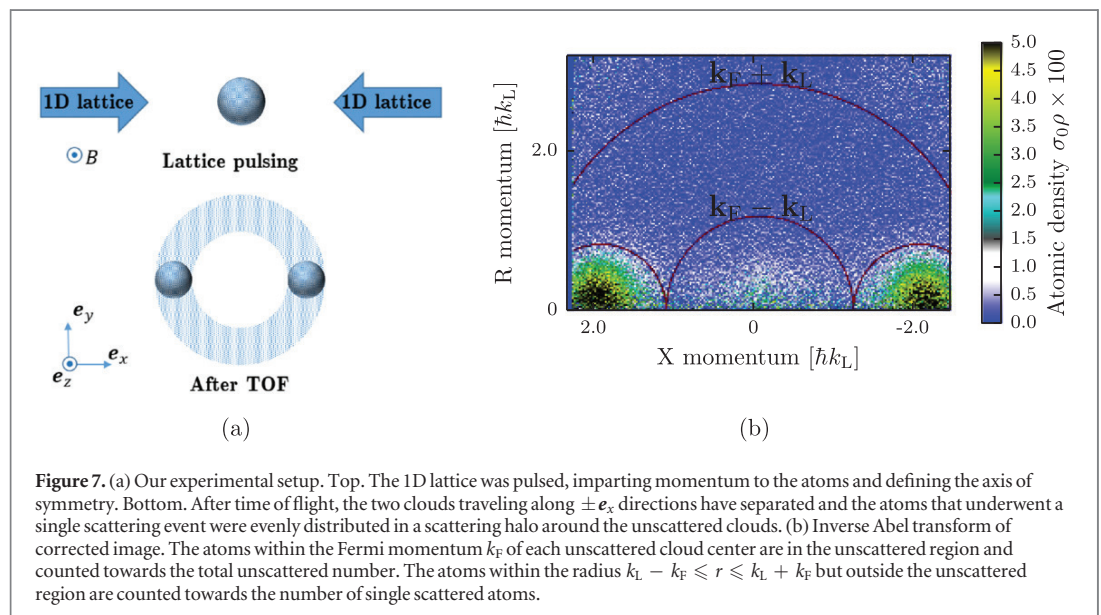
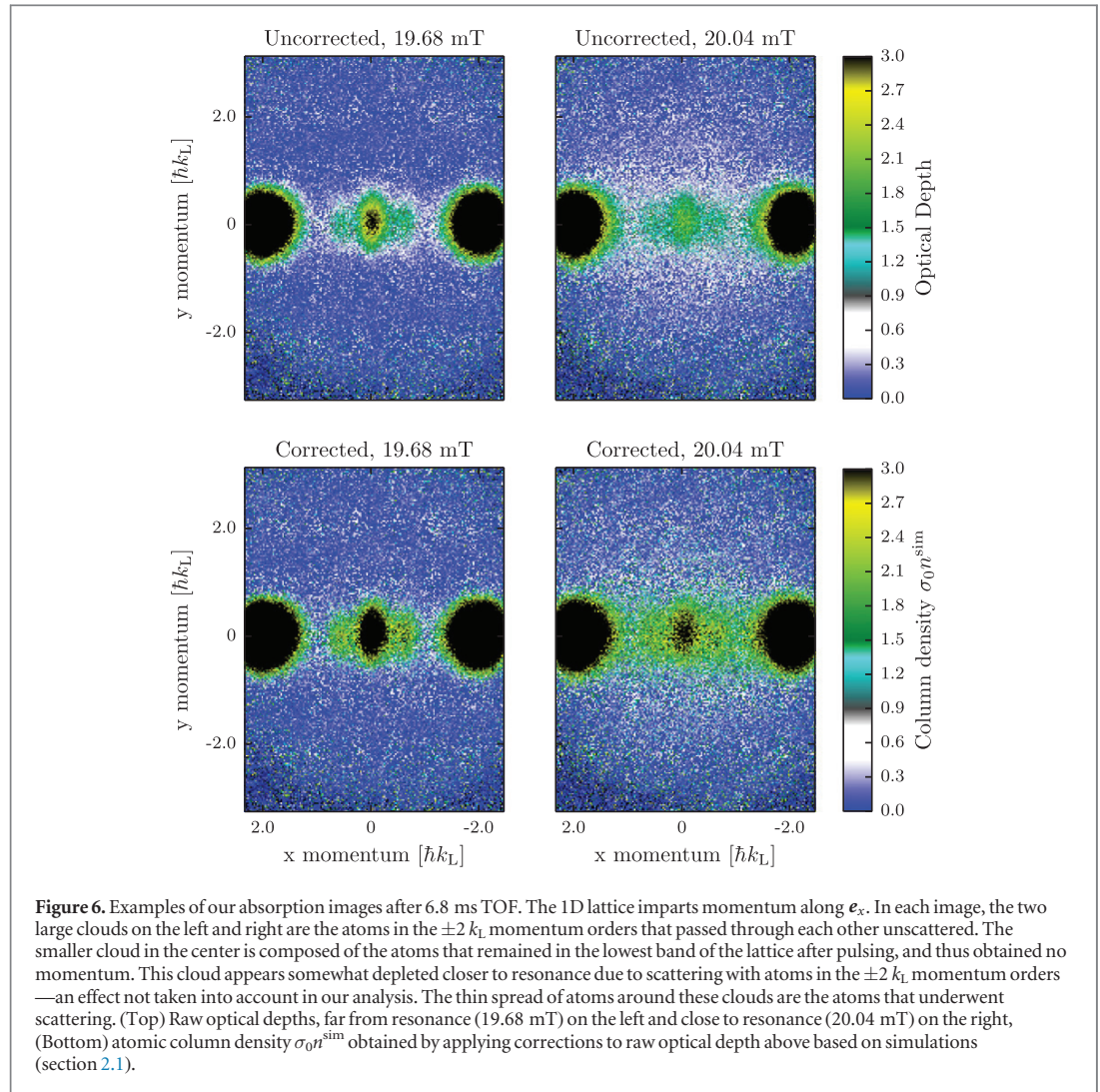
We counted the fraction of atoms that experienced a single scattering event for each image. Single scattering events are easily identified, as two atoms that scatter elastically keep the same amplitude of momentum, but depart along an arbitrary direction. Therefore, an atom traveling at $2\hbar k_L$ to the right that collides elastically with an atom traveling at $-2\hbar k_L$ to the left will depart with equal and opposite momenta $2\hbar k_L$ at an arbitrary angle, and after a time-of-flight sufficiently long to convert initial momentum into position, as ours was, such atoms will lie in a spherical shell, producing the scattering halo pictured in figure 7(a).

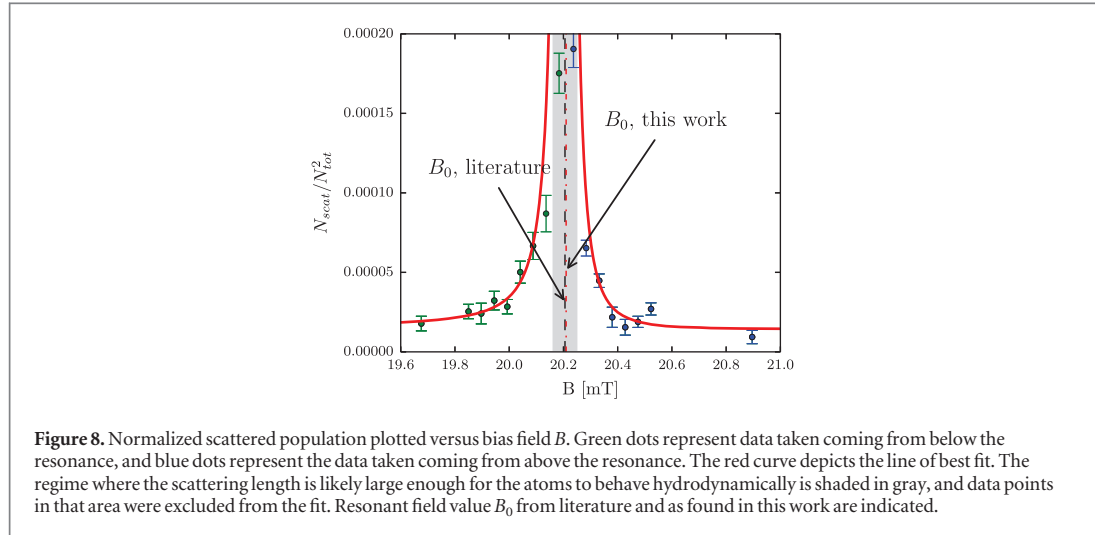
Absorption images captured the integrated column density along \mathbf{e}_z , a projected 2D atomic distribution. To extract the radial dependence of the 3D distribution from the 2D image, we performed a standard inverse Abel transform [35]. The inverse Abel transform assumes cylindrical symmetry, which was present in our case, with the axis of symmetry along \mathbf{e}_x , defined by the lattice. We thus obtained the atomic distribution $\rho(r, \theta)$ as a function of r , the radial distance from the scattering center, and θ , the angle between r and symmetry axis \mathbf{e}_x , integrated over ϕ , the azimuthal angle around the x axis.

We then extracted the number of scattered atoms N_{scat} as a fraction of the total atom number N_{tot} for each image, as shown in figure 7(b). The unscattered atom number was the number of atoms in the two unscattered clouds. The number of atoms that underwent a single scattering event was the number of atoms outside the Fermi radius of the unscattered clouds, but inside the arc created by rotating the Fermi momentum k_F around the original center of the cloud (red arcs in figure 7(b)). For both the scattered and unscattered quantities, we extrapolated to include atoms that would fall outside the field of view of our camera. The atoms in the center region were not counted as they were originally in the zero momentum state and could not contribute to the scattering halo under study. We did not account for possible *s*-wave scattering between the atoms found in the zero momentum state and one of the $\pm 2k_L$ momentum states in this treatment.

Since we were in the low energy regime (the atomic momentum was much smaller than the momentum set by the van der Waals length $k_L + k_F \ll 1/l_{\text{vdW}}$, and we were well below the *p*-wave threshold temperature [32]), the scattering cross-section was given by $\sigma = 4\pi a^2$. The scattering cross-section σ gives the probability $P_{\text{scat}} = \sigma N/A$ that a single particle will scatter when incident on a cloud of atoms with a surface density of N/A , where A is the cross-sectional area of the cloud and N is the number of atoms in the cloud. In our case, each half

⁸ Due to our low rf coupling and high noise, we did not fit to the traditional Lorentzian model.





of the initial cloud, with atoms number $N_{\text{tot}}/2$, was incident on the other half. Thus, the number of expected scattering events was $N_{\text{scat}} = (N_{\text{tot}}/2)\sigma(N_{\text{tot}}/2) = \sigma N_{\text{tot}}^2/4A$. Assuming A was constant for all our data, we defined a fit parameter $b_0 = 4\pi a_{\text{bg}}^2/4A$, where a_{bg} is the background scattering length. We thus adapted equation (1) to obtain the fit function

$$\frac{N_{\text{scat}}}{N_{\text{tot}}^2} = b_0 \left(1 - \frac{\Delta}{B - B_0} \right)^2 + C, \quad (7)$$

where B_0 is the resonant field value and Δ is the width of the resonance, the parameters in equation (1), and the offset C accounts for any systematic difference in the initial and final intensity images with no atoms present.

For each value of the bias magnetic field, we took 15 nominally identical images, allowing us to compensate for shot-to-shot atom number fluctuations. We fit the fraction of scattered atoms $N_{\text{scat}}/N_{\text{tot}}$ versus the total atom number N_{tot} for each of these 15 images to a line. The slope of this fit was taken to be the value of $N_{\text{scat}}/N_{\text{tot}}^2$ at that bias magnetic field, and the variance of the fit gave the uncertainty on that data point.

3.4. Results

Our data is presented in figure 8. The red curve depicts a best fit of the model given in equation (7). The fit parameters we extracted were $\Delta = 1.0(5)$ mT and $B_0 = 20.206(15)$ mT. To obtain the fit, we used data taken by approaching the resonance from above for points above where we expected the resonance to be and data taken approaching the resonance from below for points below. We also excluded from the fit data points very near the resonance, as there the assumption $\sigma n \ll 1$ is no longer valid and the problem must be treated hydrodynamically [8]. Due to this, we could not obtain usable data very close to the resonance, explaining the large uncertainty on the resonance width.

The accepted values for the ^{40}K s -wave Feshbach resonance for the $|9/2, -9/2\rangle$ and $|9/2, -7/2\rangle$ states are $B_0 = 20.210(7)$ mT and $\Delta = 0.78(6)$ mT [7], which is in good agreement with our findings. Although the data without the recoil induced detuning correction were $\approx 30\%$ different from the corrected data, the optimal parameters from fitting the uncorrected data were within our uncertainties from the values listed above. The resonance location was largely unaffected by the correction, as the scattering cross-section diverges there, making it insensitive to the precise values. The width may have been affected, however the uncertainty on the fit is too large for the effect to be significant. Performing the correction was still necessary to ensure the values were proportional to the scattering cross section and to obtain a trustworthy result.

Some potential sources of systematic uncertainty that we did not account for include scattering with atoms that did not receive a momentum kick from the lattice pulsing and the impact of multiple scattering events.

4. Conclusion

We studied the effects of recoil-induced detuning on absorption images and found an imaging time that maximized SNR to be ≈ 40 μs for ^{40}K atoms. We used these results to directly image s -wave scattering halos of the Fermi gas around the ≈ 20.2 mT Feshbach resonance and verify the resonance location and width. Our imaging analysis can be used in any absorption imaging application where SNR optimization is critical.

Acknowledgments

We thank Marcell Gall for helpful discussions. We thank William R McGehee and Elizabeth A Goldschmidt for a careful reading of the manuscript. This work was partially supported by the AROs Atomtronics MURI, by the AFOSRs Quantum Matter MURI, NIST, and the NSF through the PFC at the JQI. BKS acknowledges support from the National Research Council Research Associateship program. LMA acknowledges support from the National Science Foundation Graduate Research Fellowship program.

Appendix A

A.1. Perturbative treatment

By considering equations (5), (6) perturbatively in imaging time, we can obtain corrections to the column density due to recoil induced detuning to second order [36]:

$$\sigma_0 n^{(2)} = c_0 + c_1 t + c_2 t^2, \text{ where} \quad (\text{A.1})$$

$$c_0 = \sigma_0 n^{(1)}, c_1 = 0, c_2 = \frac{(k_r v_r)^2}{3} \left[\frac{1}{\tilde{I}_f + 1} - \frac{1}{\tilde{I}_0 + 1} + \ln \left(\frac{\tilde{I}_f + 1}{\tilde{I}_0 + 1} \right) \right]. \quad (\text{A.2})$$

However, as shown in figure A1(a), the perturbative treatment is only accurate to times up to the recoil time t_{recoil} —defined as the time it takes a single atom to get Doppler shifted from resonance by half a linewidth—after which this prediction begins to diverge. To adequately correct for the recoil induced detuning of the atoms, numerical simulation is necessary.

A.2. Stationary atom model

To solve equations (5), (6), we divided the cloud into spatial bins. In this approximation, the number of atoms in each bin was time-independent. The algorithm used is shown in algorithm 1, in which we took a Gaussian profile for our initial density distribution. We call the optical depth simulated by this algorithm the simulated optical depth OD^{sim1} .

Algorithm 1. Stationary atom model

```

 $\tilde{I}[n = 0, t] = \tilde{I}_0$  {  $n$  is the bin index,  $t$  is the time index }
 $\tilde{\delta}[n, t = 0] = 0$  { light initially resonant }
 $H_f = 0$  { Radiant fluence seen by camera after passing through cloud }
for  $t = 0$  to  $t_f$  do { loop over time steps }
  for  $n = 1$  to  $N$  do { loop over bins,  $N$  is total bin number }
     $A = \sigma_0 \rho[n] dz$  {  $dz$  is the size of spatial step }
     $B = v_r dt / (\hbar c \rho[n])$  {  $dt$  is the size of the time step }
     $\tilde{I}[n, t] = \tilde{I}[n - 1, t] - A \tilde{I}[n - 1, t] / (1 + 4 \tilde{\delta}[n, t - 1]^2) + \tilde{I}[n - 1, t]$  { equation (5) }
     $\tilde{\delta}[n, t] = \tilde{\delta}[n, t - 1] + B (\tilde{I}[n - 1, t] - \tilde{I}[n, t])$  { equation (6) }
  end for
   $H_f = H_f + \tilde{I}[N, t] dt$  { collecting total fluence seen by the camera }
end for
 $\text{OD}^{\text{sim1}} = -\ln(H_f / \tilde{I}_0 t_f)$ 

```

We checked the validity of our simulation in the limits where the problem is analytically solvable. In the limit where the probe intensity is much weaker than the saturation intensity, $\tilde{I}_0 \ll 1$, the atoms' velocities are hardly changed, and equation (5) reduces to

$$\frac{d\tilde{I}(z)}{dz} = -\rho \sigma_0 \tilde{I}(z), \text{ from which we recover the analytic form,} \quad (\text{A.3})$$

$$\sigma_0 n^{(0)} = -\ln \tilde{I}_0 / \tilde{I}_f. \quad (\text{A.4})$$

In the limit where the probe intensity is much larger than the saturation intensity, $\tilde{I}_0 \gg \tilde{\delta}$, even far detuned atoms will scatter light at their maximum rate. The time dependence of the detuning can thus be neglected, and equation (5) becomes

$$\frac{d\tilde{I}(z)}{dz} = -\rho \sigma_0, \text{ which integrates to} \quad (\text{A.5})$$

$$\sigma_0 n = \tilde{I}_0 - \tilde{I}_f. \quad (\text{A.6})$$

We recognize the right-hand sides of equation (A.4) and equation (A.6) as the two terms in equation (4). Thus, as shown in figure 3, OD^{sim1} coincides with the optical depth as predicted by equation (4) in both the small and large probe intensity limits.

We used the results of this simulation to check the self-consistency of the stationary atom assumption, i.e. the distance traveled by the atoms (as deduced from integrating the acquired recoil velocity over the imaging time) is less than the bin size. As shown in figure A1(b), not only do the atoms travel more than the bin size, but they travel far beyond the initial extent of the cloud. Moreover, owing to the higher initial scatter rate, the back of the cloud overtakes the front for long imaging times. Thus, the atomic distribution as a function of position changes dramatically during the imaging pulse, and the stationary assumption is invalid.

A.3. Traveling atom model

To account for the changing atomic distribution during the imaging pulse, we numerically simulated the classical kinetics of atoms subject to the recoil driven optical forces. To simulate large ensembles in a reasonable time, we modeled composite atoms, each describing the aggregate behavior of N_{ca} atoms. The amended algorithm is shown in algorithm 2.

Algorithm 2. Travelling atom model

```

 $z[n] = z_0, \tilde{\delta}[n] = 0$  { initialize position and detuning for each composite atom, labeled by index  $n$  }
 $O[i] = n$  { make a list of composite atom indexes, ordered by position }
 $\tilde{I}[n = 0, t] = \tilde{I}_0$  {  $t$  is the time index }
 $H_f = 0$  { Radiant fluence seen by camera after passing through cloud }
for  $t = 0$  to  $t_f$  do { loop over time steps }
  for  $i = 1$  to  $N_{\text{ca}}$  do { loop over composite atoms }
     $n = O[i]$  { apply probe intensity to composite atoms in order of appearance }
     $A = \sigma_0 N_{\text{ca}} dz$  {  $dz$  is length over which atoms were grouped into single composite atom }
     $B = v_r dt / (\hbar c N_{\text{sa}})$  {  $dt$  is the time step }
     $\tilde{I}[n, t] = \tilde{I}[n - 1, t] - A \tilde{I}[n - 1, t] / (1 + 4\tilde{\delta}[n]^2 + \tilde{I}[n - 1, t])$  { equation (5) }
     $\tilde{\delta}[n] + = B(\tilde{I}[n - 1, t] - \tilde{I}[n, t])$  { equation (6) }
     $z[n] + = dt \Gamma \tilde{\delta} / 2k_r$  {  $\Gamma \tilde{\delta} / 2k_r$  is the velocity at  $\tilde{\delta}$  detuning }
  end for
   $O[i] = \text{sort}(n, \text{key} = z[n])$  { sort composite atom indexes by current position }
   $H_f H_f + \tilde{I}[N, t] dt$  { collecting total fluence seen by the camera }
end for
 $\text{OD}^{\text{sim2}} = -\ln(H_f / \tilde{I}_0 t_f)$ 

```

To validate our code, we again checked the velocity predicted in this model against known limits. One such limit is that of a single composite atom. In this case, there is no attenuation, and the intensity seen by the composite atom is constant at \tilde{I}_0 . Only the detuning evolves in time, and equations (5) and (6) give

$$\frac{d\tilde{\delta}(t)}{dt} = \frac{k_r v_r}{2} \frac{\tilde{I}}{1 + 4\tilde{\delta}^2 + \tilde{I}}. \quad (\text{A.7})$$

Equation (A.7) can be solved numerically, and is in agreement with our simulation, as seen in figure A2(a).

We used this model to study the time evolution of the cloud shape during imaging and visualized the phase space evolution of superatoms, shown in figure A3. The cloud shape is strongly distorted during imaging.

We compared the optical depths predicted by each of the two models, OD^{sim1} and OD^{sim2} . As seen in figure A2(b), the predicted optical depths were hardly changed by including the full time evolution: $|\text{OD}^{\text{sim1}} - \text{OD}^{\text{sim2}}| / \text{OD}^{\text{sim1}} \leq 0.01$ for times up to 100 μs , \tilde{I}_0 up to 50 and $\sigma_0 n$ up to 2.0.

Appendix B

We used a Zeeman slower to slow both ^{87}Rb and ^{40}K before capturing in a magneto-optical trap (MOT). After 7 seconds of MOT loading ^{40}K followed by 1.5 s of loading both ^{40}K and ^{87}Rb , we cooled both species in optical molasses for 2 ms. We optically pumped both species into their maximally stretched magnetically trappable states, $|F = 9/2, m_F = 9/2\rangle$ for ^{40}K and $|F = 2, m_F = 2\rangle$ for ^{87}Rb . Both species were then loaded into a quadrupole magnetic trap with a gradient of $\approx 7.68 \text{ mT cm}^{-1}$ along \mathbf{e}_z , and cooled evaporatively via forced rf evaporation, sweeping the rf frequency from 18 to 2 MHz in 10 s. The magnetic trap was plugged by a $\lambda = 532 \text{ nm}$ beam, tightly focused to $\approx 30 \mu\text{m}$ and $\approx 5 \text{ W}$ in power, providing a repulsive potential around the

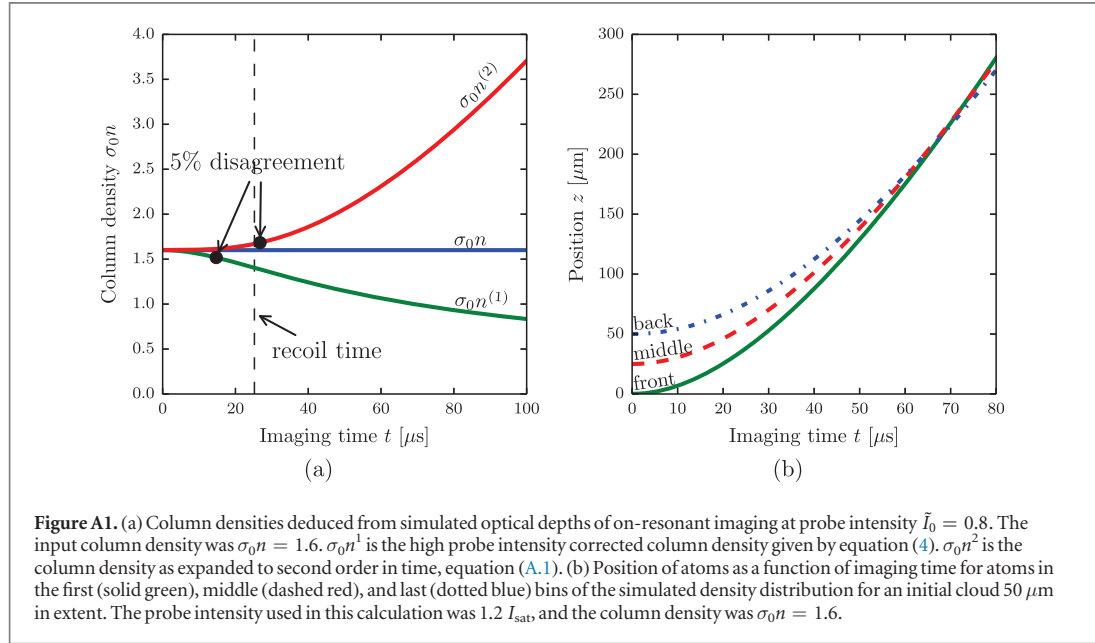


Figure A1. (a) Column densities deduced from simulated optical depths of on-resonant imaging at probe intensity $\tilde{I}_0 = 0.8$. The input column density was $\sigma_0 n = 1.6$. $\sigma_0 n^{(1)}$ is the high probe intensity corrected column density given by equation (4). $\sigma_0 n^{(2)}$ is the column density as expanded to second order in time, equation (A.1). (b) Position of atoms as a function of imaging time for atoms in the first (solid green), middle (dashed red), and last (dotted blue) bins of the simulated density distribution for an initial cloud $50 \mu\text{m}$ in extent. The probe intensity used in this calculation was $1.2 I_{\text{sat}}$, and the column density was $\sigma_0 n = 1.6$.

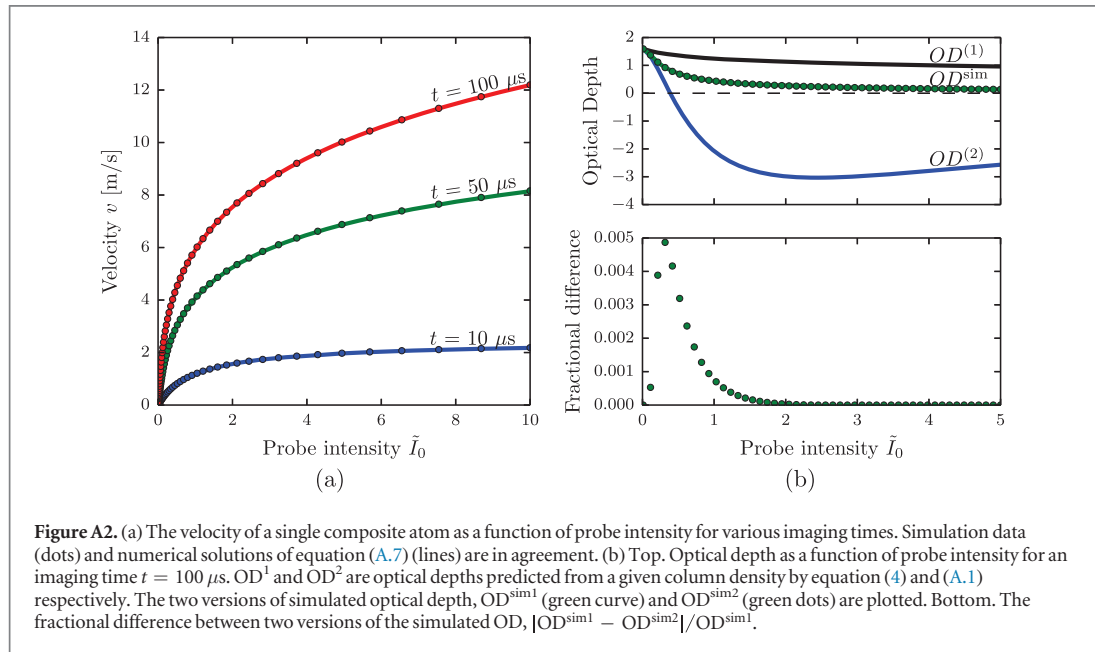
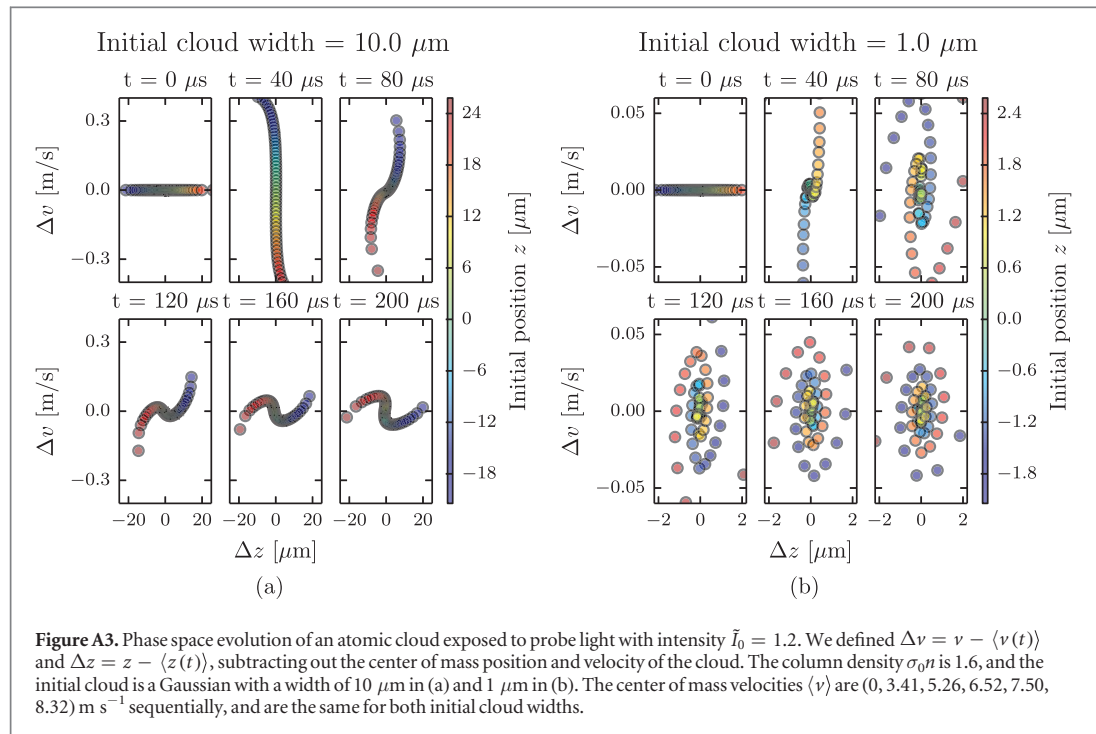


Figure A2. (a) The velocity of a single composite atom as a function of probe intensity for various imaging times. Simulation data (dots) and numerical solutions of equation (A.7) (lines) are in agreement. (b) Top. Optical depth as a function of probe intensity for an imaging time $t = 100 \mu\text{s}$. $OD^{(1)}$ and $OD^{(2)}$ are optical depths predicted from a given column density by equation (4) and (A.1) respectively. The two versions of simulated optical depth, $OD^{\text{sim}1}$ (green curve) and $OD^{\text{sim}2}$ (green dots) are plotted. Bottom. The fractional difference between two versions of the simulated OD, $|OD^{\text{sim}1} - OD^{\text{sim}2}|/OD^{\text{sim}1}$.

zero field point to prevent Majorana losses. Since the ^{40}K atoms were spin polarized and therefore only interacted by the strongly suppressed p -wave interactions, they re-thermalized largely due to sympathetic cooling with ^{87}Rb atoms.

We then loaded the atoms into a crossed optical dipole trap, provided by a 1064nm fiber laser, and continued evaporative cooling by slowly ramping down the dipole trap to trap frequencies of $(\omega_x, \omega_y, \omega_z)/2\pi = (39, 42, 124)$ Hz (for potassium atoms) in the three spatial directions, while also turning off the quadrupole field. We then used ARP to transfer the ^{87}Rb atoms from the $|F = 2, m_F = 2\rangle$ state to the $|F = 1, m_F = +1\rangle$ absolute ground state via 6.8556 GHz microwave coupling (20.02 MHz from the zero field resonance) followed by a magnetic field sweep from -0.469 to -0.486 mT in 50 ms. This state was chosen to minimize spin changing collisions with ^{40}K atoms during any further evaporation [37]. We then briefly applied an on-resonant probe laser, ejecting any remaining ^{87}Rb atoms in the $F = 2$ manifold from the trap. We again used ARP to transfer the ^{40}K atoms into the $|F = 9/2, m_F = -9/2\rangle$ state by using a 3.3 MHz rf field and sweeping the bias magnetic field from -0.518 to -0.601 mT in 150 ms.



References

- [1] Greiner M, Regal C A and Jin D S 2003 Emergence of a molecular Bose–Einstein condensate from a Fermi gas *Nature* **426** 537–40
- [2] Zwierlein M W, Stan C A, Schunck C H, Raupach S M F, Gupta S, Hadzibabic Z and Ketterle W 2003 Observation of Bose–Einstein condensation of molecules *Phys. Rev. Lett.* **91** 250401
- [3] Jochim S, Bartenstein M, Altmeyer A, Hendl G, Riedl S, Chin C, Hecker Denschlag J and Grimm R 2003 Bose–Einstein condensation of molecules *Science* **302** 2101–3
- [4] Bartenstein M, Altmeyer A, Riedl S, Jochim S, Chin C, Hecker Denschlag J and Grimm R 2004 Collective excitations of a degenerate gas at the BEC–BCS crossover *Phys. Rev. Lett.* **92** 203201
- [5] Bourdel T, Khaykovich L, Cubizolles J, Zhang J, Chevy F, Teichmann M, Tarruell L, Kokkelmans S J J M F and Salomon C 2004 Experimental study of the BEC–BCS crossover region in lithium 6 *Phys. Rev. Lett.* **93** 050401
- [6] Zwierlein M W, Stan C A, Schunck C H, Raupach S M F, Kerman A J and Ketterle W 2004 Condensation of pairs of fermionic atoms near a Feshbach resonance *Phys. Rev. Lett.* **92** 120403
- [7] Regal C A, Greiner M and Jin D S 2004 Observation of resonance condensation of fermionic atom pairs *Phys. Rev. Lett.* **92**
- [8] Chin C, Grimm R, Julienne P and Tiesinga E 2010 Feshbach resonances in ultracold gases *Rev. Mod. Phys.* **82** 1225–86
- [9] Timmermans E, Tommasini P, Hussein M S and Kerman A 1999 Feshbach resonances in atomic Bose–Einstein condensates *Phys. Rep.-Rev. Section Phys. Lett.* **315** 199–230
- [10] Tiesinga E, Verhaar B J and Stoof H T C 1993 Threshold and resonance phenomena in ultracold ground-state collisions *Phys. Rev. A* **47** 4114–22
- [11] Lysebo M and Veseth L 2009 *Ab initio* calculation of Feshbach resonances in cold atomic collisions: *s*- and *p*-wave Feshbach resonances in $^6\text{Li}_2$ *Phys. Rev. A* **79** 062704
- [12] Gao B 2011 Analytic description of atomic interaction at ultracold temperatures: II. Scattering around a magnetic Feshbach resonance *Phys. Rev. A* **84** 022706
- [13] Inouye S, Andrews M R, Stenger J, Miesner H J, Stamper–Kurn D M and Ketterle W 1998 Observation of Feshbach resonances in a Bose–Einstein condensate *Nature* **392** 151–4
- [14] Cornish S L, Claussen N R, Roberts J L, Cornell E A and Wieman C E 2000 Stable Rb–85 Bose–Einstein condensates with widely tunable interactions *Phys. Rev. Lett.* **85** 1795–8
- [15] Regal C A and Jin D S 2003 Measurement of positive and negative scattering lengths in a Fermi gas of atoms *Phys. Rev. Lett.* **90** 230404
- [16] O’Hara K M, Hemmer S L, Gehm M E, Granade S R and Thomas J E 2002 Observation of a strongly interacting degenerate Fermi gas of atoms *Science* **298** 2179–82
- [17] Monroe C, Cornell E, Sackett C, Myatt C and Wieman C 1993 Measurement of Cs–Cs elastic scattering at $T = 30 \mu\text{K}$ *Phys. Rev. Lett.* **70** 414–7
- [18] Bartenstein M et al 2005 Precise determination of ^6Li cold collision parameters by radio-frequency spectroscopy on weakly bound molecules *Phys. Rev. Lett.* **94** 103201
- [19] Zürn G, Lompe T, Wenz A N, Jochim S, Julienne P S and Hutson J M 2013 Precise characterization of ^6Li Feshbach resonances using trap-sideband-resolved RF spectroscopy of weakly bound molecules *Phys. Rev. Lett.* **110** 135301
- [20] Chikkatur A P, Görlitz A, Stamper–Kurn D M, Inouye S, Gupta S, Ketterle W 2000 Suppression and enhancement of impurity scattering in a Bose–Einstein condensate *Phys. Rev. Lett.* **85** 483–6
- [21] Thomas N R, Kjærgaard N, Julienne P S and Wilson A C 2004 Imaging of *s* and *d* partial-wave interference in quantum scattering of identical bosonic atoms *Phys. Rev. Lett.* **93** 173201
- [22] Williams R A, LeBlanc L J, Jiménez-García K, Beeler M C, Perry A R, Phillips W D and Spielman I B 2012 Synthetic partial waves in ultracold atomic collisions *Science* **335** 314–7

- [23] Aikawa K, Frisch A, Mark M, Baier S, Grimm R and Ferlaino F 2014 Reaching Fermi degeneracy via universal dipolar scattering *Phys. Rev. Lett.* **112** 010404
- [24] Lu M, Burdick N Q and Lev B L 2012 Quantum degenerate dipolar Fermi gas *Phys. Rev. Lett.* **108** 215301
- [25] Metcalf H J and van der Straten P 1999 *Laser Cooling and Trapping (Graduate Texts in Contemporary Physics vol 26)* (New York: Springer)
- [26] Reinaudi G, Lahaye T, Wang Z and Guéry-Odelin D 2007 Strong saturation absorption imaging of dense clouds of ultracold atoms *Opt. Lett.* **32** 3143–5
- [27] Konstantinidis G O, Pappa M, Wikstroem G, Condylis P C, Sahagun D, Baker M, Morizot O and von Klitzing W 2012 Atom number calibration in absorption imaging at very small atom numbers *Cent. Eur. J. Phys.* **10** 1054–8
- [28] Tiecke T G 2009 Feshbach resonances in ultracold mixtures of the fermionic quantum gases ^6Li and ^{40}K *PhD Thesis* University of Amsterdam
- [29] Williams R A, Beeler M C, LeBlanc L J, Jiménez-García K and Spielman I B 2013 Raman-induced interactions in a single-component Fermi gas near an s -wave Feshbach resonance *Phys. Rev. Lett.* **111** 095301
- [30] Lin Y-J, Perry A R, Compton R L, Spielman I B and Porto J V 2009 Rapid production of ^{87}Rb Bose–Einstein condensates in a combined magnetic and optical potential *Phys. Rev. A* **79** 063631
- [31] Jimenez-Garcia K 2012 Artificial gauge fields for ultracold neutral atoms *PhD Thesis* Joint Quantum Institute, National Institute of Standards and Technology, and the University of Maryland
- [32] DeMarco B, Bohn J L, Burke J P, Holland M and Jin D S 1999 Measurement of p -wave threshold law using evaporatively cooled fermionic atoms *Phys. Rev. Lett.* **82** 4208–11
- [33] Wu S, Wang Y-J, Diot Q and Prentiss M 2005 Splitting matter waves using an optimized standing-wave light-pulse sequence *Phys. Rev. A* **71** 043602
- [34] Edwards M, Benton B, Heward J and Clark C W 2010 Momentum-space engineering of gaseous Bose–Einstein condensates *Phys. Rev. A* **82** 063613
- [35] Bracewell R 1965 *The Fourier Transform and its Applications* (New York: McGraw-Hill)
- [36] LeBlanc L J 2011 Exploring many-body physics with ultracold atoms *PhD Thesis* University of Toronto
- [37] Best T 2010 Interacting Bose–Fermi mixtures in optical lattices *PhD Thesis* Johannes Gutenberg-Universität

APPENDIX D
GEOMETRICAL PUMPING WITH A BOSE-EINSTEIN CONDENSATE

Geometrical Pumping with a Bose-Einstein Condensate

H.-I. Lu,¹ M. Schemmer,^{1,2} L. M. Aycok,^{1,3} D. Genkina,¹ S. Sugawa,¹ and I. B. Spielman^{1,*}

¹*Joint Quantum Institute, National Institute of Standards and Technology,
and University of Maryland, Gaithersburg, Maryland 20899, USA*

²*École Normale Supérieure de Lyon, F-69364 Lyon, France*

³*Cornell University, Ithaca, New York 14850, USA*

(Received 17 August 2015; revised manuscript received 21 April 2016; published 20 May 2016)

We realized a quantum geometric “charge” pump for a Bose-Einstein condensate (BEC) in the lowest Bloch band of a novel bipartite magnetic lattice. Topological charge pumps in filled bands yield quantized pumping set by the global—topological—properties of the bands. In contrast, our geometric charge pump for a BEC occupying just a single crystal momentum state exhibits nonquantized charge pumping set by local—geometrical—properties of the band structure. Like topological charge pumps, for each pump cycle we observed an overall displacement (here, not quantized) and a temporal modulation of the atomic wave packet’s position in each unit cell, i.e., the polarization.

DOI: 10.1103/PhysRevLett.116.200402

Ultracold atoms in optical lattices provide a unique setting for experimentally studying concepts that lie at the heart of theoretical condensed matter physics, but are out of reach of current condensed matter experiments. Here, we focus on the connection between topology, geometry, and adiabatic charge pumping [1–7] for Bose-Einstein condensates (BECs) in cyclically driven lattice potentials.

Particles in periodic potentials form Bloch bands with energy $\epsilon_n(q)$ and eigenstates $|\Psi_n(q)\rangle = \exp(iq\hat{x})|u_n(q)\rangle$ labeled by the crystal momentum q along with the band index n . The states $|u_n\rangle$ retain the underlying periodicity of the lattice, set by the unit cell size a . Motion in lattices is conventionally understood in terms of these bands: metals are materials with partially filled bands, while insulators have completely filled bands. In this context, a topological charge pump is a counterintuitive device, where charge motion—conduction—accompanies the adiabatic and cyclic drive of an insulating lattice’s parameters. Thouless showed that this conduction is quantized, completely governed by the band topology [8,9]. Although various charge pumps have been realized in condensed matter devices—such as modulated quantum dots [10–12], one-dimensional (1D) channels driven by surface acoustic waves [13], and superconducting qubits [14]—Thouless pumps remain unrealized in condensed matter settings but have been demonstrated in recent experiments with cold-atom insulators [15,16].

Here, we break from this established paradigm for insulators and create a quantum charge pump for a BEC in a 1D lattice [17–19] occupying a single crystal momentum state q . This charge pump gives nonquantized motion sensitive to the Berry curvature at q integrated over the whole pump cycle, a local geometric quantity, rather than a global topological quantity. Berry curvatures play an important role in condensed matter systems. An iconic

example is the integer quantum Hall effect, where the electrons acquire an anomalous transverse velocity proportional to the Berry curvature and the quantized Hall conductance is given by the Berry curvature integrated over the whole two-dimensional (2D) Brillouin zone (BZ) [20]; recent cold-atom experiments in 2D have measured such curvatures integrated over part [21,22] or all [23] of the BZ. In an analogous way, 1D lattice systems, driven cyclically in time t , have a generalized Berry curvature defined on the 2D effective BZ in q, t space. This curvature is the source of an anomalous velocity [24], utilized to drive an adiabatic quantum pumping process.

The Rice-Mele model [25–28] of a bipartite lattice with a unit cell consisting of A and B sites is the paradigmatic system for understanding quantum pumps. The Hamiltonian for this tight-binding model is

$$\hat{H}_{\text{RM}} = - \sum_j [(t + \delta t)\hat{b}_j^\dagger \hat{a}_j + (t - \delta t)\hat{a}_{j+1}^\dagger \hat{b}_j + \text{H.c.}] + \Delta \sum_j (\hat{a}_j^\dagger \hat{a}_j - \hat{b}_j^\dagger \hat{b}_j), \quad (1)$$

where \hat{a}_j^\dagger and \hat{b}_j^\dagger describe the creation of a particle in unit cell j and sublattice site A or B , respectively. The nominal tunneling strength t is staggered by δt , and the sublattice sites are shifted in energy by Δ .

We investigated quantum pumping in a novel 1D (along \mathbf{e}_x) bipartite magnetic lattice (building on Refs. [29,30]) that in effect allowed independent control of t , δt , and Δ . As shown in Figs. 1(a) and 1(b), our magnetic lattice for ^{87}Rb arose from the interplay of one rf and two Raman fields that coupled the $|f = 1; m_F = \pm 1, 0\rangle$ “spin” states comprising the $f = 1$ ground state hyperfine manifold, which were Zeeman split by $\hbar\omega_Z$. The natural units of momentum and energy are given by the single photon recoil momentum

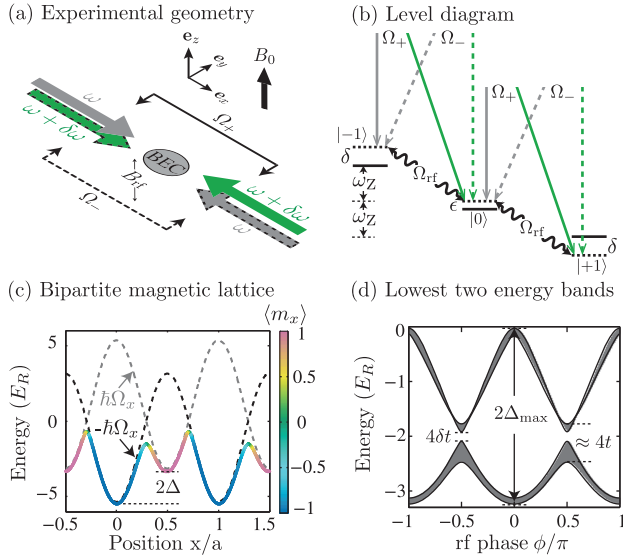


FIG. 1. Bipartite magnetic lattice. [(a) and (b)] Dipole trapped ^{87}Rb BECs subject to a bias magnetic field $B_0\mathbf{e}_z$ had a Zeeman splitting $\omega_Z/2\pi = 0.817$ MHz and a quadratic shift $\hbar\epsilon = 0.03E_R$. These BECs were illuminated by four Raman beams and an rf magnetic field. Each of the two Raman couplings (strengths Ω_{\pm}) was derived from two cross-polarized Raman laser beams with frequency components ω and $\omega + \delta\omega$. (c) Adiabatic potentials colored according to $\langle m_x \rangle$ computed for $\hbar(\bar{\Omega}, \Omega_{\text{rf}}, \delta) = (6, 2.2, 0)E_R$, $\delta\Omega/\bar{\Omega} = -0.1$, and $\phi = \pi/4$. The dashed curves plot the $\pm\hbar\Omega_x$ contributions to the potential experienced by states $|m_x = \pm 1\rangle$. (d) Lowest two energy band energies plotted as a function of ϕ , otherwise with the same parameters as (c).

$\hbar k_R = 2\pi\hbar/\lambda_R$ and its corresponding energy $E_R = \hbar^2 k_R^2/2m$, where m is the atomic mass. In the frame rotating at the rf frequency $\delta\omega$ and under the rotating wave approximation, the combined rf-Raman coupling lead [31] to the overall Hamiltonian

$$\hat{H} = \frac{\hbar^2 \hat{k}_x^2}{2m} + \Omega(\hat{x}) \cdot \hat{\mathbf{F}} + \hat{H}_Q, \quad (2)$$

where $\hat{\mathbf{F}}$ is the total angular momentum vector operator. We interpret $\Omega(\hat{x}) = [\Omega_{\text{rf}} \cos(\phi) + \bar{\Omega} \cos(2k_R\hat{x}), -\Omega_{\text{rf}} \sin(\phi) - \delta\Omega \sin(2k_R\hat{x}), \sqrt{2}\delta]/\sqrt{2}$ as a spatially periodic effective Zeeman magnetic field, in which Ω_{rf} is the rf coupling strength; $\bar{\Omega} = \Omega_+ + \Omega_-$ and $\delta\Omega = \Omega_+ - \Omega_-$ are derived from the individual Raman coupling strengths Ω_{\pm} ; $\delta = \delta\omega - \omega_Z$ is the detuning from Raman-rf resonance; and ϕ is the relative phase between the rf and Raman fields. Additionally, $H_Q = -\epsilon(\hbar^2\hat{1} - \hat{F}_z^2)/\hbar$ describes the quadratic Zeeman shift, where $\hat{1}$ is the identity operator.

This spatially varying effective magnetic field produces a 1D bipartite lattice [2,32] with lattice constant $a = \lambda_R/2$ and with adiabatic (Born-Oppenheimer) potentials depicted in Fig. 1(c). This magnetic lattice is most easily conceptualized for small $\delta\Omega$: the $\bar{\Omega} \cos(2k_R\hat{x})$ term provides

periodic potentials for the $|m_x = \pm 1\rangle$ states spatially displaced from each other by $a/2$ [dashed curves in Fig. 1(c)]; the resulting $m_x = \pm 1$ sites are then staggered in energy, giving $\Delta \approx \Delta_{\text{max}} \cos(\phi)$, with $\Delta_{\text{max}} = \Omega_{\text{rf}}/\sqrt{2}$. The Ω_y term couples these sublattices together: the rf term $-\Omega_{\text{rf}} \sin(\phi)$ generates constant height barriers (largely specifying t), which become staggered by the $-\delta\Omega \sin(2k_R\hat{x})$ contribution (largely specifying δt).

Figure 1(d) plots the energies of the resulting lowest two bands as a function of ϕ (modulating Δ sinusoidally). Although our lattice is not in the tight-binding limit, the band structure qualitatively matches that of the Rice-Mele model. In the remainder of this Letter, we focus on the lowest band $n = 0$ and henceforth omit the band index.

As illustrated by the shading in Fig. 1(c), in each unit cell the sublattice sites are labeled by their \hat{F}_x spin projection with the $|m_x = -1\rangle$ site on the left and $|m_x = +1\rangle$ site on the right. To confirm this, we adiabatically loaded $|m_z = -1\rangle$ BECs into the lattice's ground state by simultaneously ramping the detuning from $5E_R$ to 0 while ramping on the coupling fields in 10 ms. Following preparation, our measurement sequence began with a $\pi/2$ spin rotation along \mathbf{e}_y , allowing us to measure the eigenstates of \hat{F}_x in our \hat{F}_z measurement basis. We achieved this $\pi/2$ rotation (rot) with a $44 \mu\text{s}$ pulse from an additional rf field with phase $\phi_{\text{rot}} = \pi/2$ and strength $\hbar\Omega_{\text{rf,rot}} = 2.2E_R$, applied while the Raman coupling was greatly reduced ($\bar{\Omega} \ll \Omega_{\text{rf,rot}}$) and the lattice rf coupling was off ($\Omega_{\text{rf}} = 0$). We then abruptly removed the remaining control fields along with the confining potential and absorption imaged the resulting spin-resolved momentum distribution after a 20 ms time-of-flight period in the presence of a magnetic field gradient along \mathbf{e}_y .

Figure 2 shows the measured \hat{F}_x spin composition [33] and magnetization for adiabatically loaded BECs as a function of ϕ with $\delta\Omega = 0$. Because $\Delta(\phi)$ controls the relative depth of the $|m_x = \pm 1\rangle$ wells, we observe ground state spin populations that follow this ‘‘tilt.’’ For example, when $\phi = 0$ or π the double well is strongly tilted and we observe the near perfect spin magnetization, consistent with atoms residing in the individual sublattices; in contrast, when $\phi = \pi/2$, the double wells are balanced and we observe equal populations in each $|m_x\rangle$ state as expected for equal occupancy of both sublattices. Thus, the magnetization [Fig. 2(b)] measures the mean atomic position within each unit cell, i.e., the polarization.

Having constructed a physical realization of the Rice-Mele model, and demonstrated the requisite control and measurement tools, we now turn our attention to topological and geometrical charge pumping. These fundamentally quantum mechanical effects rely on the canonical commutation relation between position and momentum. Consider a finite wave packet with a center of mass (c.m.) position $\langle x \rangle = \langle \Psi | \hat{x} | \Psi \rangle$, subject to a lattice Hamiltonian \hat{H} that is

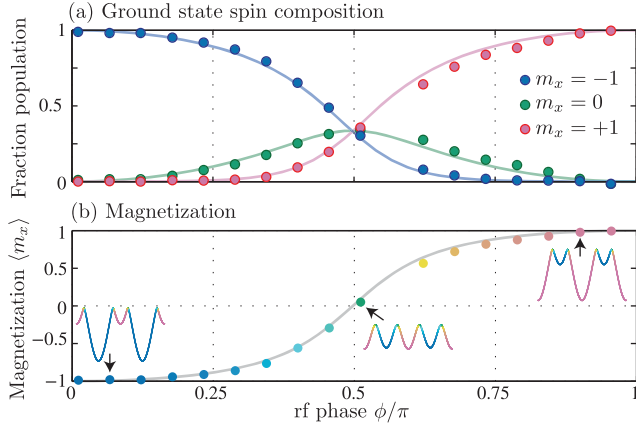


FIG. 2. Ground state spin projections. (a) Ground state spin projections at various ϕ along with the predicted populations for $\hbar(\bar{\Omega}, \delta\Omega, \Omega_{\text{rf}}, \delta) = (4.4, 0, 2.2, 0)E_R$. The associated adiabatic potentials [insets in (b)] have minima with spin projection following the observed population's trends. (b) Magnetization derived from data in (a).

adiabatically modulated with period T , i.e., $\hat{H}(t) = \hat{H}(t + T)$. After one cycle, any initial crystal momentum state is transformed, $|\Psi(q)\rangle \rightarrow \exp[i\gamma(\hat{q})]|\Psi(q)\rangle$, at most acquiring a phase, where \hat{q} is the crystal momentum operator; this defines the single-period evolution operator $\hat{U}_T = \exp[i\gamma(\hat{q})]$. The time-evolved position operator $\hat{U}_T^\dagger \hat{x} \hat{U}_T = \hat{x} - \partial_{\hat{q}}\gamma(\hat{q})$ is displaced after a single pump cycle.

The displacement is particularly simple in two limits: when just a single crystal momentum state is occupied or when every crystal momentum state in the BZ, $-\pi/a \leq q < \pi/a$, is occupied with equal probability. As for our BEC, when a single $|q_0\rangle$ state is occupied the displacement is $\Delta x(q_0) = -\partial_q \gamma(q)|_{q_0}$. Both the dynamical (D) phase $\gamma_D(q) = -\bar{\epsilon}(q)T/\hbar$ from the time-average energy $\bar{\epsilon}(q)$ and the geometric Berry (B) phase $\gamma_B(q) = i \int_0^T \langle u | \partial_t u \rangle dt$ contribute to $\gamma(q) = \gamma_D(q) + \gamma_B(q)$. In agreement with conventional descriptions [18,24,27], this predicts a mean velocity $\bar{v}(q) = \partial_q \bar{\epsilon}(q)/\hbar - T^{-1} \int_0^T F(q, t) dt$. The first term is the usual group velocity and the second term—the anomalous velocity—derives from the Berry curvature $F(q, t) = i(\langle \partial_q u | \partial_t u \rangle - \langle \partial_t u | \partial_q u \rangle)$. In our experiment, the BEC occupied the minimum of $\epsilon(q, t)$ at $q = 0$ during the whole pump cycle giving $\partial_q \bar{\epsilon}(q) = 0$, so only the geometric phase $\gamma_B(q)$ contributed to the per-cycle displacement $\Delta x(q = 0) = -\int_0^T F(q = 0, t) dt$.

In the contrasting case of a filled band, the average group velocity is also 0 and the displacement is $\Delta x = -a \int_{\text{BZ}} \partial_q \gamma_B(q) dq / 2\pi$; this is often expressed as $\Delta x = a \int_0^T \partial_t \gamma_{\text{Zak}}(t) dt / 2\pi$. The Zak phase $\gamma_{\text{Zak}} = i \int_{\text{BZ}} \langle u | \partial_q u \rangle dq$, a topological property of 1D bands, is the Berry's phase associated with traversing the 1D BZ once, in the same way that $\gamma_B(q)$ is a Berry's phase taken over a pump cycle.

Our lattice's Zak phase is plotted in Fig. 3(a); this Zak phase is qualitatively indistinguishable from that of the Rice-Mele model, with singularities at $\phi = \pm\pi/2$ and $\delta\Omega = 0$, signaling topological phase transitions across these points. For filled band experiments, pumping trajectories encircling these points give quantized charge pumping [15,16]. Figure 3(b) shows the richly structured Berry curvature $F(q = 0, \phi)$ relevant to our experiment, which is explored next.

For our charge pump experiments, we linearly ramped the pump control parameter $\phi(t) = 2\pi t/T$, effectively modulating the lattice potential in two qualitatively different regimes (separated by a critical $|\delta\Omega/\bar{\Omega}| \approx 0.63$). In the first [Fig. 3(c), left panel] the sublattice sites rise and fall but the local potential minima are essentially fixed in space; in the second [Fig. 3(c), right panel] each minimum is only present for part of the pump cycle (the potential appears to “slide” by $\pm a$ per cycle). As these schematics imply, the associated pumping process gives either no displacement or a quantized per-cycle displacement $\pm a$ for classical trajectories [34]. In quantum systems, however, geometrical

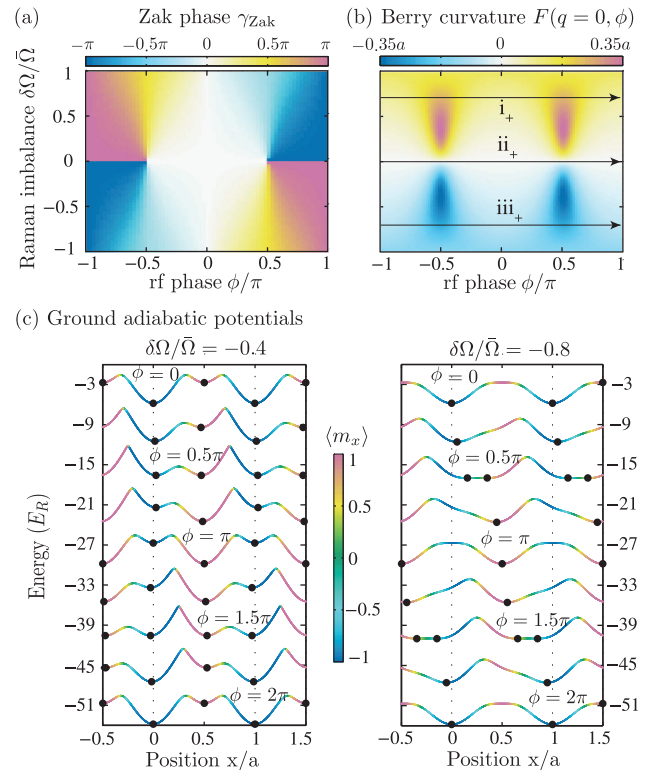


FIG. 3. Band geometry and topology computed for $\hbar(\bar{\Omega}, \Omega_{\text{rf}}, \delta) = (6, 2.2, 0)E_R$. [(a) and (b)] Zak phase and $q = 0$ Berry curvature showing the dependence on both $\delta\Omega/\bar{\Omega}$ and ϕ . In (b), the arrows show experimental charge pump trajectories in Fig. 4(b). (c) Adiabatic potentials (displaced vertically for clarity) computed for a range of ϕ constituting a complete pump cycle at $\delta\Omega/\bar{\Omega} = -0.4$ (left panel) and -0.8 (right panel). Filled circles mark the local energy minima.

pumping is controlled by the Berry curvature, giving nonquantized per-cycle displacements that can, in principle, take on any value.

We studied adiabatic charge pumping in this lattice in two ways: in the first we observed the \hat{F}_x magnetization, giving the polarization within the unit cells, and in the second we directly measured the displacement Δx of our BEC. In both cases we loaded into the lattice's ground state and linearly ramped $\phi = 2\pi t/T$, driving the Hamiltonian with period T [34]. As shown in Fig. 4(a), the magnetization oscillated with the $T = 2$ ms period, demonstrating the periodic modulation of polarization per cycle. In good agreement with our data, the solid curves in Fig. 4(a) show the predicted behavior given our known system parameters. This agreement persists to long times: for example, after 50 pumping cycles (for $t = 100$ ms to 110 ms) the contrast is unchanged, confirming the adiabaticity of the process [34].

Lastly, we performed a charge pumping experiment by directly measuring the cloud's position *in situ* for a range of $\delta\Omega/\bar{\Omega}$. We obtained *in situ* density distributions using partial-transfer absorption imaging [35] in which ≈ 6.8 GHz microwave pulses transferred $\approx 5\%$ of the atoms from $|f, m_z\rangle = |1, -1\rangle$ to $|2, 0\rangle$ where they were absorption imaged. This technique allowed us to repeatedly measure the *in situ* density distribution for each BEC. Each observed displacement was derived from differential measurements of the cloud position taken just before and just after the pumping process, rendering our observations insensitive to micron-level drift in the trap position between different realizations.

Figure 4(b) shows data taken for $\delta\Omega/\bar{\Omega} = 0.7, 0$, and -0.7 along trajectories i, ii, and iii, respectively, with both increasing and decreasing phases. Our data display two expected symmetry properties. First, since the displacement $\Delta x(q = 0) = -\int F(q, \phi)d\phi$ depends on the sign of the acquired phase, the direction of motion is reversed when the ramp direction is inverted. Second, as shown in Fig. 3(b),

$F(q = 0, \phi)$ is an odd function of $\delta\Omega/\bar{\Omega}$, so the direction of motion is also reversed when $\delta\Omega/\bar{\Omega} \rightarrow -\delta\Omega/\bar{\Omega}$. Thus, Δx is an odd function of both ϕ and $\delta\Omega/\bar{\Omega}$, and as expected we observe no motion when $\delta\Omega/\bar{\Omega} = 0$.

The displacement was markedly nonlinear when the pumping time became comparable to our trap's 80 ms period, showing the influence of the confining potential [36]. We included the harmonic potential in our real-space simulations by directly solving the time-dependent Schrödinger equation for our system [37]. The simulated results [Fig. 4(b), solid curves] agree with our observations. To extract the per-cycle displacement due to geometric pumping, we fit the sinusoidal predictions of our model to each data trace, with only the overall amplitudes and a small vertical offset as free parameters, giving the short-time per-cycle displacement [34]. Figure 4(c) shows these per-cycle displacements for a range of Raman imbalances.

The *in situ* cloud typically had a Thomas-Fermi radius of $30 \mu\text{m}$, corresponding to a small momentum width of $0.004k_R$ for our BEC. We estimated the thermal fraction to be $\approx 5\%$ given by our ≈ 20 nK temperature (momentum width of $0.24k_R$). Moreover, the per-cycle displacement is nearly independent of q for $|q| < 0.25k_R$ [34]. These allow us to compare the data with the expected displacement from integrating $q = 0$ Berry curvature [Fig. 4(c), solid line], showing an excellent agreement and confirming the geometric origin of our quantum charge pump.

Our magnetic lattice enables new experiments with 1D topological lattices. Berry curvatures at $q \neq 0$ can be probed by performing the charge pump pairwise at $\pm|q|$ (for example, prepared via Bloch oscillations [38]). The dynamical phases in these cases are opposite and therefore cancel while Berry curvatures (even in q) contribute equally to the displacements [34]. Furthermore, protected edge states, a hallmark of topological systems, are present at the interface between regions characterized by different

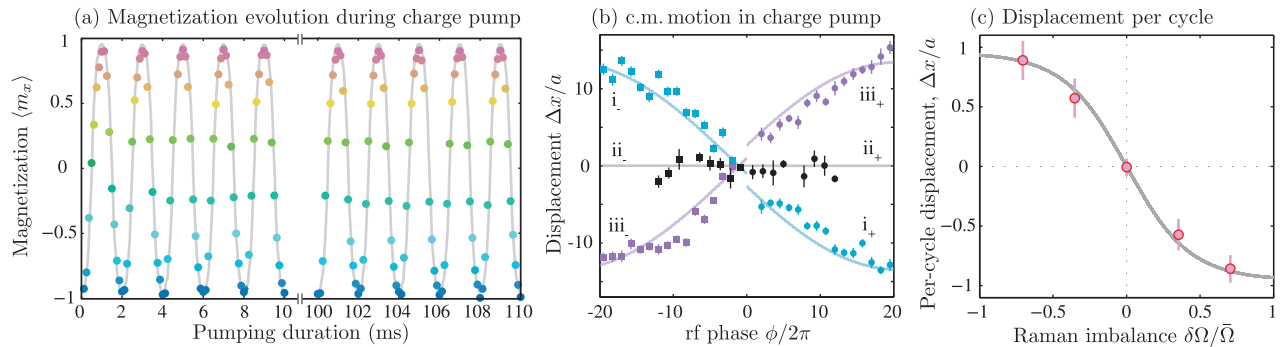


FIG. 4. Geometric charge pumping. (a) Magnetization measured while linearly ramping ϕ with period $T = 2$ ms, along with the prediction for $\hbar\bar{\Omega} = 6.38(2)E_R$, $\hbar\delta\Omega = 4.50(2)E_R$, and $\hbar\Omega_{\text{rf}} = 2.20(3)E_R$. (b) Displacement plotted versus $\phi/2\pi$ (number of pump cycles). Trajectories i–iii are taken at $\delta\Omega/\bar{\Omega} = 0.7, 0$, and -0.7 , respectively; in each case $\hbar\bar{\Omega} \approx 6E_R$ and $\hbar\Omega_{\text{rf}} = 2.20(3)E_R$. Solid curves: simulation of a charge pump in the trap. The small displacement near $\phi = 0$ is introduced by our loading procedure. (c) Measured displacement Δx per pump cycle (symbols), along with the prediction obtained by integrating the Berry curvature over our pumping trajectory (solid curve). The uncertainty bars represent the 95% confidence interval.

topological invariants [39–41]. Since in our lattice the topological index is set by the rf phase, a bulk topological junction can be generated by replacing the rf field with an additional copropagating pair of Raman laser beams in which just one beam has an abrupt π phase shift in its center. This provides a static model of the soliton excitation mode in polyacetylene [25,42]. Terminating our lattice with hard-wall boundaries gives rise to similar end states—somewhat analogous to Majorana fermions in 1D topological superconductors [40,43]—with a spin character.

We appreciate the constructive discussions with W. D. Phillips, E. Mueller, L. J. LeBlanc, and L. Wang. This work was partially supported by the ARO’s Atomtronics MURI, and by the AFOSR’s Quantum Matter MURI, NIST, and the NSF through the PFC at the JQI. M. S. was supported by Ampère Scholarships of Excellence of the École Normale Supérieure (ENS) de Lyon. S. S. acknowledges support from JSPS Postdoctoral Fellowship for research abroad.

*ian.spielman@nist.gov

- [1] F. Mei, J.-B. You, D.-W. Zhang, X. C. Yang, R. Fazio, S.-L. Zhu, and L. C. Kwek, *Phys. Rev. A* **90**, 063638 (2014).
- [2] D.-W. Zhang, F. Mei, Z.-Y. Xue, S.-L. Zhu, and Z. D. Wang, *Phys. Rev. A* **92**, 013612 (2015).
- [3] L. Wang, M. Troyer, and X. Dai, *Phys. Rev. Lett.* **111**, 026802 (2013).
- [4] R. Wei and E. J. Mueller, *Phys. Rev. A* **92**, 013609 (2015).
- [5] T.-S. Zeng, C. Wang, and H. Zhai, *Phys. Rev. Lett.* **115**, 095302 (2015).
- [6] P. Marra, R. Citro, and C. Ortix, *Phys. Rev. B* **91**, 125411 (2015).
- [7] N. R. Cooper and A. M. Rey, *Phys. Rev. A* **92**, 021401 (2015).
- [8] D. J. Thouless, *Phys. Rev. B* **27**, 6083 (1983).
- [9] Q. Niu and D. J. Thouless, *J. Phys. A* **17**, 2453 (1984).
- [10] M. Switkes, C. M. Marcus, K. Campman, and A. C. Gossard, *Science* **283**, 1905 (1999).
- [11] M. D. Blumenthal, B. Kaestner, L. Li, S. Giblin, T. J. B. M. Janssen, M. Pepper, D. Anderson, G. Jones, and D. A. Ritchie, *Nat. Phys.* **3**, 343 (2007).
- [12] B. Kaestner, V. Kashcheyevs, S. Amakawa, M. D. Blumenthal, L. Li, T. J. B. M. Janssen, G. Hein, K. Pierz, T. Weimann, U. Siegner *et al.*, *Phys. Rev. B* **77**, 153301 (2008).
- [13] V. I. Talyanskii, J. M. Shilton, M. Pepper, C. G. Smith, C. J. B. Ford, E. H. Linfield, D. A. Ritchie, and G. A. C. Jones, *Phys. Rev. B* **56**, 15180 (1997).
- [14] M. Möttönen, J. J. Vartiainen, and J. P. Pekola, *Phys. Rev. Lett.* **100**, 177201 (2008).
- [15] S. Nakajima, T. Tomita, S. Taie, T. Ichinose, H. Ozawa, L. Wang, M. Troyer, and Y. Takahashi, *Nat. Phys.* **12**, 296 (2016).
- [16] M. Lohse, C. Schweizer, O. Zilberberg, M. Aidelsburger, and I. Bloch, *Nat. Phys.* **12**, 350 (2016).
- [17] E. Yaschenko, L. Fu, L. Resca, and R. Resta, *Phys. Rev. B* **58**, 1222 (1998).
- [18] R. Resta, *J. Phys. Condens. Matter* **12**, R107 (2000).
- [19] Y. Qian, M. Gong, and C. Zhang, *Phys. Rev. A* **84**, 013608 (2011).
- [20] D. J. Thouless, M. Kohmoto, M. P. Nightingale, and M. den Nijs, *Phys. Rev. Lett.* **49**, 405 (1982).
- [21] G. Jotzu, M. Messer, R. Desbuquois, M. Lebrat, T. Uehlinger, D. Greif, and T. Esslinger, *Nature (London)* **515**, 237 (2014).
- [22] L. Duca, T. Li, M. Reitter, I. Bloch, M. Schleier-Smith, and U. Schneider, *Science* **347**, 288 (2015).
- [23] M. Aidelsburger, M. Lohse, C. Schweizer, M. Atala, J. T. Barreiro, S. Nascimbène, N. R. Cooper, I. Bloch, and N. Goldman, *Nat. Phys.* **11**, 162 (2015).
- [24] S.-Q. Shen, *Topological Insulators: Dirac Equation in Condensed Matters* (Springer, New York, 2012), Vol. 174.
- [25] W. P. Su, J. R. Schrieffer, and A. J. Heeger, *Phys. Rev. Lett.* **42**, 1698 (1979).
- [26] M. J. Rice and E. J. Mele, *Phys. Rev. Lett.* **49**, 1455 (1982).
- [27] D. Xiao, M.-C. Chang, and Q. Niu, *Rev. Mod. Phys.* **82**, 1959 (2010).
- [28] M. Atala, M. Aidelsburger, J. T. Barreiro, D. Abanin, T. Kitagawa, E. Demler, and I. Bloch, *Nat. Phys.* **9**, 795 (2013).
- [29] K. Jiménez-García, L. J. LeBlanc, R. A. Williams, M. C. Beeler, A. R. Perry, and I. B. Spielman, *Phys. Rev. Lett.* **108**, 225303 (2012).
- [30] L. W. Cheuk, A. T. Sommer, Z. Hadzibabic, T. Yefsah, W. S. Bakr, and M. W. Zwierlein, *Phys. Rev. Lett.* **109**, 095302 (2012).
- [31] G. Juzeliūnas and I. B. Spielman, *New J. Phys.* **14**, 123022 (2012).
- [32] N. Lundblad, S. Ansari, Y. Guo, and E. Moan, *Phys. Rev. A* **90**, 053612 (2014).
- [33] The data presented in Fig. 2 contain a small correction from the known imperfect state rotation.
- [34] See Supplemental Material at <http://link.aps.org/supplemental/10.1103/PhysRevLett.116.200402> for simulations of classical pumps, Berry curvatures and geometric pumps at nonzero, and other experimental details.
- [35] A. Ramanathan, S. R. Muniz, K. C. Wright, R. P. Anderson, W. D. Phillips, K. Helmerson, and G. K. Campbell, *Rev. Sci. Instrum.* **83**, 083119 (2012).
- [36] The effective mass in the lattice can increase the period.
- [37] W. Bao, D. Jaksch, and P. A. Markowich, *J. Comput. Phys.* **187**, 318 (2003).
- [38] M. B. Dahan, E. Peik, J. Reichel, Y. Castin, and C. Salomon, *Phys. Rev. Lett.* **76**, 4508 (1996).
- [39] J. Ruostekoski, J. Javanainen, and G. V. Dunne, *Phys. Rev. A* **77**, 013603 (2008).
- [40] M. Z. Hasan and C. L. Kane, *Rev. Mod. Phys.* **82**, 3045 (2010).
- [41] S. Ganeshan, K. Sun, and S. D. Sarma, *Phys. Rev. Lett.* **110**, 180403 (2013).
- [42] A. J. Heeger, S. Kivelson, J. R. Schrieffer, and W. P. Su, *Rev. Mod. Phys.* **60**, 781 (1988).
- [43] S. Nadj-Perge, I. K. Drozdov, J. Li, H. Chen, S. Jeon, J. Seo, A. H. MacDonald, B. A. Bernevig, and A. Yazdani, *Science* **346**, 602 (2014).

BIBLIOGRAPHY

- [1] "SOURCE: National Science Foundation, National Center for Science and Engineering Statistics, Survey of Research and Development at Universities and Colleges, 2008, Integrated Science and Engineering Resources Data System (WebCASPAR), 2016.
- [2] J R Abo-Shaer, C Raman, J M Vogels, and W Ketterle. Observation of vortex lattices in Bose-Einstein condensates. *Science*, 292(5516):476–479, 2001.
- [3] M. Aidelsburger, M. Atala, M. Lohse, J. T. Barreiro, B. Paredes, and I. Bloch. Realization of the Hofstadter Hamiltonian with Ultracold Atoms in Optical Lattices. *Physical Review Letters*, 111(18):185301, oct 2013.
- [4] M. Aidelsburger, M. Lohse, C. Schweizer, M. Atala, J. T. Barreiro, S. Nascimbène, N. R. Cooper, I. Bloch, and N. Goldman. Measuring the Chern number of Hofstadter bands with ultracold bosonic atoms. pages 1–18, 2014.
- [5] K Aikawa, A Frisch, M Mark, S Baier, R Grimm, and F Ferlaino. Reaching Fermi degeneracy via universal dipolar scattering. *Phys. Rev. Lett.*, 112(1):10404, jan 2014.
- [6] B. P. Anderson, P. C. Haljan, C. A. Regal, D. L. Feder, L. A. Collins, C. W. Clark, and E. A. Cornell. Watching dark solitons decay into vortex rings in a Bose-Einstein condensate. *Physical Review Letters*, 86(14):2926–2929, 2001.
- [7] M H Anderson, J R Ensher, M R Matthews, C E Wieman, and E A Cornell. Observation of Bose-Einstein Condensation in a Dilute Atomic Vapor. *Science*, 269, 1995.
- [8] Neil W. Ashcroft and N. David Mermin. *Solid State Physics*. Saunders College Publishing, Philadelphia, 1976.
- [9] R C Ashoori, H L Stormer, L N Pfeiffer, K W Baldwin, and K West. Edge magnetoplasmons in the time domain. *Phys. Rev. B*, 45(7):3894–3897, feb 1992.
- [10] Marcos Atala, Monika Aidelsburger, Michael Lohse, Julio T. Barreiro,

- Belén Paredes, and Immanuel Bloch. Observation of chiral currents with ultracold atoms in bosonic ladders. *Nature Physics*, 10(July):588–593, 2014.
- [11] Timothy J. Atherton, Ramón S. Barthelemy, Wouter Deconinck, Michael L. Falk, Savannah Garmon, Elena Long, Monica Plisch, Elizabeth H. Simmons, and Kyle Reeves. *LGBT Climate in Physics: Building an Inclusive Community*. American Physical Society, College Park, MD, 2016.
- [12] Carrie N. Baker. The Emergence of Organized Feminist Resistance to Sexual Harassment in the United States in the 1970s. *Journal of Women’s History*, 19(3):161–184, 2007.
- [13] Waseem S Bakr, Jonathon I Gillen, Amy Peng, Simon Fölling, and Markus Greiner. A quantum gas microscope for detecting single atoms in a Hubbard-regime optical lattice. *Nature*, 462(7269):74–77, 2009.
- [14] Michael Balter. After the ACCUSATION: A complex case of alleged sexual misconduct rattles a field and signals a cultural shift. *Science*, 351(6274):652–657, 2016.
- [15] Victoria L. Banyard, Mary M. Moynihan, and Elizabeth G. Plante. Sexual violence prevention through bystander education: An experimental evaluation. *Journal of Community Psychology*, 35(4):463–481, 2007.
- [16] Weizhu Bao, Dieter Jaksch, and Peter A Markowich. Numerical solution of the Gross-Pitaevskii equation for Bose-Einstein condensation. *Journal of Computational Physics*, 187(1):318–342, 2003.
- [17] Ryan P Barone, Jennifer R Wolgemuth, and Chris Linder. Preventing sexual assault through engaging college men. *Journal of College Student Development*, 48(5):585–594, 2007.
- [18] M Bartenstein, A Altmeyer, S Riedl, S Jochim, C Chin, J Hecker Denschlag, and R Grimm. Collective excitations of a degenerate gas at the BEC-BCS crossover. *Phys. Rev. Lett.*, 92(20):203201, 2004.
- [19] Ramón S Barthelemy, Melinda McCormick, and Charles Henderson. Gender Discrimination in Physics and Astronomy : Graduate Student Experiences of Sexism and Gender Microaggressions. *Private Communications*, pages 1–28, 2016.
- [20] C. Becker, S. Stellmer, P. Soltan-Panahi, S. Dörscher, M. Baumert, E. M.

- Richter, J. Kronjäger, K. Bongs, and K. Sengstock. Oscillations and interactions of dark and dark-bright solitons in Bose-Einstein condensates. *Nature Physics*, 4(June):9, 2008.
- [21] Jennifer L Berdahl. The sexual harassment of uppity women. *The Journal of applied psychology*, 92(2):425–437, 2007.
- [22] Thorseten Best. *Interacting Bose-Fermi mixtures in optical lattices*. PhD thesis, Johannes Gutenberg-Universität, 2010.
- [23] O Boada, A Celi, J I Latorre, and M Lewenstein. Quantum Simulation of an Extra Dimension. *Phys. Rev. Lett.*, 108(13):133001, mar 2012.
- [24] Octavi Boada, Alessio Celi, Maciej Lewenstein, Javier Rodríguez-Laguna, and José I Latorre. Quantum simulation of non-trivial topology. *arXiv:1409.4770*, sep 2014.
- [25] T Bourdel, L Khaykovich, J Cubizolles, J Zhang, F Chevy, M Teichmann, L Tarruell, S J J M F Kokkelmans, and C Salomon. Experimental study of the BEC-BCS crossover region in Lithium 6. *Phys. Rev. Lett.*, 93(5):50401, 2004.
- [26] R Bracewell. *The Fourier Transform and its Applications*. McGraw-Hill, New York, 1965.
- [27] Susan Brownmiller and Dolores Alexander. From Carmita Wood to Anita Hill. *Ms*, 2(4):70, jan 1992.
- [28] Ch Buggle, J. Leonard, W. Von Klitzing, and J. T M Walraven. Interferometric determination of the s and d-wave scattering amplitudes in ^{87}Rb . *Physical Review Letters*, 93(17):1–4, 2004.
- [29] Nathaniel Q Burdick, Andrew G Sykes, Yijun Tang, and Benjamin L Lev. Anisotropic collisions of dipolar Bose-Einstein condensates in the universal regime. *arXiv:1607.06743v1*.
- [30] S Burger, K Bongs, S Dettmer, W Ertmer, and K Sengstock. Dark Solitons in Bose-Einstein Condensates. *Physical Review Letters* 83, 83(25):5198–5201, 1999.
- [31] M Büttiker. Absence of backscattering in the quantum Hall effect in multiprobe conductors. *Phys. Rev. B*, 38(14):9375–9389, nov 1988.

- [32] D Cantor and WB Fisher. Report on the AAU Campus Climate Survey on Sexual Assault and Sexual Misconduct Assault and Sexual Misconduct. *Sexualassaulttaskforce.Harvard.Edu*, 3129(301), 2015.
- [33] L. L. Carli, L. Alawa, Y. Lee, B. Zhao, and E. Kim. Stereotypes About Gender and Science: Women = Scientists. *Psychology of Women Quarterly*, 2016.
- [34] Y. Castin and R. Dum. Bose-Einstein Condensates in Time Dependent Traps. *Physical Review Letters*, 77(27):5315–5319, dec 1996.
- [35] A Celi, P Massignan, J Ruseckas, N Goldman, I. B. Spielman, G. Juzelinas, and M Lewenstein. Synthetic Gauge Fields in Synthetic Dimensions. *Physical Review Letters*, 112(4):043001, jan 2014.
- [36] R. G. Chambers. Shift of an electron interference pattern by enclosed magnetic flux. *Physical Review Letters*, 5(1):3–5, 1960.
- [37] Lawrence Cheuk, Ariel Sommer, Zoran Hadzibabic, Tarik Yefsah, Waseem Bakr, and Martin Zwierlein. Spin-Injection Spectroscopy of a Spin-Orbit Coupled Fermi Gas. *Phys. Rev. Lett.*, 109(9):95302, aug 2012.
- [38] A P Chikkatur, A Görlitz, D M Stamper-Kurn, S Inouye, S. Gupta, and W Ketterle. Suppression and Enhancement of Impurity Scattering in a Bose-Einstein Condensate. *Phys. Rev. Lett.*, 85:483, 2000.
- [39] Cheng Chin, Rudolf Grimm, Paul Julienne, and Eite Tiesinga. Feshbach resonances in ultracold gases. *Rev. Mod. Phys.*, 82(2):1225–1286, 2010.
- [40] Kathryn B H Clancy, Robin G. Nelson, Julienne N. Rutherford, and Katie Hinde. Survey of Academic Field Experiences (SAFE): Trainees report harassment and assault. *PLoS ONE*, 9(7):1–9, 2014.
- [41] S. P. Cockburn, H. E. Nistazakis, T. Phorikis, P. G. Kevrekidis, N. P. Proukakis, D. J. Frantzeskakis, T P Horikis, P G Kevrekidis, N P Proukakis, and D J Frantzeskakis. Fluctuating and dissipative dynamics of dark solitons in quasicondensates. *Physical Review A*, 84(4):43640, 2011.
- [42] S L Cornish, N R Claussen, J L Roberts, E A Cornell, and C E Wieman. Stable Rb-85 Bose-Einstein condensates with widely tunable interactions. *Phys. Rev. Lett.*, 85(9):1795–1798, 2000.

- [43] John H. Davies. *The physics of low-dimensional semiconductors: an introduction*. Cambridge University Press, Cambridge, UK, 1998.
- [44] B DeMarco. *Quantum Behavior of an Atomic Fermi Gas*. PhD thesis, University of Colorado, 2001.
- [45] B DeMarco, J L Bohn, J P Burke, M Holland, and D S Jin. Measurement of p -wave threshold law using evaporatively cooled Fermionic atoms. *Phys. Rev. Lett.*, 82(21):4208–4211, 1999.
- [46] B DeMarco and D S Jin. Onset of Fermi degeneracy in a trapped atomic gas. *Science*, 285(5434):1703–1706, 1999.
- [47] J. Denschlag. Generating Solitons by Phase Engineering of a Bose-Einstein Condensate. *Science*, 287(5450):97–101, 2000.
- [48] M Edwards, B Benton, J Heward, and C W Clark. Momentum-space engineering of gaseous Bose-Einstein condensates. *Phys. Rev. A*, 82(6):63613, 2010.
- [49] Dmitry K. Efimkin, Johannes Hofmann, and Victor Galitski. Non-Markovian quantum friction of bright solitons in superfluids. *Physical Review Letters*, 116:225301, 2016.
- [50] A. Einstein. On the Movement of Small Particles Suspended in Stationary Liquids Required by the Molecular-Kinetic Theory of Heat. *Annalen der Physik*, 17:549–560, 1905.
- [51] Fang Fang, Ryan Olf, Shun Wu, Holger Kadau, and Dan M. Stamper-Kurn. Condensing magnons in a degenerate ferromagnetic spinor Bose gas. *Phys. Rev. Lett.*, 116:095301, 2016.
- [52] P O Fedichev, A E Muryshev, and G V Shlyapnikov. Dissipative dynamics of a kink state in a Bose-condensed gas. *Phys. Rev. A*, 60(4):3220, 1999.
- [53] M C Geisler, J H Smet, V Umansky, K von Klitzing, B Naundorf, R Ketzmerick, and H Schweizer. Detection of a Landau Band-Coupling-Induced Rearrangement of the Hofstadter Butterfly. *Phys. Rev. Lett.*, 92(25):256801, jun 2004.
- [54] D. Genkina, L. M. Aycok, B. K. Stuhl, H. I. Lu, R. A. Williams, and I. B. Spielman. Feshbach enhanced s -wave scattering of fermions: Direct

- observation with optimized absorption imaging. *New Journal of Physics*, 18(1), 2016.
- [55] Kurt Gibble, Seongsik Chang, and Ronald Legere. Direct Observation of *s*-Wave Atomic Collisions. 75(14):2666–2669, 1995.
- [56] Allison J. Gonsalves. "Physics and the girly girl—there is a contradiction somewhere": Doctoral students' positioning around discourses of gender and competence in physics. *Cultural Studies of Science Education*, 9(2):503–521, 2014.
- [57] M Greiner. *Ultracold quantum gases in three-dimensional optical lattice potentials*. PhD thesis, Ludwig-Maximilians-Universität München, 2003.
- [58] M Greiner, C A Regal, and D S Jin. Emergence of a molecular Bose-Einstein condensate from a Fermi gas. *Nature*, 426(6966):537–540, 2003.
- [59] Markus Greiner, Immanuel Bloch, Olaf Mandel, Theodor Hänsch, and Tilman Esslinger. Exploring Phase Coherence in a 2D Lattice of Bose-Einstein Condensates. *Phys. Rev. Lett.*, 87(16), oct 2001.
- [60] R Grimm, M Weidemüller, and Y Ovchinnikov. Optical dipole trap for neutral atoms. *Adv. At. Mol. Opt. Phys.*, 42:95, 2000.
- [61] Daniel Z. Grunspan, Sarah L. Eddy, Sara E. Brownell, Benjamin L. Wiggins, Alison J. Crowe, and Steven M. Goodreau. Males Under-Estimate Academic Performance of Their Female Peers in Undergraduate Biology Classrooms. *Plos One*, 11(2):e0148405, 2016.
- [62] M Hafezi, S Mittal, J Fan, A Migdall, and J M Taylor. Imaging topological edge states in silicon photonics. *Nat. Photon.*, 7(12):1001–1005, oct 2013.
- [63] Amy Harmon. Chicago Professor Resigns Amid Sexual Misconduct Investigation. *The New York Times*, page A11, feb 2016.
- [64] P G Harper. Single Band Motion of Conduction Electrons in a Uniform Magnetic Field. *Proc. Phys. Soc. A*, 68:874–878, 1955.
- [65] M Z Hasan and C L Kane. Colloquium: Topological insulators. *Rev. Mod. Phys.*, 82(4):3045–3067, nov 2010.

- [66] Akira Hasegawa and Masayuki Matsumoto. *Optical solitons in fibers*, volume 2. Springer-Verlag, Heidelberg, third edition, 2003.
- [67] Zahra Hazari, Geoff Potvin, Robynne M. Lock, Florin Lung, Gerhard Sonnert, and Philip M. Sadler. Factors that affect the physical science career interest of female students: Testing five common hypotheses. *Physical Review Special Topics - Physics Education Research*, 9(2):1–8, 2013.
- [68] Douglas R Hofstadter. Energy levels and wave functions of Bloch electrons in rational and irrational magnetic fields. *Phys. Rev. B*, 14(6):2239–2249, sep 1976.
- [69] Kerson Huang. *Introduction to Statistical Physics*. CRC Press, Boca Raton, USA, 2001.
- [70] Dario Hügél and Belén Paredes. Chiral ladders and the edges of quantum Hall insulators. *Phys. Rev. A*, 89(2):23619, feb 2014.
- [71] B Hunt, J D Sanchez-Yamagishi, A F Young, M Yankowitz, B J LeRoy, K Watanabe, T Taniguchi, P Moon, M Koshino, P Jarillo-Herrero, and R C Ashoori. Massive Dirac Fermions and Hofstadter Butterfly in a van der Waals Heterostructure. *Science*, 340:1427, 2013.
- [72] REMUS ILIES, NANCY HAUSERMAN, SUSAN SCHWOCHAU, and JOHN STIBAL. Reported Incidence Rates of Work-Related Sexual Harassment in the United States: Using Meta-Analysis To Explain Reported Rate Disparities. *Personnel Psychology*, 56(3):607–631, 2003.
- [73] S Inouye, M R Andrews, J Stenger, H J Miesner, D M Stamper-Kurn, and W Ketterle. Observation of Feshbach resonances in a Bose-Einstein condensate. *Nature*, 392(6672):151–154, 1998.
- [74] D Jaksch and P Zoller. Creation of effective magnetic fields in optical lattices: the Hofstadter butterfly for cold neutral atoms. *New. J. Phys.*, 5:56, 2003.
- [75] Liang Jiang, Takuya Kitagawa, Jason Alicea, A. R. Akhmerov, David Pekker, Gil Refael, J. Ignacio Cirac, Eugene Demler, Mikhail D. Lukin, and Peter Zoller. Majorana fermions in equilibrium and in driven cold-atom quantum wires. *Physical Review Letters*, 106(22):1–4, 2011.
- [76] K. Jiménez-García, R. L. Compton, Y.-J. J. Lin, W. D. Phillips, J. V. Porto,

- and I. B. Spielman. Phases of a two-dimensional bose gas in an optical lattice. *Physical Review Letters*, 105(11):20–23, sep 2010.
- [77] Karina Jimenez-Garcia. *Artificial gauge fields for ultracold neutral atoms*. PhD thesis, Joint Quantum Institute, National Institute of Standards and Technology, and the University of Maryland, 2012.
- [78] S Jochim, M Bartenstein, A Altmeyer, G Hendl, S Riedl, C Chin, J Hecker Denschlag, and R Grimm. Bose-Einstein condensation of molecules. *Science*, 302(5653):2101–2103, 2003.
- [79] Gregor Jotzu, Michael Messer, Rémi Desbuquois, Martin Lebrat, Thomas Uehlinger, Daniel Greif, and Tilman Esslinger. Experimental realization of the topological Haldane model with ultracold fermions. *Nature*, 515(7526):237–240, nov 2014.
- [80] Mehran Kardar. *Statistical Physics of Particles*. Cambridge University Press, Cambridge, UK, 2007.
- [81] K Kern, D Heitmann, P Grambow, Y H Zhang, and K Ploog. Collective excitations in antidots. *Phys. Rev. Lett.*, 66(12):1618–1621, mar 1991.
- [82] G O Konstantinidis, M Pappa, G Wikstroem, P C Condylis, D Sahagun, M Baker, O Morizot, and W von Klitzing. Atom number calibration in absorption imaging at very small atom numbers. *Central European Journal Of Physics*, 10(5):1054–1058, 2012.
- [83] Mark J H Ku, Wenjie Ji, Biswaroop Mukherjee, Elmer Guardado-Sanchez, Lawrence W. Cheuk, Tarik Yefsah, and Martin W. Zwierlein. Motion of a solitonic vortex in the BEC-BCS crossover. *Physical Review Letters*, 113(6):1–5, 2014.
- [84] R Laughlin. Quantized Hall conductivity in two dimensions. *Phys. Rev. B*, 23(10):5632–5633, may 1981.
- [85] L. J. Leblanc, M. C. Beeler, K Jiménez-García, A. R. Perry, S. Sugawa, R. A. Williams, and I. B. Spielman. Direct observation of zitterbewegung in a Bose-Einstein condensate. *New Journal of Physics*, 15(7):73011, 2013.
- [86] E. M. Lifschitz and L. P Pitaevskii. *Physical kinetics*, volume 10. Butterworth-Heinenann, Oxford, 1983.

- [87] Y.-J. J. Lin, A. R. Perry, R. L. Compton, I. B. Spielman, and J. V. Porto. Rapid production of ^{87}Rb Bose-Einstein condensates in a combined magnetic and optical potential. *Physical Review A - Atomic, Molecular, and Optical Physics*, 79(6):1–8, 2009.
- [88] Y.-J. J. Lin, R. L. Compton, K. Jimenez-Garcia, J. V. Porto, I. B. Spielman, K. Jiménez-García, J. V. Porto, and I. B. Spielman. Synthetic magnetic fields for ultracold neutral atoms. *Nature*, 462(7273):628–632, 2009.
- [89] Christine Logel, Gregory M Walton, Steven J Spencer, Emma C Iserman, William von Hippel, and Amy E Bell. Interacting with sexist men triggers social identity threat among female engineers. *Journal of personality and social psychology*, 96(6):1089–103, 2009.
- [90] M Lu, N Q Burdick, and B L Lev. Quantum degenerate dipolar Fermi gas. *Phys. Rev. Lett.*, 108(21):215301, may 2012.
- [91] V J Magley, C L Hulin, L F Fitzgerald, and M DeNardo. Outcomes of self-labeling sexual harassment. *The Journal of applied psychology*, 84(3):390–402, 1999.
- [92] Jan A Makkinje. An Analysis of Physics Graduate Admission Data. 02215:2–4, 2015.
- [93] M Mancini, G Pagano, G Cappellini, L Livi, M Rider, J Catani, C Sias, P Zoller, M Inguscio, M Dalmonte, and L Fallani. Observation of chiral edge states with neutral fermions in synthetic Hall ribbons. *Science*, 349(6255):1510–1513, 2015.
- [94] Antonio Muñoz Mateo and Joachim Brand. Stability and dispersion relations of three-dimensional solitary waves in trapped Bose-Einstein condensates. *New Journal of Physics*, 17(12):125013, 2015.
- [95] Harold J. Metcalf and Peter van der Straten. *Laser Cooling and Trapping*. Springer-Verlag, New York, 1999.
- [96] Gwendolyn Mink. *Hostile Environment: the Political Betrayal of Sexually Harassed Women*. Cornell University Press, Ithaca, NY, 2000.
- [97] Hirokazu Miyake, Georgios a. Siviloglou, Colin J. Kennedy, William Cody Burton, and Wolfgang Ketterle. Realizing the Harper Hamiltonian with

- Laser-Assisted Tunneling in Optical Lattices. *Physical Review Letters*, 111(18):185302, oct 2013.
- [98] C Monroe, E Cornell, C Sackett, C Myatt, and C Wieman. Measurement of Cs-Cs elastic scattering at $T = 30 \mu\text{K}$. *Phys. Rev. Lett.*, 70(4):414–417, 1993.
- [99] G Montambaux. Semiclassical quantization of skipping orbits. *Eur. Phys. J. B*, 79(2):215–224, jan 2011.
- [100] Liberty J. Munson, Andrew G. Miner, and Charles Hulin. Labeling sexual harassment in the military: An extension and replication. *Journal of Applied Psychology*, 86(2):293–303, 2001.
- [101] a. Muryshev, G. V. Shlyapnikov, W. Ertmer, K. Sengstock, and M. Lewenstein. Dynamics of Dark Solitons in Elongated Bose-Einstein Condensates. *Physical Review Letters*, 89(11):110401, 2002.
- [102] Chetan Nayak, Steven H. Simon, Ady Stern, Michael Freedman, Sankar Das Sarma, and Sankar Das Sarma. Non-Abelian anyons and topological quantum computation. *Reviews of Modern Physics*, 80(3):1083–1159, 2008.
- [103] K M O’Hara, M E Gehm, S R Granade, and J E Thomas. Scaling laws for evaporative cooling in time-dependent optical traps. *Phys. Rev. A*, 64(5):51403, oct 2001.
- [104] K M O’Hara, S L Hemmer, M E Gehm, S R Granade, and J E Thomas. Observation of a Strongly Interacting Degenerate Fermi Gas of Atoms. *Science*, 298(5601):2179–2182, 2002.
- [105] Ryan Olf, Fang Fang, G Edward Marti, Andrew MacRae, and Dan M. Stamper-Kurn. Thermometry and cooling of a Bose-Einstein condensate to 0.02 times the critical temperature. *Nature Physics*, 11(September):06196, 2015.
- [106] N. G. Parker, N. P. Proukakis, and C. S. Adams. Dark soliton decay due to trap anharmonicity in atomic Bose-Einstein condensates. *Physical Review A - Atomic, Molecular, and Optical Physics*, 81(3):1–10, 2010.
- [107] C J Pethick and H Smith. *Bose-Einstein Condensation in Dilute Gases*. Cambridge University Press, Cambridge, second edi edition, 2008.

- [108] Geoff Potvin, Zahra Hazari, Robert H. Tai, and Philip M. Sadler. Unraveling bias from student evaluations of their high school science teachers. *Science Education*, 93(5):827–845, 2009.
- [109] C A Regal. Experimental realization of BCS-BEC crossover physics with a Fermi gas of atoms. *PhD Thesis*, pages 1–149, 2006.
- [110] C. A. Regal, M. Greiner, and D. S. Jin. Lifetime of Molecule-Atom Mixtures near a Feshbach Resonance in $^4\text{K}/\text{mI}$. *Physical Review Letters*, 92(8):083201, 2004.
- [111] C A Regal, M Greiner, and D S Jin. Observation of resonance condensation of fermionic atom pairs. *Phys. Rev. Lett.*, 92(4), 2004.
- [112] C A Regal and D S Jin. Measurement of positive and negative scattering lengths in a Fermi gas of atoms. *Phys. Rev. Lett.*, 90(23):230404, 2003.
- [113] G Reinaudi, T Lahaye, Z Wang, and D Guéry-Odelin. Strong saturation absorption imaging of dense clouds of ultracold atoms. *Opt. Lett.*, 32(21):3143–3145, 2007.
- [114] Christina R. Richey, Kathryn B H Clancy, Katharine M Lee, and Erica Rodgers. The CSWA Survey on Workplace Climate. 2015.
- [115] V Schweikhard, I Coddington, P Engels, V P Mogendorff, and E a Cornell. Rapidly rotating Bose-Einstein condensates in and near the lowest Landau level. *Physical review letters*, 92(4):040404, 2004.
- [116] Carroll Seron, Susan S. Silbey, Erin Cech, and Brian Rubineau. Persistence Is Cultural: Professional Socialization and the Reproduction of Sex Segregation. *Work and Occupations*, 43(2):178–214, 2016.
- [117] Isis H. Settles, Lilia M. Cortina, Janet Malley, and Abigail J. Stewart. The climate for women in academic science: The good, the bad, and the changeable. *Psychology of Women Quarterly*, 30(1):47–58, 2006.
- [118] Jason M Sheltzer and Joan C Smith. Elite male faculty in the life sciences employ fewer women. *Proceedings of the National Academy of Sciences of the United States of America*, 111(28):10107–12, 2014.

- [119] Jacob F Sherson, Christof Weitenberg, Manuel Endres, Marc Cheneau, Immanuel Bloch, and Stefan Kuhr. Single-atom-resolved fluorescence imaging of an atomic Mott insulator. *Nature*, 467(7311):68–72, 2010.
- [120] I B Spielman. Raman processes and effective gauge potentials. *Phys. Rev. A*, 79:63613, 2009.
- [121] Daniel Adam Steck. Rubidium 87 D Line Data, 2010.
- [122] Kevin E Strecker, Guthrie B Partridge, Andrew G Truscott, and Randall G Hulet. Formation and propagation of matter-wave soliton trains. *Nature*, 417(6885):150–153, may 2002.
- [123] J Struck, C Ölschläger, M Weinberg, P Hauke, J Simonet, A Eckardt, M Lewenstein, K Sengstock, and P Windpassinger. Tunable Gauge Potential for Neutral and Spinless Particles in Driven Optical Lattices. *Phys. Rev. Lett.*, 108:225304, 2012.
- [124] B K Stuhl, H.-I Lu, L M Ayccock, D Genkina, and I B Spielman. Visualizing edge states with an atomic Bose gas in the quantum Hall regime. *Science*, 349(6255):1514, 2015.
- [125] N R Thomas, N Kjæ rgaard, P S Julienne, and A C Wilson. Imaging of s and d partial-Wave interference in quantum scattering of identical Bosonic atoms. *Phys. Rev. Lett.*, 93(17):173201, oct 2004.
- [126] R. Thomas, K. O. Roberts, E. Tiesinga, A. C. J. Wade, P. B. Blakie, A. B. Deb, and N. Kjæ rgaard. Multiple scattering dynamics of fermions at an isolated p -wave resonance. *Nature Communications*, 7(May):12069, 2016.
- [127] Tobias Gerard Tiecke. *Feshbach resonances in ultracold mixtures of the fermionic quantum gases 6Li and 40K* . 2010.
- [128] E Timmermans, P Tommasini, M S Hussein, and A Kerman. Feshbach resonances in atomic Bose-Einstein condensates. *Physics Reports-review Section Of Physics Letters*, 315(1-3):199–230, 1999.
- [129] K von Klitzing. The quantized Hall effect. *Rev. Mod. Phys.*, 58:519–531, 1986.
- [130] A. Weller, J. P. Ronzheimer, C. Gross, J. Esteve, M. K. Oberthaler, D. J. Frantzeskakis, G. Theocharis, and P. G. Kevrekidis. Experimental Obser-

- vation of Oscillating and Interacting Matter Wave Dark Solitons. *Physical Review Letters*, 101(13):1–4, 2008.
- [131] Frank Wilczek. Majorana returns. *Nature Physics*, 5(9):614–618, 2009.
- [132] Joan C. Williams, Katherine W. Phillips, and Erika V. Hall. Double jeopardy? Gender Bias Against Women of Color in Science. *WorkLifeLaw*, 2014.
- [133] R. A. Williams, M. C. Beeler, L. J. LeBlanc, K. Jimenez-Garcia, and I. B. Spielman. A Raman-induced Feshbach resonance in an effectively single-component Fermi gas. 2013.
- [134] R. A. Williams, L. J. LeBlanc, K Jiménez-Garcia, M. C. Beeler, A. R. Perry, W. D. Phillips, and I. B. Spielman. Synthetic partial waves in ultracold atomic collisions. *Science*, 335(6066):314–317, 2012.
- [135] Alexandra Witze. Astronomy roiled again by sexual-harassment allegations. *Nature News*, jan 2016.
- [136] Saijun Wu, Ying-Ju Y.-J. Wang, Quentin Diot, and Mara Prentiss. Splitting matter waves using an optimized standing-wave light-pulse sequence. *Phys. Rev. A*, 71(4):43602, 2005.
- [137] E. Zaremba. Sound propagation in a cylindrical Bose-condensed gas. *Phys. Rev. A*, 57(1):57, 1998.
- [138] Chuanwei Zhang, Sumanta Tewari, Roman M Lutchyn, and S Das Sarma. $p_x + ip_y$ Superfluid from s-Wave Interactions of Fermionic Cold Atoms. *Phys. Rev. Lett.*, 101:160401, 2008.
- [139] M Zwierlein, C Stan, C Schunck, S Raupach, A Kerman, and W Ketterle. Condensation of Pairs of Fermionic Atoms near a Feshbach Resonance. *Phys. Rev. Lett.*, 92, 2004.
- [140] M W Zwierlein, C A Stan, C H Schunck, S M F Raupach, S Gupta, Z Hadzibabic, and W Ketterle. Observation of Bose-Einstein condensation of molecules. *Phys. Rev. Lett.*, 91(25):250401, 2003.